



SAIMM

JOURNAL OF THE SOUTHERN AFRICAN INSTITUTE OF MINING AND METALLURGY

VOLUME 117 NO. 5 MAY 2017

We are Leaders in Slurry Systems Engineering

www.PatersonCooke.com



ESTABLISHED 1991



PATERSON & COOKE

We are Leaders in Slurry Systems Engineering

www.PatersonCooke.com



Long Distance Slurry Pipelines

Process Engineering

Mine Backfill and Pastefill

Mine Tailings Systems

Field Services

Plants and Products

Marine and Coastal

Specialist Engineering

Laboratories

Courses

Paterson & Cooke was formed in 1991 as a partnership between Dr. Robert Cooke and Dr. Angus Paterson, with the aim of providing consulting services specializing in hydraulics and hydrotransport to the local mining industry.

Since then the company has grown and extended its range of services so that it now offers comprehensive specialist and slurry handling solutions from its offices in Cape Town and Johannesburg in South Africa, Santiago in Chile, Denver in the USA, Sudbury, Vancouver and Calgary in Canada, Perth in Australia and Cornwall in the UK.

We pride ourselves on the quality of our work and on being able to offer innovative solutions to our clients.

Our engineering operations are supported through comprehensive laboratory services covering rheology, pipe loop tests, pump performance tests, clay behaviour analysis, thickening, filtration, cycloning and backfill material characterization.

Our strength lies in the intellect, commitment and creativity of the people who work for Paterson & Cooke.

CAPE TOWN

Paterson & Cooke Consulting Engineers (Pty) Ltd

Tel +27 (0) 21 531 2955

Fax +27 (0) 86 546 9876

CapeTown@PatersonCooke.com

JOHANNESBURG

Paterson & Cooke Field Services

Tel +27 (0) 86 010 6129

Fax +27 (0) 86 546 9876

Johannesburg@PatersonCooke.com

E S T A B L I S H E D 1 9 9 1



PATERSON & COOKE

QUALITY CRMs

FOR MINING AND EXPLORATION



BUY AMIS MATRIX CRMs

ASSAY STANDARDS PRICED FOR ROUTINE LABORATORY QUALITY CONTROL

- Affordable multi-element "Matrix CRMs"
- Choose from a wide range of AMIS product groups, grades and matrices
- Strong technical support

CREATE CRMs

FROM YOUR OWN ORE

- Improve assay with custom CRMs made from your own ore
- Any batch size from .5 to 5 tonnes
- Shipments accepted from anywhere in the world
- Made according to ISO Guide 34 requirements (for RM producers)
- An ISO 9001:2008 Certified Producer

ROUND ROBINS

JOIN THE AMIS INTER-LABORATORY TESTING SCHEMES

- Assessing mineral laboratory performance against global peers
- For continuous laboratory improvement
- Approximately 50 AMIS proficiency testing schemes (AITS) per year
- According to ISO Guide 43 requirements (for PT schemes)



A Part of
Torre
Industries



www.tuv.com
TÜV Rheinland
ID: 9705069383



TÜV Rheinland[®]
CERT
ISO 9001

ISO 9001:2008
CERTIFIED
COMPANY

WWW.amis.co.za

The Southern African Institute of Mining and Metallurgy

OFFICE BEARERS AND COUNCIL FOR THE 2016/2017 SESSION

Honorary President

Mike Teke
President, Chamber of Mines of South Africa

Honorary Vice-Presidents

Mosebenzi Zwane
Minister of Mineral Resources, South Africa

Rob Davies
Minister of Trade and Industry, South Africa

Naledi Pandor
Minister of Science and Technology, South Africa

President

C. Musingwini

President Elect

S. Ndlovu

Senior Vice-President

A.S. Macfarlane

Junior Vice-President

M. Mthenjane

Immediate Past President

R.T. Jones

Honorary Treasurer

J. Porter

Co-opted Member

Z. Botha

Ordinary Members on Council

V.G. Duke	A.G. Smith
I.J. Geldenhuys	M.H. Solomon
M.F. Handley	M.R. Tlala
W.C. Joughin	D. Tudor
M. Motuku	D.J. van Niekerk
D.D. Munro	A.T. van Zyl
G. Njowa	

Past Presidents Serving on Council

N.A. Barcza	S.J. Ramokgopa
R.D. Beck	M.H. Rogers
J.R. Dixon	D.A.J. Ross-Watt
M. Dworzanowski	G.L. Smith
H.E. James	W.H. van Niekerk
G.V.R. Landman	R.P.H. Willis
J.C. Ngoma	

Branch Chairpersons

Botswana	L.E. Dimbungu
DRC	S. Maleba
Johannesburg	J.A. Luckmann
Namibia	N.M. Namate
Northern Cape	C.A. van Wyk
Pretoria	P. Bredell
Western Cape	C.G. Sweet
Zambia	D. Muma
Zimbabwe	S. Matutu
Zululand	C.W. Mienie

Corresponding Members of Council

Australia:	I.J. Corrans, R.J. Dippenaar, A. Croll, C. Workman-Davies
Austria:	H. Wagner
Botswana:	S.D. Williams
United Kingdom:	J.J.L. Cilliers, N.A. Barcza
USA:	J-M.M. Rendu, P.C. Pistorius

PAST PRESIDENTS

Deceased

- * W. Bettel (1894–1895)
- * A.F. Crosse (1895–1896)
- * W.R. Feldtmann (1896–1897)
- * C. Butters (1897–1898)
- * J. Loevy (1898–1899)
- * J.R. Williams (1899–1903)
- * S.H. Pearce (1903–1904)
- * W.A. Caldecott (1904–1905)
- * W. Cullen (1905–1906)
- * E.H. Johnson (1906–1907)
- * J. Yates (1907–1908)
- * R.G. Bevington (1908–1909)
- * A. McA. Johnston (1909–1910)
- * J. Moir (1910–1911)
- * C.B. Saner (1911–1912)
- * W.R. Dowling (1912–1913)
- * A. Richardson (1913–1914)
- * G.H. Stanley (1914–1915)
- * J.E. Thomas (1915–1916)
- * J.A. Wilkinson (1916–1917)
- * G. Hildick-Smith (1917–1918)
- * H.S. Meyer (1918–1919)
- * J. Gray (1919–1920)
- * J. Chilton (1920–1921)
- * F. Wartenweiler (1921–1922)
- * G.A. Watermeyer (1922–1923)
- * F.W. Watson (1923–1924)
- * C.J. Gray (1924–1925)
- * H.A. White (1925–1926)
- * H.R. Adam (1926–1927)
- * Sir Robert Kotze (1927–1928)
- * J.A. Woodburn (1928–1929)
- * H. Pirow (1929–1930)
- * J. Henderson (1930–1931)
- * A. King (1931–1932)
- * V. Nimmo-Dewar (1932–1933)
- * P.N. Lategan (1933–1934)
- * E.C. Ranson (1934–1935)
- * R.A. Flugge-De-Smidt (1935–1936)
- * T.K. Prentice (1936–1937)
- * R.S.G. Stokes (1937–1938)
- * P.E. Hall (1938–1939)
- * E.H.A. Joseph (1939–1940)
- * J.H. Dobson (1940–1941)
- * Theo Meyer (1941–1942)
- * John V. Muller (1942–1943)
- * C. Biccard Jeppé (1943–1944)
- * P.J. Louis Bok (1944–1945)
- * J.T. McIntyre (1945–1946)
- * M. Falcon (1946–1947)
- * A. Clemens (1947–1948)
- * F.G. Hill (1948–1949)
- * O.A.E. Jackson (1949–1950)
- * W.E. Gooday (1950–1951)
- * C.J. Irving (1951–1952)
- * D.D. Stitt (1952–1953)
- * M.C.G. Meyer (1953–1954)
- * L.A. Bushell (1954–1955)
- * H. Britten (1955–1956)
- * Wm. Bleloch (1956–1957)

Honorary Legal Advisers

Scop Incorporated

Auditors

Messrs R.H. Kitching

Secretaries

The Southern African Institute of Mining and Metallurgy
Fifth Floor, Chamber of Mines Building
5 Hollard Street, Johannesburg 2001 • P.O. Box 61127, Marshalltown 2107
Telephone (011) 834-1273/7 • Fax (011) 838-5923 or (011) 833-8156
E-mail: journal@saimm.co.za

Editorial Board

R.D. Beck
J. Beukes
P. den Hoed
M. Dworzanowski
B. Genc
M.F. Handley
R.T. Jones
W.C. Joughin
J.A. Luckmann
C. Musingwini
S. Ndlovu
J.H. Potgieter
T.R. Stacey
M. Tlala
D.R. Vogt

Editorial Consultant

D. Tudor

Typeset and Published by

The Southern African Institute of Mining and Metallurgy
P.O. Box 61127
Marshalltown 2107
Telephone (011) 834-1273/7
Fax (011) 838-5923
E-mail: journal@saimm.co.za

Printed by

Camera Press, Johannesburg

Advertising Representative

Barbara Spence
Avenue Advertising
Telephone (011) 463-7940
E-mail: barbara@avenue.co.za
The Secretariat
The Southern African Institute of Mining and Metallurgy
ISSN 2225-6253 (print)
ISSN 2411-9717 (online)



THE INSTITUTE, AS A BODY, IS NOT RESPONSIBLE FOR THE STATEMENTS AND OPINIONS ADVANCED IN ANY OF ITS PUBLICATIONS.

Copyright© 1978 by The Southern African Institute of Mining and Metallurgy. All rights reserved. Multiple copying of the contents of this publication or parts thereof without permission is in breach of copyright, but permission is hereby given for the copying of titles and abstracts of papers and names of authors. Permission to copy illustrations and short extracts from the text of individual contributions is usually given upon written application to the Institute, provided that the source (and where appropriate, the copyright) is acknowledged. Apart from any fair dealing for the purposes of review or criticism under *The Copyright Act no. 98, 1978, Section 12*, of the Republic of South Africa, a single copy of an article may be supplied by a library for the purposes of research or private study. No part of this publication may be reproduced, stored in a retrieval system, or transmitted in any form or by any means without the prior permission of the publishers. *Multiple copying of the contents of the publication without permission is always illegal.*

U.S. Copyright Law applicable to users in the U.S.A.

The appearance of the statement of copyright at the bottom of the first page of an article appearing in this journal indicates that the copyright holder consents to the making of copies of the article for personal or internal use. This consent is given on condition that the copier pays the stated fee for each copy of a paper beyond that permitted by Section 107 or 108 of the U.S. Copyright Law. The fee is to be paid through the Copyright Clearance Center, Inc., Operations Center, P.O. Box 765, Schenectady, New York 12301, U.S.A. This consent does not extend to other kinds of copying, such as copying for general distribution, for advertising or promotional purposes, for creating new collective works, or for resale.



SAIMM

JOURNAL OF THE SOUTHERN AFRICAN INSTITUTE OF MINING AND METALLURGY

VOLUME 117 NO. 5 MAY 2017

Contents

Journal Comment by J. Selby	iv
President's Corner—Mine of the Future — A mining CEO's perspective by C. Musingwini	v
Obituary — Emeritus Professor Charles Timothy Shaw by D. Buchanan	vi-vii

HEAVY MINERALS CONFERENCE PAPERS

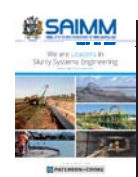
Naturally occurring radioactive materials and the regulatory challenges to the zircon industry by K. Harlow	409
Solid-state reduction of an ilmenite concentrate with carbon by A. Bhalla, C.S. Kucukkargoz, and R.H. Eric	415
Gold and associated industrial heavy minerals in the Icy Cape District: White River to Icy Cape, Alaska, USA by K. Eden, A.E. Grosz, J.E. Grosz, C.J. Giles, and J.Y. Foley	423
Geotechnical characterization and 3D modelling of the biologically cemented Mandena heavy mineral sand deposit - a case study by L.I. Boshoff, A.H. Bracken, and F. Hees	429
The influence of trash minerals and agglomerate particles on spiral separation performance by J. Grobler and J. Zietsman	435

PAPERS OF GENERAL INTEREST

Selection of an appropriate leaching method for light REEs from Esfordi flotation concentrate based on mineral characterization by F. Soltani, M. Abdollahy, S.M. Javad Koleini, and D. Moradkhani	443
Static recrystallization behaviour of Ti-Nb microalloyed high-strength steel by C-Y. Zhou, G-L. Wu, and X-B. Liu	451
Techno-economic feasibility of a pre-oxidation process to enhance prereduction of chromite by E.L.J. Kleynhans, J.P. Beukes, P.G. van Zyl, and J.I.J. Fick	457
Numerical and physical modelling of tundish slag entrainment in the steelmaking process by A. Mabentsela, G. Akdogan, and S. Bradshaw	469
Towards an inclusive model to address unsuccessful mine closures in South Africa by E.S. van Druten and M.C. Bekker	485
Methodology for evaluation of mud rush risk in block caving mining by J. Vallejos, K. Basaure, S. Palma, and R.L. Castro	491
An improved flotation test method and pyrite depression by an organic reagent during flotation in seawater by R.I. Jeldres, D. Calisaya, and L.A. Cisternas	499
The use of fuzzy-weighted binary integer goal programming to select the optimum site for a central processing plant by E. Bakhtavar, D. Khademi, and R. Mikaeil	505

International Advisory Board

R. Dimitrakopoulos, *McGill University, Canada*
D. Dreisinger, *University of British Columbia, Canada*
E. Esterhuizen, *NIOSH Research Organization, USA*
H. Mitri, *McGill University, Canada*
M.J. Nicol, *Murdoch University, Australia*
E. Topal, *Curtin University, Australia*



Journal Comment

The papers in this issue of the *Journal* are selected from the Heavy Minerals Conference held at Sun City from 16–18 August 2016. This conference, which has been held every two years since 1997, is the main technically focused conference covering the heavy minerals industry. The venue moves between various countries where heavy minerals processing is important. The 2016 conference, the 10th in the series, was attended by representatives from 17 countries covering all the major continents.

The three keynote speakers were John Elder from Hatch Africa, Mike Rossouw from the Department of Energy, and Dr Victor Hugo from Iluka Resources. Twenty-five papers were presented covering a wide range of topics from exploration and mining through mineral beneficiation, smelting, and downstream processing.

Performance of, and improvements to, mineral processing equipment was covered by J. Grobler, C. Ramotsabi, W. Slabbert, and H. Baloyi. Topics around the chlorination of titanium feedstocks were presented by H. Kotze, S. Hockaday, and A. Kale. Pyrometallurgy was discussed in papers by D. Zeelie, K. Bisaka, and A. Bhalla.

Heavy minerals from different parts of the world were covered by C. Concalves (Brazil), V. Subramanian (India), L. Boshoff (Madagascar), K. Eden (Alaska), and E. Akon (Bangladesh).

Health and safety issues, which have become increasingly important in the minerals industry were discussed in the paper by Keven Harlow, who presented on a topic that is assuming greater prominence in the minerals industry, namely the impact of international regulations. The paper focused on two aspects – regulations governing the handling of radioactive materials, which are relevant to the processing and sale of zircon, with zircon being classed as a naturally occurring radioactive material, and recent changes to the International Maritime Organization code for transport of bulk materials. The Zircon Industries Association was introduced as a forum for all aspects related to zircon.

Amit Bhalla presented a paper on the solid-state reduction of ilmenite with carbon. The intention of the work was to develop a process to reduce the iron content of ilmenite so as to present a higher titanium feedstock to the smelting process. Optimum particle sizes and temperatures are quoted to achieve an 80% reduction. The metallic particles produced in this process were very small, but suitable as feed to a

leaching process. With the demand for higher grade feedstocks, such work is significant for deposits which contain lower grades of ilmenite.

Dr Karsten Eden presented data on the heavy mineral deposits of the Icy Cape region in Alaska. The paper discussed the history of the deposits and some more recent studies that showed the presence of the usual heavy mineral assemblages in addition to gold. The deposits have previously been worked for gold. Data was presented on the heavy mineral compositions and contents. As the deposits in the traditional mining areas become exhausted, such new deposits will become more important, and smaller quantities of very valuable by-products will be significant in the economics of such projects.

Lysandra Boshoff presented a paper on the geotechnical properties of the Mandena deposit in Madagascar. This deposit is characterized by being particularly hard due to the biological cement between the sand grains. The work reported on the development of a three-dimensional geotechnical model of the deposit to allow the throughput of the dredge mining system to be optimized. The level of cementation in this deposit is unusual in the industry, so without such important management tools the viability of such operations can be adversely affected.

Jac Grobler discussed some of the important variables that control the performance of a spiral separator. The paper looked at the impact of variations in the non-economic minerals in the feed to the unit. Spiral separators have been used for many years in the heavy minerals industry, but often the fundamental science behind their operation has been neglected. Such contributions enhance the understanding of one of our most commonly used tools.

The conference was sponsored very generously by Multotec, Alicoco, Derrick Solutions, Safeway, Tega, Eriez, Polypipe, Mineral Technologies, Weir Minerals, Hatch, and Blue Cube Systems. We are grateful for the support of these sponsors without which the conference would not have been possible.

J. Selby



Mine of the Future – A mining CEO's perspective

The School of Mining Engineering at the University of the Witwatersrand held its 120th anniversary celebration on 23 March 2017. The keynote speaker at this momentous occasion was the Chief Executive Officer (CEO) of Gold Fields Limited, Mr Nick Holland. He spoke passionately about his vision on the Mine of the Future and indicated how Gold Fields was positioning itself for the future. The presentation was extremely insightful and well received by the audience, and I thought I should share with you some of the issues that were articulated.

Does the vision on the Mine of the Future have anything to do with our readership of the Journal or the SAIMM membership in general? I think it is very relevant, because mining professionals must have a sense of, and plan for, how their profession will be affected by decisions shaping the future. This understanding also helps us to participate meaningfully in shaping the future of our industry. I will sketch below an overview of the Mine of the Future as presented by Mr Holland.

The Mine of the Future will be sustainable and create value for all its stakeholders by focusing on four key areas: operating practices and technology, talent and leadership, partnerships with key stakeholders, and governance. The first two areas are directly relevant to professional bodies in the mining industry. Operating practices will entail embracing mechanization and automation, as the technology of the Mine of the Future will be characterized by remote controlled mining operations. The technology should be energy- and water-efficient in view of the increasing scarcity of these resources, which are critical for a successful mining operation. However, this technology will generate attendant 'big data', requiring mining professionals to develop competencies in advanced analytics for converting the data into useful information to enhance cost-effectiveness, productivity improvements, and create safer mining environments. All these technical innovations demand a different skills set from the mining workforce. Therefore mining companies, universities, and professional bodies such as the SAIMM need to work together more closely to develop and train the personnel required for the Mine of the Future.

The mining CEO of the future will be a strategist capable of navigating complex integrated stakeholder management, forging sustainable win-win partnerships, and enforcing regulatory adherence and good governance. Such a CEO is likely to succeed as he or she can enlist the support of shareholders, governments, employees, and communities that are increasingly, and rightfully, demanding to share in the benefits of the resources mined in their jurisdictions.

It is important that educational institutions revisit their curricula so that graduates in mining-related disciplines are adequately prepared for the Mine of the Future. Professional bodies such as the SAIMM need to ensure that continual professional development (CPD) activities embrace the articulation of new technologies, big data analytics, creative leadership, and good governance. This process begins with you!

This edition of the *Journal* contains papers selected from the Heavy Minerals Conference held a few months ago by the SAIMM. Heavy minerals are minerals for the future. Heavy minerals generally occur in placer-type deposits containing zircon, titanium minerals such as ilmenite, rutile, and leucoxene, and other minerals such as staurolite, garnet, and chromite. These deposits are typically formed by gravity concentration of the mineral grains. They are important for the future because developing economies such as China require increasing quantities of zircon for ceramic tiles for urban floor space construction. What will the future heavy mineral sands mine look like? One sure thing is that it will need a more skilled workforce. Preparing that workforce begins with us!

C. Musingwini
President, SAIMM

Obituary — Emeritus Professor Charles Timothy Shaw

Professor Tim Shaw, who died on Friday 21st April at the age of 82, was Emeritus Professor of Mining Engineering at Imperial College London, having retired in 2001 after being appointed to the Chair in Mining Engineering at the Royal School of Mines in 1980. Prior to that he held an academic appointment at the Virginia Polytechnic Institute. He entered the academic environment after a successful career in the South African mining industry where he reached the level of Chief Consulting Engineer with the Johannesburg Consolidated Investment Company. Professor Shaw had extensive experience as a technical consultant and company director and held honorary doctorates from two Central European Universities.

Tim was born into a mining family and spent part of his schooldays at the Consolidated Murchison gold-antimony mine in South Africa, where his father was general manager. Tim was educated at Bishops Diocesan College in Cape Town before going on to study mining engineering at the University of the Witwatersrand, where he met his future wife Tuulike through their shared love of music. He then joined Johannesburg Consolidated Investment Co. Ltd. He was given study leave by JCI to complete an MSc in mineral exploration at McGill in Montreal, Canada.



The traditional training in JCI's underground Witwatersrand gold mines gave Tim a detailed understanding of the practical aspects of mining. This also left him not only with a wonderful ability to communicate with all levels in the hierarchical structure of the South African mining industry, but also a legacy of collateral damage to his hearing. Regardless of the proximity of rockdrills and blasting operations, ear protection was not considered necessary in those days.

Tim's rapid rise within JCI gave him eventual overall technical responsibility for their large gold, platinum, coal, and antimony operations (including Cons Murch) as Chief Consulting Engineer. It was from this elevated appointment and while poised to reach the top position in JCI that he and Tuulike decided that their young family would have a brighter future outside South Africa. Tuulike's family was originally from Estonia and the consequences of political uncertainty on their lives was perhaps a driver. This is how Tim found himself as a Professor at Virginia Polytechnic Institute in the mid-1970s and essentially having to start a completely new career.

After the death of Robert Pryor in 1979 the Chair of Mining Engineering at the Royal School of Mines fell vacant and Imperial College was able to offer the appointment to Tim, so he and his family made their next, but last, big move. Tim brought over his comfortable US sedan and was furious to find challenges in getting it licensed for the road in the UK because it was not compliant with local safety standards – it exceeded them. The fenders on the vehicle were designed for US standards, which meant it would have demolished a local car in a collision and the authorities objected. Tim applied his engineering knowledge to demonstrate the absurdity of this view, and won.

Tim went on to act as a bastion of traditional mining engineering training at Imperial College. He also served a period as Dean of the Royal School of Mines, which gave him the confidence to continue to use the crest on business cards, notwithstanding later official disapproval. The guidance was that only the approved Imperial College London font be used under the re-branding and re-organization that was implemented after his retirement in 2001. He was delighted when the use of the RSM crest was reinstated and the building again became an institution, not just an address.

The slow demise of the undergraduate mining engineering degree at the RSM was due to society's ambivalence towards mining, not Tim's commitment. He launched the European Mining degree with several institutions on the Continent, including Delft and Aachen. This legacy continues as the Joint Master European Mining, Minerals and Environmental Program.

He contributed to the teaching of MSc students in Metals and Energy Finance, together with Imperial College's related continuing professional development programme. He demonstrated time and again that the theoretical relationship between mining finance and technical risk that I taught was simply re-visiting real scenarios that he had been involved in when with JCI. When it came to the transition from technical and financial to business leadership roles at a board level, his extensive experience as a company director brought in the importance of sound decision-making in value creation. Tim could also take a complex case history and break it down into its basic elements, and then illustrate the points from a vast store of apposite anecdotes.

Obituary (*continued*)

Right up to last month we were delivering team teaching to postgraduate students and he was scheduled to deliver a continuing professional development course with me in July. He provided direct support for three MSc dissertations last summer. The only concession made to his age was that at the start of a teaching session we would advise students or delegates of his loss of hearing (notwithstanding the use of the latest electronic aids). I explained that if a question appeared to go unanswered, a wave of the hand would catch his eye. At my suggestion, Tim would then repeat the question to make sure that deafness was not being confused with a decline in cognitive abilities. Often, he would then go on to re-phrase the question as a simple premise, and in doing so would provide the answer.

Tim understood the need not to rest on his laurels and always kept himself academically and professionally up to date. He attended MINExpo 2016 in Las Vegas as part of the meeting of the Society of Mining Professors, of which he was a founding member. The visit to America included the usual mine visits. He was constantly updating his teaching slides and incorporating current technical developments from personal observation.

Tim's knowledge of information technology and the application of computers and operations research in the minerals industry spanned the period from his time as a young engineer with JCI (when he set up their first mainframe) through to the modern age of the internet. He was always harvesting the very latest in audio-visual material for his teaching, putting considerable strain on the processing resources of anything but a top-of-the-range laptop. Yet he also became fascinated with the archaeology of ancient mining through working with academics at Tel Aviv University. He secured numerous research grants in the fields of dimension stone and non-explosive techniques in mining. His academic achievements were recognized by the award of two honorary doctorates.

Tuulike's death in 2009 hit Tim hard and his screensaver was a picture of her which was projected at the start of every lecture he gave. He was never maudlin about her passing, though – she was simply part of his life, past and present, and his annual presence at Glyndebourne was a tradition he continued to observe on her behalf.

It was invaluable working with him on the many shared professional assignments we took on, as he was never happier than when undertaking a site visit – the more remote and challenging the better. He was quite miffed that his family holiday in Botswana last month clashed with my request that he carry out a site visit for me – in Peru. In offering some comfort to him that the mine was at 5000 metres and perhaps it would not be prudent for him to go up to that altitude I got a dusty response. He pointed out that he was brought up on the Highveld and if Grasberg at 4000 metres left him unaffected then Peruvian mines would not be a problem. It was in Botswana that he suffered a stroke and died in Johannesburg on Friday 21st April at the age of 82. A transient ischemic attack he had had three years ago might have been a warning, but if so he did not pay it much heed.

That reflected the essence of the man – a thirst and an enthusiasm for life. While I consciously attempted to capture Tim's fund of knowledge and experience in a new e-learning course we have only just launched on EduMine, there will be no substitute for having him present in the lecture room. He will be sorely missed, but his legacy will continue through the many students he taught.

Professor C. Tim Shaw joined the SAIMM as a Student Member on the 14th October 1960. During his over 56 years of membership with the SAIMM Professor Shaw transferred from Student to Associate in 1966, Associate to Member in 1970 and has been a valued Fellow of the Institute since 1976.

D. Buchanan



CM SOLUTIONS
Metallurgical consultancy & laboratories

maximizing metallurgy



Our four-in-one solution.
We do your test work,
interpret it,
model it
and integrate the results
in metallurgical designs.

Our laboratory areas of expertise

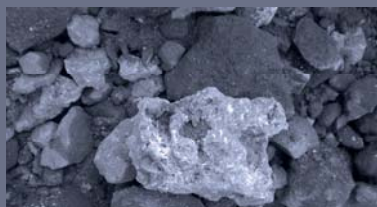
- Mineral processing
- Hydrometallurgy
- Chemical analysis
- Process development
- Solid liquid separation
- Pyrometallurgy



T 011 608 0019
F 011 608 4067
C 082 441 2788
E consultants@cm-solutions.co.za

Pinelands Office Park
Unit T5, 1 Ardeer Road
Modderfontein, 1609
South Africa

Find us on [f](#) [t](#) [in](#) www.cm-solutions.co.za



conductivity leaching test rig calcining wet chemistry sulfides shaking agitation electrowinning
filtration furnace ion exchange **Open tanks** roasting solvent extraction batch tests milling DMS
pressure oxidation TCLP cyclone Isotherms PSD pilot plant cathode kinetics **Cell design**
flocculant screening flotation crushing ICP-OES crushing pyrometallurgy cyanidation attritioning
water analysis thickening pressure oxidation heap pH control solid liquid separation

PAPERS IN THIS EDITION

These papers have been refereed and edited according to internationally accepted standards and are accredited for rating purposes by the South African Department of Higher Education and Training

Heavy Minerals Conference Papers

Naturally occurring radioactive materials and the regulatory challenges to the zircon industry

by K. Harlow

409

This paper summarizes the regulatory processes and their implementation, and highlights the key issues affecting zircon and zirconia.

Solid-state reduction of an ilmenite concentrate with carbon

by A. Bhalla, C.S. Kucukkargoz, and R.H. Eric

415

The solid-state reduction of ilmenite concentrate with graphite under argon atmosphere was studied, with the aim of removing the iron and increasing the titanium oxide content of the ilmenite to produce a high-titanium containing charge for subsequent smelting.

Gold and associated industrial heavy minerals in the Icy Cape District: White River to Icy Cape, Alaska, USA

by K. Eden, A.E. Grosz, J.E. Grosz, C.J. Giles, and J.Y. Foley

423

The Icy Cape District hosts a large and varied body of unconsolidated sediments. The geological framework and textural, mineralogical, and chemical data indicates a large, but as yet incompletely understood, resource potential for gold, garnet, and other heavy minerals.

Geotechnical characterization and 3D modelling of the biologically cemented Mandena heavy mineral sand deposit - a case study

by L.I. Boshoff, A.H. Bracken, and F. Hees

429

Biological cementation of the Mandena heavy mineral sand deposit in Madagascar was causing difficulty in dredge mining. The paper describes an investigation that was conducted to define the distribution and geotechnical properties of the cemented strata in order to generate a site-specific geotechnical model for the deposit. The outcomes were incorporated into the mine and production planning to ultimately optimize operational planning and control.

The influence of trash minerals and agglomerate particles on spiral separation performance

by J. Grobler and J. Zietsman

435

This study illustrates a systematic approach to evaluate spiral separation performance in a case of increased trash mineral content and unliberated minerals in the feed. The performance information was used in a circuit simulation to clearly illustrate the importance of correct setting of the spiral splitter position and resulting spiral mass loading to ensure optimal circuit stability and maximum valuable heavy mineral recovery.

Papers of General Interest

Selection of an appropriate leaching method for light REEs from Esfordi flotation concentrate based on mineral characterization

by F. Soltani, M. Abdollahy, S.M. Javad Koleini, and D. Moradkhani

443

The objective of this study was to determine the type and distribution of rare earth elements (REEs) in phosphate concentrate from the Esfordi flotation plant in order to understand their behaviour from the leaching point of view. Two process options are suggested for treating the Esfordi concentrate to produce phosphoric acid and recover REEs.

Static recrystallization behaviour of Ti-Nb microalloyed high-strength steel

by C-Y. Zhou, G-L. Wu, and X-B. Liu

451

The static recrystallization behaviour of Ti-Nb microalloyed high-strength steel during hot deformation was studied, and the effects of deformation temperature, strain rate, strain, and initial austenite grain size on the static recrystallization fraction determined. The static recrystallization kinetics were modelled, and comparison of the experimental results and predicted results indicated that the effects of deformation parameters on static recrystallization in multi-stage hot deformation are significant.

These papers will be available on the SAIMM website
<http://www.saimm.co.za>

PAPERS IN THIS EDITION

These papers have been refereed and edited according to internationally accepted standards and are accredited for rating purposes by the South African Department of Higher Education and Training

Techno-economic feasibility of a pre-oxidation process to enhance prereduction of chromite
by E.L.J. Kleynhans, J.P. Beukes, P.G. van Zyl, and J.I.J. Fick

457

This paper presents the first attempt at conceptualizing the techno-economic feasibility of integrating chromite pre-oxidation into the prereduction process. Sensitivity analysis indicated that the parameter with the greatest influence on project NPV and IRR is the level of prereduction. The relationship between maintaining the optimum pre-oxidation temperature and the degree of prereduction achieved would therefore be critical for maximum process efficiency.

Numerical and physical modelling of tundish slag entrainment in the steelmaking process
by A. Mabentsela, G. Akdogan, and S. Bradshaw

469

Physical and numerical modelling techniques were used to identify mechanisms for tundish slag entrainment in a bare tundish and one fitted with a flow control device. Two possible mechanisms for slag entrainment are proposed – mass transfer across the steel-slag interface and low- velocity shearing below the interface.

Towards an inclusive model to address unsuccessful mine closures in South Africa
by E.S. van Druten and M.C. Bekker

485

The purpose of this investigation was to determine, categorize, and rank reasons for unsuccessful mine closures. Public and private stakeholders were identified and surveyed through a structured, rank order questionnaire. The findings identified a number of requirements and aspects that should be considered in the development of an integrated mine closure model.

Methodology for evaluation of mud rush risk in block caving mining
by J. Vallejos, K. Basaure, S. Palma, and R.L. Castro

491

The aim of this study was to develop a decision matrix that would enable safe ore extraction from drawpoints at the Diablo Regimiento mine in Chile. The results showed that a criterion for drawpoint ore classification must be developed for each ore type, thus enabling drawpoint operation until the ore reaches its critical value for specific water content.

An improved flotation test method and pyrite depression by an organic reagent during flotation in seawater
by R.I. Jeldres, D. Calisaya, and L.A. Cisternas

499

Rougher flotation of copper-molybdenum sulphide ores in seawater was investigated using a modified Denver cell and a standard commercial cell, and the effect of an organic reagent on the flotation performance tested. The fast/slow-floating model was found to be appropriate for describing the flotation kinetics.

The use of fuzzy-weighted binary integer goal programming to select the optimum site for a central processing plant
by E. Bakhtavar, D. Khademi, and R. Mikaeil

505

A fuzzy-weighted integer goal programming was developed and used to select the most suitable site to construct a central processing plant for several adjacent small-scale dimension stone quarries, based on criteria such as the availability of utilities and labour, distances to quarries and markets, and land price.

These papers will be available on the SAIMM website
<http://www.saimm.co.za>

The best blast, on time, every time

The future of mining is
electronic initiation

DetNet strives towards excellence in electronic initiation. As a world leader in our field, we aim to deliver world-class safety, the latest technology and consistent quality resulting in improved loading and fragmentation, all to ensure mining becomes more sustainable today and into the future. You can rely on DetNet to provide the best blast, on time, every time.




detnet



Smart drilling

Improve production, productivity and profitability with the ground-breaking Atlas Copco SmartROC down-the-hole drill rig. Equipped with smart technology, the SmartROC sets the industry benchmark in intelligent, powerful and efficient high-precision drilling. Optimise drilling and blasting, improve accuracy, extend machine availability and life-cycle, reduce fuel consumption, and enhance operator safety and performance.

www.atlascopco.co.za

Sustainable Productivity

Atlas Copco





Naturally occurring radioactive materials and the regulatory challenges to the zircon industry

by K. Harlow

Synopsis

Zircon is a naturally occurring radioactive material (NORM) and as such is subject to a variety of regulations around the world. The regulatory processes and their implementation are summarized and the key issues affecting zircon and zirconia highlighted. Having absorbed the activities of the former Zircon Minerals Committee, the strategy of the Zircon Industry Association (ZIA) is to be the 'go-to place' for information on these matters, and its activities in the NORM space are described. Chemical industry regulations such as REACH are spreading around the world, and the paper provides an update of their status in the key jurisdictions. As mineral sands are transported to market in oceangoing vessels, they are subject to the regulations of the International Maritime Organization, which are summarized in the paper.

Keywords

zircon, zirconia, radioactivity, safety and health, environment, regulatory issues.

Introduction

From a global perspective, zircon is generally not found in high concentrations other than in placer and dune deposits where it has been deposited along with other heavy minerals such as ilmenite, rutile, and monazite. Such deposits have been sorted and concentrated over geological time by the action of tides, waves, and wind to form concentrated deposits of heavy minerals along old coastlines and in river beds and deltas. Consequently, zircon is mostly found in association with the principal titanium minerals ilmenite and rutile. These secondary concentrations in placer deposits provide the commercial sources of zircon.

All geological materials contain natural radioactivity, although the term NORM (naturally occurring radioactive material) is mostly used for minerals and other materials with above-average uranium and thorium concentrations. Importantly, the radioactive nature of zircon has not changed, but the way in which radioactivity is viewed by regulators has, affecting the zircon industry throughout the value chain.

The Zircon Industry Association (ZIA) has 23 members spanning a good part of the value chain and representing some 80% of the

globally traded zircon supply. Geographically, ZIA's members are in the USA, Latin America, Europe, Africa, and Asia. South Africa accounts for a quarter of the world's production of zircon, being second only to Australia (40%). Major dunal sand deposits are mined in the coastal regions of ZwaZulu-Natal and Namakwaland. ZIA producer members are listed in Table I.

This paper describes some of the work that ZIA has commissioned over the past two years to support its members' NORM activities, as well as on the impact of Europe's REACH (Registration, Evaluation and Authorisation of Chemicals) regulations and their derivatives around the world.

Zircon and radiation exposure

Materials are classified based on the level of radioactivity they contain, and further classification is based on the possible radiation exposure to workers or the public. The radioactive properties are an inherent feature of the material and cannot be changed without

Table I

Producer members of the Zircon Industry Association

Member	Country
Iluka Resources Ltd	Australia
Kenmare Moma Processing (Mauritius) Ltd	Ireland
Rio Tinto Iron & Titanium Ltd.	United Kingdom
Sibelco Australia Limited	Australia
Tronox Mineral Sands (Pty) Ltd.	South Africa
TiZir Limited	United Kingdom
Base Resources Limited	Australia

* Zircon Industry Association (ZIA)
© The Southern African Institute of Mining and Metallurgy, 2017. ISSN 2225-6253. This paper was first presented at the Heavy Minerals Conference 'Expanding the Horizon', 16–17 August 2016, Sun City, South Africa.

Naturally occurring radioactive materials and the regulatory challenges

altering the material itself. The radiation exposure that can result from the material, however, varies according to the handling procedures.

The radioactivity of a material is measured in becquerels per gram (Bq/g), where one becquerel is equal to 1 count (disintegration) per second. NORMs contain radionuclides of the uranium and thorium decay series and a radioactive potassium isotope. The uranium decay series has 14 members, starting with U²³⁸ and ending with Pb²⁰⁶, while the thorium series has 10 members, starting with Th²³² and ending with Pb²⁰⁸ (Figure 1).

If the decay series is not disturbed, each member will have the same activity level; this is known as secular equilibrium. Many NORMs show secular equilibrium due to their age, and in order to classify a material, the state of equilibrium needs to be known.

The activity levels in zircon vary depending on the source, but are generally in the ranges shown in Table II.

Most zirconia (ZrO_2) is manufactured from zircon due to the scarcity of natural zirconia. The radioactivity of manufactured zirconia depends on the activity of the source zircon and the production process used. Thermal zirconia contains higher levels of radionuclides than the parent zircon, whereas chemically-produced zirconia may contain very low levels of radionuclides.

Regulation of NORMs

In terms of legislation applied to materials, the activity level where regulatory attention can be expected varies between countries, but a threshold value of 1 Bq/g is generally used internationally (International Atomic Energy Agency, 2004). Individual countries may apply stricter limits than these international standards, and if a material contains > 1 Bq/g it is classified as radioactive.

Zircon and zirconia containing above 1 Bq/g are subject to regulatory attention in all jurisdictions. Whether regulations are applied to the handling of these materials depends on the country in question; however, from the focus that NORMs have received from both the International Commission on Radiological Protection (ICRP) and the

International Atomic Energy Agency (IAEA) it should be assumed that possession, handling, and use of zircon and zirconia will receive some level of regulatory attention in most countries. This attention may vary from simple 'notification' through 'registration' to the highest level – 'licensing'.

Regulation of radiation exposure

The exposure of workers to radiation is closely regulated in all countries and the limits applied in most cases follow the ICRP and IAEA recommendations. The current internationally-agreed exposure limit is 20 millisieverts (mSv) per year for a 'radiation worker'. Exposure in a single year may exceed this value provided that the exposure over a 5-year period does not exceed 100 mSv, (*i.e.* an average of 20 mSv/a).

Regulation also requires that if a person's exposure exceeds 1 mSv/a that person is considered as occupationally exposed and is classed as a radiation worker. If the operation has areas where exposure can exceed 1 mSv/a, these areas are classified as *supervised* areas where a specific set of monitoring requirements is mandatory. If the exposure levels exceed 6 mSv/a, the areas where this occurs are classed as *controlled* areas and more stringent forms of monitoring and control are required.

Radiation exposure of the public due to a zircon/zirconia handling operation is also regulated, with members of the public being limited to an exposure of 1 mSv/a from all

Table II
Typical activity ranges of radionuclides in natural raw materials

Nuclide	Activity range (Bq/g)
Uranium-238 in zircon	2–4
Thorium-232 in zircon	0.5–1.0
Potassium-40 in zircon	Approx. 0.002
Uranium-238 in natural zirconia	3–13
Thorium-232 in natural zirconia	0.1–26

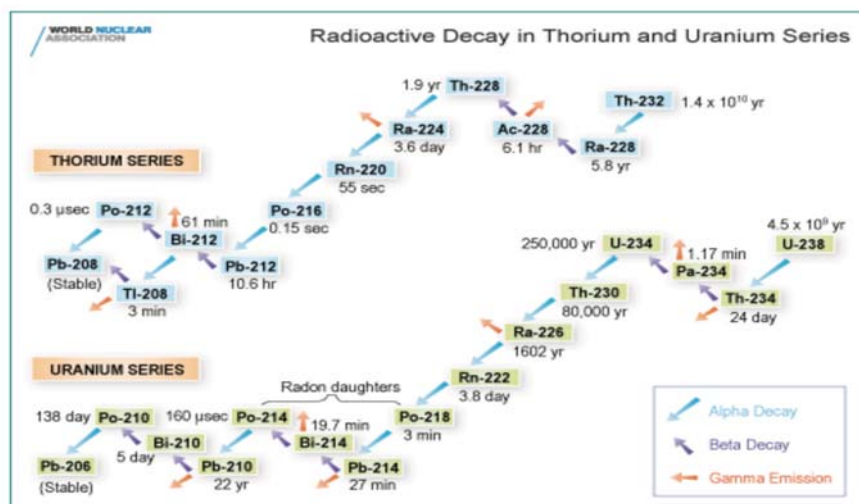


Figure 1—Radioactive decay in the Th and U series

Naturally occurring radioactive materials and the regulatory challenges

sources, with constraints being applied for a single source. These single-source constraints are typically set at 0.3 mSv/a. For example, when zircon/zirconia is transported the exposure of the public from any spillages must be kept below 0.3 mSv/a. Corrective action would be required if this limit is exceeded.

Regulation of NORMs in the EU

EU Member States are required to comply with the latest version of the Basic Safety Standards – ‘Council Directive, 2013/59/EURATOM’ of 2013, by 6 February 2018. For the first time, zircon is specifically referenced in the annexes to this update; namely:

‘Annex VI: List of industrial sectors involving naturally-occurring radioactive material as referred to in Article 23 ... When applying Article 23 the following list of industrial sectors involving naturally-occurring radioactive material, including research and relevant secondary processes, shall be taken into account: — Zircon and zirconium industry’.

While the requirement of the 2013 version should be comfortably met by zircon operators in the EU, the fact that zircon is noted in the Annex could lead to greater examination from local authorities. In preparation for this, those operating in the EU should:

- Recognize that their operations will be subject to the scrutiny of the local regulator and prepare for an inspection
- Inform their regulators that they are processing ‘radioactive materials’ and conduct radiation risk assessments to ascertain the potential or actual exposure situation.
- Establish the levels in terms of U and Th activity of wastes and be prepared for negotiations with regulators
- Ensure that they have adequate dose data to support the claim that the impact on the public from their operation is less than 0.3 mSv/a.

The ZIA is maintaining a watching brief over the development of these regulations throughout the EU with the aim of forewarning members about any impending differences between Member States.

EU-REACH

The REACH (Registration, Evaluation and Authorisation of Chemicals) Regulation entered into force on 1 June 2007 with the aim of streamlining and improving the former legislative framework for chemicals management in the EU. REACH also created the European Chemicals Agency (ECHA) in Helsinki, which has a central coordination and implementation role in the overall process by managing the registration, evaluation, and authorization steps to ensure consistency across the EU.

Two basic concepts are attributable to REACH: the shift of the burden-of-proof of safe use from authorities to industry, and the stated ‘No data no market’ (REACH Regulation, Article 5), whereby substances shall not be manufactured in or placed on the EU market unless they have been registered in accordance with the relevant provisions of the Regulation.

To date, some 45 000 registrations covering 9500 unique substances have been received by ECHA. Table III shows the top five registrations by country, and Table IV, by substance.

EU REACH and zircon

Although the term ‘chemical’ is not generally associated with metals, ores, and minerals, it is clear that reference to chemical substance, or substance, does include all organic, inorganic, and natural substances found in the periodic table along with all combinations, or mixtures, of these. In fact, substance is defined in REACH Article 3(1) as:

‘... a chemical element and its compounds in the natural state or obtained by any manufacturing process, including any additive necessary to preserve its stability and any impurity deriving from the process used, but excluding any solvent which may be separated without affecting the stability of the substance or changing its composition’.

Importantly, there are some notable exemptions from registration obligations as detailed in Annexes IV and V of the Regulation. For example, substances for R&D purposes, substances used in the interests of defence, and those substances managed by other legislation, such as food additives, radioactive substances, or medical applications are exempt for a period of time.

For the minerals industry, exempted substances in Annex V(7) include: *‘The following substances which occur in nature, if they are not chemically modified. Minerals, ores, ore concentrates, cement clinker, natural gas, liquefied petroleum gas, natural gas condensate, process gases and components thereof, crude oil, coal, coke.’*

Zircon, along with other minerals, is therefore exempted from REACH registration obligations.

Table III
Overview of top five countries to 13 May 2016 (ECHA)

Country	Number of registrations
Germany	11 677
United Kingdom	5 488
France	4 008
Netherlands	3 932
Italy	511

Table IV
Overview of top five substances to 13 May 2016 (ECHA)

Substance	Number of registrations
Calcium dihydroxide	457
Ethanol	459
Ethylene oxide	398
Iron	391
Calcium sulphate	300

Naturally occurring radioactive materials and the regulatory challenges

Chemical derivatives of zircon are, however, subject to REACH registration at >1 t/a per legal entity registrant. Analyses of some zirconia-based substances are given in Table V.

Parallel to the REACH registration process was the introduction of the Classification, Labelling, and Packaging (CLP) regulation—the EU's equivalent to the Globally Harmonised System of Classification and Labelling (or GHS)—where all substances, including those exempt from REACH registration obligations, are classified through a process of notification. It is here that we see zircon and entries for zirconium orthosilicate and zirconium silicate. These notifications include a number of different classifications for the same substance: *e.g.* zircon is classified variously by different producers as:

- ▶ Unclassified
- ▶ Skin irritation 2 [H315—causes skin irritation]
- ▶ Eye irritation 2 [H319—causes serious eye irritation]
- ▶ Carcinogen 1A [H350—may cause cancer].

It is not unusual for there to be different classifications for the same substance: some may be default classifications; others may be precautionary. However, these classifications are in the public domain and must be addressed to reflect an industry-agreed, single classification.

REACH around the world

While REACH pertains to the EU, regulatory derivatives are developing in other jurisdictions as industrialized nations grapple with the complexities of chemicals management. A strong motivation for this is the UN Strategic Approach to International Chemicals Management (SAICM); a policy framework to foster the sound management of chemicals around the world. SAICM aims to achieve the sound management of chemicals throughout their life cycle so that, by 2020, chemicals will be produced and used in ways that minimize significant adverse impacts on human health and the environment. This '2020 goal' was adopted by the World Summit on Sustainable Development in 2002 as part of the Johannesburg Plan of Implementation.

In order to meet this goal, many regions have been encouraged by the reported successes of EU-REACH to look at implementation of a similar legislative framework, some with an almost copy/paste approach, from China to South Korea and Turkey, each of which have implemented, or are in the process of introducing, REACH-like laws. While many of the legislative terms may be familiar to those involved with EU-REACH (*e.g.* 'downstream user', 'only representative', 'exposure scenario'), care should be taken to understand the

detail of these derivatives as there are some important differences, *e.g.* the requirement for annual tonnage reporting in Korea's K-REACH.

Other industrialized countries that have not fully implemented regulatory change are starting with the cataloguing of all existing chemicals on their market (*e.g.* Brazil, Taiwan, and India). Care has to be taken to monitor each list as it is published, as these often then lead to the classification and prioritization of substances for future registration.

Ocean shipping and the International Maritime Organization

While regulatory developments progress on land, the updating of various ocean shipping codes by the International Maritime Organization (IMO) also has an impact on international trade. Based in London, the IMO is a specialized agency of the UN that is responsible for measures to improve the safety and security of international shipping and to prevent pollution from ships. Its stated objective is '*safe, secure and efficient shipping on clean oceans*'.

IMO's governing body is the Assembly, which is made up of all 171 Member States, and a Council of 40 Member States acts as its governing body between Assembly sessions. In practice, the main technical work is carried out by five committees—Maritime Safety, Marine Environment Protection, Legal, Technical Co-operation, and Facilitation—supported by a number of sub-committees. Outputs from these committees include several codes that lay out the legal framework for the shipping of goods in bulk and in containers.

Two codes can have an impact on the shipping of zircon and other minerals; namely the International Maritime Solid Bulk Cargoes (IMSBC) Code and the International Convention for the Prevention of Pollution from Ships (MARPOL).

The aim of the IMSBC Code is to enable the safe stowage and shipment of solid bulk cargoes by providing information on the dangers and precautions associated with the shipment of certain types of cargo in bulk. The IMSBC Code categorizes cargoes into three groups:

Group A: Cargoes that may liquefy

Group B: Cargoes that pose a chemical hazard that could give rise to a dangerous situation on a ship

Group C: Other cargoes that can still be hazardous (*e.g.* very dense cargoes that can damage a vessel's structure due to poor loading procedures).

Importantly, these characteristics refer to the bulk cargo properties rather than a hazard from the material itself. For

Table V

The top five REACH-registered Zr-based substances

Name	Chemical Abstracts Service (CAS) number	No. of registrants	Total tonnage band (t/a)
Zirconium	7440-67-7	4	1000–10 000
Zirconium dioxide	1314-23-4	37	10 000–100 000
Zirconium dioxide Y-doped	64417-98-7	7	100–1000
Calcium zirconium oxide	11129-15-0	3	1000–10 000
Zirconium sulphate	14644-61-2	10	1000–10 000

Naturally occurring radioactive materials and the regulatory challenges

example, liquefaction (where a bulk cargo becomes fluid) is a property displayed only in bulk form. Cargoes prone to liquefaction contain a certain quantity of moisture and small particles, although they may look relatively dry and granular when loaded. Liquefaction can lead to vessel instability and even to capsize and total loss of the ship, and can occur even when cargoes are cohesive and trimmed level.

Zircon sand is currently cargo Group C, whereas other minerals are assigned different codes—for example ilmenite sand is Group A or C.

Importantly, there is an ongoing review to classify ilmenite sand as Group A due to its liquefaction potential. In addition, the reference to 'sand' in the cargo description erroneously introduces an association with the health effects due to the inhalation of silica dust. Efforts are underway to inform and educate the relevant IMO technical committees that such reference to sand in mineral cargo descriptions relates to the physical form of the cargo rather than the presence of silica sand.

Transport of materials by ocean freight also has to comply with the requirements of the International Maritime Dangerous Goods Code (IMDG). This code is controlled by the IMO, but fortunately the IMO has aligned its standards with those of the IAEA so the same limits apply. By not exceeding the 10 Bq/g limit, zircon and zirconia may be shipped internationally without the requirement to comply with the IAEA transport regulations or the IMDG Code. Being not classified as a radioactive material in the IMDG Code means the concentrates avoid classification as 'Hazard Class 7 radioactive substances.' Shipping companies are reluctant to handle Class 7 materials, so this is a distinct advantage for the export of this material.

The status of radiation-based regulations in the destination port also needs to be confirmed. Although the country may subscribe to the IAEA standards, there have been situations where port officials apply different standards

to those defined internationally. This inconsistency may also vary between ports in the same country. The radioactivity of zircon/zirconia does not require it to be governed by the IAEA transport regulations, and storage as part of transportation is also not mandated by the international standards. However, the detection of a radioactive signature from the material may trigger some reaction from port officials, which could delay the movement of cargo.

Conclusions

- Although NORM and radiation developments are at the end of a cycle, zircon operations should aim to proactively manage regulatory developments (*e.g.* meeting with relevant authorities and targeted advocacy)
- For those areas of potential higher worker exposure to NORM dust, such as dry milling of zircon, appropriate risk assessments should be undertaken and kept updated
- Regulations are harmonizing globally (land and sea), becoming more stringent and shifting the burden of proof from regulators to industry. It is vital to be aware of developments globally and plan/act accordingly.

The Zircon Industry Association (ZIA) is working to support its members' knowledge of and compliance with major regulations impacting the full supply chain.

Acknowledgements

The author would like to express his thanks to colleagues at ZIA, and to J.H. Selby for his various reports to the ZIA.

References

INTERNATIONAL ATOMIC ENERGY AGENCY. 2004. Application of the Concepts of Exclusion, Exemption and Clearance. IAEA Safety Standards Series, Safety Guide No. RS-G-1.7. Vienna.

Zircon Industry Association. www.zircon-association.org ◆

FOR **EXPLOSIVES**
THINK

www.bme.co.za

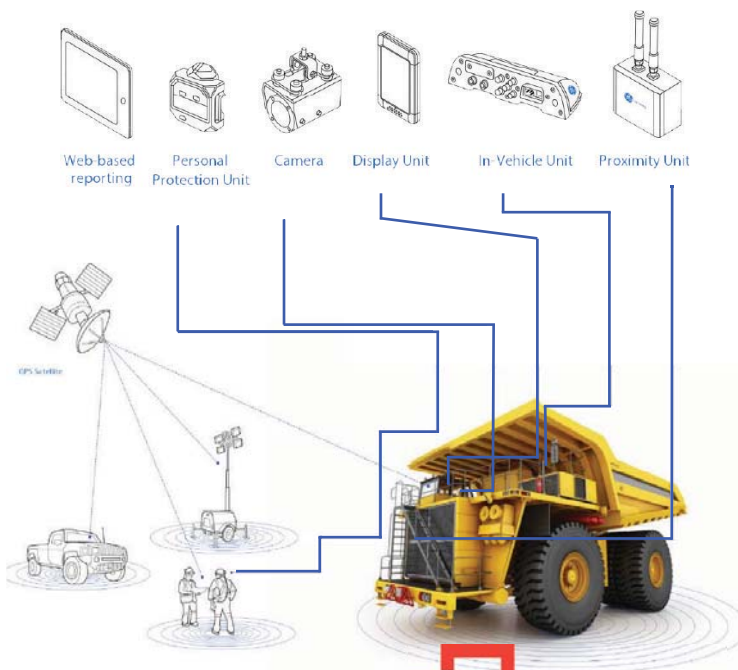


A member of the Omnia Group

The 360° Safety Solution

Key benefits

- Proven proximity detection technology that sets new standards for workplace safety and facilitates 'zero harm' objectives.
- Improve operator situational awareness and reduce the incidence of injury.
- Fully configurable and adaptable to site-specific requirements.
- Real-time and historical reporting on interactions, near misses and system health.
- Supported worldwide by expert GE Mining teams.
- Effective, reliable and intuitive operation.
- Whole of mine solution:
 - OEM independent
 - Stand-alone system
 - Low "total cost of ownership"
- Proven in use over 10 years and 200 million hours of operation.



CAS-SURFACE

The benchmark in Collision Avoidance Systems

Johannesburg (HO) Gert - 083 451 0797 / Nic - 082 901 1206



Witbank Wihan Brits - 081 850 1150 | Kuruman & Kathu Leon Jordaan - 082 452 6459 | Rustenburg Stefan van Wyk - 060 971 0408

DEVELOPING THE FLOWSHEET

METALLURGICAL LABORATORY

We specialise in commercial mineral processing and metallurgical testwork for process design and the application of Maelgwyn's proprietary technologies and processes in gold, base metals, PGMs and other commodities.

Successful testwork programmes have included process development on common sulphide minerals, as well as non-sulphide minerals including tin, rare earths and coal fly-ash.



Maelgwyn Mineral Services Africa (Pty) Ltd

Tel +27 (0)11 474 0705 Fax +27 (0)11 474 5580 Email MMSA@maelgwynafrica.com www.maelgwynafrica.com





Solid-state reduction of an ilmenite concentrate with carbon

by A. Bhalla*, C.S. Kucukkargoz*, and R.H. Eric*

Synopsis

The solid-state reduction of ilmenite concentrate with graphite was studied under argon atmosphere at temperatures between 1050°C and 1350°C. The rate of reduction increased with increasing temperature and decreasing particle size, with the maximum extent of reduction found to be 80% at 1350°C with a particle size in the range of -106 +90 µm. The activation energy for the reduction reaction was calculated to be 257 kJ/mole. The trivalent iron oxide was reduced first to divalent iron oxide and then to metallic iron. An annular ring of a partially reduced oxide phase containing metallic nuclei was formed around the core of ilmenite, which grew in size as the original ilmenite core shrank with progressive reduction. The reduction of titanium dioxide also took place during this stage, which produced the Magnéli oxides in the form of Ti_nO_{2n-1} . The metallic phase had very high Fe and low Ti contents throughout the reduction, whereas the partially reduced oxide phase adjacent to the metallic phase was high in Ti and depleted in Fe. The metallic phase globules formed during this stage were small and are considered suitable only for leaching and not for other concentration processes. The core of the particle generally retained the composition of the original ilmenite. The purpose of this work was to remove iron and increase the titanium oxide content of the ilmenite to produce a high-titanium containing charge for subsequent smelting.

Keywords

ilmenite, carbon, solid-state reduction, activation energy.

Introduction

The titanium-bearing minerals ilmenite ($FeTiO_3$) and rutile (TiO_2) are the primary natural raw materials used in industry to produce titanium metal and titanium-based products. The common titanium-bearing minerals are ilmenite, rutile, anatase, brookite, leucoxene, arizonite, and perovskite. Although the formula of ilmenite is commonly expressed as $FeTiO_3$, the mineral can accommodate Mn and Mg, which are chemically bound in the form of $(Fe,Mn,Mg)TiO_3$. Ilmenite concentrate can also contain Fe_2O_3 and Al_2O_3 in addition to the physically separable oxides such as SiO_2 and CaO . The crystal structure of ilmenite is an ordered derivative of the corundum structure with a trigonal-rhombohedral symmetry. Fe^{2+} and Ti^{4+} ions occupy the octahedral sites, leaving the tetrahedral sites unoccupied. In each $FeTiO_3$ unit, there are three O^{2-} ions creating three octahedral sites, two of which are occupied by Fe^{2+} and Ti^{4+} (Wilson *et al.*, 2005).

The Ti-O system is complex, involving various Ti_xO_y phases with y/x ratios varying

from 2 to 1.0. The general chemical formula representing the Magnéli oxides is interpreted in the form of Ti_nO_{2n-1} where n ranges from 4 to 10. The crystalline structures of Ti_2O_5 , Ti_3O_5 , and Ti_5O_9 are trigonal, monoclinic, and triclinic respectively. At higher temperatures, the Magnéli phases decompose to form a pseudobrookite solid solution (Pesl, 1997).

The methods used to produce titanium and titanium-based products from titanium-containing ores involve various pyrometallurgical, electrochemical, and hydrometallurgical processes. There are two main methods used in industry by which ilmenite is upgraded to prepare a feedstock that is later chemically treated to produce pure TiO_2 . In the first method, a mixture of metallic iron and rutile is produced in the solid state, whereas in the second method, a titania-rich slag and metallic iron are produced in the liquid state (Zietsman and Pistorius, 2004). In both methods, the reduction of ilmenite is considered an important step that requires a detailed knowledge of the mechanism of reduction with carbonaceous reducing agents under both inert and reducing gas atmospheres.

El-Guindy and Davenport (1970) found that the reduction of ilmenite was initiated at the contact between solid carbon and ilmenite particles, which controlled the reduction in the temperature range 860–1020°C. The reduction was carried out by CO due to its high rate of regeneration through the reaction between graphite and CO_2 at temperatures above 1020°C. The diffusion of CO through the product layer was found to be the rate-controlling step. In a study conducted by Wouterlood (1979), the ilmenite was reduced with char instead of solid carbon so that the reduction conditions would closely simulate plant conditions. The simulation conditions were complicated by the regeneration of CO

* School of Chemical and Metallurgical Engineering, University of the Witwatersrand, Johannesburg, South Africa.

© The Southern African Institute of Mining and Metallurgy, 2017. ISSN 2225-6253. This paper was first presented at the Heavy Minerals Conference 'Expanding the Horizon', 16–17 August 2016, Sun City, South Africa.

Solid-state reduction of an ilmenite concentrate with carbon

through reaction between carbon and CO₂ as well as by the presence of hydrogen in the char. To overcome this difficulty, additional experiments were conducted using CO directly as the reducing gas. The results indicated that ferric iron was reduced to ferrous iron in the first, fast reduction stage and the ferrous iron was reduced to metallic iron in the second, slower reduction stage. Application of kinetic models proved that the unreacted core model (mixed control) was the most representative model.

Grey, Jones, and Reid (1973) identified the sequence of reduction as being reduction of Fe³⁺ to Fe²⁺ in the first stage and to Fe (metal) in the second stage, followed by the reduction of TiO₂ to the lower oxide forms represented by Ti_nO_{2n-1} in the final stage. Merk and Pickles (1988) indicated that the metallic shell which was formed around the ilmenite grain due to the reduction of iron oxides by CO in the temperature range 500–1100°C inhibited CO diffusion in later stages and played an important role in the kinetics of reduction. Welham and Williams (1999) proposed that the reduction of ilmenite proceeded rapidly to form metallic iron and rutile. The rutile was then reduced to the lower oxides in the form of (Ti_nO_{n-1}), culminating in a more stable oxide, Ti₃O₅. The formation of TiC was observed at 1100°C, but this was favoured only at higher temperatures. Wang *et al.* (2008) identified the reaction products as mostly reduced iron, iron carbide, rutile, reduced rutile, and reduced rutile in solid solution with Ti₃O₅. The reaction rate was controlled by chemical reaction at lower temperatures and by diffusion through the product layer at higher temperatures. Sai (2008) applied various mathematical models based on selected data obtained from operational practices conducted in a rotary reactor, in which ilmenite was reduced with char. The rate-controlling step was identified as solid-solid reaction during the initial stages and CO diffusion through the product layers during the later stages of reduction.

In a recent study (Lobo, Kolbeinsen, and Seim, 2013), the gaseous prereduction of ilmenite was studied using natural gas as the main reductant. It was shown that the iron oxides in ilmenite were reduced more effectively in the presence of hydrogen compared to CO. The shrinking core model with multi-interfaces was found to represent the reduction behaviour of the titanium oxides.

Preliminary results on the kinetics and mechanism of ilmenite reduction with carbon reported by Kucukkaragöz and Eric (2005, 2006) indicated the strong effect of temperature and particle size on the reduction rate.

The objective of the present work is to study the reduction sequence of ilmenite by carbon; in particular, to define the reduction stage during which the majority of the iron oxide is reduced to the alloy phase before any significant reduction of the titanium oxide in the solid state. The relative (preferential) reduction of iron oxides over titanium oxides becomes important (Pistorius, 2002). The aim is to arrive at a product that has two physically separable phases—namely the metallic phase containing most of the iron, and the partially reduced oxide phase containing most of the titanium present in the ore. The subsequent step then involves the development of a suitable process for separating the metallic phase from the titanium oxide phase in the solid state.

Experimental

Apparatus

The thermogravimetric apparatus consisted of a vertical tube furnace, an electronic balance attached to a computer, a temperature controlling unit, a deoxidation furnace, and a gas regulator (manometer) unit for controlling the reaction gas

atmosphere. The details of the experimental set-up can be found elsewhere (Soykan, Eric, and King, 1991). The furnace, which enclosed an alumina reaction tube, was heated using a molybdenum wire heating element. The temperature of the hot zone (reaction zone) was controlled by a B-type thermocouple (Pt-6%Rh/Pt-30%Rh) within a range of 2°C; the temperature was checked with another B-type thermocouple positioned at the hot zone. The molybdenum heating element was protected from oxidation by purging anhydrous NH₃, which decomposed to nitrogen and hydrogen at reaction temperatures. An alumina pedestal attached to an electronic balance with a sensitivity of ± 0.1 mg was used to position the crucible in the reaction zone. The mass change with respect to time was transmitted by the electronic balance and recorded on the computer. The system was closed and sealed with an expandable rubber bellows fitted between the work tube and the balance case before the work tube was purged with argon.

Procedure

A South African ilmenite concentrate was used in the experiments. The composition, as provided by the plant, is given in Table I. The sample was crushed, ground, and screened into three particle size groups: -125+109 µm, -109+90 µm, and -90+63 µm. Graphite was ground and screened to the same particle sizes as the concentrate splits. The samples were prepared by mixing 4.5 g of ilmenite concentrate with 3.5 g of graphite, which was 50% in excess of the stoichiometric requirement to form Fe₃C and TiC (according to the expected reaction). The furnace was heated to the required temperature, and each sample was placed in an alumina crucible and positioned on top of the pedestal which was attached to the balance. The expandable rubber bellows was connected to form a sealed zone between the work tube and the balance, and the reaction tube was purged with argon at a rate of 1 litre per minute for 15 minutes. The sample was then lifted over a period of around 5 minutes and located in the reaction zone under sealed conditions. The start of each experimental run was recorded as the zero-time for reaction as soon as the sample reached the reaction zone, and the recording of mass with respect to time was started by the computer. A series of experiments was conducted to study the influence of temperature and particle size on the reduction process at temperatures ranging from 1050°C to 1350°C.

Another series of experiments was conducted by reacting the samples of -106+90 µm particle size at 1350°C to identify the phases formed at different stages of reduction. Each experimental run was conducted until a predetermined mass change, corresponding to the target reduction percentage, was observed. The mass change curves were examined to determine the regions indicating different reduction rates. The reduction stages were identified with the support of the analytical results obtained by scanning electron microscopy-energy-dispersive X-ray spectrometry (SEM-EDX) and X-ray diffractometry (XRD).

Table I
Chemical analysis of ilmenite concentrate

	TiO ₂	FeO	Fe ₂ O ₃	Al ₂ O ₃	MnO	MgO	SiO ₂
Mass %	46.30	34.20	12.30	0.80	1.20	0.40	2.30
Mole %	48.35	39.68	6.43	0.65	1.41	0.83	2.65

Solid-state reduction of an ilmenite concentrate with carbon

Analytical work

Each of the reacted samples was divided into two parts. One part was mounted in bakelite, polished, and examined by SEM and the other was subjected to XRD for phase identification. Point analysis for the distribution of elements was conducted by SEM-EDX.

Stoichiometric calculations

The samples were prepared so as to contain 50% excess C calculated on the basis of the stoichiometric mass of carbon required for completion of the following reduction reactions:



The mass change recorded during an experiment was assumed to represent the mass of CO evolved from the sample as a result of reactions [1], [2], and [3]. The reduction percentage was calculated using Equation [4]:

$$\text{Reduction \%} = \frac{\text{Mass of CO}}{\text{Mass of oxygen} * \frac{28}{16}} * 100 \quad [4]$$

where mass of oxygen indicates the total mass of removable oxygen present in the reducible oxides in the original ilmenite concentrate under the experimental conditions.

Results and discussion

The kinetic data obtained in the experimental work is presented in the form of reduction curves plotted as percentage reduction against reaction time. The kinetic curves indicating the influence of temperature and particle size on the reduction rate are given in Figures 1 and 2 respectively.

The rate and extent of reduction, as expected, increased with increasing temperature and decreased with increasing particle size. The differences in rates were noticeable at all temperatures and particle size ranges, and the results indicate a strong influence of temperature and particle size on the reduction rate.

Mechanism of reduction

A series of experiments was conducted by reducing -106 +90 µm particle size samples at 1350°C and stopping the reaction at specific points representing varying degrees of reduction. The reduction curves obtained are presented in Figure 3.

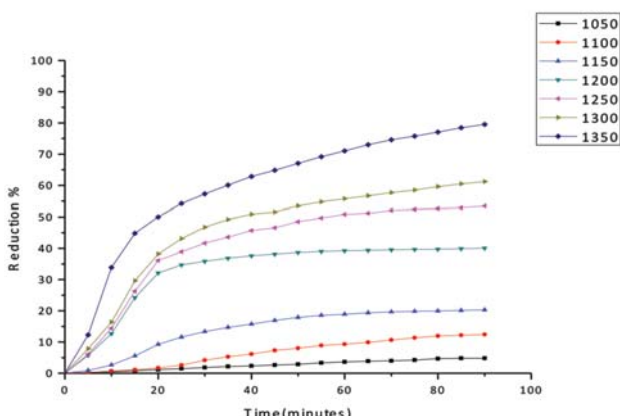


Figure 1—Effect of temperature (°C) on reduction rate at particle size -106 +90 µm

The phases formed in the reacted samples were examined by SEM and analysed by EDX to obtain the elemental point analysis. The SEM images and the elemental analytical results are given in Figures 4 to 11. The reduced samples were also analysed by X-ray diffractometry to identify the phases formed during reduction, as illustrated in Figure 12. The phases detected are given in Table III.

Formation of metallic iron was first seen at 11% reduction (Figure 4). The metallic phase and the partially reduced oxide phase containing $\text{Ti}_{n}\text{O}_{2n-1}$ were detected between 11 and 40% reduction. The partially reduced oxide phase with a high titanium content and very low iron grew in size as the core of the particle shrank at the later stages of reduction.

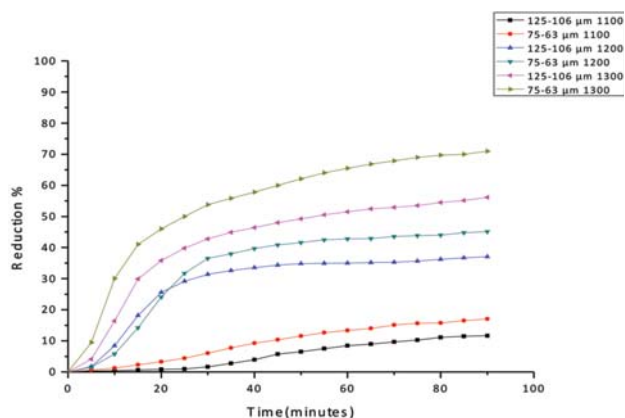


Figure 2—Effect of particle size on reduction rate at 1100°C, 1200°C, and 1300°C

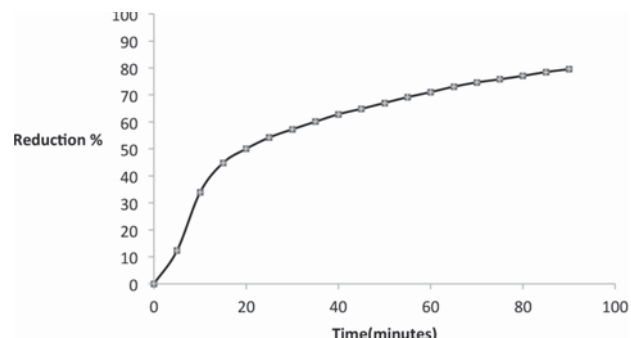


Figure 3—Reduction curve for -106 +90 µm sample at 1350°C

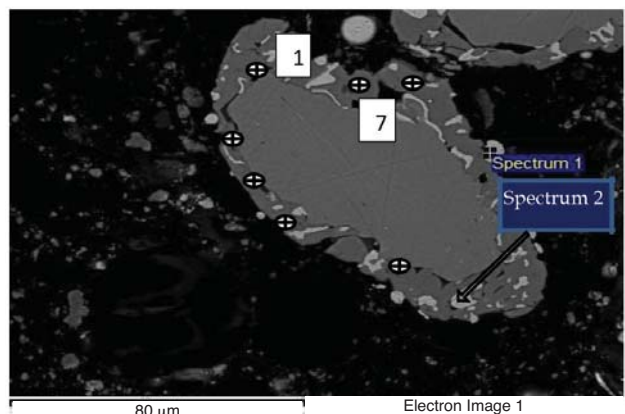


Figure 4—SEM backscattered image of particle at 11% reduction at 1350°C (-109+90) µm. Spot number (1-7) on reduced oxide phase (anticlockwise). Spectrum 1 and 2 on metal phase

Solid-state reduction of an ilmenite concentrate with carbon

According to the results, the metallic phase formed during the initial reduction stages had a high iron content and low titanium content, whereas the oxide phase region adjacent to the metallic phase had a high titanium content and low iron content.

Table II SEM-EDX analysis of metal phase at spectrum points 1 and 2, Figure 4			
Spectrum no.	Ti (mass %)	Fe (mass %)	C (mass %)
1	1.12	80.14	18.18
2	1.49	80.14	18.18

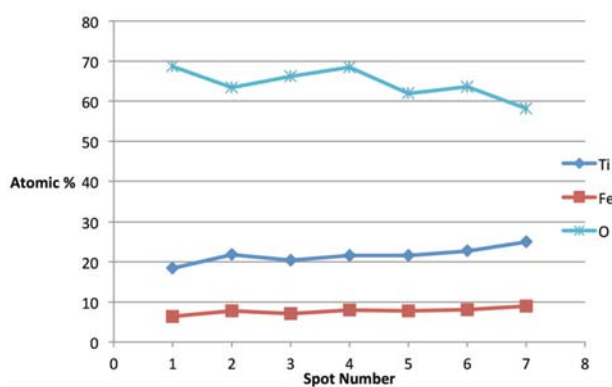


Figure 5—EDX elemental analysis of reduced oxide phase at spot points 1–7 in Figure 4

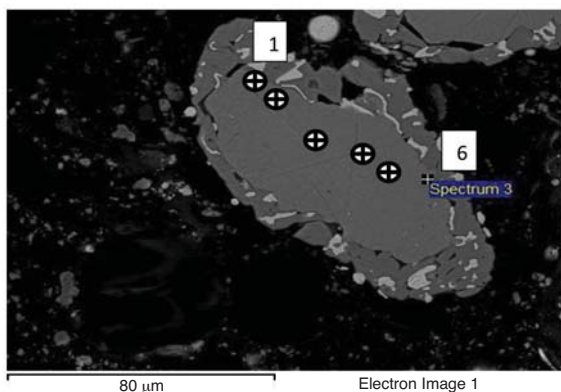


Figure 6a—Backscattered SEM image of particle at 11% reduction at 1350°C (-109+90 µm fraction). ⊕ Spot number 1–6 anticlockwise

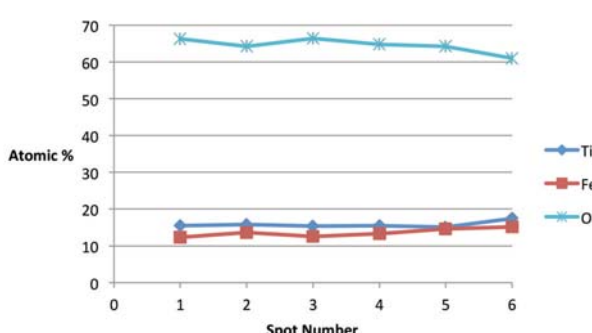


Figure 6b—SEM-EDX analysis of reduced oxide phase/ilmenite at spot points in Figure 6a

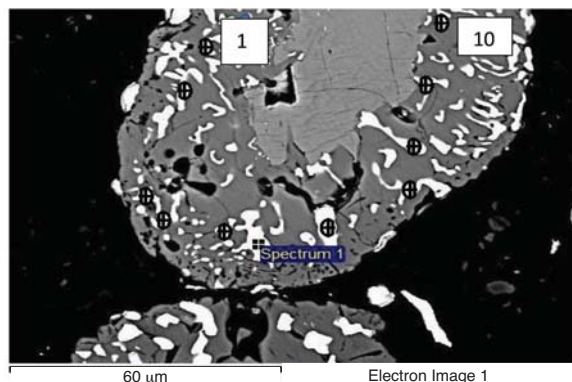


Figure 7a—Backscattered SEM image of particle at 40% reduction at 1350°C (-109+90 µm fraction) ⊕ Spot number 1–10 anticlockwise

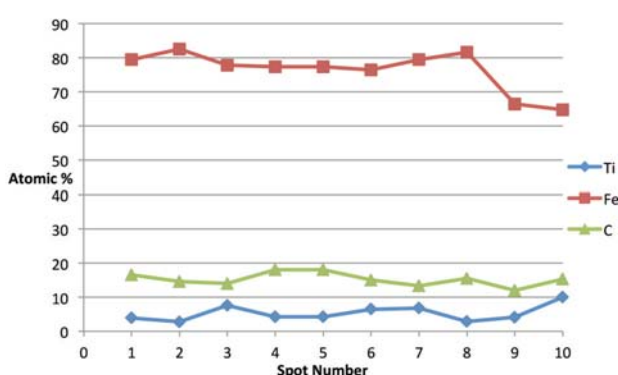


Figure 7b—SEM-EDX analysis of metal phase (spots 1–10) across the particle in Figure 7a

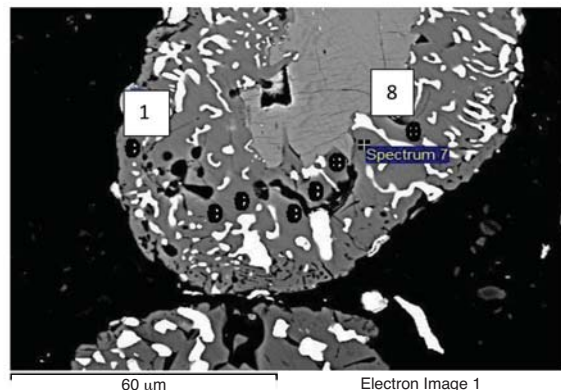


Figure 8a—Backscattered SEM image of particle at 40% reduction at 1350°C (-109+90 µm fraction). ⊕ Spot number 1–8 anticlockwise

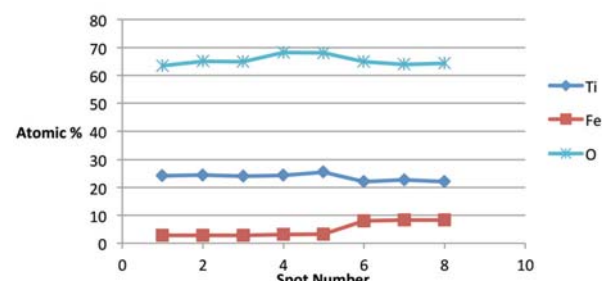


Figure 8b—SEM-EDX analysis of reduced oxide phase at spot points across the particle in Figure 8a

Solid-state reduction of an ilmenite concentrate with carbon

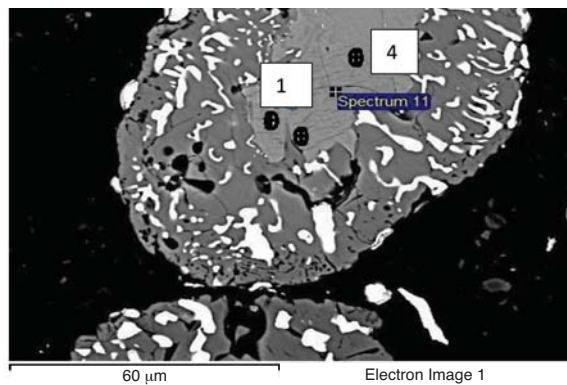


Figure 9a—SEM image of particle at 40% reduction at 1350°C (-109+90 µm fraction). \oplus Spot numbers 1–4 anticlockwise

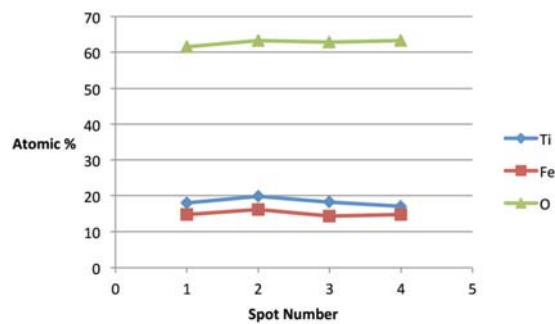


Figure 9b—SEM-EDX analysis of the core ilmenite at spot points in Figure 9a

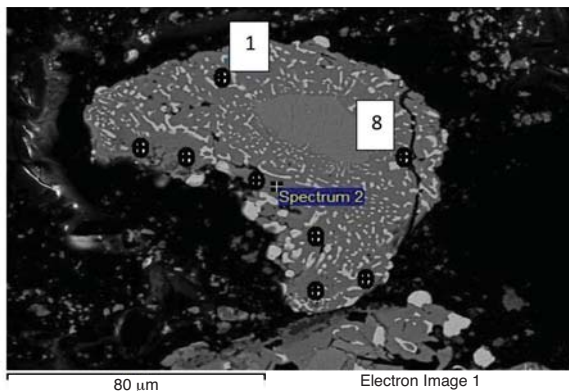


Figure 10a—Backscattered SEM image of particle at 61% reduction at 1350°C (-109+90 µm fraction). \oplus (Spot numbers 1–8 anticlockwise

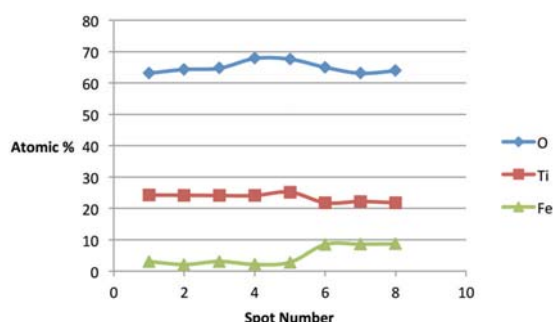
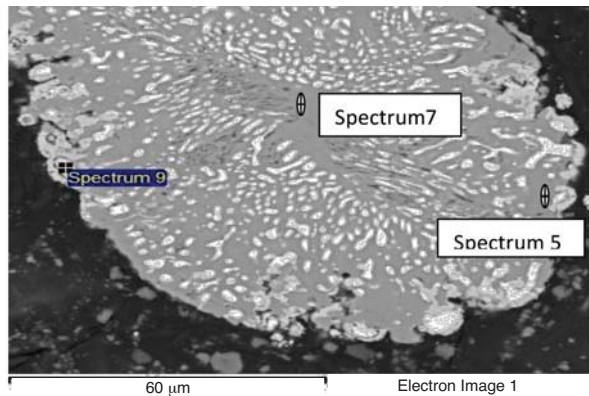


Figure 10b—SEM-EDX analysis of the partially reduced oxide phase surrounding the core across the particle in Figure 10a



Metal phase (Spectrum 9) Reduced oxide phase (Spectrum 5) Centre core (Spectrum 7)

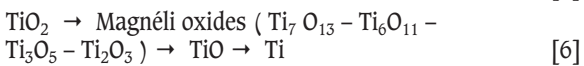
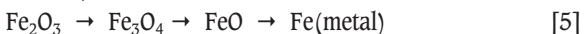
Element	Mass %	At. %
C	3.37	13.93
Ti	1.40	1.45
Fe	95.23	84.62
Totals	100	100

Element	Mass %	At. %
O	41.89	68.49
Ti	55.05	30.06
Mn	1.90	0.91
Fe	1.16	0.55
Totals	100	100

Figure 11—SEM image and EDX analysis (at spot points) of particle at 80% reduction at 1350°C (-109+90 µm fraction)

Stages of reduction

In the literature, the reduction of ilmenite concentrate with carbon is reported to take place in the following sequence (Pesl, 1997):



The phases detected by XRD in the reacted samples at varying reduction percentages are presented in Table III. According to the results, Fe was first detected at 11% reduction, Ti_7O_{13} at 40%, both Ti_6O_{11} and Ti_5O_5 at 60%, and TiO at 80% reduction, which is in good agreement with the following theoretical approach based on stoichiometric calculations on the reduction of ilmenite concentrate with the given chemical composition.

Reduction of Fe_2O_3 to FeO 0.0–4.0% reduction range

Reduction of FeO to Fe 4.0–34% reduction range

Reduction of TiO_2 to TiO 35%–65% reduction range

Reduction of TiO to Ti 65–100% reduction range

The highest reduction level obtained in the present work was 80%, which indicates the possibility of partial reduction of TiO to TiO_{1-x} where (x) is the corresponding mass of oxygen removed.

First stage of reduction

The initial reduction reaction started at the contact points between the solid carbon and the ilmenite particles. This was followed by the reaction between CO and ilmenite. The regeneration of CO through the Boudouard reaction became effective at temperatures above 1050°C. Nucleation of a metallic phase took place at the most favourable sites on the surface of ilmenite particles during this stage, as can be observed in Figure 4. The high number of metallic nuclei covering the surface of the particle indicates a gaseous-type reaction. Mostly iron oxides were reduced in this stage as the metallic nuclei, which were rich in Fe and low in Ti, formed

Solid-state reduction of an ilmenite concentrate with carbon

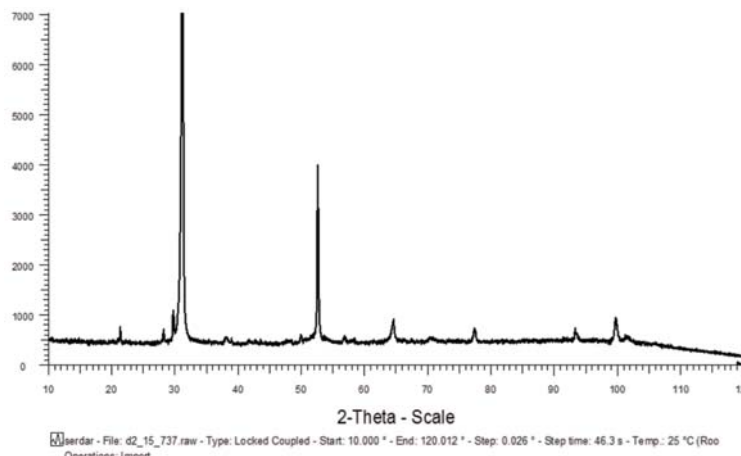


Figure 12—X-ray diffraction of the sample at 50% reduction

Table III Phases detected by X-ray diffraction		
T (°C)	Reduction (%)	Phases detected
1100	12	C, FeTi ₂ O ₅ , TiO ₂ , Fe
1200	40	C, Ti ₇ O ₁₃ , Fe, Fe ₃ C
1300	60	C, Fe ₃ C, Ti ₆ O ₁₁ , Ti ₃ O ₅ ,
1350	80	C, Fe ₇ C ₃ , TiO

and grew in size as the reduction progressed. During the initial stages of reaction (until 35% reduction), a high concentration gradient of iron was developed due to reduction, which was the driving potential for iron diffusion across the particle. As the reduction proceeded, most of iron was reduced to the metallic state, causing a change in the Fe concentration profile across the particle (Figure 10). The initial stages of partial reduction of titanium oxide also took place during this stage, and formed, together with the metallic nuclei, a shell of a partially reduced oxide phase covering the core of the ilmenite particles as can be seen in Figure 4. This stage took place between zero and 35% reduction and involved the part of the reduction during which the reduced oxide phase, together with the metallic nuclei, grew in size until the shell reached a certain thickness. The reduction rate was likely influenced by the formation and growth of the metallic nuclei, which was completed within this stage as seen in Figures 6a and 7a.

Second stage of reduction

This stage took place at greater than 35% reduction, during which the shell of the partially reduced oxide phase, together with the already formed metallic nuclei, grew in size as the core ilmenite phase shrank. Theoretically, the reduction mechanism involved steps such as the mass transfer of the reactants to the reaction interface, reaction between the oxides and the CO prevailing at the interface, and the mass transfer of products from the reaction interface. The reduction reactions took place at the interface between the partially reduced oxide and ilmenite. Microscopical examination of the reduced particles revealed that each particle retained its original shape and size during the course of reduction. The removal of oxygen from the oxide phase therefore created a

porous structure that allowed the passage of CO to, and CO₂ from, the reaction interface. Removal of oxygen also resulted in a higher oxygen concentration in the unreduced ilmenite than in the partially reduced oxide, thus causing the transfer of oxygen to react with CO at the reaction interface.

SEM-EDX analysis indicated the possibility of the mass transfer of the reaction elements due to their high concentration gradients through the product layers across the particle. During the later stages of reduction, the original ilmenite was reduced almost completely to the partially reduced oxide phase containing most of the titanium oxides present in the original ilmenite, as can be seen in the microstructures and elemental analysis in Figure 11.

Kinetics of reduction

Examination of the representative reduction curve in Figure 3 reveals that the reduction process was characteristically separable into different stages, with each stage representing a different reduction rate. The first stage of reduction was defined as the linear part of the curve between zero and 35% reduction, and the second stage as the part of the curve representing 35% reduction and above. These stages are proposed to represent a fast initial stage followed by a slower second stage.

The activation energy for the first stage of reduction (0–35% reduction) can be calculated according to the procedure described below.

The temperature dependence of the rate of a chemical reaction can be expressed by the Arrhenius equation:

$$k = Ae\left(\frac{-E_A}{RT}\right) \quad [7]$$

where k is the reaction rate constant, A is a frequency factor (s^{-1}), R is the gas constant ($J/mol.K$), T is temperature (kelvin), and E_A the activation energy (J/mol).

The calculation procedure follows that of El-Guindy and Davenport (1970) and Kekkonen, Xiao, and Holappa (1995). The following assumptions were made for calculation of the activation energy:

The activation energy is valid for the reduction stage between zero and approximately 35% reduction, during which only iron oxide was reduced.

The set of kinetic data taken from the reduction curves obtained at 1050°C, 1100°C, and 1150°C (Figure 1) was used in the activity energy calculations.

Solid-state reduction of an ilmenite concentrate with carbon

Taking the logarithm of each side of Equation [7] yields:

$$\ln(k) = \ln(A) - (E_A / R) \left(\frac{1}{T}\right) \quad [8]$$

which is a straight line with a slope of $-E_A/R$. Rate constant (k) values were derived from the straight line portions of the kinetic curves given in Figures 1 for the first stage of the reduction. The slopes of the straight lines representing $\ln(k)$ versus $1/T$ were used to calculate the average activation energy for the reduction reaction. In this work, the $\ln(k)$ and $1/T$ values were substituted into Equation [8] in order to calculate the activation energy (EA) for the reduction reaction.

Using the experimental data given in Figure 1 for temperatures of 1050°C, 1100°C, and 1150°C, the $\ln(k)$ vs $1/T$ curves were plotted and the slopes of the straight line sections of Figure 13 were used to calculate the average activation energy as 257 kJ/mole for the initial stages of reduction (zero to 35% reduction). This value was found to be close to the activation energy value reported in the literature as 64 kcal/mole (El-Guindy and Davenport, 1970).

Conclusion

The reduction rate increased with increasing temperature and decreasing particle size. The metallic phase contained high Fe and low Ti values, whereas the oxide phase adjacent to the metallic phase contained high titanium oxide and low iron oxide.

The reduction of ilmenite proceeded through stages during which iron oxides were first reduced to form metallic iron and then to form iron carbides, whereas titanium oxides were reduced to form $Ti_{n}O_{2n-1}$ during the initial stages with the possible formation of lower oxides at the later stages. The core of the particle (the original ilmenite grain) retained its composition with slight reduction of both iron and titanium oxides at the initial stages of reduction, and was reduced partially at the later stages.

The metallic nuclei formed in the partially reduced oxide phase were very small and are therefore not considered suitable for separation by mineral concentration processes. The kinetics of reduction were greatly influenced by the formation and growth of metallic nuclei during the initial stages of reduction and by the mass transfer (diffusion) process at the later stages. The overall activation energy for the initial stages of reduction of ilmenite with carbon was calculated as 257 kJ/mole in the temperature range 1050–1150°C.

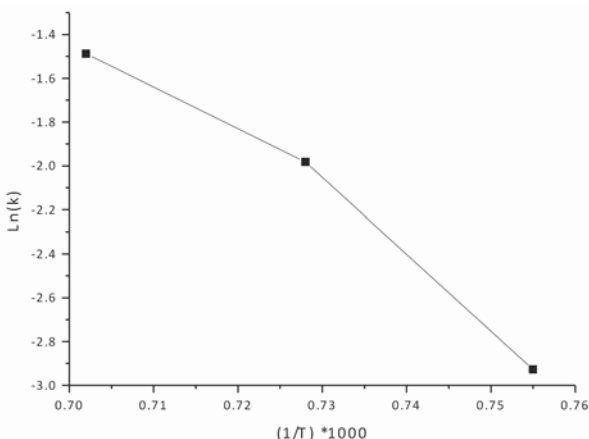


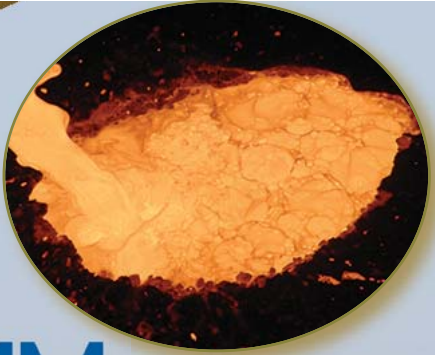
Figure 13— $\ln(k)$ vs $1/T$ curve

Acknowledgements

The authors wish to express their thanks to the School of Chemical and Metallurgical Engineering, University of the Witwatersrand for the laboratory facilities and the analytical services used. Thanks are also due to O. Netshifamadi, T.J. Molokwane, and S. Mokgadi (fourth-year project students) for carrying out some of the laboratory work, and to B. Nelwalani (SEM Technician) for the SEM-EDX analytical work.

References

- EL-GUINDY, M.I. and DAVENPORT, W.G. 1970. Kinetics and mechanism of ilmenite reduction with graphite. *Metallurgical Transactions*, vol. 1. pp. 1729–1734.
- GREY, I.E., JONES, D.G., and REID, A.F. 1973. Reaction sequences in the reduction of ilmenite. (1): Introduction. *Transactions of the Institution of Mining and Metallurgy*, vol. 82C. pp. 151–152.
- KEKKONEN, M., XIAO, Y., and HOLAPPA, L. 1995. Kinetic study on solid state reduction of chromite pellets. *Proceedings of INFACON 7*, Trondheim, Norway, June 1995. Tveit, H., Tuset, J.K., and Page, I.G. (eds.). Norwegian Ferroalloy Producers Research Organization (FFF).
- KUCUKKARAGOZ, C.S. and ERIC, R.H. 2005. Phase changes in solid state reduction of a natural ilmenite. *Proceedings of Heavy Minerals 2005*. Society for Mining, Metallurgy and Exploration, Littleton, CO. pp. 229–233.
- KUCUKKARAGOZ, C.S. and ERIC, R.H. 2006. Solid state reduction of a natural ilmenite. *Minerals Engineering*, vol. 19, no. 3. pp. 334–337.
- LOBO S., KOLBEINSEN, L., and SEIM, S. 2013. Pre-reduction of ilmenite with natural gas-model development and use. *Proceedings of the 13th International Ferroalloys Congress: Efficient Technology in Ferroalloy Industry*, Almaty, Kazakhstan, 9–13 June 2013. pp. 857–868.
- MERK, R. and PICKLES, C.A. 1988. Reduction of ilmenite by carbon monoxide. *Canadian Metallurgical Quarterly*, vol. 27, no. 3. pp. 179–185.
- PESL, J. 1997. Thermodynamics and phase equilibria in the Fe-Ti-O System at 1500°C and 1600°C and metal-slag-equilibria pertinent to ilmenite smelting. PhD thesis, University of the Witwatersrand, Johannesburg.
- PISTORIUS, P.C. 2002. The relationship between FeO and TiO₂ in ilmenite smelter slags. *Scandinavian Journal of Metallurgy*, vol. 31, no. 2. pp. 120–125.
- SAI, P.S.T. 2008. Evaluation of mathematical models for the reduction of ilmenite with char in a rotary reactor. *Journal of the Indian Institute of Chemical Engineers*, vol. 50, no. 4. pp. 312–322.
- SOYKAN, O., ERIC, R.H., and KING, R.P. 1991. Kinetics of reduction of the Bushveld Complex chromite ore at 1416°C. *Metallurgical and Materials Transactions B*, vol. 22 B. pp. 801–810.
- WANG, Y.M., YUAN, Z.F., GUO, Z.C., TAN, Q.Q., LI, Z.Y., and JIANG, W.Z. 2008. Reaction mechanism of natural ilmenite with graphite. *Transactions of the Nonferrous Metals Society of China*, vol. 18. pp. 962–968.
- WELHAM, N.J. and WILLIAMS, J.S. 1999. Carbothermic reduction of ilmenite (FeTiO₃) and rutile (TiO₂). *Metallurgical and Materials Transactions B*, vol. 30B, December. pp. 1075–1081.
- WILSON, N.C., MUSCAT, J., MKHONTO, D., NGOEPE, P.E., and HARRISON, N.M. 2005. Structure and properties of ilmenite from first principles. *Physical Review B*, vol. B71, 075202.
- WOUTERLOOD, J.H. 1979. The reduction of ilmenite with carbon. *Journal of Chemical Technology and Biotechnology*, vol. 29. pp. 603–618.
- ZIETSMAN, J.H. and PISTORIUS, P.C. 2004. Process mechanisms in ilmenite smelting. *Journal of the South African Institute of Mining and Metallurgy*, vol. 104, no. 11. pp. 653–660. ♦



SAIMM
THE SOUTHERN AFRICAN INSTITUTE
OF MINING AND METALLURGY

is proud to host the

CHROME COLLOQUIUM 2017

What's next for Chrome? A debate on the tough questions

19–20 June 2017

Mintek, Randburg, South Africa

BACKGROUND

Chrome beneficiation has been at the core of driving South Africa's ferroalloy industry for many years. Various technical, economic, environmental and social issues have seen an industry transform over decades.

OBJECTIVES

Debate the tough questions around issues across the entire chrome value chain.

WHO SHOULD ATTEND

- ⇒ Policy makers
- ⇒ Investors
- ⇒ Engineers, technicians and scientists in the chrome industry across the entire value chain (mine to furnace)
- ⇒ Engineering companies
- ⇒ Experts in production, economics and the environment
- ⇒ Stainless steel producers
- ⇒ Mine managers
- ⇒ Smelter managers
- ⇒ Process engineers and specialists
- ⇒ Researchers/Academics
- ⇒ Students

TOPICS

- ⇒ The future of chrome in South Africa
- ⇒ The impact of UG2 from the PGM industry
- ⇒ The cost and availability of electricity in the chrome industry
- ⇒ Fines, tailings and low grade ores: beneficiation, processing and use in processes
- ⇒ Market demand uncertainties

- ⇒ New technology in the ferrochrome industry
- ⇒ New processes and processing techniques
- ⇒ Sale of ore versus production
- ⇒ Sale of chromite ore *versus* production of ferrochrome
- ⇒ Why do we need chrome?
- ⇒ How do we extract maximum value from this key resource of which SA has an abundance of?
- ⇒ Government policy around:
 - Carbon Tax
 - Export restrictions
 - Subsidies
 - Sustainability?
- ⇒ Techno-economics of chrome in SA
- ⇒ Environmental issues related to the industry

SPONSOR

LANXESS
Energizing Chemistry

LANXESS Chrome Mining (Pty) Ltd.



FOR FURTHER INFORMATION CONTACT:

Head of Conferencing, Camielah Jardine, SAIMM,
Tel: +27 11 834-1273/7 · Fax: +27 11 833-8156
E-mail: camielah@saimm.co.za · Website: <http://www.saimm.co.za>

Conference Announcement



Gold and associated industrial heavy minerals in the Icy Cape District: White River to Icy Cape, Alaska, USA

by K. Eden*, A.E. Grosz†, J.E. Grosz†, C.J. Giles†, and J.Y. Foley‡

Synopsis

Portions of the Icy Cape placer Au district have been described and exploited since the early 1900s. Industrial studies of Au-bearing garnet-rich intervals established a 3.5 million troy ounce resource in the western half of the district. This estimate is not compliant with CIM and SME definition standards for Mineral Resources and Mineral Reserves. We note high variability in the textures of sediments and their heavy mineral (HM) content and composition in the district, probably as a function of the depositional environment. Sediments are medium- to fine-grained sands with a valuable HM assemblage that averages 26.0% in a range of 1.1–72.6%. Valuable heavy minerals (VHMs) garnet, magnetite, ilmenite, rutile, and zircon, but excluding Au, average 7.9% in a range of 1.0–37.6% of the HM assemblage. Trace quantities of uraninite, thorite, monazite, xenotime, and others are noted. Garnets have an average Y content of 726 ppm with a range of 0–2150 ppm. Energy-dispersive X-ray fluorescence confirms compositions commensurate with Ca, Al, and Mg silicates. We provide empirical analytical data and note high variability in the textures, HM content, and compositions as a probable function of depositional environment. Icy Cape District land and resources are owned by the Alaska Mental Health Trust Authority and managed by the Trust Land Office (TLO).

Keywords

placer gold, heavy minerals, beach sands, mineralogical characterization, depositional environment.

Introduction

The Icy Cape Heavy Minerals (HM) District in Alaska subtends more than 200 km² fronting the Pacific Ocean and backing to the foot of the Robinson Mountains at about 1700 m above sea level. We classify the district into geomorphic provinces; the eastern region as deltaic (Figure 1) and the western region as coastal plain (Figure 2), based on geomorphologic expressions. The coastal plain is entirely built up of unconsolidated outwash sediments and ancient beach sand deposits.

The area from the White River to Icy Cape has intermittently produced placer gold since the initial discovery in 1897. Gold production reports are nonexistent, but it is estimated that at least 16 000 troy ounces of gold have been mined from small-scale placer operations that concentrated on the active beaches and the White River sediments. It

was not until the mid-1980s to the early 1990s that mining companies such as Noranda Exploration from Canada and Paraclete Resources from Australia began exploration for large-scale placer gold deposits. Paraclete Resources defined areas for gold placer mining as presented in Figure 2 and delineated a 3.5 million troy ounce resource (Rossetti, 1992). This resource estimate is a historical estimate and is not compliant with CIM and SME definition standards for Mineral Resources and Mineral Reserves.

Placer Au occurs primarily as fine-grained (averaging 0.250 mm in diameter) flat and rounded plates and is strongly associated with garnet-rich layers (inset in Figure 2). Test work demonstrated recoveries in excess of 93%, at an estimated 81% purity (Trust Land Office document archives).

In 1996 the land and minerals ownership of the Icy Cape land block was transferred from the State of Alaska to the Alaska Mental Health Trust Authority. The land and mineral resources are managed by the Trust Land Office (TLO). Natural resources between mean high tide and three nautical miles (5.56 km) offshore are managed by the State of Alaska. The nature and distribution of HMs in offshore sediments is unknown.

Over the next decade the TLO will develop timber resources in the heavily vegetated region of the coastal plain and delta regions. This will allow synergy with mineral resources development strategies.

Background

The first published systematic study of HMs in the region is one of titanium mineral

* Trust Land Office, Anchorage, AK, USA.

† Global Minerals Sands, Inc. Herndon, VA, USA.

‡ Exploration Geologist (Retired), Anchorage, AK, USA.

© The Southern African Institute of Mining and Metallurgy, 2017. ISSN 2225-6253. This paper was first presented at the Heavy Minerals Conference 'Expanding the Horizon', 16–17 August 2016, Sun City, South Africa.

Gold and associated industrial heavy minerals in the Icy Cape District

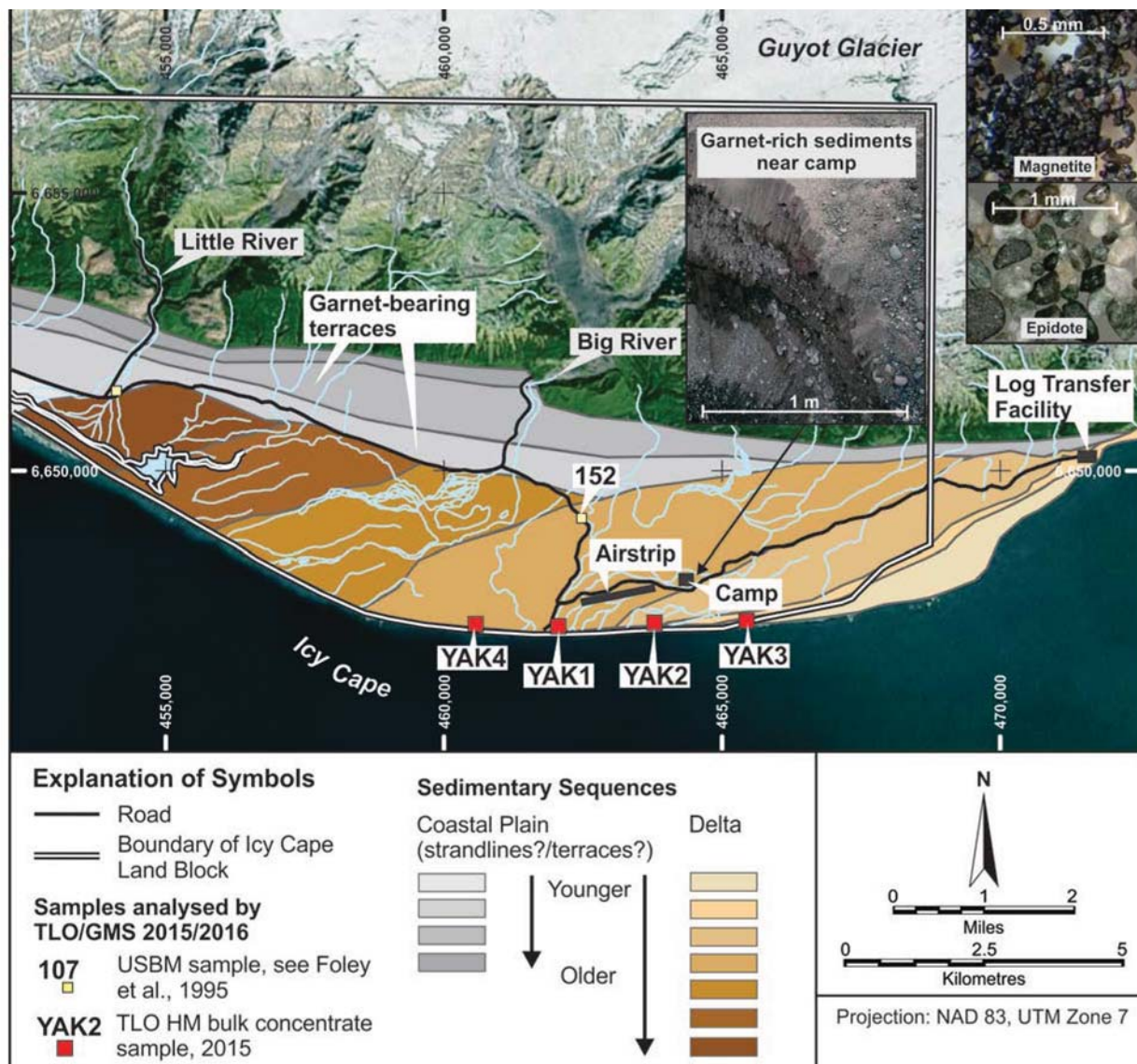


Figure 1—Sample locations and sedimentary sequences in the eastern Icy Cape District

resource potential by Foley *et al.*, (1995). They sampled at about 2 km intervals traversing the modern beach environment using solid-stem power and hand augers in the intertidal zone, beach face, and back beach, and channel sampling of wave-cut beach terraces. Samples collected during that study averaged 1.5 m intervals ranging to 9.6 m in depth. Foley *et al.*, (1995) estimate 0.57% valuable heavy minerals (VHMs: 0.49% ilmenite; 0.05% rutile; 0.03% zircon) with a range of <0.1% to 2.9% VHMs in modern shoreline sands of a portion of the district west of the Little River. Foley *et al.* note that dynamic depositional processes result in large variations in grain size distribution and in HM content. These large variabilities make the determination of statistical central tendencies difficult. Median and modal values are better measures of this tendency, but we present mathematical averages bracketed by ranges.

Foley *et al.*, (1995) note that the HM fractions contain polymimetic grains, 'rock fragments', interlocked grains of magnetite, pyroxene, plagioclase, sphene, and ilmenite. They note the extensive deltaic sediments at Icy Cape, and their

reconnaissance Ti, Zr, and Au assays for samples from this area indicated that VHMs are present. Trace quantities of platinum group metals (PGMs) are associated with the placer gold (Foley *et al.*, 1995, Table 3).

Formerly confidential industry assessments of Au shown in Figure 2 (TLO document archive) note the sands contain other potentially recoverable minerals. Of these, zircon, garnet, and ilmenite are the most likely recoverable, with PGMs regarded as a possibility. The PGMs are apparently associated with magnetite. These reports also note that rutile is present and should be evaluated as a potential by-product of the proposed gold operations.

The stratigraphy of the coastal region (coastal plain and delta) is not well known. Corporate models are based on the major unconsolidated sediment types, which are classified according to lithological character and origin. The sediments comprise well-sorted sand and gravel formed at or near the present beach and on former beaches, including strandlines elevated by Holocene tectonic uplift; well-sorted dune sand on or near the present or former beaches; interbedded mud

Gold and associated industrial heavy minerals in the Icy Cape District

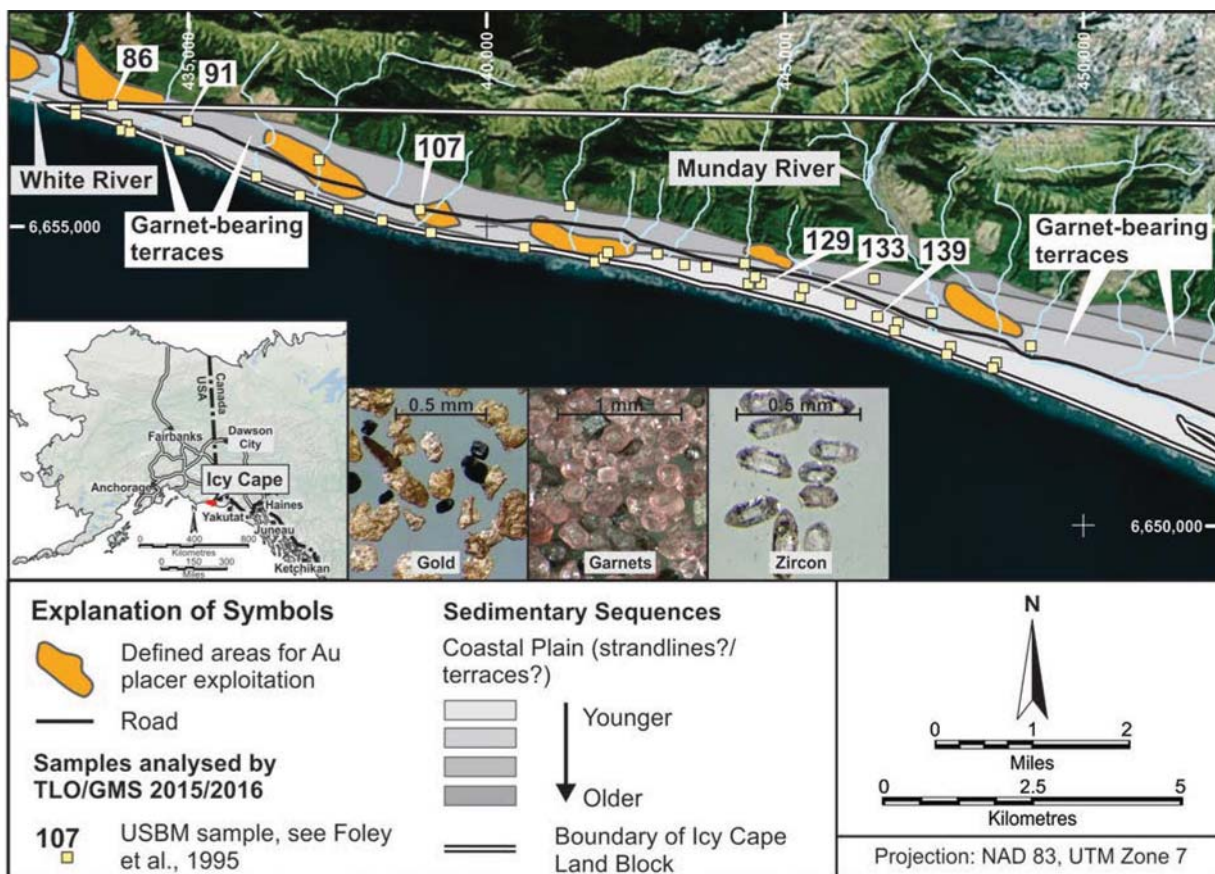


Figure 2—Sample locations, sedimentary sequences, and outlined areas for gold placer mining in the western Icy Cape District

and sand containing much organic debris, which were formed on tidal flats, in bays or lagoons, and in clear lakes and swamps; and interbedded mud and poorly sorted to moderately well-sorted sand and gravel, which were formed on the floodplains or fans of streams on the outwash aprons of glaciers, including terminal and ground moraine and ice-raftered deposits. The thickness of the unconsolidated deposits on the coastal lowland and along the raised beach ridges is not known but is estimated to be of the order of tens of metres.

Current work

Our studies relied on methods, procedures, and techniques commensurate with those of the placer Ti-Zr-REE HM industry. Particle size distribution (PSD) analyses were conducted using US Standard stainless steel sieves and are reported for some bulk samples and for their HM fractions. An average mass of 120 g was separated in lithium metatungstate (LMT), a heavy liquid with a specific gravity of >2.96. Technical aspects are detailed by Foley *et al.* (1995) and by Grosz, Berquist, and Fischler (1990).

A Frantz barrier magnetic separator was used to separate minerals in the HM concentrate into seven fractions. After a low field-strength (0.05 A) pass through the apparatus set at 15 degree forward- and 25 degree side-slopes, the HMs were concentrated according to their magnetic susceptibilities at 0.15, 0.25, 0.35, 0.50, and 1.00 A, yielding a nonmagnetic 1.00 A residue, and their weights were recorded. This approach recovered, for example, over 90% of the garnet into

the 0.25 A fraction, over 95% of the rutile and zircon into the nonmagnetic residue, and epidote, pyroxene, and amphibole minerals into the intermediate fractions. Due to variations in chemical composition and the presence of inclusions and complex intergrowths, a particular mineral may report to more than one magnetic fraction. Magnetic fractionation reduces the number of mineral species in each fraction and thus facilitates qualification and quantification of the HM species.

Each magnetic fraction was examined by reflected and transmitted light microscopy. Modal mineralogical compositions were determined by point counts of at least 500 grains in combination with visual estimates of field percentage compositions. Mineral percentages were calculated on the basis of their weight in each fraction. The calculated weights of a mineral in the various magnetic fractions were then summed and divided by the total weight of the HMs. The densities of individual mineral species were not compensated for by this method. XRD, XRF, SEM, and microprobe analysis were used to confirm petrographic mineral determinations and to obtain detailed compositions.

In this paper, we provide PSD, HM content, modal mineralogical, and adjunct analytical data for samples. We also generated conductive, nonconductive, and trace element determinations, but these results are not included in this brief report.

More than 100 samples from Foley's (1995) study were retrieved from archives at the Geologic Materials Center in Anchorage, AK. From these, 87 samples averaging 275 g

Gold and associated industrial heavy minerals in the Icy Cape District

were collected by use of Jones splitters. Five samples of garnet-rich beach concentrate collected by the TLO in 2015 were also included. The average HM content of the 87 samples is 19.3% in a range of 0.7–72.6%. The PSD of these sands is predominantly between 0.149 mm and 0.297 mm. With the exception of a few beach samples containing significant amounts of very coarse sand- to gravel-sized material, samples were predominantly less than 0.595 mm and greater than 0.105 mm in particle size.

The analytical results for 21 samples representing seven locations as selected for this report are presented in Table I. They represent thicknesses of sediments above mean high tide, as modern beach sediments are outside the TLO property boundaries. Each location has defined sampling intervals. For example, samples SN 86.1 through SN 86.4 denote a core location with successively deeper sampled intervals. Sample numbers from Foley *et al.*, (1995) are present as map numbers for ease of cross-reference. Table I shows their locations (coordinates in metres, North American Datum 1983, UTM Zone 7), depth intervals in metres, and %HM (SG >2.96) expressed as a percentage of the bulk sample collected. Analyses of these widely distributed power-auger, hand-auger, and channel samples show an average 26.0% HMs in a range of 1.1–72.6%.

Results

Medium- to fine-grained sands with locally significant coarse- or fine-grained components dominate the coastal plain and delta portions of the district. With the exception of a few samples of relatively very coarse sand to gravel-sized material, the particle size is from 0.6 mm to 0.11 mm. The PSDs of 21 sediment samples and some of the HMs are given in Table II. Note the high variability in size distribution of both bulk sediments and their HMs.

Mineralogy

The HMs of coastal plain and deltaic sediments in the district comprise a large and varied assemblage.

Table I

Analytical results for 21 bulk sediment samples showing sample locations, depth intervals sampled, and HM content

SN	UTM E	UTM N	From m	To m	Interval m	Wt% HM
86.1	433723	6657013	0.0	2.1	2.1	44.89
86.2	433723	6657013	2.1	4.0	1.9	33.82
86.3	433723	6657013	4.0	5.8	1.8	24.12
86.4	433723	6657013	5.8	7.3	1.5	72.58
91.1	434966	6656749	0.9	2.1	1.2	13.85
91.2	434966	6656749	2.1	4.0	1.9	64.91
91.3	434966	6656749	4.0	5.8	1.8	38.72
107.1	438874	6655268	0.9	2.7	1.8	38.87
107.2	438874	6655268	2.7	5.8	3.1	17.18
107.3	438874	6655268	5.8	6.7	0.9	10.44
129.1	444575	6654017	0.0	2.1	2.1	33.86
129.2	444575	6654017	2.1	4.0	1.9	12.88
129.3	444575	6654017	4.0	5.8	1.8	6.97
129.4	444575	6654017	5.8	7.6	1.8	1.50
129.5	444575	6654017	7.6	9.6	2.0	1.10
133	445248	6653788	0.0	0.8	0.8	21.27
139.1	446545	6653484	0.0	2.1	2.1	48.78
139.2	446545	6653484	2.1	4.0	1.9	10.92
139.3	446545	6653484	4.0	5.8	1.8	8.32
139.4	446545	6653484	5.8	7.2	1.4	2.91
152	462481	6649158	0.0	4.6	4.6	38.99

Table III shows the distribution of HMs in 21 samples. Magnetite (MAG), ilmenite (ILM), garnet (GAR), rutile (RUT), zircon (ZIR), others (OTH), and VHM, (MAG, ILM, GAR, RUT, and ZIR) are given as modal percentages of the total HMs. A value of 0.00 denotes <0.01%. Images of minerals are shown as insets in Figure 1 and Figure 2, and they are described in the following section. Small, flat (with irregular and/or curled edges) gold particles as well as uraninite and thorite particles were noted in many samples (example in Figure 1).

XRF analyses confirmed the chemical compositions commensurate with the relative abundances of Ca, Al, and Mg silicate minerals, which have not been examined for their potential value as abrasives, water filtration agents, drilling mud components, or other commercial applications.

Magnetite and ilmenite

MAG and ILM are strongly magnetic components of the HMs. They are technically best classified as oxides as they include

Table II

Particle size distribution (in mm) of 21 bulk sediment samples and some of their HMs. Blank cells have no data

SN	BULK SIZE DISTRIBUTION (Wt% retained)						HM SIZE DISTRIBUTION (Wt% retained)					
	0.595	0.420	0.297	0.250	0.149	<0.149	0.595	0.420	0.297	0.250	0.149	<0.149
86.1	0.7	1.6	10.5	13.9	70.2	3.2	0.1	0.4	4.2	5.3	84.4	5.6
86.2	4.6	3.8	17.2	17.6	53.2	3.6	0.9	0.8	3.6	10.1	79.7	4.8
86.3	10.8	6.1	21.7	17.9	40.2	3.3	2.6	1.8	9.6	7.2	77.1	1.5
86.4	12.5	6.3	21.4	17.5	39.0	3.4	16.9	0.7	2.6	2.1	49.4	28.2
91.1	3.8	2.6	6.8	10.3	65.6	10.9						
91.2	0.6	0.1	1.0	2.8	66.4	29.2						
91.3	2.5	2.6	10.8	10.8	70.5	2.8						
107.1	2.3	0.7	7.5	15.9	66.7	6.9						
107.2	0.5	0.9	11.9	20.2	64.2	2.2						
107.3	6.2	7.3	21.5	18.5	40.8	5.6						
129.1	0.1	0.3	10.2	23.3	65.2	0.8	0.0	0.0	0.9	1.3	95.0	2.8
129.2	2.4	3.2	18.7	25.6	48.3	1.8	0.0	0.0	4.4	8.6	85.0	1.7
129.3	4.0	2.9	17.8	23.0	51.7	0.7	6.2	2.3	4.5	9.0	67.9	10.1
129.4	1.2	1.0	6.7	11.3	52.5	27.2	19.7	3.9	12.1	9.1	53.0	2.2
129.5	0.1	0.4	8.6	17.4	72.2	1.4						
133	0.0	0.1	5.1	19.6	73.1	2.1						
139.1	1.8	3.0	20.4	24.6	47.6	2.7	0.0	0.0	2.0	1.7	3.2	93.0
139.2	1.8	2.3	19.9	24.4	50.6	1.0	2.8	1.4	12.3	10.6	38.6	34.2
139.3	2.5	3.5	21.6	25.1	44.7	2.6	1.5	2.0	2.5	50.9	31.3	2.9
139.4	2.0	0.7	7.2	15.3	68.0	6.8						
152	52.7	16.6	13.1	4.3	8.5	4.8						

Table III

Modal mineralogical composition of the samples in Table II

SN	MINERAL COMPOSITION (Wt% of HM)						
	MAG	ILM	GAR	RUT	ZIR	OTH	VHM
86.1	0.73	0.17	10.21	0.47	0.42	88.00	12.00
86.2	0.79	0.17	8.70	0.43	0.31	89.60	10.40
86.3	0.15	0.66	12.70	0.08	0.11	86.30	13.70
86.4	0.14	0.00	1.66	2.89	2.76	92.55	7.45
91.1	1.86	0.07	8.42	0.34	0.23	89.08	10.92
91.2	1.47	0.54	11.75	0.76	0.53	84.96	15.04
91.3	1.70	0.05	6.72	1.94	0.74	88.84	11.16
107.1	1.90	0.18	9.11	0.37	0.45	87.99	12.01
107.2	0.28	0.00	3.94	0.20	0.66	94.92	5.08
107.3	0.48	0.03	3.52	0.32	0.50	95.16	4.84
129.1	0.85	0.00	0.76	0.17	0.02	98.20	1.80
129.2	0.51	0.00	0.42	0.06	0.00	99.01	0.99
129.3	0.44	0.06	0.56	0.02	0.02	98.90	1.10
129.4	0.59	0.08	0.68	0.01	0.04	98.60	1.40
129.5	0.56	0.00	1.24	0.00	0.03	98.17	1.83
133	1.51	0.03	0.34	0.03	0.00	98.09	1.91
139.1	1.93	0.76	34.73	0.07	0.14	62.37	37.63
139.2	1.95	0.03	7.75	0.28	0.08	89.91	10.09
139.3	1.31	0.00	1.82	0.26	0.00	96.61	3.39
139.4	1.43	0.00	0.65	0.06	0.07	97.78	2.22
152	0.40	0.00	0.67	0.04	0.01	98.88	1.12

Gold and associated industrial heavy minerals in the Icy Cape District

Ti-free iron oxides with sphene and amphibole inclusions, haemo-ilmenite, chromite, octahedral and rounded magnetite, and magmatic haematite-ilmenite-magnetite showing exsolution features at 2 µm to >50 µm scale. Sphalerite, pyrite, and REE-rich phases from 2 µm to 10 µm in size occur as inclusions in the oxide group minerals. Ilmenite is present in all samples but is not liberated (52.7% TiO₂), and it appears not to be suitable for pigment manufacture because of trace impurities that include Si, Cr, V, and Al (Foley *et al.*, 1995). Figure 3A shows a backscattered SEM image of a typical titaniferous magnetite with titanium-rich exsolution lamellae (thin black bands). Black spots are Al-rich spinel. Figure 3B shows intergrowth of magnetite and ilmenite. Black areas near the centre are hornblende inclusions. Oxides average 1.13% of the HM suite, with a range of 0.14% to 1.98% (Table III).

Garnet

The garnet group was examined in more detail than other HMs as the co- or by-product potential of garnet was alluded to in the past but was not addressed. Garnet comprises an average of 6.02% of the HM suite with a range of 0.34% to 34.73% (Table III). Our analyses reveal that end-members almandine, pyrope, grossular, and spessartine (not including andradite and uvarovite) comprise 67%, 12%, 6%, and 15% respectively of the garnet group. We distinguish pink, orange, and dark garnets that are mostly euhedral to slightly rounded, with a crushed shard component. Figure 4 shows the principal types. Many garnets have varying amounts of inclusions that include monazite-(Ce) (up to 25 µm), pyrite

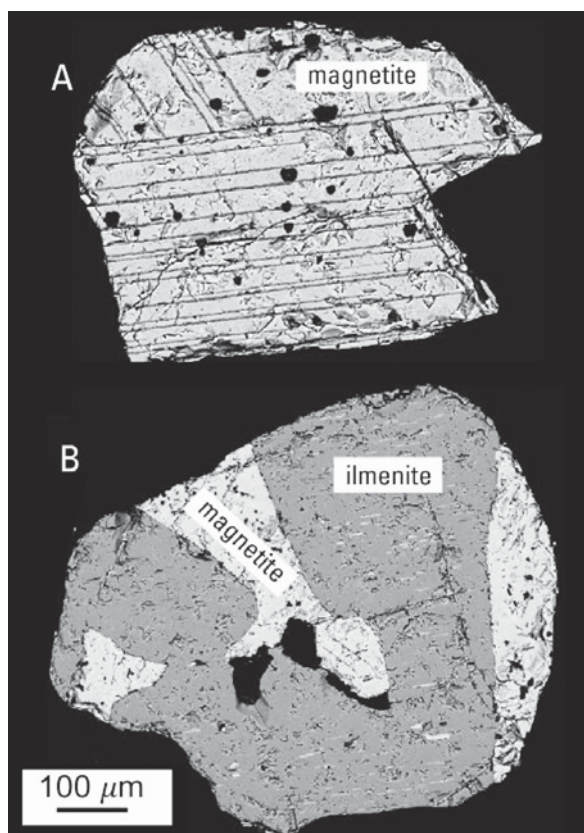


Figure 3—Backscattered SEM image of oxide mineral particles classified as magnetite and ilmenite (MAG and ILM; Table III)

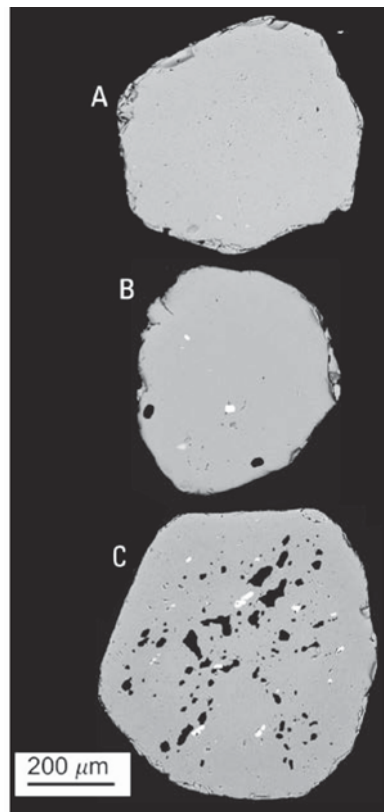


Figure 4—Backscattered SEM electron image of typical garnet particles (GAR, Table III) A: pink, euhedral; B: orange, rounded, with zircon (white) and quartz (black) inclusions; C: dark, rounded, with quartz (black) and ilmenite (white) inclusions

(up to 25 µm), ilmenite (up to 50 µm), and xenotime (up to 20 µm). Microprobe analyses show garnets have an average Y content of 726 ppm with a range of 0 to 2150 ppm, with pink and orange types having the highest overall values. The reader interested in Y distribution in garnet-group minerals is referred to Jaffe (1951), Pyle and Spear (1999), references therein, and to subsequent publications.

Rutile

The rutile group ($\geq 90\%$ TiO₂) includes rutile, anatase, and sphene. This group of minerals averages 0.42% of the HM suite with a range of <0.01% to 2.89% (Table III). Particles appear liberated and are finer-grained than other HMs, including gold.

Zircon

Zircon is present as fine-grained, clear, doubly terminated euhedral crystals and as crushed shard fragments with low U and Th content (<300 ppm combined). Figure 5 shows euhedral zircon (A) and a broken fragment of euhedral zircon (B). ZR comprises an average of 0.34% of the HM suite with a range of <0.01% to 2.76% (Table III). Some zircons contain chalcopyrite inclusions up to 20 µm, monazite inclusions up to 10 µm, uraninite inclusions up to 5 µm, thorianite inclusions up to 2 µm, and thorite inclusions in the order of 1 µm. Arsenopyrite is also occasionally present as inclusions. Zircons are finer-grained than other the HMs, including gold.

Gold and associated industrial heavy minerals in the Icy Cape District

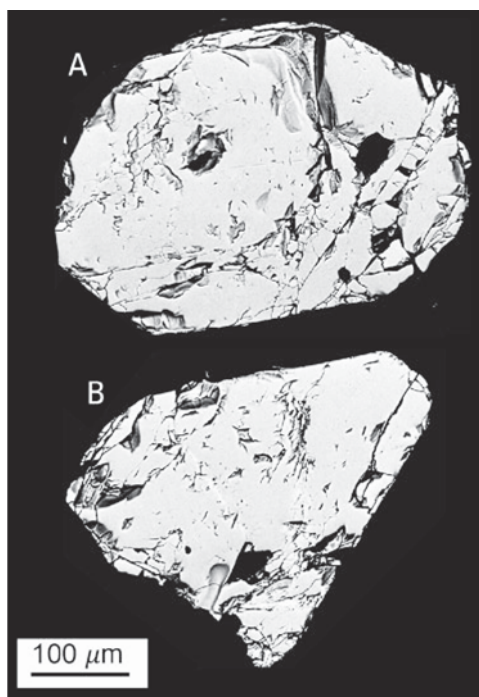


Figure 5—Backscattered SEM image of typical zircon particles (ZIR, Table III)

Other

For the purposes of this study, large and varied groups of HMs are classified as 'others' (OTH, Table III) and retained for follow-up analyses. This group accounts for an average 92.09% of the HM suite with a range of 62.37–99.01%. It includes dominant epidote, zoisite, clinozoisite, pyroxene, amphibole, olivine, serpentine, as well as unidentified opaque and non-opaque sand- and finer-grained particles made up of HM and non-HM fragments. Included in this group are very small but persistent traces of spinels, monazite, cassiterite, uraninite (100 µm particles), chromite (high Al/low Fe), thorite, thorianite, albite, barite, scheelite, and localized carbonate fragments.

VHMs

Reported VHMs reflect on potential as co- and by-product HMs from gold recovery operations. Excluding gold, VHMs average 7.91% of the HM suite in a range of 0.99–37.63% (Table III). Values are considered underestimates because the OTH group contains a larger, though lower-value, suite of industrial minerals than VHMs. Nonetheless, the VHM contents reach very high values in comparison to traditional titanium-zirconium deposits.

Conclusions

The Icy Cape District is host to a large and varied body of unconsolidated sediment with documented placer Au resources and associated HM resources that are primarily industrial in nature. We estimate the district to contain in excess of 1.7×10^9 t of resource-bearing sediments to 10 m depth. Our analyses confirm the potential for mineable HMs with associated Au concentrations. The geological

framework, textural, mineralogical, and chemical data indicates a large, but as yet incompletely understood, resource potential for gold, garnet, and other HMs. Very large vertical and lateral variations in PSD and HM content and composition are noted, likely as a function of depositional environment. This, and supportive (and formerly proprietary) information, enhances knowledge of the factors controlling the potential commercial viability of HMs in the Trust Land area, and provides a better understanding of resource potential with a view to exploration and development. The TLO will conduct high-resolution aeromagnetic surveys of the district in 2016 and stratigraphic and resource drilling campaigns in 2017.

Acknowledgments

This work was funded by the Trust Land Office and Iluka Resources. The authors would like to thank John Morrison, Wyn Menefee, Leann McGinnis, Paul Slenkamp, and Mike Franger of the Trust Land Office for their enthusiastic support. We are grateful for the invaluable assistance and cooperation of Iluka Resources; specifically of Thomas Hartzog, Adam Karst, Charles Acker, and Doug Holtman. We appreciate the easy availability of data, samples, facilities, and curator support of the Geologic Materials Center of the Alaska Department of Natural Resources in Anchorage, Alaska (<http://dggs.alaska.gov/gmc/general-info.php>), and in particular the assistance and support provided by Kurt Johnson, Jean Riordan, and Alexandra Busk. James Barker, retired USBM research geologist, provided invaluable information on previous research and exploration campaigns. We also would like to thank Jim R. Tuttle of Sealaska Timber Corporation for his support of this project. Last but not least, we are sincerely indebted to the knowledge, skills, expertise, and time that Harvey E. Belkin and Frank T. Dulong of the USGS provided and their expertise in SEM and microprobe, and XRD, respectively. Their world-class analytical expertise was invaluable to our study.

References

- FOLEY, J.Y., LABERGE, R.D., GROSZ, A.E., OLIVER, F.S., and HIRT, W.C. 1995. Onshore titanium and related heavy-mineral investigations in the eastern Gulf of Alaska region, southern Alaska. *Open-File Report 14-90*. US Bureau of Mines. 125 pp.
- GROSZ, A.E., BERQUIST, C.R., Jr., and FISCHLER, C.T. 1990. A procedure for assessing heavy-mineral resources potential of continental shelf sediments. *Heavy Mineral Studies - Virginia Inner Continental Shelf*. Berquist, C.R., Jr., (ed.). Publication 103. Virginia Division of Mineral Resources. pp. 13–30.
- JAFFE, H.W. 1951. The role of yttrium and other minor elements in the garnet group. *American Mineralogist*, vol. 36, no. 1, Jan-Feb. 1951. pp. 133–155.
- PYLE, J.M. and SPEAR, F.S. 1999. Yttrium zoning in garnet: coupling of major and accessory phases during metamorphic reactions. *Geological Materials Research* vol. 1. <http://www.minsocam.org/gmr/papers/v1/v1n6/v1n6.pdf>
- ROBSON, J.M. 1983. Yakataga beaches reconnaissance report, Project 50034-1983. Noranda Exploration Inc., Anchorage, Alaska, USA. 30 pp.
- ROSSETTI, L. 1992. The Yakataga Gold Project, Alaska, USA – predevelopment statement. Paraclete Resources Pty Ltd, Beulah Park, SA, Australia. 45 pp., 9 appendices. ♦



Geotechnical characterization and 3D modelling of the biologically cemented Mandena heavy mineral sand deposit - a case study

by L.I. Boshoff*, A.H. Bracken*, and F. Hees†

Synopsis

Biological cementation of the Mandena heavy mineral sand deposit in Madagascar was causing difficulty in dredge mining and hence in planning and control of production rates. An investigation was initiated to better evaluate the geotechnical properties of the orebody by defining the distribution and geotechnical properties of the cemented strata, in order to generate a site-specific geotechnical model for the deposit. The geotechnical characterization was developed by an integrated approach using several ground investigation techniques such as piezocene (CPTu) testing, geotechnical drilling, standard penetration testing (SPT), as well as laboratory testing. The final outcomes of the investigation included a 3D geotechnical model showing the distribution and extent of the cemented areas, as well as the typical geotechnical parameter ranges associated with each of the defined geotechnical units. The interpretations developed were incorporated into the mine and production planning to ultimately optimize operational planning and control.

Keywords

Madagascar, heavy minerals, cemented sand, geotechnical characterization, Leapfrog, piezocene.

Introduction

QIT Madagascar Minerals (QMM) is a heavy mineral sand mining operation at Mandena, near Fort Dauphin in Madagascar. During the final planning and commissioning stages of the project, the need to fully characterize the unusual geotechnical conditions was identified and a geotechnical investigation became necessary.

Nature of the problem

During the commissioning phase it was found that mining production was being hampered by biologically cemented/indurated layers encountered within the sands. Closer inspection of the indurated horizons in the dredging face revealed that these layers contain a high loading of bacteria and fungi. It appears that the bacteria produce an extracellular (outside the cell) polysaccharide (*i.e.* sugar and carbon salts), which form a gelling biofilm to trap nutrients. There are a number of different bacteria. The fungi, on the other hand, produce a network of fibrous strands that bind the sand grains together. Thus both bacteria and fungi probably

contribute to the 'apparent cohesive' strength or binding of the indurated sand (Lynn, 2008).

The main challenge in this project was the many unknowns surrounding the nature and extent of this biological cementation. Typically, the following questions arose.

- Is this a biological, geological, or geotechnical problem, or all of the above?
- How does one go about modelling a phenomenon that is not necessarily governed by apparent geological processes or markers?
- What tools and techniques would be suited to cope with the variable conditions being investigated? How effective will they be?
- How does one ensure the tools and techniques used can provide useful data that can be verified?
- How does one combine all the available data collected to generate a practical geotechnical model that will assist in a mining production environment?
- How does one approach the modelling of geotechnics and relate this to the geological resource model and mine plan?

Data gathering and evaluation

The scoping of the investigation was defined during various brainstorming sessions that considered existing data, the most crucial engineering parameters required for mine and dredge design, and which geotechnical investigation techniques available could potentially obtain the required data

* SRK Consulting, Johannesburg, South Africa.

† Rio Tinto and Titanium-RITT, Johannesburg, South Africa.

© The Southern African Institute of Mining and Metallurgy, 2017. ISSN 2225-6253. This paper was first presented at the Heavy Minerals Conference 'Expanding the Horizon', 16–17 August 2016, Sun City, South Africa.

Geotechnical characterization and 3D modelling

effectively. The scoping study also included trials using different rotary and vibracore drilling techniques to confirm which would be most appropriate to use.

This process culminated in an investigation methodology involving two phases. Phase 1 focused on high-density geotechnical rotary core drilling, logging, sampling, and standard penetration testing (SPT) as well as piezocone with pore pressure measurement (CPTu) testing within a limited area. Laboratory tests of soil and rock samples retrieved from the boreholes was also completed. Following the trials, it was decided not to use a vibracore drill as it was found that the vibration of the drill broke the intergranular bonds in the indurated layers, resulting in the indurated materials being recovered as soils.

Phase 2 focused on a lower density of testing on the remainder of the orebody. During phase 2 all available historical information was used, including existing exploration borehole log data, where appropriate, to generate a 3D geotechnical model and typical geotechnical parameter ranges for the most important geotechnical properties.

In-situ measurements using a piezocone (CPTu) rig provided direct measurements of cone resistance (q_c), sleeve friction (f_s), and pore water pressure (u), which can be used to derive various geotechnical parameters. Due to the expected variable conditions, the CPTu equipment was expected to be ineffective on the hardest indurated layers. A standard drilling rig or hydro vibracore rig (sonic method) was therefore provided to advance through the hardest layers.

Selected CPTu locations were paired with high-quality rotary core drilling, using a triple-tube barrel and a mud flush, to obtain cores of indurated sands and more cohesive/dense soil layers. Limited SPT was also completed in the holes and used to provide a comparison with the CPTu data. Detailed geotechnical logging of the rotary tube drilling core was completed. Laboratory testing of core samples

assisted in confirming the parameters derived from the CPTu interpretations and to determine parameters on the very hardest indurated sand layers that could not be derived from the CPTu testing.

The combined phase 1 and phase 2 geotechnical database consisted of 147 CPTu locations, and 48 borehole and SPT locations. More than 200 disturbed samples and approximately 80 core samples were tested in the laboratory. Figure 1 provides a general location map and test location layout of the area investigated.

Field logging of rotary drilling samples

Owing to poor recoveries, drilling provided little material within the un-indurated zones and this posed various challenges during field logging. To ensure consistent capturing of information that could later be calibrated and refined when combined with the other data gathered (such as the CPTu and laboratory information), a site-specific approach to logging was adopted to ensure that a consistent account of the indurated materials was captured. Generally, zones registering SPT N_{field} values of over 50 blow counts (noted as 'refusal') were deemed to be of very dense consistency or possibly of Extremely Soft to Soft rock with a uniaxial compressive strength (UCS) of 0.5–3.0 MPa. The presence of rock-like indurated material was logged only if core samples were available for confirmation, irrespective of the SPT N_{field} values recorded. Where this could be confirmed from core or SPT samples, the thickness, spacing, and depth of the indurated beds were recorded.

Based on this approach, zones with similar geotechnical characteristics were identified and provided with an overall description. This process was the first step in the generation of a site-specific geotechnical unit model.

Correlation of *in-situ* testing methods

A numerical correlation between the CPTu-derived SPT N_{60} values, q_c , and the SPT N_{field} values obtained in the paired

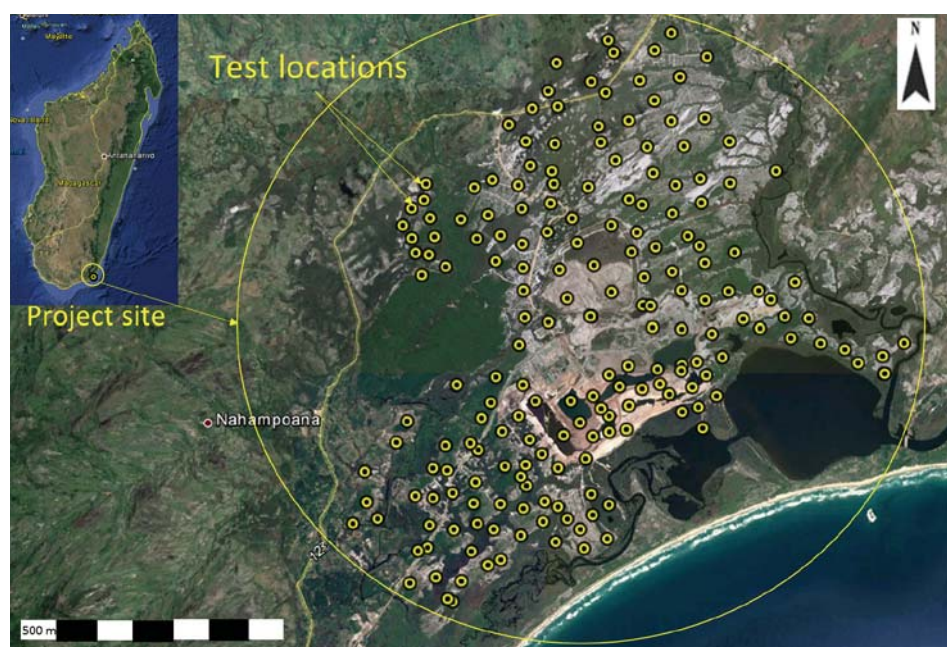


Figure 1—Schematic of project site locality in Madagascar and the planned drilling and test location layout

Geotechnical characterization and 3D modelling

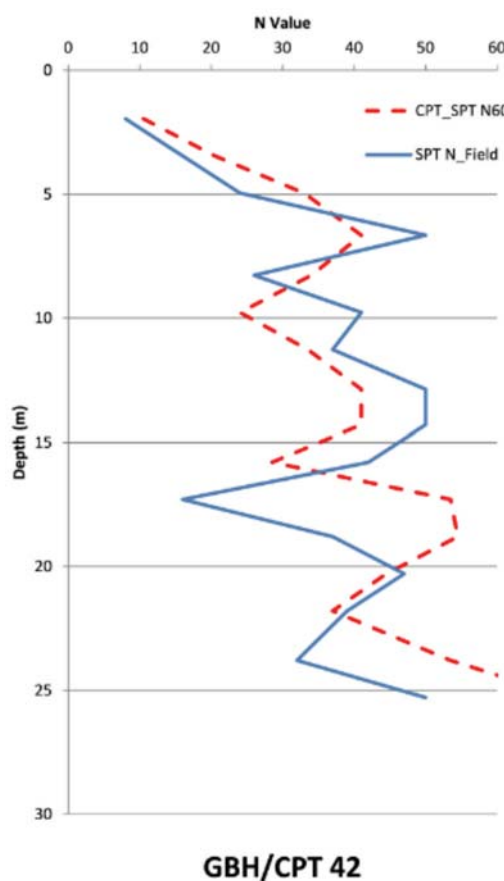


Figure 2—Comparison of CPTu-derived SPT N_{60} trend with SPT N_{field} values – test location no. 42

locations was completed. To obtain a point value that correlates with the SPT N_{field} values recorded, a linear average output value from the CPTu at the start and end of the SPT testing depths was assumed. A typical CPT-derived SPT N_{60} trend and SPT N_{field} values plotted against depth is shown in Figure 2.

Acceptable correlations were found to exist for 58% of the test positions, providing correlation coefficients from 0.5 to 0.94 (Boshoff and Bracken, 2011). Visual assessment indicated that trends were offset in several of the poorer correlating cases, but that the overall trends were similar.

Correction factors were applied to the SPT N_{field} values, but none of the standard correction factors such as rod energy, overburden, and anvil size, as described by Clayton (1995), provided a consistent improvement in the correlations obtained compared to the raw data.

CPTu interpretations and borehole logs vs laboratory results

Good correlation was found between the rotary drill sample logging, laboratory results, and the soil behaviour classes for the CPTu as defined by soil behaviour charts developed by Campenella and Robertson (1988).

CPTu identified sands and silty sands as dominating the profile with some materials, typically those found at the base of the probe holes, classifying as silts or sandy clay-type materials.

The laboratory UCS test results agreed well with the rock strengths identified during borehole logging, with most

falling within the strength range (UCS of 0.5 to 3.0 MPa) predicted during logging (Extremely Soft to Very Soft rock). The permeabilities measured in the laboratory for the core samples were in line with permeability predictions based on the CPTu-derived soil behaviour types for sands and silty sands (Robertson, 1992).

However, some exceptions occurred when correlating CPTu information with samples extracted from the paired rotary drill-holes, indicating that significant variation in induration strength can exist over small distances.

Generation of a geotechnical unit model

The processes described above led to the definition of a geotechnical unit framework within which the data could be further evaluated. The framework focused mainly on defining zones that would have specific engineering implications for the mining operation.

General internationally accepted guidelines as provided in the literature and summarized in the TRH10 (1994) document compiled by the Committee for State Road Authorities, South Africa (1994) relate CPT q_c to SPT N_{field} values and corresponding density descriptions, as shown in Table I.

Spikes in q_c values could be correlated with very dense to indurated layers located within generally Medium Dense to Very Dense silty sand layers. This finding agreed with observations during logging of the boreholes. It also became clear that the CPTu was more effective in detecting the presence of very thin indurated layers that would not be identified during drilling and SPT testing. The conceptual geotechnical unit framework was defined considering all the available data and is shown in Table II.

Simple principles were developed to ensure a consistent evaluation and optimization of the geotechnical zone boundaries that would constitute the final zone interval database. These include:

Table I

Internationally accepted consistency descriptors as a function of SPT N and CPT q_c value ranges obtained (adopted from TRH10)

Density description	SPT N	CPT q_c (MPa)
Very Loose	4	2
Loose	4-10	2-5
Medium Dense	10-30	5-15
Dense	30-50	15-20
Very Dense	>50	>20

Table II

Geotechnical unit model derived from phase 1 fieldwork data and observations

Zone	Name	Geotechnical description	Distribution
1	Aeolian sands	Firm flowing to non-free flowing Loose to Medium Dense sands.	Usually the surface deposit. Occasionally absent.
2	Strandline sands	Non-free flowing clean to organic, occasionally ferruginized, Medium Dense to Very Dense sands.	Usually underlying aeolian sands. Occasionally exposed at surface. Seldom (but may be) absent.
3	Strandline sands with indurations	Non-free flowing Medium Dense to Very Dense sands of interbedded with Extremely Soft (UCS 0.5–1 MPa) to Very Soft (UCS 1–3 MPa) indurated sands /sandstone.	Lenses generally within Zone 2. Occasionally at top or base. Apparently random distribution. Sometimes absent.
*4	Deposit base strandline sands, silts, and clays	Interbedded sands, silts, and clays of variable consistency.	At base of and occasionally interleaved with Zone2/3. Sometimes absent.
*5	Residual sandy clay	Firm clay, silt, or clayey sand.	At base of Zones 2/3 or 4.

*Zone 5 represents the clay basement and is not part of the resource, whereas Zone 4 is a transitional zone between the resource and basement.

Geotechnical characterization and 3D modelling

- Adopting CPTu data as the more accurate and continuous record of *in-situ* conditions due to generally low sample recoveries in the boreholes
- When delineating and optimizing geotechnical zone boundaries, density would have priority over descriptive properties (such as colour)
- Zone 3 conditions were inferred where significant spikes in the CPTu q_c (30–40 MPa) could be observed, where vibracore drilling was required, or where recovery of core samples confirmed the presence of indurated layers
- If a section was logged in boreholes as Zone 2 and the CPTu data indicated hard layers, this zone would be upgraded or adjusted to Zone 3 in accordance with CPTu data.

3D modelling approach

The spatial modelling was completed using implicit modelling software, Leapfrog3D Mining (ARANZ Geo, New Zealand). This module has since been superseded by Leapfrog Geo.

Implicit modelling uses a rapid 3D interpolation engine to construct 3D models. Implicit modelling techniques have been refined by developers over the past 10 years to suit geological modelling problems, and in this case implicit modelling was also applied to modelling specific geotechnical zones and gathered numerical data in much the same way as when modelling geological features and ore grades. The benefit of using implicit modelling is that it allows for the automatic construction of wireframes from scattered downhole data with no need for manual digitization (Cowan *et al.*, 2003).

During phase 2, the phase 1 interpretations were verified. Phase 2 also included scrutinizing the geological exploration data gathered to supplement 3D modelling. This in itself constituted a challenge as geological logging had been completed from a 'geological and resource modelling perspective', whereas the 'geotechnical zones' were based mostly on the engineering properties of the materials as logged and measured using specific *in-situ* measurement techniques.

Geotechnical zones were modelled as separate 'lithologies'. The geotechnical zone modelling and numerical modelling were approached separately. The measured data was considered 'hard' data, whereas the zone boundary interpretations were based on a combination of the descriptive and *in-situ* measured data.

Geotechnical zone lithology modelling

Geotechnical zone volumes were generated using spheroidal variogram settings with constant kriging and a range of approximately 300 m. The ellipsoid ratios were optimized to reflect the general dimensions of the volumes being modelled (*i.e.* disk-shaped with small Z relative to ellipse radius).

Zones 1, 2, and 3 were modelled separately; however, Zones 4 and 5 were combined and modelled as one composite region delineating the clayey deposit base consisting of either marine clays and/or residual clayey sands. Areas not defined by the interpolants developed from existing geotechnical data were inferred as comprising of geotechnical Zone 2-type sands.

The following age succession was assumed:

- Zone 3 is considered the youngest, generally cutting

indiscriminately through all deposited sands, as cementation took place after deposition of the strandline deposits

- Zones 1 to 5 (excluding Zone 3) were assumed to be of increasing age; however, Zone 2 could be interleaved with Zone 4-type materials (clays and silty sand lenses) due to the nature of deposition of the strandline sands.

Correlation between the geological database generated during exploration drilling and the geotechnical database was considered. After some review, it was confirmed that the merging of the two data-sets would not be ideal and would possibly skew the presentation of the geotechnical information gathered. The two data-sets were therefore kept separate within the modelling software. However, the geological data had to be utilized to some extent during modelling to supplement the limited geotechnical data-points available. To correlate indurated conditions captured within the geological database, an approach introduced by the project geologist was used to include an 'induration' interval to identify zones where described/indicated and inferred indurated conditions can be expected (Hees, 2010). This interval could be used to group key lithologies within the modelling space to reflect the distribution of the indurated conditions as per the geological database. This could then be compared with the geotechnical zone boundaries and integrated manually.

In areas where little data was available, the Zone 3 model was extrapolated by utilizing the reviewed and grouped geological data as well as geological cross-sections imported into the modelling software. However, areas did exist where indurated conditions were identified that were not captured in the geological database. Geotechnical data therefore took precedence in most cases when interpreting the Zone 3 material boundaries.

Numerical data analyses in 3D

A design chart was developed by the dredge designers matching SPT N number to output in tons per hour for the existing dredge when production issues ensued. For this reason, the first attempts in modelling of geotechnical properties were focused on the SPT N numerical data as known relationships existed. Numerical modelling of the SPT N_{60} and SPT N_{field} values was undertaken and run using similar settings to the lithological model.

A separate 3D interpretation was made using only the numerical data gathered to interpolate areas associated with specific numerical parameter thresholds within specific orebody areas. Numerical data within each modelled zone could also be extracted and analysed statistically. The numerical model can currently provide 3D contour maps of a specific geotechnical parameter modelled at any level or on any section through the orebody volume. The numerical interpretations do not agree in all areas with the zone interpretations, as selected locations were modelled using only descriptive logging information with no numerical geotechnical background data *e.g.* hydrogeological borehole positions or exploration data (Boshoff and Bracken, 2012). Gaps in the numerical data coverage still existed; however, the process demonstrated that numerical modelling of a geotechnical parameter can be very useful in this case.

Geotechnical characterization and 3D modelling

Modelling results

The model completed for the North West Satellite orebody is provided in Figure 3 as an example.

Of most significance to the mining operation is the spatial distribution of Zone 3, which is the most indurated zone. Zone 3 modelling showed relatively continuous, but gently undulating, indurated beds and/or lenses across the majority of the Mandena area. Zone 3 is absent or underdeveloped in some locations. The macro appearance of the indurated zones is large- to small-scale lensing rather than distinct indurated horizons, but these macro lenses can be made up of various indurated horizons of variable thickness.

Zone 3 conditions are expected to be concentrated around elevations ranging from +4 m msl (mean sea level) to -1 m msl.

Table III contains the numerical information extracted for each geotechnical zone modelled, providing parameter ranges and typical values of the SPT N_{field} and SPT N_{60} values measured within these areas. Numerical data available for the indurated conditions (Zone 3) is likely to be less representative due to early refusal of the CPTu, and the relatively small number of boreholes drilled also limiting conventional SPT measurement.

Laboratory testing results confirmed the expected UCS values associated with the most indurated Zone 3 materials. Based on the test results, the maximum strength/hardness of the indurated materials recovered and tested is assumed to be around 2 MPa. Although the properties of Zones 2 and 3 are highly variable, the median SPT N value exceeds 30 for Zone 2 for the majority of the orebody. The Zone 3 median SPT N value is estimated at 53, but possibly higher if adjustments are made for rock-like materials on which the CPTu and SPT refused (Table IV). Current measured SPT N values for Zone 3 ranged from as low as 3 to as high as 100.

It is therefore clear from the data evaluation shown in Table III that the numerical data and the zone model have been successful in delineating distinct geotechnical zones that can be applied to the mine planning and design process.

Application to mining operation

Based on existing design charts, the dredge should be able to achieve an average dredging rate of around 1900 t/h in Zone 2 material and no more than 1300 t/h in Zone 3 material. By applying typical expected weighted SPT N values to certain

mining blocks (e.g. by determining the weighted average volume that each geotechnical zone represents in a specific mining block), one can more accurately predict advance rates and set realistic production targets and/or plan which areas should rather be earmarked for mechanical preconditioning to obtain the desired throughputs. This information was also used to specify a larger dredge that would be able to deal with most of the geotechnical conditions predicted by the model.

Geotechnical parameters associated with the various zones modelled and the nature of the zones as reviewed in 3D have the following implications for the mining operations:

- The Zone 1 deposits will be easily excavated or dredged
- Zone 4 and 5 materials may result in process inefficiencies due to their more cohesive nature causing blockages and build-up on processing equipment, and hindering heavy mineral separation due to increased slimes contents
- All areas will be excavatable using mechanical excavators and bulldozers, although Zones 1 and 2 would be easier to excavate than Zone 3
- Dredging of Zone 1 and Zone 2 is considered possible, but dredging of Zone 3 could result in significant drops in productivity when the stronger indurations are encountered
- In terms of the stability of excavated slopes in the dry mining pits, it is expected that Zone 3 materials can stand vertically over long periods (days to weeks). Deterioration of the factor of safety for this vertical slope is unpredictable. Zone 2 materials may stand vertically for several metres over short periods (hours, sometimes days), but will collapse to lower angles over time. The aeolian sands are generally free-flowing and excavated slopes will collapse to an angle of 30° to 35°. Due to the variable nature of the deposit (introduced by the combination of the geotechnical zone thicknesses, the presence and scale of the Zone 3 indurations, and localized hydrogeological factors) no single specific slope stability solution or factor of safety (FoS) can be assigned. Slope stability management must be approached as a daily planning and production task requiring ongoing assessment by a competent person.

Feedback from the mining operation confirmed that the geotechnical model was utilized as a decision trigger to identify areas destined for dry and dredge mining in 2014. However, dry mining was suspended from November 2014 onwards.

The Zone 3 solid was imported into the Surpac mining software package, and then into the block model attribute to represent how much of a block is in Zone 3 (partial percentage). This helped to estimate the production rate of the dredge. Surpac Minesched software has a production factor (PRODFACT) attribute, which can be written on a block model. This represents how effective the mining system is compared with its capacity according to orebody conditions. The mining rate for each block is then represented by the PRODFACT, which is the mining rate divided by capacity on a given time unit (1 day). This is a function of bench height and cutting rate (which, in turn, is a function of hardness and therefore a function of Zone 3 percentage).

The new dredger utilized, as specified following the outcome of the phase 1 investigations, is able to cut Zone 3 material at the reach of the cutter. Preconditioning was

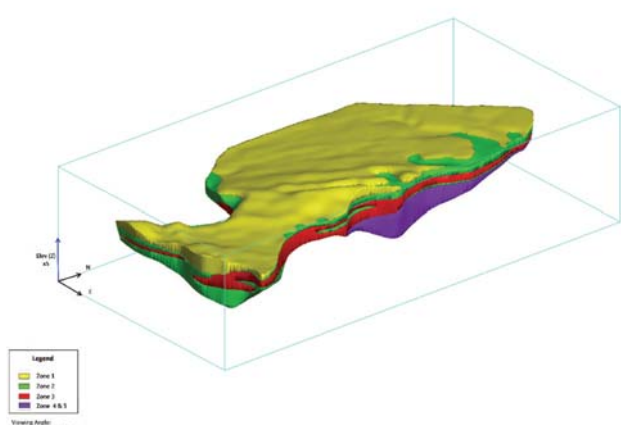
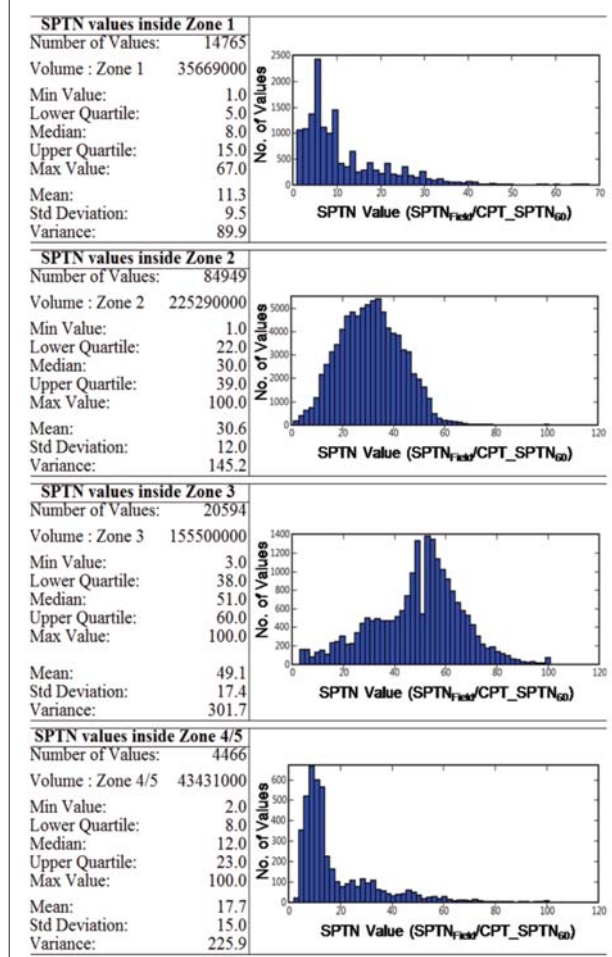


Figure 3 –3D spatial geotechnical model of the North West Satellite orebody ('The Fish'), Mandena deposit, Madagascar

Geotechnical characterization and 3D modelling

Table III

Numerical SPT N_{field} and SPT N60 data extracted within each geotechnical zone



planned based on the geotechnical model as part of safety mitigation to prevent unexpected falls of big blocks onto the dredge ladder. Preconditioning was eventually cancelled as the mine was able to cope with the hanging face by managing the risk through a modification of the dredging technique, which basically entails cutting horizontally (*i.e.* laterally) at the base of Zone 3, gradually moving the cutter upwards and thus minimize the size of blocks that could fall and damage the equipment.

The above methods of planning or anticipating production have therefore been of some benefit to the mine. However, the complexity of the dredging productivity model makes it difficult to confirm the specific contribution of the geotechnical model to efficient production planning, as other constraints in the process also influence how the dredge throughput is planned.

However, by anticipating mining conditions the mine is able to plan the best way for dredging to proceed (*i.e.* planning of cutting faces). An additional benefit to the operation is the ability to plan how to deal with the downstream influence of Zone 3 mining conditions, as this has an impact on the wear rate of the cutter tooth and hence on inspection frequency, spares management, and preventing overload of the hydraulic system.

The geotechnical characterization of the orebody has therefore provided several ways of optimizing the planning and control of the mining operation.

Conclusions

The Mandena case study demonstrates the importance of geotechnical investigations in the early phases of a project to ensure understanding of the geotechnical parameters of an orebody and the potential limitations that these could pose to the chosen mining process. Unfortunately, the importance of these investigations in the early phases of mining projects is commonly forgotten, or more focus is placed on civil or resource estimation applications rather than on the understanding of how unusual geotechnical conditions could affect the mining process. It must be added that the conditions encountered at Mandena were unusual compared to the typical well-known heavy mineral sand deposits mined on South Africa's northeast coastline (Zulti North, Hillendale, Zulti South, and Fairbreeze deposits).

The case study further demonstrates the importance of using an integrated approach that includes various geotechnical and geological techniques to successfully characterize unusual and variable geotechnical conditions.

By using an integrated approach and combining data from geological and geotechnical sources it was possible to generate a geotechnical zone model in 3D into which any of the *in-situ* measured and/or derived parameters obtained from CPTu testing can be imported, modelled, and/or data extracted and analysed statistically for application to the mining requirements. This integrated method of investigating, defining, and presenting large-scale, and unusual geotechnical problems allowed the Mandena operation to enhance its production planning capabilities.

References

- BOSHOFF, L.I. and BRACKEN, A.H. 2012. Project TiO4 - Mandena North West and North East Satellite Areas Geotechnical Investigation. *SRK Report no.r 437868/3.1. Draft Report*. Rio Tinto Management Services, Johannesburg, South Africa.
- BOSHOFF, L.I. and BRACKEN, A.H. 2011. QMM Mandena Phase 1 Geotechnical Investigation. *SRK Report no. 414630/2. Final Draft Report*. Rio Tinto Management Services, Johannesburg, South Africa.
- CAMPANELLA, R.G. and ROBERTSON, P.K. 1988. Current status of the piezocene test. *Proceedings of Penetration Testing 1988: the First International Symposium on Penetration Testing, ISOPT-1*, Orlando, Florida, 20-24 March 1988. Vol. 1. Balkema, Rotterdam. pp. 93-116.
- CLAYTON, C.R.I. 1995. The standard penetration test (SPT): methods and use. *Report 143*, Construction Industry Research and Information Association (CIRIA), London. 143 pp.
- COMMITTEE FOR STATE ROAD AUTHORITIES, SOUTH AFRICA. 1994. Technical recommendations for highways, TRH10 – the design of road embankments. Department of Transport, Pretoria. pp. 62–64.
- COWAN, E.J., BEATSON, R.K., ROSS, H.J., FRIGHT, W.R., McLENNAN, T.J., EVANS, T.R., CARR, J.C., LANE, R.G., BRIGHT, D.V., GILLMAN, A.J., OSHUST, P.A., and TILLEY, M. 2003. Practical implicit geological modelling. *Australasian Institute of Mining and Metallurgy Publication Series no. 8/2003*. BPA Digital, Australia.
- HEES, F. 2010. Orebody knowledge workshop report and presentation. *Biocrete Model Stream 2 Area-Mandena Project*. Rio Tinto Management Services, Johannesburg, South Africa.
- LYNN, B. 2008. Summary report on the results of laboratory testing carried out on indurated sand samples. *Ref. 30141*. Rio Tinto Management Services, Johannesburg, South Africa.
- ROBERTSON, P.K. 1992. Estimating *in-situ* soil permeability from CPT and CPTu. Gregg Drilling and Testing Inc., Signal Hill, California, USA. ♦



The influence of trash minerals and agglomerate particles on spiral separation performance

by J. Grobler* and J. Zietsman†

Synopsis

Understanding the influence of feed material mineral assemblage on spiral separation is paramount for the successful and consistent operation of a spiral plant. Plant stability is required to maintain high recovery of valuable heavy minerals (VHM). Standard material analysis methods used in the heavy mineral industry to evaluate spiral separation behaviour are unable to quantify performance differences in the case of large variations in feed assemblage. This study illustrates a systematic approach to evaluate spiral separation performance. This technique was applied on a four-stage spiral plant. The performance information was used in a circuit simulation to clearly illustrate the importance of correct setting of the spiral splitter position and resulting spiral mass loading to ensure optimal circuit stability and maximum VHM recovery.

Keywords

spiral separation, zircon, recovery, optimization.

Introduction

Heavy mineral sands deposits generally consist of naturally fine-grained, free-flowing sand due to the way in which the deposit was formed. The size of the heavy minerals market is roughly 8 Mt/a of zircon and titanium combined (Iluka, 2013). If an average combined feed grade of 5% zircon and titanium and an average combined overall product recovery of 80% are assumed, the resulting run-of-mine feed tons that would require primary spiral beneficiation is 200 Mt/a. The number of spirals required for the processing of this material, assuming 6500 operating hours per annum, an average of 2 t/h per start, and the same number of rougher spirals as other duty spirals, is over 30 000 spirals for the heavy mineral sands business alone. These numbers clearly illustrate the importance of the spiral in the heavy mineral industry.

The aim of a spiral plant in the primary processing value chain of a heavy mineral process is to reject non-valuable quartz (a light mineral) from various valuable heavy minerals (VHM). The product from the spiral plant is a heavy mineral concentrate that has a reasonable grade (more than 90% heavy minerals) at a reasonable heavy mineral recovery (greater than 90%). This benchmark is fairly easy to achieve if all the mineral particles are well liberated (as in the case of

free-flowing sand), the feed is properly deslimed (-45 µm fraction removed to less than 5% of the solids mass), and the spirals are fed within design solids concentration (water to solids ratio) and design spiral load (dry tons per hour per start).

Consistently achieving a high-grade heavy mineral concentrate at high valuable mineral recovery is paramount to business success. The forecast VHM recovery (especially of zircon) is an important input into monthly and annual budgets. A 10% decline in zircon recovery over a month equates to significant revenue losses for a medium-sized operation, without considering other valuable mineral losses. The quick investigation and understanding of the reasons for a decline in zircon recovery and an appropriate response with corrective actions can save the business millions of dollars. The purpose of this article is to illustrate the systematic approach that was followed to identify recovery losses of a typical four-stage spiral circuit and the corrective actions taken to minimize the impact.

Procedure

The spiral plant that was evaluated in this study has four separation stages, as indicated in Figure 1. The first three duties are all equipped with Mineral Technology MG6.3 spirals and the final cleaner stage utilizes Mineral Technology HG10S spirals. The primary performance indicator of the plant is zircon recovery, which is determined by the two-product formula (using XRF assay of ZrO_2 in the feed, concentrate, and combined tail stream). Three Vezin samplers take composite samples of these three streams on a

* Exxaro Metallurgical Services, Pretoria, South Africa.

† Ex-Mente, Pretoria, South Africa.

© The Southern African Institute of Mining and Metallurgy, 2017. ISSN 2225-6253. This paper was first presented at the Heavy Minerals Conference 'Expanding the Horizon', 16–17 August 2016, Sun City, South Africa.

The influence of trash minerals and agglomerate particles

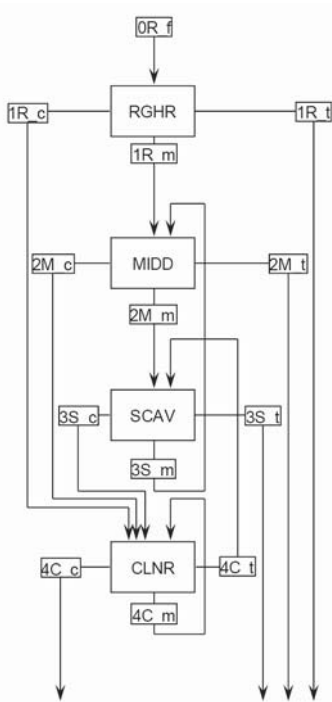


Figure 1—Flow sheet of four-stage spiral circuit. RGHR (1R) = rougher duty, MIDD (2M) = middling duty, SCAV (3S) = scavenger duty, CLNR (4C) = cleaner duty. Spiral concentrate = c, spiral middling = m, spiral tail = t

four-hourly basis. This study was initiated after a 10% decline in zircon recovery that persisted for a considerable period. This decline was correlated with changes in plant feed material. However, since there were large volumes of this feed material, the plant had to process it at the highest achievable zircon recovery.

The following procedure was applied to minimize the zircon losses while maintaining a reasonable zircon product grade for the downstream process.

- *Theoretical maximum recovery:* determine how much of the zircon in the feed is recoverable by spiral separation
- *Feed mineral assemblage impact:* determine the mineralogical composition of the feed material and assess what the impact is on the individual spiral separation
- *Spiral circuit performance assessment:* evaluate the performance of the spiral circuit by sampling the four duties. Apply mass balance techniques using the spiral duty mass splits and stream analyses
- *Corrective measures:* implement corrective measures based on the interpretation of the circuit performance results.

Each step is presented in the next four sections with a method description, followed by illustration and discussion of the results.

Step 1: determine theoretical maximum recovery

A spiral circuit feed sample was fractionated on a laboratory shaking table under controlled feed conditions. The sample was divided into four mass fractions based on the band colours. The first band constituted the 'clear black band', the

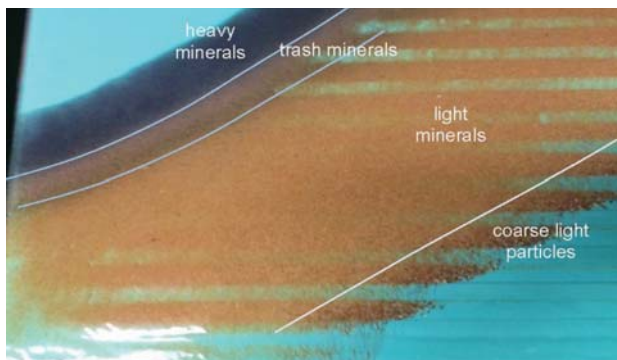


Figure 2—Shaking table fractionation with low trash content

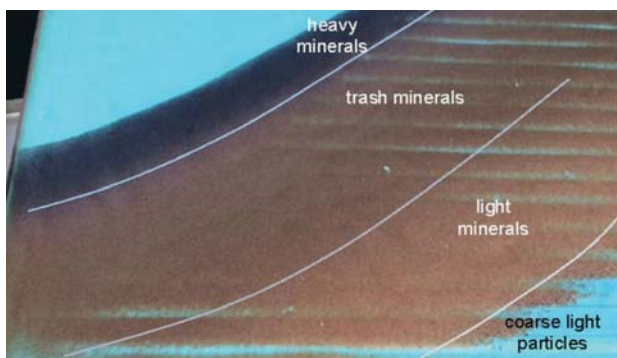


Figure 3—Shaking table fractionation with high trash content

second band constituted the 'other' coloured heavy minerals, the third band the fine quartz, and the last band the coarse tail particles. Figure 2 illustrates the coloured bands on the shaking table during fractionation for a condition of low trash, while Figure 3 illustrates the coloured bands for high trash content. Each mass fraction was assayed by X-ray fluorescence (XRF) and a recovery-yield curve was drawn (Figure 4). The shaking table result presents the best case, or theoretical maximum recovery that can be achieved for a specific feed material, since the shaking table provides sufficient separation space and separation time for each particle to reach its equilibrium position from a particle density, size, and shape perspective.

Figure 4 illustrates a 91% zircon recovery at 21% mass yield, which implies that 9% of the zircon is trapped in the remaining 79% of the mass. This zircon recovery is quite low, and further investigation indicated that fine agglomerates (less than 500 µm) were present in the feed. These agglomerates trapped zircon particles (and other VHM) in a low-density clay and quartz matrix, causing them to be misplaced to the tail fraction. The same feed sample was attrition-scrubbed in a laboratory unit and processed on the shaking table after desliming. The result from the scrubbed feed fractionation is presented in Figure 5. A clear step change (5–10%) in recovery is apparent for all three of the heavy elements (Zr, Fe, and Ti), which shows that the VHM particles were liberated by the scrubbing process. Detailed QEMSCAN analyses of some of these agglomerates are illustrated in Figure 6. The spiral circuit is unable to recover the zircon contained in these agglomerates due to their

The influence of trash minerals and agglomerate particles

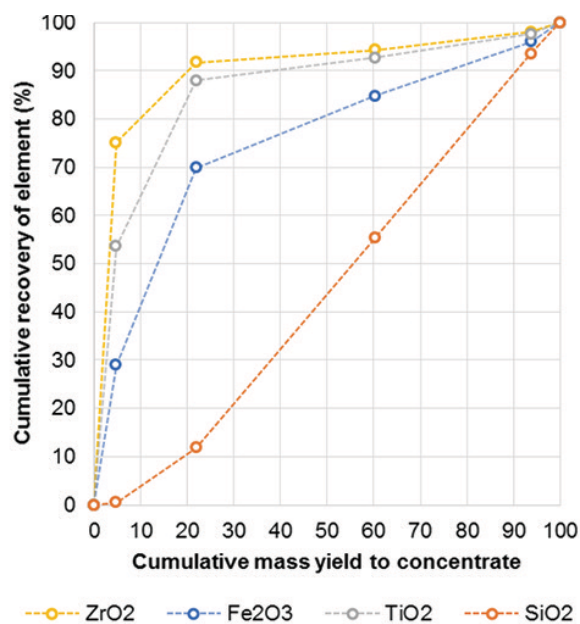


Figure 4—Recovery-yield relationship of the four main elements in spiral feed fractionated on a shaking table

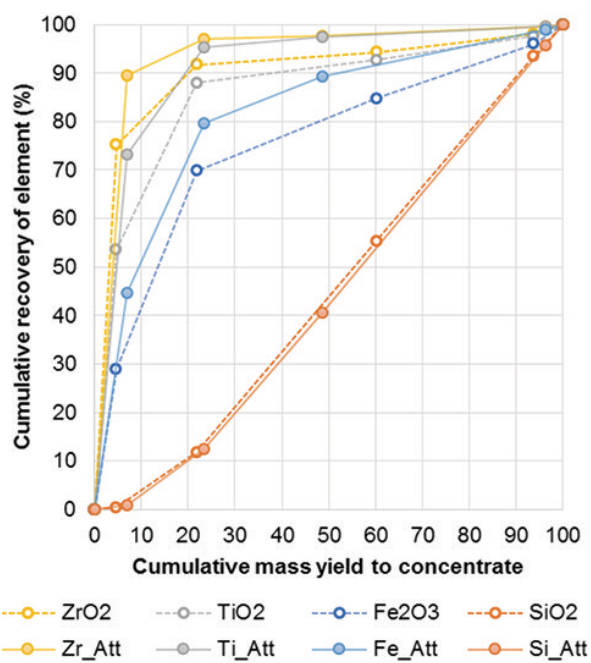


Figure 5—Recovery-yield relationship of the four main elements in spiral feed fractionated on a shaking table – before and after attrition scrubbing

combined low density, larger size, and irregular shape. This material needs to be liberated before it reaches the spiral circuit, and the spiral separation performance should be measured against a new ‘baseline’. That is, a theoretical maximum recovery as achieved by the shaking table; 91% in the case of Figure 4. The results indicated in Figure 5 can be achieved only with improved feed preparation in the plant (milling and/or scrubbing) to liberate VHM from agglomerates prior to spiral separation, with significant power input.

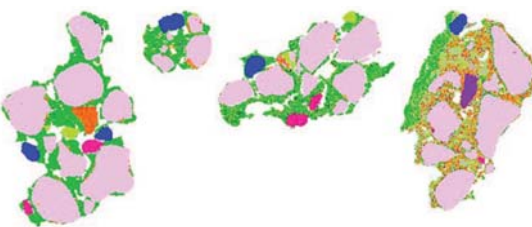


Figure 6 – Agglomerate cross-sections: blue particles are zircon, green is clay matrix, light pink particles are quartz. The round particle, second from the left, is 200 µm in diameter

Step 2: determine impact of feed mineral assemblage

The feed mineral assemblage, especially the concentration of near-density heavy mineral particles, can have a significant impact on spiral recovery. The heavy mineral industry gets its name from the particle class ‘heavy minerals’. Traditionally this class contains mineral particles that sink in an organic medium (usually tetrabromoethane or bromoform) with a liquid density of 2.96 g/cm³, and which constitute total heavy minerals (THM). The THM thus have a density greater than 2.96 g/cm³. These heavy mineral particles are further classified. Valuable heavy minerals (VHM, for example zircon, rutile, and ilmenite) usually have a density greater than 4 g/cm³. The term ‘trash’ is used to describe a particle class with a specific density range. In this article, that range is considered as being between 3 g/cm³ and 4 g/cm³, and therefore this material has an intermediate density between ‘light’ particles and ‘heavy’ particles. It is called trash because it contains no valuable or saleable minerals, but the minerals are considered as ‘heavy’ since their density is greater than 2.96 g/cm³. This paper makes reference to three distinct particle classes, heavy minerals (>4 g/cm³), trash minerals (3–4 g/cm³), and light minerals (<3 g/cm³). To illustrate the difference in separation response between these different mineral groupings, a shaking table fractionation was carried

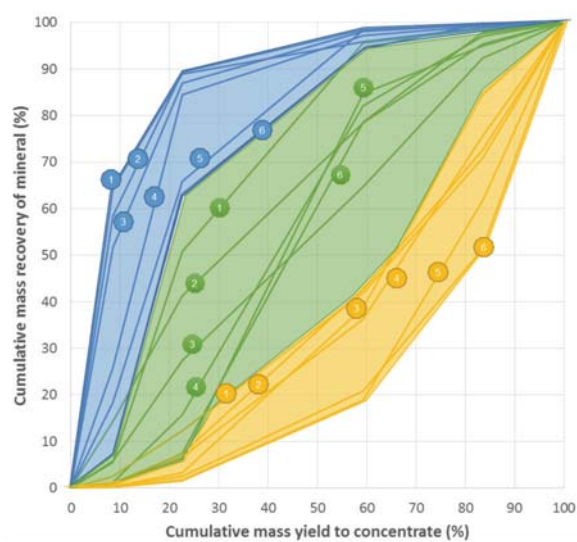


Figure 7—Shaking table density fractionation of cleaner spiral feed. Numbers correspond with ranking in Table I. Actual data points (not shown) were connected with straight lines – no curve smoothing was applied

The influence of trash minerals and agglomerate particles

Table I

Mineralogical composition and classification of the sample used for the density fractionation shown in Figure 7

No.	Heavy minerals	%	No.	'Trash' minerals	%	No.	Light minerals	%
1	Monazite	0.1	1	Almandine	8.7	1	Mica	2.3
2	Zircon	2.2	2	Fe oxides	3.0	2	Kyanite	0.9
3	Ilmenite	10.8	3	Grossular	1.3	3	Dolomite	0.2
4	Fe (HiTi) oxides	.5	4	Apatite	3.0	4	Plagioclase	2.4
5	Rutile	1.8	5	Pyroxene	23.0	5	Quartz	38.0
6	Spessartine (garnet)	0.4	6	Chlorite	0.9	6	K-feldspar	0.5
	Total (blue)	15.8		Total (green)	39.9		Total (yellow)	44.3

out on the cleaner spiral feed. The fractions were analysed by QEMSCAN to quantify the minerals present in the assemblage. Figure 7 illustrates the three density response bands, and Table I lists the mineral types and percentages in each band.

Since there is sufficient separation space on a shaking table the trash minerals can easily achieve their respective equilibrium positions. However, on a spiral the separation space is limited, and the residence time for separation is short (less than 15 seconds). Trash minerals will concentrate towards the middle of the spiral, between the heavy minerals and light minerals (Figure 8). This implies that there is probably a threshold of trash mineral content that can be accommodated on the spiral, beyond which separation will be adversely affected.

Literature reports on the influence of trash minerals on spiral separation are limited, since most mineral sands deposits contain low trash concentrations, seldom exceeding 5% of the mineral assemblage. In this investigation the trash mineral content was as high as 25%. To measure the impact of trash on spiral separation, shaking table separation response (ideal separation) was compared with spiral separation response (on the same spiral profile) for completely liberated particles with increasing trash content (three trash content scenarios, based on actual plant feed variation). QEMSCAN particle mineral analysis (PMA) enables the classification of particles into different quality classes. This analytical technique has been effectively applied in many other density fractionation studies (Grobler and Bosman, 2011). One of the PMA mineral classes is Zircon I, a clean, completely liberated particle with ZrO_2 content greater

than 66%. Zircon I was used as an indicator particle class to compare its recovery at different trash contents. The pyroxene particle class was selected as the most predominant trash mineral particle, and quartz was selected as the most predominant light mineral particle.

Figure 9 illustrates the three trash content scenarios. The enhanced Holland-Batt equation was used to fit the test work data points. This fitting technique for spiral data was described by Grobler, Naude, and Zietsman (2016). In all three feed scenarios the Zircon I recovery was above 95% for the shaking table. However, the Zircon I recovery for the spiral decreased significantly with increasing trash (from 95% to 83% to 78% at 20% mass yield to concentrate – Figure 9).

It is well known that particle size can also play a role in spiral separation (Grobler and Bosman, 2011). To illustrate that trash content had a more pronounced effect than particle size distribution, the particle size distributions of the three feed materials from Figure 9 were drawn up using the QEMSCAN size distribution data from the Zircon I and Pyroxene particle classes. Figure 10 illustrates that the particle size distributions were similar for the three trash content scenarios, while the spiral separation response (Figure 9) varied significantly due to the trash content itself.

The impact of unliberated zircon particles as well as trash content has been illustrated for the spiral in isolation; the next step is to determine the impact on the spiral circuit as a whole.

Step 3: spiral circuit performance assessment

The four-stage spiral circuit was sampled by selecting an individual spiral column in each spiral duty and taking a timed sample of the feed, concentrate, middling, and tail streams. Feed distribution checks were done beforehand to confirm that the selected spiral column was representative of the entire spiral duty. The feed to the rougher spiral bank was fractionated into four samples on the laboratory shaking table to determine the theoretical maximum recovery. The four spiral duty sample sets with the four shaking table fractions resulted in 20 samples, which were deslimed and assayed by XRF. No sink-float analyses were done. The XRF assays were used in a mass balance model using the Limn flow sheet processor (Excel add-in) to determine the mass-balanced zircon recovery considering the main elements in the mass balance solver. The circuit mass balance calculated the total mass yield contributions of the rougher duty tail,

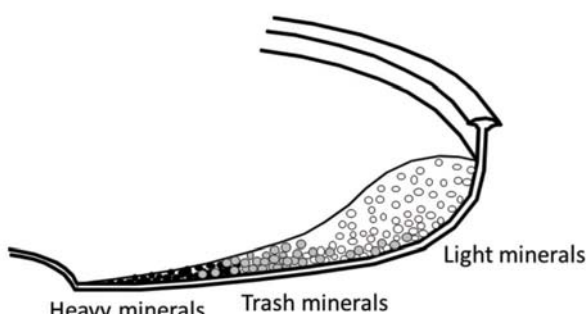


Figure 8—Positions of different mineral density classes on the spiral cross-section

The influence of trash minerals and agglomerate particles

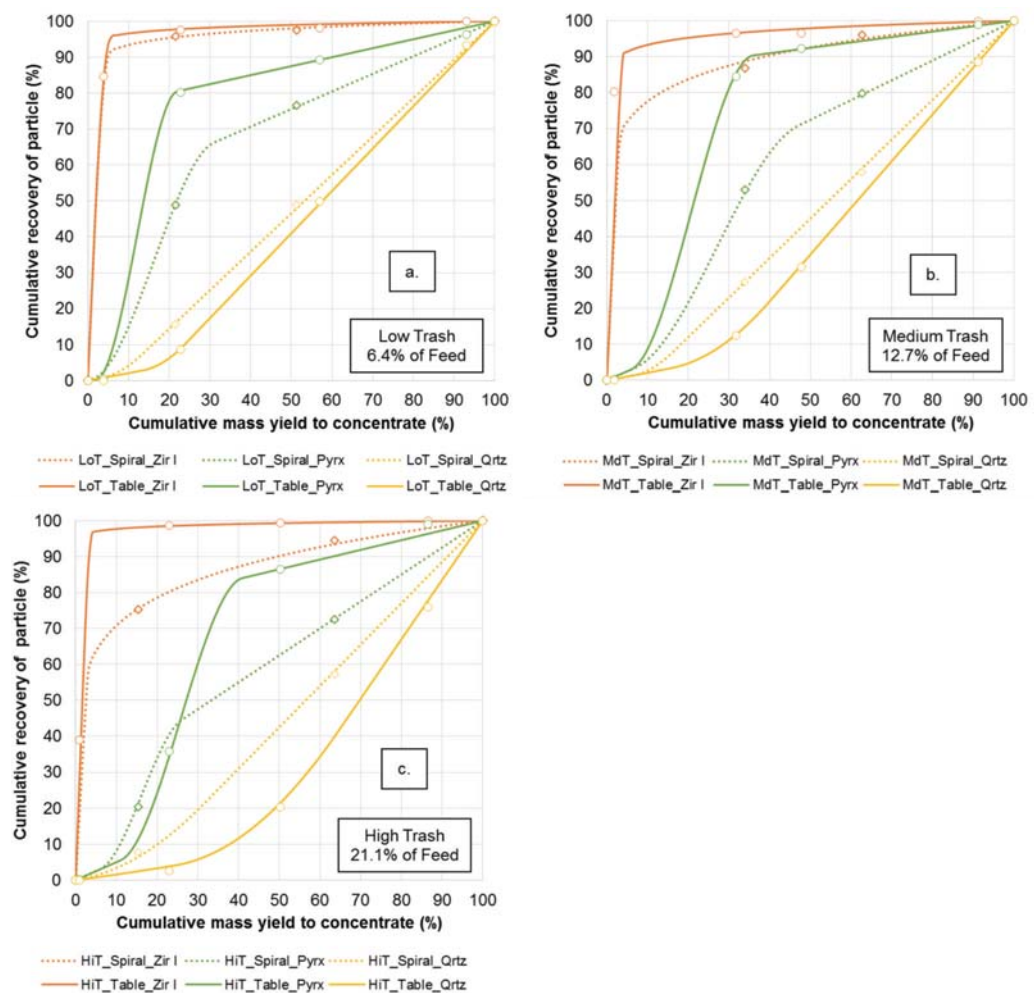


Figure 9—Yield-recovery relationships for three different trash content scenarios. (a) 6.4% trash, (b) 12.7% trash, (c) 21.1% trash)

middling duty tail, and scavenger duty tail in relation to the mass yield to concentrate. Refer to Figure 1 for the spiral circuit flow sheet.

The following three feed scenarios were used to illustrate the impact of trash and agglomerates on the spiral circuit performance.

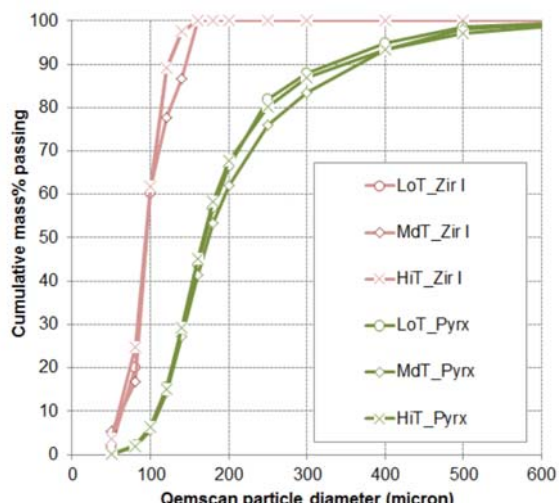


Figure 10—Particle size distribution data for Zircon I and Pyroxene in spiral feed for three trash content scenarios

Case 1: the circuit was sampled under normal feed conditions when the circuit zircon recovery was at acceptable levels (above 90%).

Case 2: the circuit was sampled after the feed had changed and the zircon recovery declined by more than 15%, creating an unacceptable performance condition.

Case 3: the circuit was sampled after corrective measures were employed on the new feed condition to minimize zircon losses.

The three feed conditions are depicted in Table II. The trash content in the feed increased in cases 2 and 3, while the ZrO_2 grade decreased. The most significant difference is shown in the zircon recovery for the three cases. Each of the three cases is discussed in the next three sections. Table III gives the normalized mass yield to the different tail and concentrate streams. The design load for middling and scavenger spirals is 2 t/h per start, and for the cleaner 1.85 t/h per start. Figure 11 gives the zircon recovery to concentrate response, and Figure 12 the zircon grade to concentrate response, over the entire mass yield spectrum.

Case 1: low-trash feed (normal feed conditions)

Figure 13 compares the ideal zircon recovery with spiral circuit zircon recovery. The ideal recovery was determined to be 94%, indicating that 6% of the zircon is not available for

The influence of trash minerals and agglomerate particles

Table II
Feed and circuit response for the three cases

Case no.	Feed grade %ZrO ₂	Feed grade %trash	Recovery %ZrO ₂	Conc. grade %ZrO ₂
1	0.61	11.1	90.1	3.49
2	0.44	17.2	72.2	3.80
3	0.46	19.0	83.2	5.12

Table III
Normalized mass balance and circuit loading summary for the three cases

Case no.	Rougher tail mass%	Midd. tail mass%	Scav. tail mass%	Clnr conc. mass%	Midd. load t/h/start	Scav. load t/h/start	Clnr load t/h/ start
1	64.6	12.6	7.0	15.8	1.7	1.3	1.9
2	54.7	16.3	20.7	8.3	3.0	3.4	3.4
3	64.0	19.2	9.3	7.6	2.5	1.6	2.6

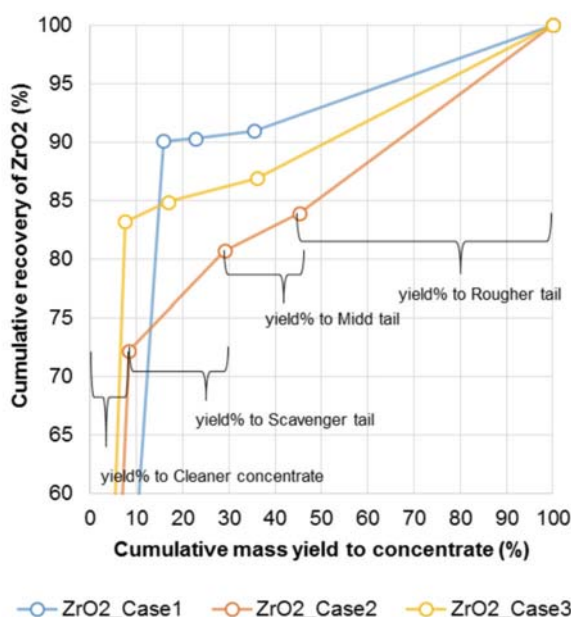


Figure 11—Recovery-yield relationship for the three spiral circuit separation cases. The respective yields to the different exiting process streams are indicated by the four horizontal lines (for Case 2 only)

spiral concentration due to lack of liberation (indicated by the red arrow in Figure 13). The circuit zircon recovery response was 90%, which implies that 96% of the available zircon was successfully recovered by the four-stage spiral circuit. The trash content was at the low end at 11.1% (Table II). The downstream spiral loading (midd, scavenger, and cleaner) was acceptably low. Case 1 demonstrates an acceptable circuit separation response with high zircon recovery (96% with consideration of irrecoverable zircon) to concentrate, and the bulk of the zircon losses occurring in the rougher tail stream.

Case 2: high-trash feed conditions (normal operating conditions)

Figure 14 compares the ideal zircon recovery with spiral circuit zircon recovery. The ideal zircon recovery was determined to be 87%, indicating that 13% of the zircon is not available for spiral concentration due to lack of liberation

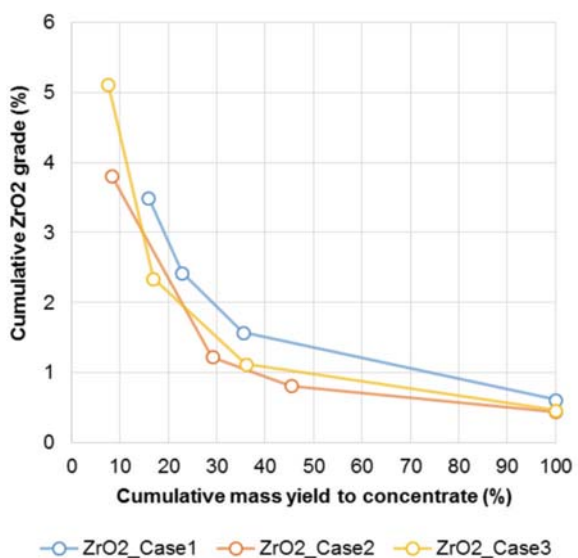


Figure 12—Grade-yield relationship for the three spiral circuit separation cases

(indicated by the red arrow in Figure 14). The circuit zircon recovery response was 72%, which implies that 83% of the available zircon was successfully recovered by the four-stage spiral circuit. The trash content was on the high end at 17.2% (Table II). The downstream spiral loading (midd, scavenger, and cleaner) was unacceptably high, with every spiral duty exceeding the design loading. Case 2 illustrates the impact that high feed trash content has on the spiral circuit. Firstly, it decreases the separation space and reduces the recovery potential on the spiral. Secondly, it increases the loading (tons per hour per start) on the downstream spiral duty, causing a further decrease in zircon recovery. These are the two main reasons for the drop in zircon recovery of 13%, from 96% in Case 1 to 83% in Case 2. Case 2 demonstrates an unacceptable circuit separation response with low zircon recovery to concentrate (only 83% with consideration of irrecoverable zircon), and zircon losses occurring in all three tail streams. A high zircon loss in the scavenger tail stream is a clear indication of overload in the spiral circuit.

The influence of trash minerals and agglomerate particles

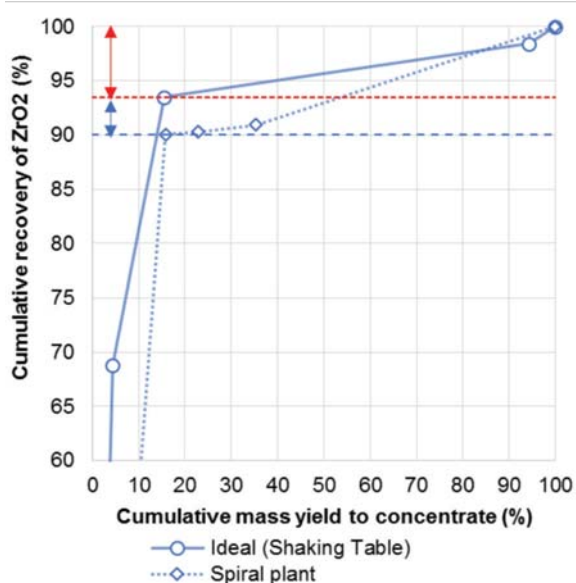


Figure 13—Case 1: ideal recovery versus spiral circuit recovery

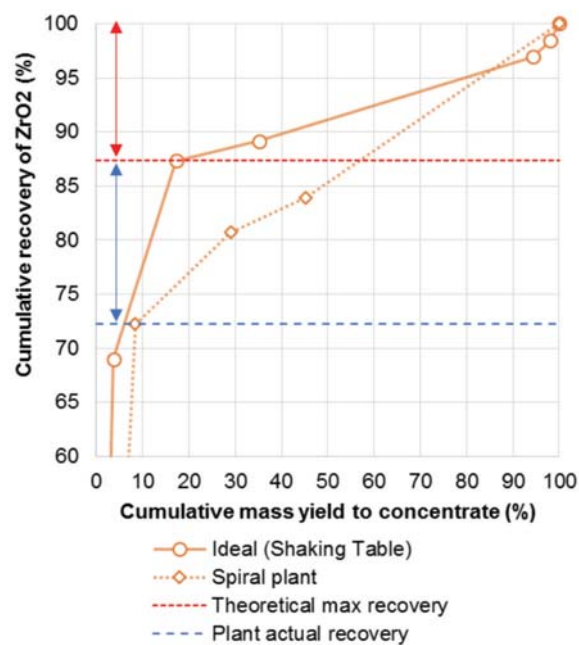


Figure 14—Case 2: ideal recovery versus spiral circuit recovery

Step 4: implement corrective measures

Since Case 2 resulted in an unacceptable zircon recovery, corrective measures were implemented in Case 3. The feed composition cannot be changed, therefore the only remaining control parameters are the operating conditions, total feed to the plant, and more specifically the spiral splitter positions.

Case 3: high-trash feed conditions (changed operating conditions)

Figure 15 compares the ideal zircon recovery with spiral circuit zircon recovery. The ideal zircon recovery was determined to be 90%, indicating that 10% of the zircon is not available for spiral concentration due to lack of liberation (indicated by the red arrow in Figure 15). No corrective

measures could be applied to the ideal zircon recovery, since this depends on the nature of the feed material entering the spiral circuit and can only be addressed by upgrades in the feed preparation circuits, which was not part of this investigation. The trash content was at the high end (19%) as indicated in Table II. The feed trash content can be diluted by blending with other low-trash mining zones, but this was not part of this investigation since this feed condition persisted for a considerable period due to large volumes of this type of material being mined. The negative impact of trash on individual spiral performance has to be tolerated (Figure 9). However, the increased loading on the downstream spiral duties can be managed by the operational personnel.

In Case 3 the tail splitters on the rougher and midd duties were opened ‘abnormally’ wide to reject mass to the rougher tail and midd tail streams. The rougher and midd duty outer splitter position was changed (set inward) by more than 60 mm due to the mass flow shift that occurred with the high percentage of trash in the feed. A splitter template was designed and implemented to set every spiral splitter in each duty at exactly the same position in the spiral trough. This counter-intuitive operational change rejected 85% of the feed mass to the rougher tail and midd tail streams (Case 3) instead of only 71% in Case 2, as shown in Table III. Table III further shows that the mass loading per spiral duty reduced to more acceptable levels for Case 3, with a significant decrease in recirculating loads.

After this intervention the overall circuit zircon recovery response was 83%, which implies that 93% of the recoverable zircon was successfully recovered to concentrate by the four-stage spiral circuit (indicated by the blue arrow in Figure 15). The change in spiral control approach resulted in a recovery increase of 10% (from Case 2 to Case 3, with consideration of irrecoverable zircon) while at the same time increasing the concentrate grade by more than 1% ZrO₂ as indicated in Figure 12.

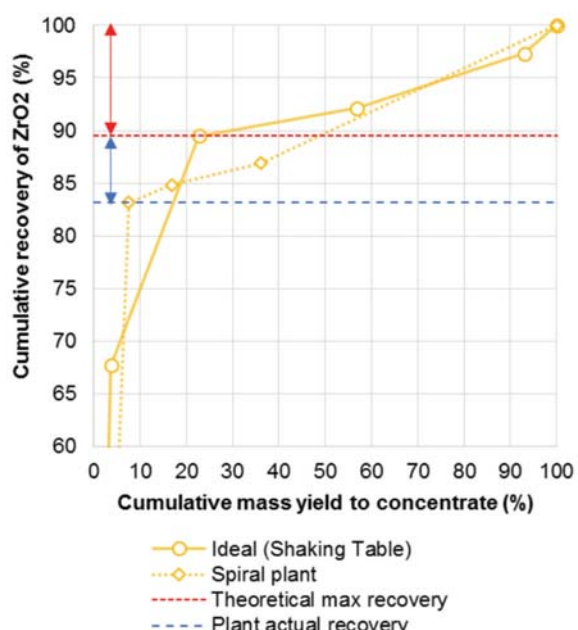


Figure 15—Case 3: ideal recovery versus spiral circuit recovery

The influence of trash minerals and agglomerate particles

Conclusions

Trash mineral content in the feed to spiral plants is increasing as more 'difficult' mineral deposits are being beneficiated. It is therefore important to understand the impact of increased trash mineral content and unliberated minerals on an individual spiral profile, as well as on the spiral circuit as a whole.

QEMSCAN analyses provided important insight for differentiating between trash minerals and valuable heavy minerals, which can easily be misinterpreted when considering heavy mineral content (typical sink-float results) in new deposits or new mining areas of existing deposits. The characterization of the separation response of ideal feed material using a laboratory shaking table assisted considerably in identifying the portion of the recovery problem that addressed by the spiral operator, and the portion that is not.

Using different techniques simultaneously to measure the same initial observation can speed up understanding of the problem. The application of attrition scrubbing to liberate agglomerates and QEMSCAN to define the content of the agglomerates is an excellent example of this, resulting in a clear explanation of the 'irrecoverable' zircon phenomenon.

An increase in feed trash content was shown to adversely impact zircon recovery by decreasing the separation space on the spiral trough. An increase of trash from 6% to 21% resulted in a decrease in liberated zircon particle recovery from 95% to 80%. Limited operational control can be applied

to reduce this impact, other than reducing the spiral loading to below design feed capacity.

An increase in feed trash content was shown to adversely impact the zircon recovery of the total circuit by increasing the load to the downstream circuits and increasing recirculating load, since a large portion of the mass moved to the middle of the spiral trough. This zircon recovery loss can be minimized by adjusting the spiral splitter to reject as much mass as possible (more than 85%) in the first two separation stages, resulting in a recovery improvement for recoverable zircon of more than 10%.

The mass balance of the spiral circuit enabled the measurement of the total circuit response. Although some effort is required to configure the calculations initially, it provides invaluable insight into the recirculating loads and interaction between different spiral separation duties. It is important to verify the mass balanced information with all available measurement data.

References

- GROBLER, J.D. and BOSMAN, J.B. 2011. Gravity separator performance evaluation using Qemscan® particle mineral analysis. *Journal of the Southern African Institute of Mining and Metallurgy*, vol. 111, pp. 401–408.
- GROBLER, J.D., NAUDE, N., and ZIETSMAN, J.H. 2016. Enhanced Holland-Batt spline for describing spiral concentrator performance. *Minerals Engineering*, vol. 92, pp. 189–195.
- ILUKA. 2013. Mineral Sands Industry. Fact Book. http://www.zircon-association.org/Websites/zircon/images/The_Mineral_Sands_Industry_Factbook.pdf [accessed 4 January 2015]. ◆

PIPELINE

CONSTRUCTION

BROWNFIELDS

SHUTDOWN

SERVICE

VALUE

INNOVATION

AMTEC
Applied Mineral Technologies
Engineering and Construction

Tel: +(27) 13 650 2270
Fax: +(27) 13 650 2260
Email: info@amtec.co.za
Web: www.amtec.co.za



Selection of an appropriate leaching method for light REEs from Esfordi flotation concentrate based on mineral characterization

by F. Soltani*, M. Abdollahy*†, S.M. Javad Koleini*, and D. Moradkhani†

Synopsis

The objective of the study was to determine the type and distribution of rare earth elements (REEs) in the phosphate flotation concentrate from the Esfordi flotation plant in central Iran, in order to understand their leaching behaviour. Samples of the concentrate were prepared and analysed using XRF, XRD, ICP, and EMPA. The Ce, Nd, La, and Y contents were 5608, 2227, 1959, and 679.7 mg/kg, respectively. The main REE-bearing minerals in the concentrate are fluorapatite, monazite, and xenotime. Apatite is the chief mineral of the concentrate and the ratio of apatite to monazite is greater than 60. From EMPA analysis, monazite contains a much higher proportion of REEs than apatite, but more than 50% of the REE content of the concentrate is in apatite, as this is the main mineral constituent of the concentrate. During the leaching of REEs in the phosphoric acid production process, more than 99% of the total rare earth values report to the large amounts of phosphogypsum ($\text{CaSO}_4 \cdot 2\text{H}_2\text{O}$) formed during the dissolution reaction. Accordingly, two process options are suggested for treating the Esfordi concentrate. In the first option, the concentrate is treated with 98% H_2SO_4 at 200–300°C. After digestion and water leaching, phosphorus and REEs are precipitated out of solution. In the second option, the concentrate is treated in a pre-leach stage. The process residue from the pre-leach stage is then subjected to acid digestion at elevated temperature for phosphoric acid production.

Keywords

Esfordi phosphate, mineral characterization, rare earth elements, leaching.

Introduction

The rare earth elements (REEs) comprise a set of 17 chemical elements in the periodic table, specifically the 15 lanthanides plus scandium and yttrium. REEs and alloys that contain them are used in devices such as computer memory, rechargeable batteries, cell phones, catalytic converters, magnets, fluorescent lighting, and many more (Krishnamurthy and Gupta, 2004). China supplies about 94% of the REE demand, with the remaining 6% coming from Russia and Estonia, the USA, India, Malaysia, and Brazil (Zhanheng, 2011). Increased industrial development in China has prompted the Chinese government to limit annual export quotas to approximately 35 kt of rare earth oxides (REOs), while non-Chinese annual demand is expected to reach 80 kt by the year 2015. This constriction of supply is being met by the development of many new rare earth mining projects, each of which has its own unique mining and processing

challenges (Jordens, Cheng, and Waters, 2013). One of these projects is the Esfordi phosphate project, which is located in Yazd Province in central Iran. The concentrate from the Esfordi flotation plant contains 1.2–1.5% REEs.

The REEs occur in over 160 discrete minerals. Most of these minerals are rare but the REE contents, expressed as oxide, can be as high as 60% REOs. Among these, bastnasite ($(\text{Ce},\text{La})\text{FCO}_3$) occurs most frequently, monazite ($(\text{Ce},\text{La},\text{Nd},\text{Th},\text{U},\dots)\text{PO}_4$) is second, and xenotime (YPO_4) is the distant third. Other rare earth minerals that have been or are now used as REE resources include apatite, brannerite, euxenite, gadolinite, loparite, and uraninite. Allanite, apatite, and other phosphorite sources, eudialyte, fergusonite, floreneite, parisite, perovskite, pyrochlore, zircon, and a few other naturally occurring rare-earth-bearing materials are also considered potential rare earth resources (Krishnamurthy and Gupta, 2004). Ion adsorption clays containing about 0.05–0.2 wt.% REOs are another group of REE deposits (Moldoveanu and Papangelakis, 2012). The general formula for apatite is $\text{Ca}_5(\text{PO}_4)_3\text{X}$, where X is a fluoride or chloride ion or a hydroxyl group. Apatite, containing an average of 0.1–0.8% REOs, is the main source of phosphate fertilizers and phosphoric acid (Krishnamurthy and Gupta, 2004). The mode of occurrence and distribution of the rare-earth minerals in phosphate concentrates has generally ensured that they could be recovered only as by-products or co-products. Chemical beneficiation or chemical processing of the concentrate obtained after physical beneficiation usually involves hydrometallurgical, and sometimes pyrometallurgical, operations (Krishnamurthy and Gupta, 2004).

* Department of Mining Engineering, Tarbiat Modares University, Tehran, Iran.

† Department of Mining Engineering, University of Zanjan, Zanjan, Iran.

‡ Corresponding Author.

© The Southern African Institute of Mining and Metallurgy, 2017. ISSN 2225-6253. Paper received Jun. 2016; revised paper received Oct. 2016.

Selection of an appropriate leaching method for light REEs

The Esfordi deposit is the most REE-rich and P-rich member of the iron deposits in the Bafgh (Yazd Province) district. In the Esfordi plant (Figure 1), flotation is used to recover apatite from the ore. Numerous minerals occur intimately intergrown in the rare-earth-bearing Esfordi phosphate ore. The objective of the present study is to determine the type and distribution of REEs in the products of the Esfordi flotation plant in order to predict their behaviour during leaching REEs. In this regard, the leaching behaviour of the Esfordi flotation concentrate in the wet process for phosphoric acid production was investigated and compared to leaching with HNO_3 and HCl .

Experimental

Esfordi flotation concentrate

The Esfordi plant is situated 35 km northeast of Bafgh, Yazd Province, in central Iran. Samples containing 1.2–1.5% REEs were obtained from the Esfordi flotation plant. Sub-samples, with a size distribution of 80 wt.% $< 54 \mu\text{m}$, were used for the characterization and leaching studies without any further size reduction. Optical mineralogy using polished and thin sections, semi-quantitative X-ray diffraction (SQXRD), X-ray fluorescence (XRF), inductively coupled plasma (ICP), scanning electron microscopy with wavelength dispersive spectroscopy (SEM-WDX), and electron microprobe analysis (EMPA) techniques were applied for ore characterization. The elemental analysis of the concentrate sample is shown in Table I. XRD analysis (Figure 2) showed that fluorapatite, magnetite, montmorillonite, calcite, talc, quartz, and haematite are present in the Esfordi concentrate. As shown in Figure 2, the iron ore minerals are magnetite and haematite.

More than 25 different elements have been reported to occur in fluorapatite. At Esfordi, chlorine, fluorine, iron, calcium, and the REEs are of particular importance if the concentrate is to be used for the production of phosphoric acid..

Quantitative analysis of the apatite and monazite minerals was carried out using a Superprobe Jeol JXA8100 microprobe at the Geology Department, University of Cape Town.

Leaching experiments

High-purity deionized water and analytical-grade acids were

used throughout all experiments. The leaching experiments simulating the conventional wet process were performed in a stirred 1-litre glass reactor immersed in a thermostatically controlled water bath. A total of 500 mL of the leaching solution was prepared using reagent-grade phosphoric/sulphuric acid and deionized water. 100 g of

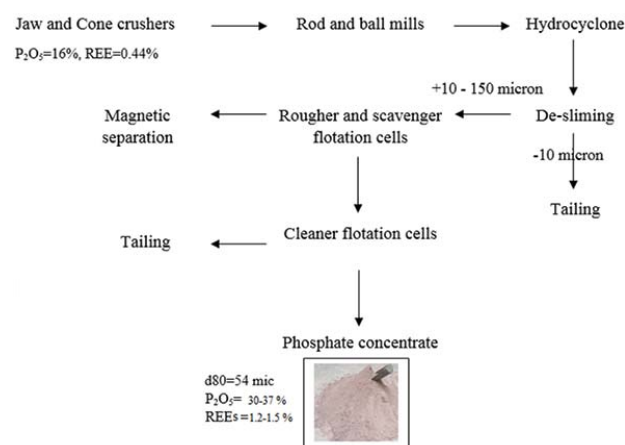


Figure 1—Main unit operations of the Esfordi flotation plant

Table I
Elemental analysis of the concentrate sample

Major elements		Minor elements		Rare earths	
Element	Mass %	Element	ppm (mg/kg)	Element	ppm (mg/kg)
Ca	37.13	Si	7500	Ce	5608
P	14.04	Mg	2055	Nd	2227
Fe	2.91	Na	1476	La	1959
F	3.00	Al	1127	Y	679.7
Cl	0.33	S	692	Pr	614.05
		Sr	333.8	Sm	342.85
		Ti	213	Dy	154.05
		K	220	Er	129.77
		V	123	Eu	29.4
		Mn	88	Lu	4.26
		Th	82.48	Tb	42.6
		U	4.6	Yb	31.7
				Gd	188.07

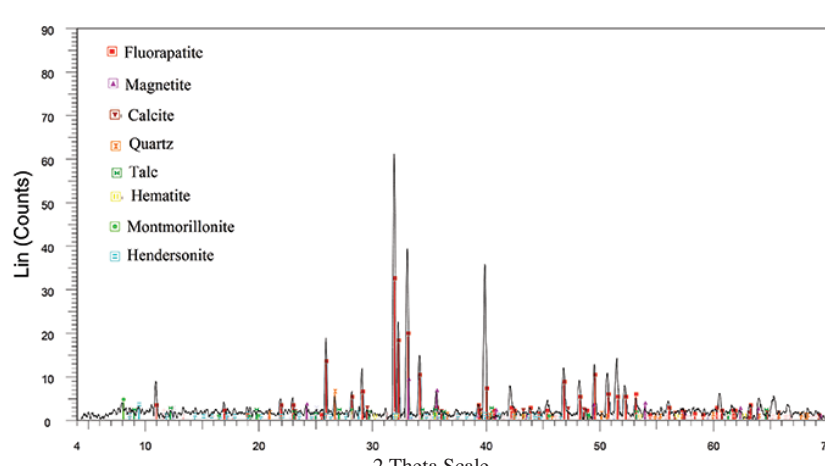


Figure 2—XRD analysis of the Esfordi flotation concentrate

Selection of an appropriate leaching method for light REEs

apatite concentrate was added to the leaching solution when the temperature reached the pre-set value (80°C). The pH, redox potential, and elemental concentrations in the leach solution were measured regularly. After completion of the leaching experiment (3 hours for leaching-precipitation), the pulp was filtered, and the solid residue was washed three times with 5% phosphoric acid, and dried to a constant weight. The HNO₃ and HCl leaching experiments were conducted at 30% (w/w) solids with 500 mL of each acid at the desired concentrations. The rotation speed of the agitator was maintained at 500 r/min for all experiments.

The pregnant leach solution and wash solutions were combined for assay. All the solid and liquid samples were analysed to provide data to calculate the mass balance and leaching efficiency. The redox potential was monitored using a Metrohm 827 Lab unit with an Ag/AgCl reference electrode. Ca, Fe, and REEs were determined by ICP (induced coupled plasma). P was analysed by spectrophotometry.

Results and discussion

Genesis of the Esfordi phosphate ore

The representative results of EMPA analysis for apatite and monazite are presented in Table II. Results for apatite and monazite grains in the flotation concentrate samples were close to those reported for original feed samples (Booomeri,

2011). As can be seen from Table II, the main phosphate mineral in the Esfordi ore is essentially fluorapatite. Apatite samples have F and Cl ranges of 3.12–5.27 wt.% and 0.35–1.34 wt.%, respectively, and contain low values of Fe and Si. Quartz is the main source of Si in the concentrate (Figure 2). It was not possible to analyse the composition of fine xenotime particles by EMPA.

The deposit is regarded as being intrusive in origin. All the Esfordi ore types show evidence of a complex cooling history, involving processes such as primary igneous crystallization (formation of clinopyroxene, andradite, apatite, and massive magnetite), followed by infiltration by late silica-, carbonate-, and iron-bearing fluids (formation of actinolite, chlorite, epidote, and calcite-quartz veins). Subsequent hydrothermal infill formed monazite and allanite inclusions in apatite grains. First-stage fluids depleted apatite in Na and Si and formed monazite-allanite minerals as inclusion within apatite grains (Booomeri, 2011; Bonyadi *et al.*, 2011).

Rare earth minerals in the Esfordi phosphate ore

As can be seen from Figure 3, light REEs (lanthanum, cerium, and neodymium) and the heavy REE Y are the most prominent in the concentrate. The total REE content in the concentrate is 1.20%. The concentrate contains 5608 mg/kg Ce, 1959 mg/kg La, 2227 mg/kg Nd, and 679.7 mg/kg Y. As can be seen from Figure 3, the light and heavy REEs total 1.10 and 0.1 wt.%, respectively.

Table II

Selected major and minor element concentrations (wt.%) in apatite and monazite minerals (WDS-EMPA data)

Mineral		SiO ₂	P ₂ O ₅	CaO	La ₂ O ₃	Y ₂ O ₃	Cl	Ce ₂ O ₃	F	Nd ₂ O ₃	FeO
Apatite	1	0.07	41.69	55.21	0.18	0.19	0.58	0.47	3.48	0.19	0.07
	2	0.22	42.10	55.53	0.04	0.14	0.35	0.23	5.27	0.16	0.04
	3	0.16	43.08	55.54	0.23	0.11	0.66	0.64	3.67	0.24	0.07
	4	0.23	42.35	53.89	0.24	0.54	1.32	0.77	3.12	0.33	0.10
	5	0.16	42.99	54.85	0.20	0.17	0.73	0.64	2.66	0.24	0.10
	6	0.21	43.63	54.38	0.22	0.14	1.05	0.48	3.40	0.26	0.07
	7	0.26	41.92	53.63	0.31	0.10	1.34	0.90	4.22	0.37	0.10
	8	0.04	44.04	55.45	0.10	0.03	0.50	0.29	4.77	0.11	0.06
	9	0.07	44.26	55.09	0.14	0.06	0.58	0.33	4.08	0.14	0.08
	10	0.16	43.06	54.40	0.25	0.13	0.84	0.64	3.18	0.27	0.07
		SiO ₂	P ₂ O ₅	CaO	La ₂ O ₃	Y ₂ O ₃	Cl	Ce ₂ O ₃	F	Nd ₂ O ₃	FeO
Monazite	1	0.06	33.49	0.84	13.45	0.93	0.19	35.01	0.77	10.37	-
	2	0.09	33.95	0.91	13.48	1.03	0.17	33.83	0.52	10.47	-
	3	0.17	32.91	0.77	11.80	0.16	0.23	33.83	0.61	12.80	-
	4	0.17	32.91	0.77	11.80	0.16	0.23	33.83	0.61	12.80	-
	5	0.41	30.66	0.33	11.76	0.53	0.20	34.55	0.79	12.75	-
	6	0.03	28.05	0.61	11.89	0.26	0.18	34.00	0.90	12.77	-

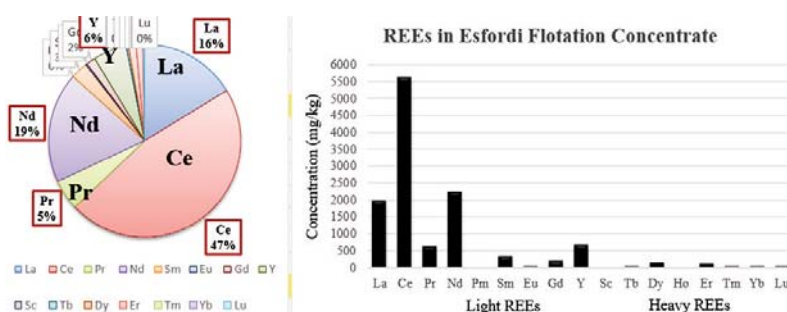


Figure 3—REE content in the Esfordi flotation concentrate

Selection of an appropriate leaching method for light REEs

As leaching of REEs from the concentrate is strongly governed by the types and concentrations of the different mineral phases within the concentrate, a comparative evaluation of REE distribution in apatite and monazite minerals using EMPA was carried out. As shown in Figure 4, the REE minerals are closely associated with apatite and formed mainly in or around apatite grains and within veins and veinlets. The REE-bearing minerals are mainly phosphates. Monazite is highly enriched in light REEs such as Ce, La, and Nd. Xenotime is the main source of Y in the concentrate (Figure 4).

The fluid interaction introduced the silicate components responsible for the formation of allanite, talc, tremolite, chlorite, quartz, and carbonates along apatite grain boundaries (Boomeri, Nakashima, and Lentz, 2009). Allanite ($(Ce, Ca, Y)_2(Al, Fe^{3+})_3Si_5O_{12}(OH)$) occurs in the Esfandi ore, but it was not observed in the flotation concentrate.

Boomeri (2011) found five groups of REE minerals in the Esfandi ore samples. These are apatite, monazite-xenotime, allanite, parsite-synchysite, and britholite. Apatite, monazite, and xenotime are the main REE minerals in the Esfandi flotation plant concentrate (Figure 4).

Values for Ce_2O_3 , La_2O_3 , and Nd_2O_3 cover a range of 0.23–0.90, 0.04–0.31, and 0.110.37 wt.%, respectively, in the apatite grains, and 33.83–35.01, 11.76–13.48, and 10.37–12.80 wt.%, respectively, in the monazite grains (Table II). Monazite contains high Ce, La, and Nd values, but low Y (0.16–1.03 wt.%). In all samples, the brighter internal areas

of the apatite have significantly higher contents of REE than the dark areas (Figure 4).

Nucleation of monazite in apatite in an open system is shown in Figure 5. Monazite is one of the stable minerals in oxidative pre-treatment and leaching processes (Jorjani, Bagherieh, and Chelgani, 2011).

Mineral particle counts (Figure 6) were performed on BSE images with a manual microscope-based particle counting system. Results showed that the Esfandi phosphate concentrate contains more than 57% fluorapatite and about 1.5% monazite and xenotime. As shown in Table II, monazite has a higher REE content than apatite. However, the majority of the REEs are contained in apatite, since the ratio of apatite to monazite is greater than 60.

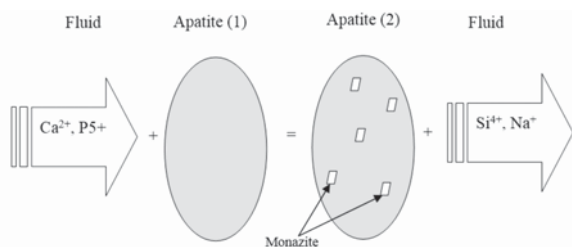


Figure 5—Model for development of monazite inclusions in apatite (based on the reaction proposed by Boomeri, Nakashima, and Lentz, 2009)

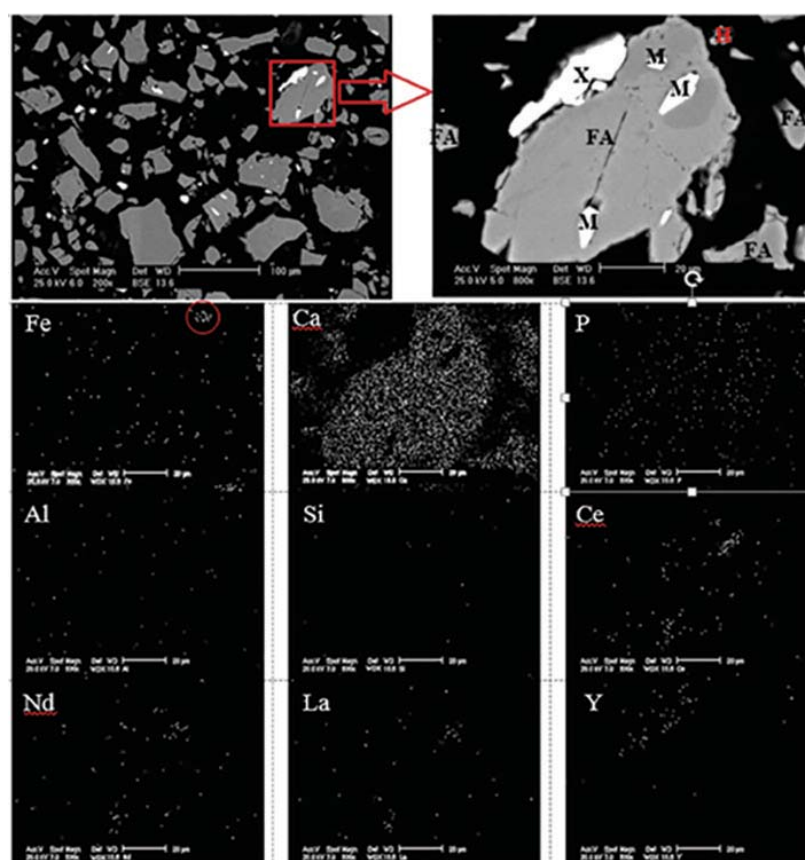


Figure 4—Backscattered electron image showing coarse apatite grains (grey) in the Esfandi flotation concentrate. White monazite (M) and xenotime (X) inclusions (1–10 µm) are detected in the apatite grains

Selection of an appropriate leaching method for light REEs

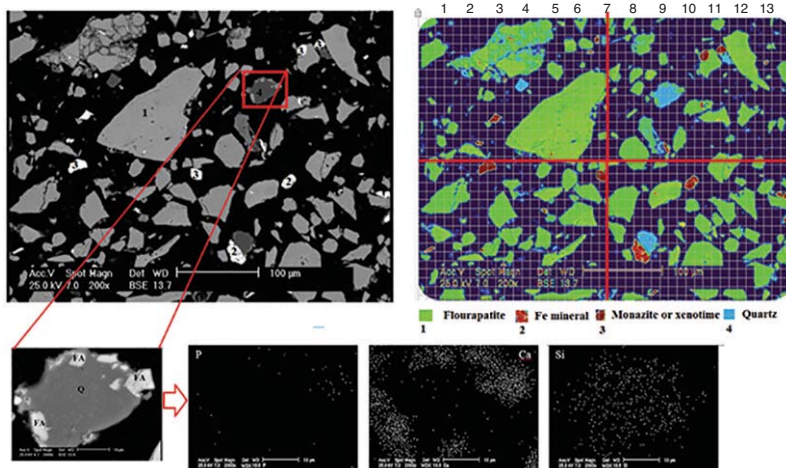
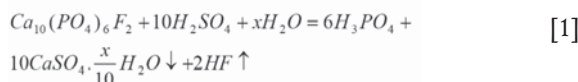


Figure 6—BSE high-contrast image of monazite-xenotime inclusion (4) in apatite (1), quartz, and Fe-minerals (200x and 2000x magnification)

Leaching of concentrate samples

Chemical behaviour of REEs in the wet process for phosphoric acid production

In the wet process for phosphoric acid production, phosphate rock is leached with a mixture of H_2SO_4 and H_3PO_4 . The main reaction in the phosphoric acid production is as follows:



where $x=0$ for calcium sulphate anhydrate, $x=0.5$ for hemihydrate, and $x=2$ for dehydrate (Wang *et al.*, 2010).

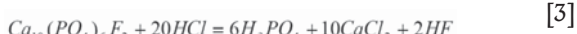
In the wet process leaching tests, concentrate samples were digested at 80°C by a mixture of concentrated sulphuric and phosphoric acids. A summary of the conditions of the leaching experiments at different acid concentrations and a solid-to-liquid ratio of 1: 5 is shown in Table III.

As shown in Table III, the leaching efficiency of REEs from the concentrate is only around 1%. More than 99% of the total RE values end up in the large quantities of phosphogypsum ($CaSO_4 \cdot 2H_2O$) formed during the dissolution reaction (Table. III). This may be due either to monazite-xenotime not being attacked during leaching, or to encapsulation of REEs by the growth of phosphogypsum crystals during the crystallization process (Figure 7). It has been found that the lanthanides are present in isomorphous substitution with Ca^{2+} in the gypsum (Wang *et al.*, 2010; Habashi, 1985).

XRD analysis of the white residue obtained from leaching of the apatite sample with 2 mol/L H_2SO_4 and 25% P_2O_5 solution showed (Figure 8) that the residue consisted mainly of calcium sulphate dihydrate ($CaSO_4 \cdot 2H_2O$) and calcium sulphate hemihydrate ($CaSO_4 \cdot 0.5H_2O$). The mass ratio of residue to leaching feed was 1.28. This indicates that the REE content in the solid residue is not enriched, but diluted. The amount of phosphogypsum produced in the wet process exceeds the mass of the target product, *i.e.* 4.5–5.5 t of phosphogypsum are generated per ton of phosphorus pentoxide (Binnemanns *et al.*, 2015).

Leaching studies in HNO_3 and HCl

The reaction of phosphate rock with HNO_3 or HCl can be represented by Equations [2] and [3] (Habashi, 1985):



When apatite is leached with HNO_3 or HCl , calcium does not precipitate due to high solubility of calcium nitrate and calcium chloride (Sandström and Fredriksson, 2012).

As shown in Table IV, leaching efficiencies of calcium and phosphate using HCl or HNO_3 are close to 100%. Unlike calcium and phosphate, REEs show a low leaching efficiency in either acid (Table. IV). This could be attributed to the complexation of REEs with fluoride (Krishnamurthy and Gupta, 2004; Khawassek *et al.*, 2015). Monazite-xenotime is not attacked by HNO_3 or HCl at low temperatures (Jordens, Cheng, and Waters, 2013). The behaviour of all four REEs in HCl is similar to that in HNO_3 .

Table III

Effect of H_2SO_4 and P_2O_5 concentrations on REE leaching efficiency (1 h leaching and 2 h precipitation)

Test no.	H_2SO_4 (mol/l)	P_2O_5 (%)	% leached (mean \pm 0.1%)			
			Ce	La	Nd	Y
1	0.2	25	0.56	0.49	0.61	1.12
2	0.5	25	0.81	0.83	0.60	1.30
3	0.8	25	0.85	0.85	0.78	1.29
4	1.1	25	0.90	0.89	1.01	1.30
5	1.4	25	0.88	0.89	0.95	1.25
6	0.2	30	0.68	0.56	0.70	1.30
7	0.5	30	0.90	0.85	0.71	1.30
8	0.8	30	0.90	0.89	0.75	1.30
9	1.1	30	0.92	0.95	0.75	1.35
10	1.4	30	0.88	0.95	0.78	1.35

Selection of an appropriate leaching method for light REEs

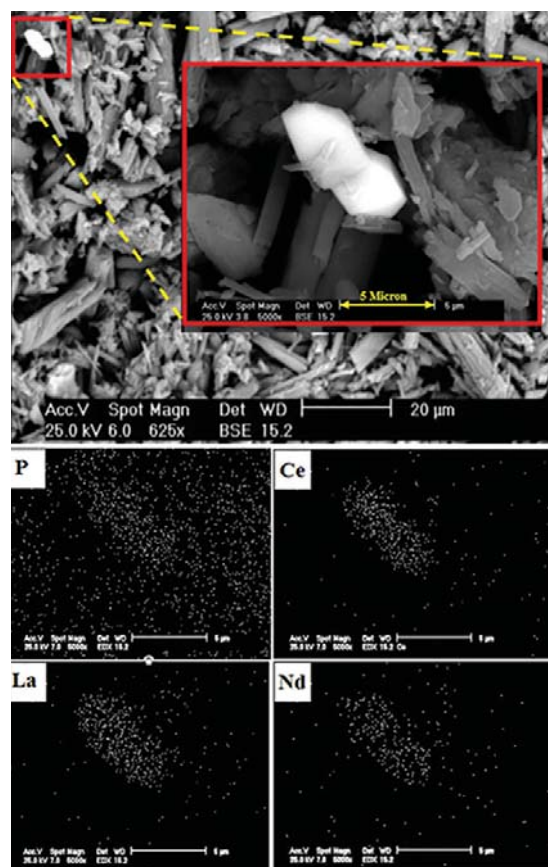


Figure 7—Backscattered electron image showing monazite grains (white) in the phosphogypsum residue (grey)

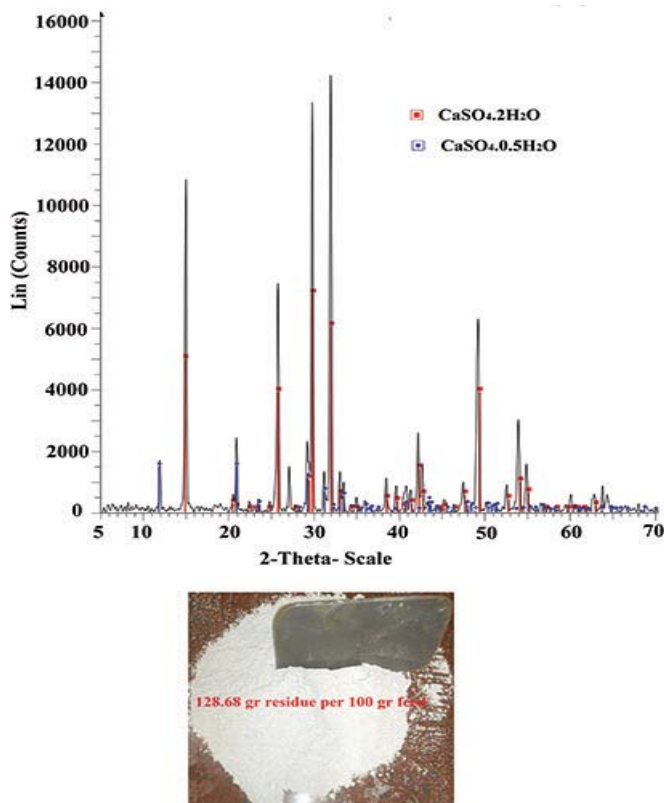


Figure 8—XRD analysis of the leach residue

Selection of an appropriate leaching method for light REEs

Table IV

Leaching efficiencies of calcium, phosphate, and REEs from concentrate samples in HNO₃ and HCl

Acid	Concn (%)	S/L (wt.%)	Leaching time (h)	T (°C)	Agitation (r/min)	Leaching efficiency (%)					
						Ca	P	Ce	La	Nd	Y
HNO ₃	30	25	2	60	500	100	97.83	1.56	1.31	1.22	0.72
HCl	20	25	2	60	500	100	98.11	1.48	1	1.32	0.56

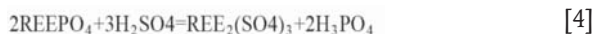
Leaching studies in HNO₃ and HCl solutions showed that these acids can be used for selective leaching of calcium and phosphate from the concentrate.

Selection of the appropriate leaching method

Chemical processing of monazite and xenotime

Monazite should be digested at high temperatures as it is one of the most stable REE minerals. Monazite is decomposed using two main methods:

- **Acid treatment**—Baking with 98% sulphuric acid at temperatures ranging from 200–220°C (Equation [4]) is typically used (Krishnamurthy and Gupta, 2004; Abhilash, Meshram, and Pandey, 2016). With this method, depending on the acid/ore ratio, temperature, and concentration, either thorium or the REEs can be selectively solubilized or both thorium and REEs totally solubilized
- **Alkali treatment**—The reaction of rare earth phosphates with hot (about 140°C), concentrated alkali (50–75%) proceeds according to Equation [5] in 3–4 hours.



The hydroxide produced is treated using hot water (trisodium phosphate is soluble, whereas the REE hydroxides are not). The hydroxide precipitates are filtered off and subsequently leached with HNO₃ or HCl. The monazite alkali digestion method is useful for concentrates with REE grades of more than 30% (Krishnamurthy and Gupta, 2004).

Chemical processing of apatite

As discussed, apatite is the main REE-bearing mineral of the Esfordi flotation concentrate as it is much more abundant than the other REE-bearing minerals. Thus, it is necessary to find an appropriate leaching route to extract REEs from the apatite.

Normally, apatite is the feed material to a wet-process phosphoric acid plant, where it is dissolved in a mixture of sulphuric acid and recycled dilute phosphoric acid. As mentioned, most of the rare earth values end up in the significant amounts of phosphogypsum formed in the dissolution reaction (Figures 7 and 8). Although various techniques to recover rare earths from the phosphogypsum have been developed, these are considered too complex and uneconomical to be industrialized (Wang *et al.*, 2010).

Proposed routes for processing the Esfordi concentrate

Given the foregoing discussion, it seems that potential process options for treating the Esfordi phosphate

concentrate to produce phosphoric acid and recover REEs are as follows.

- Acid bake of the concentrate. In the acid bake stage, the concentrate is treated with 98% H₂SO₄ at 200–300°C. After cooling, the decomposition products are leached with water (Jha *et al.*, 2016). It is assumed that the REE sulphates formed will dissolve with the phosphoric acid and not become associated with the CaSO₄ residue. During acid dissolution, the phosphate ions are converted to a low-grade phosphoric acid which is not suitable for further upgrading by conventional methods (evaporation or solvent extraction). The phosphorus is then precipitated, for example by the addition of iron to the solution. Iron (III) phosphate can be used in steel and other metal manufacturing processes as it prevents oxidation of the metal. Iron phosphate coatings are also primarily used as base coatings for paint (Wikipedia, 2016). Finally, the REEs are converted to hydroxide with caustic soda (Li *et al.*, 2009)
- Acid leaching of the concentrate with HNO₃, HCl, or H₃PO₄ to dissolve apatite prior to the acid digestion stage (Bandara and Senanayake, 2015). Hydrochloric acid could in principle be used, but is not in practice due to its high corrosivity. Dissolution in nitric acid is relatively common, with about 100 plants throughout the world producing complex fertilizers (Sandström and Fredriksson, 2012). Phosphoric acid is produced from the dissolved apatite, which still contains dissolved Ca. The dissolved Ca could be precipitated as gypsum (CaSO₄·2H₂O) by the addition of a stoichiometric amount of sulphuric acid (Stone *et al.*, 2016). Process residue from the pre-leach stage is subjected to acid baking at elevated temperature.

Conclusion

The type and distribution of REE minerals in the phosphate concentrate of the Esfordi flotation plant play an important role in the selection of REE processing methods. Apatite is the main REE-bearing mineral in the concentrate, and the ratio of apatite to monazite is greater than 60. However, apatite contains only 2% REE oxides, whereas the monazite phase contains around 45%. Therefore meaningful recovery of REEs from this material needs to take both minerals into account.

Two options for treating the Esfordi concentrate are hence proposed:

- Acid digestion of the concentrate followed by water leaching and sequential precipitation of phosphorus and REEs
- Acid leaching of the concentrate with HNO₃ or HCl to

Selection of an appropriate leaching method for light REEs

dissolve apatite prior to the acid digestion stage. In this method, the leach residue from the first stage is digested in the second stage.

Acknowledgments

The authors wish to acknowledge the contribution by Professor J. Petersen and Dr M. Becker, Department of Chemical Engineering at the University of Cape Town, to the mineralogical work and for critical input to this paper.

References

- ABHILASH, S.S., MESHRAM, P., and PANDEY, B.D. 2016. Metallurgical processes for the recovery and recycling of lanthanum from various resources—a review. *Hydrometallurgy*, vol. 160. pp. 47–59.
- BANDARA, A.M.T.S. and SENANAYAKE, G. 2015. Leachability of rare-earth, calcium and minor metal ions from natural fluorapatite in perchloric, hydrochloric, nitric and phosphoric acid solutions: effect of proton activity and anion participation. *Hydrometallurgy*, vol. 153. pp. 179–189.
- BINNEMANS, K., JONES, P.T., BLANPAIN, B., VAN GERVEN, T., and PONTIKES, Y. 2015. Towards zero-waste valorisation of rare-earth-containing industrial process residues: a critical review. *Journal of Cleaner Production*, vol. 99. pp. 17–38.
- BONYADI, Z., DAVIDSON, G.J., MEHRABI, B., MEFFRE, S., and GHAZBAN, F. 2011. Significance of apatite REE depletion and monazite inclusions in the brecciated Se-Chahun iron oxide-apatite deposit, Bafq district, Iran: insights from paragenesis and geochemistry. *Chemical Geology*, vol. 281, no. 3. pp. 253–269.
- BOOMERI, M. 2011. Rare earth minerals in Esfandi magnetite-apatite ore deposit, Bafgh district. *Iranian Journal of Geosciences*, vol. 85, no. 22. pp. 71–82.
- BOOMERI, M., NAKASHIMA, K., and LENTZ, D.R. 2009. RE minerals in Esfandi apatite-magnetite deposit, Central Iran. *Proceedings of the 24th International Applied Geochemistry Symposium*, Fredericton, New Brunswick, Canada, 1–4 June 2009.
- HABASHI, F. 1985. The recovery of the lanthanides from phosphate rock. *Journal of Chemical Technology and Biotechnology*. *Chemical Technology*, vol. 35, no. 1. pp. 5–14.
- JHA, M.K., KUMARI, A., PANDA, R., KUMAR, J.R., YOO, K., and LEE, J.Y. 2016. Review on hydrometallurgical recovery of rare earth metals. *Hydrometallurgy*, vol. 165, no. 1. pp. 2–26.
- JORDENS, A., CHENG, Y.P., and WATERS, K.E. 2013. A review of the beneficiation of rare earth element bearing minerals. *Minerals Engineering*, vol. 41. pp. 97–114.
- JORJANI, E., BAGHERIEH, A.H., and CHELGANI, S.C. 2011. Rare earth elements leaching from Chadormalu apatite concentrate: Laboratory studies and regression predictions. *Korean Journal of Chemical Engineering*, vol. 28, no. 2. pp. 557–562.
- KHAWASSEK, Y., ELIWA, A., GAWAD, E., and ABDO, S. 2015. Recovery of rare earth elements from El-Sela effluent solutions. *Journal of Radiation Research and Applied Sciences*, vol. 8, no. 4. pp. 583–589.
- KRISHNAMURTHY, N. and GUPTA, C.K. 2004. Extractive Metallurgy of Rare Earths. CRC Press.
- LI, H., NA, Z., ZHANG, G., LIU, Y., LONG, Z., and HUANG, X. 2009. A process of smelting monazite rare earth ore rich in iron. Australian patent AU2008286599B2.
- MOLDOVEANU, G.A. and PAPANGELAKIS, V.G. 2012. Recovery of rare earth elements adsorbed on clay minerals: I. Desorption mechanism. *Hydrometallurgy*, vol. 117–118. pp. 71–78.
- SANDSTRÖM, A. and FREDRIKSSON, A. 2012. Apatite for extraction - leaching of Kirunavaara apatite for simultaneous production of fertilizers and REE. *Proceedings of the 26th International Mineral Processing Congress (IMPC 2012)*, New Delhi, India, 24–28 September 2012. Technowrites. p. 476.
- STONE, K., BANDARA, A.M.T.S., SENANAYAKE, G., and JAYASEKERA, S. 2016. Processing of rare earth phosphate concentrates: A comparative study of pre-leaching with perchloric, hydrochloric, nitric and phosphoric acids and deportment of minor/major elements. *Hydrometallurgy*, vol. 163. pp. 137–147.
- WANG, L., LONG, Z., HUANG, X., YU, Y., CUI, D., and ZHANG, G. 2010. Recovery of rare earths from wet-process phosphoric acid. *Hydrometallurgy*, vol. 101, no. 1. pp. 41–47.
- Wikipedia. 2016. Iron(III) phosphate. [https://en.wikipedia.org/wiki/Iron\(III\)_phosphate](https://en.wikipedia.org/wiki/Iron(III)_phosphate) [accessed October 2016].
- ZHENG, C. 2011. Global rare earth resources and scenarios of future rare earth industry. *Journal of Rare Earths*, vol. 29, no. 1. pp. 1–6. ♦



The banner features the SAIMM logo (The Southern African Institute of Mining and Metallurgy) and the text "WATER 2017 CONFERENCE lifeblood of the mining industry". It also includes the host logos for the Southern African Institute of Mining and Metallurgy & Mine Metallurgical Managers Association (MMMA), and information about the conference dates (10-11 July 2017) and location (Emperors Palace Hotel Casino Convention Resort Johannesburg). A contact box provides details for further information, including Camielah Jardine's contact information and the website <http://www.saimm.co.za>.



Static recrystallization behaviour of Ti-Nb microalloyed high-strength steel

by C-Y. Zhou*, G-L. Wu*, and X-B. Liu*

Synopsis

The static recrystallization behaviour of Ti-Nb microalloyed high-strength steel during hot deformation was studied by conducting double-hit hot compression experiments using a Gleeble-3500 thermomechanical simulator. The effects of deformation temperature, strain rate, strain, and initial austenite grain size on the static recrystallization fraction are discussed. The static recrystallization kinetics were modelled, and the results show that the static recrystallization fraction increased with deformation temperature, strain rate, and strain and interpass time. The static recrystallization activation energy Q_s was 326.05 kJ mol⁻¹. Comparison of the experimental results and predicted results indicates that the effects of deformation parameters on the static recrystallization in multistage hot deformation are significant. The predicted results are in good agreement with the experimental results.

Keywords

Ti-Nb microalloyed high-strength steel, static recrystallization, activation energy, kinetic model.

Introduction

In hot-forming processes, complex microstructures are often induced by multiple hot deformation mechanisms (Zhang *et al.*, 2014; Liang *et al.*, 2015). The softening behaviour during hot processing has generated considerable interest because component properties are influenced significantly by the corresponding microstructural evolution (Wu *et al.*, 2010). It is well known that dynamic recrystallization (DRX); metadynamic recrystallization (MDRX), which occurs by the growth of DRX nuclei during intervals of deformation; and static recrystallization (SRX), which occurs by nucleation and growth during the intervals of deformation, can significantly alter the austenite grain size (Chen *et al.*, 2015; Chen, Sui, and Cui, 2014; Mao *et al.*, 2014). The long interpass times allow complete SRX to take place if the steel is being rolled above the interpass recrystallization stop temperature (T_{nr}), *i.e.* in the absence of carbonitride precipitation (Siciliano, 2000). In recent research, microalloying technology coupled with new-generation thermomechanical control processing (NG-TMCP) has proved efficient in achieving the proper balance between strength, toughness, ductility, and formability by means of a suitable

combination of chemical composition and thermomechanical treatment parameters (Shukla *et al.*, 2012; Bandyopadhyay *et al.*, 2011). The alloying elements Nb, V, Ti are widely used in high-strength low-alloy (HSLA) steel to achieve the desired strength and toughness properties with solid-solution strengthening, precipitation hardening, grain refinement, and dislocation strengthening (Opiela, 2014; Chen and Yu, 2012). The wide applicability of alloying elements in HSLA steel is due to the fact that heat treatments are not required after forming of the parts, which results in time and cost savings.

When microalloying elements are added to steel, the dissolved alloying additions in solid solution raise the temperature of recrystallization of plastically deformed austenite. This is due to segregation on the dislocations and grain boundaries, causing a decrease in the recovery rate and grain boundary mobility (Ferdowsi *et al.*, 2014). Instead, alloying elements precipitating on dislocations in the form of dispersive carbides and/or carbonitrides slow the course of recrystallization during plastic deformation (Cabrera *et al.*, 1997; Mirzadeh, Cabrera, and Najafizadeh, 2012). The SRX behaviour depends on the processing parameters, such as strain rate, deformation temperature, and strain. A finer initial grain size accelerates recrystallization, and precipitation can retard recrystallization (Miao *et al.*, 2012). Therefore, in order to optimize the hot processing parameters, it is important to understand the characteristics of hot deformation to control the microstructure evolution. In this article, the SRX behaviour of Ti-Nb microalloyed high-strength steel during hot deformation was studied using a Gleeble-

* School of Minerals Processing and Bioengineering, Central South University, China.

© The Southern African Institute of Mining and Metallurgy, 2017. ISSN 2225-6253. Paper received Sep. 2015; revised paper received Oct. 2016.

Static recrystallization behaviour of Ti-Nb microalloyed high-strength steel

3500 thermomechanical simulator. The effects of deformation temperature, strain rate, strain, and initial austenite grain size on the SRX fraction are discussed and the SRX kinetics modelled, which will be helpful for optimizing the rolling process.

Experimental

The chemical composition of the high-strength steel used in this investigation was 0.078C-0.25Si-1.78Mn-0.12Ti-0.035Nb-0.008P-0.003S-0.003Al-0.0038N (bal. Fe), in wt%. Cylindrical specimens were machined with a diameter of 8 mm and height of 12 mm. To prevent possible non-uniform temperature distribution in the sample, special cemented carbide products were fixed to both ends of the deformed sample. The uniaxial hot compression tests were conducted using a Gleeble-3500 thermomechanical simulator. In order to determine the critical strain for the start of DRX, the hot compression tests were performed in the temperatures range of 950–1050°C, at intervals of 50°C, under constant strain rates of 0.1, 1, and 5 s⁻¹, up to a true strain of 0.9. Double-hit tests were performed to study the progress of SRX. As shown in Figure 1, the specimens were heated to 1200°C at a heating rate of 10°C s⁻¹ and held at temperature for 5 minutes. The specimens were then cooled to the deformation temperature at 10°C s⁻¹ and held for 1 minute to eliminate thermal gradients. Temperatures of 950, 1000, and 1050°C, strain rates of 0.1, 1, and 5 s⁻¹, strains of 0.10, 0.15, and 0.20, and interval times between the two deformation passes of 1, 5, 10, 30, and 100 seconds were used. In order to research the effect of initial austenite grain sizes on SRX, the specimens were heated to 1200°C and held for different times to obtain different initial austenite grain sizes.

Optical metallographic samples were prepared by conventional grinding and polishing techniques, and were subsequently etched with saturated aqueous picric acid solution and sodium dodecyl benzene sulphonate for 200 seconds. The austenite grain size was analysed by determining the mean lineal intercept and lineal intercept distribution with the aid of image analysis software. A minimum of 600 intercepts were counted for each tested condition from a minimum of 10 randomly chosen fields of view.

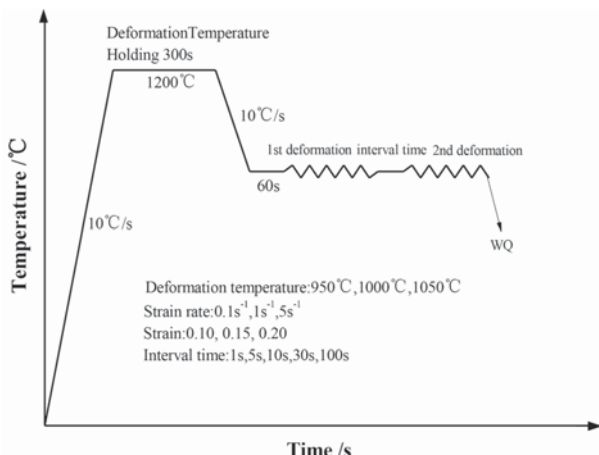


Figure 1—Schematic diagram of the hot simulation test

The interrupted hot compression tests are based on the principle that the yield stress at high temperatures is sensitive to the structural changes. The 0.2% offset yield strength was used to determine the softened fraction due to SRX and recovery (Chen, Sui, and Cui, 2014):

$$F_s = (\sigma_m - \sigma_2)/(\sigma_m - \sigma_1) \quad [1]$$

where σ_m is the flow stress at the interruption, and σ_1 and σ_2 are the 0.2% offset stresses of the first and the second compressions respectively, as shown in Figure 2.

Assuming that recrystallization starts at some critical softening fraction value, which is 0.2, the SRX fraction, X_s , can be determined from the softening data using the following formula (Miao *et al.*, 2012):

$$X_s = (F_s - 0.2)/(1 - 0.2) \quad [2]$$

Results and discussion

To illustrate the effects of the process parameters on the SRX of Ti-Nb microalloyed high-strength steel, the stress-strain curves at different interpass times, deformation temperatures, strain rates, and strains were recorded to calculate the SRX fraction. The influence of the abovementioned variables on SRX was analysed.

Effect of interpass time

True stress-strain curves for Ti-Nb high-strength steel deformed at a temperature of 950°C and a strain rate of 0.1 s⁻¹ are shown in Figure 3. It can be observed that by increasing the interpass time, more static softening occurred in the deformed specimen, and the second curve dropped further compared to the previous test. In other words, the yield stress of the second deformation decreases with increasing interpass time. Similar results were obtained under other test conditions. The increase in interval time allows a longer time for atomic diffusion, increasing the SRX as SRX is a thermal activation process related to atomic diffusion (Lin, Chen, and Zhong, 2008; Chen, Sui, and Cui, 2014; Mao *et al.*, 2014).

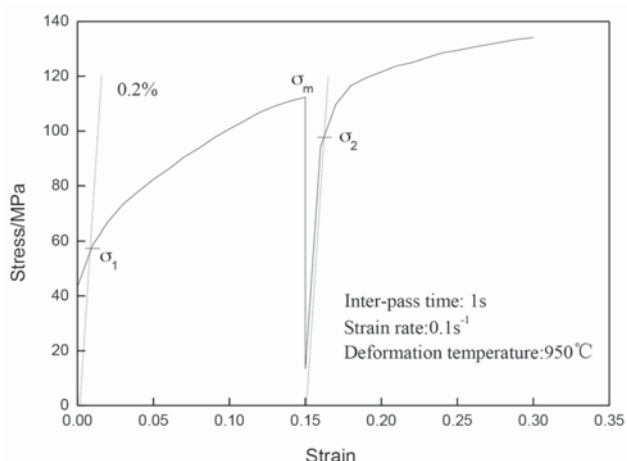


Figure 2—The true stress-strain curves of the double-hit compression test

Static recrystallization behaviour of Ti-Nb microalloyed high-strength steel

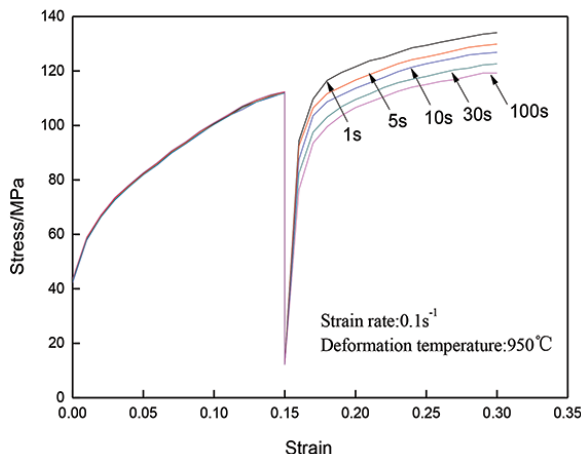


Figure 3—Flow stress curves of Ti-Nb microalloyed high-strength steel with different interpass times

Effect of deformation temperature

Figure 4a shows the relationship between the SRX fraction and the interval time under different deformation temperatures at a strain rate of 0.1 s^{-1} and strain of 0.2. It can be seen that the softening kinetics of the specimen were accelerated by increasing the deformation temperature. Initially, the SRX fraction at a deformation temperature of 1050°C was higher than at 950°C , while the SRX fraction at 950°C was below 60% at the interval time of 100 seconds. This result indicates that SRX could not proceed to completion at lower temperatures, but occurred much faster at high temperature. This is due mainly to the fact that the

higher deformation-stored energy at higher temperatures accelerates SRX (Chen, Sui, and Cui, 2014). As SRX is thermally activated, the SRX fraction increases with increasing deformation temperature (Mao *et al.*, 2014).

Effect of strain rate

The effects of strain rate on the SRX fraction were obtained at a deformation temperature of 1000°C and pre-strain of 0.15, as shown in Figure 4b. The softening was slightly accelerated with increasing strain rate, which indicates that strain rate had a small influence on the SRX fraction. Furthermore, the softening curve corresponding to 0.1 s^{-1} is lower than those for strain rates of 1 s^{-1} or 5 s^{-1} , especially at shorter interpass times. This is due to the higher strain energy stored in the deformed sample under high strain rate conditions (Lin, Chen, and Zhong, 2008). The reduced extent of dynamic recovery at higher strain rates results in a higher dislocation density and increases the driving force for SRX during the interpass time (Lin, Chen, and Zhong, 2008).

Effect of pre-strain

The first deformation should be interrupted below the critical strain required for DRX. The critical strain for the start of DRX should therefore be known accurately. Generally speaking, DRX can be initiated at a critical level of stress accumulation during hot deformation. However DRX actually starts at a critical strain (ε_c) which is lower than the strain at peak stress. Only when the strain exceeds ε_c does DRX occur in a hot deformation process (Ferdowsi *et al.*, 2014). The point on the flow curve at which the strain hardening rate equals zero represents the peak stress (σ_p), and the inflection

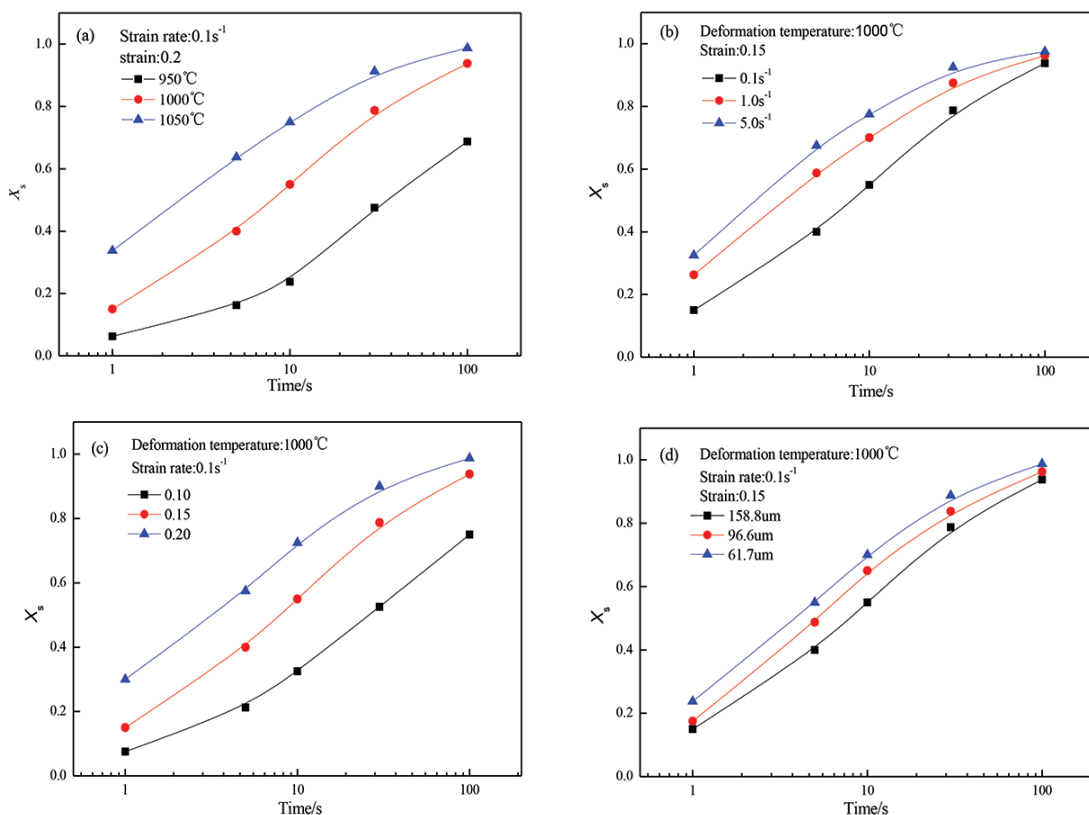


Figure 4—Static softening fraction with different process parameters: (a) deformation temperature, (b) strain rate, (c) strain, (d) initial austenite grain size

Static recrystallization behaviour of Ti-Nb microalloyed high-strength steel

point indicates the critical stress (σ_c) for the initiation of DRX. The critical strains can be determined from the inflection points of the $\ln \theta - \varepsilon$ plots, and the critical stresses can be subsequently obtained either from the $\theta - \sigma$ plots or from the initial flow curves (Poliak and Jonas, 2003). The relationship between $\ln \theta$ and ε can be expressed as (Poliak and Jonas, 2003):

$$\ln \theta = A_1 \varepsilon^3 + A_2 \varepsilon^2 + A_3 \varepsilon + A_4 \quad [3]$$

where A_1 , A_2 , A_3 , and A_4 are constant parameters for each deformation condition. The second derivative of Equation [3] with respect to ε can be expressed as:

$$\frac{d^2 \ln \theta}{d\varepsilon^2} = 6A_1\varepsilon + 2A_2 \quad [4]$$

At critical strain for initiation of DRX, the second derivative becomes zero. Therefore

$$\varepsilon_c = -A_2/(3A_1) \quad [5]$$

The $\ln \theta - \varepsilon$ curve and its corresponding third-order polynomial can yield some data. Using the flow curves, the values of peak and critical stresses and strains can be determined. The results are shown in Table I.

DRX occurs at high temperatures and low strain rates, which means the critical strain for DRX will increase with increasing strain rate at a given temperature, or increase with decreasing temperature at a constant strain rate. According to Table I, the most likely condition for DRX is 1050°C and 0.1 s⁻¹, and the critical strain at this condition is 0.22, which is higher than the experimental conditions of strain (0.1, 0.15, and 0.2). It can therefore be concluded that DRX could not occur under the given deformation conditions.

The SRX fraction was plotted against the interval time for three pre-strains of 0.1, 0.15, and 0.2 at a strain rate of 0.1 s⁻¹ and a deformation temperature of 1000°C, as shown in Figure 4c. It can be observed that an increase in pre-strain led to an acceleration of the softening kinetics. The figure also shows that the rate of softening with a pre-strain of 0.1 was low, while the softening fraction was 75% with the interval time of 100 seconds. This means that softening under the relatively mild pre-deformation conditions resulted from recovery. However, for the higher pre-strain conditions of 0.15 and 0.20, the rate of softening was higher, which indicates that softening was caused mainly by SRX. This is due to the increase in dislocation density with pre-deformation, leading to an increase in the stored energy, thus resulting in increasing driving force for recrystallization, thereby speeding up the recrystallization process (Chen, Sui, and Cui, 2014; Mao *et al.*, 2014).

Table I

Critical and peak strains at different deformation conditions

Temperature, °C	Strain rate 0.1 s ⁻¹		
	ε_c	ε_p	$\varepsilon_c/\varepsilon_p$
950	0.25	0.35	0.71
1000	0.23	0.32	0.72
1050	0.22	0.31	0.71

Effect of initial grain size

The deformation temperature, strain rate, and pre-strain were held constant as 1000°C, 0.1 s⁻¹, and 0.15, respectively. The initial austenite grain sizes were 158.8, 96.6, and 61.7 μm, respectively. The effects of the initial grain size and interval time on the SRX fractions are shown in Figure 4d. It can be observed that the softening fraction decreased with an increase in initial grain size. This is because the nucleation of SRX occurs mainly on the grain boundaries, and larger grains have less grain boundary area per unit volume, which leads to a decrease in the density of potential nucleation sites for SRX (Chen, Sui, and Cui, 2014; Lin, Chen, and Zhong, 2008).

Modelling the kinetics of SRX

The kinetics of SRX softening can be described by an Avrami equation of the following form (Choi, 2002):

$$X_s = 1 - \exp[-0.693(\frac{t}{t_{0.5}})^n] \quad [6]$$

where X_s is the SRX fraction, n is a material-dependent constant, and $t_{0.5}$ is the time taken to form a recrystallization volumetric fraction of 50%. The expression most widely used for $t_{0.5}$ is (Choi, 2002):

$$t_{0.5} = Ad_0^r \varepsilon^q \dot{\varepsilon}^s \exp[Q_s/(RT)] \quad [7]$$

where A , r , q , and s are material-dependent constants, ε is the true strain, $\dot{\varepsilon}$ is the strain rate, R is the gas constant (Jmol⁻¹K⁻¹), T is the absolute temperature (K), Q_s is the activation energy of recrystallization (kJ mol⁻¹), and d_0 is the initial austenite grain size (μm).

Taking the logarithm of both sides of Equation [6] twice, the following expression can be obtained:

$$\ln[\ln(\frac{1}{1-X_s})] = n \ln t - n \ln t_{0.5} + \ln 0.693 \quad [8]$$

The Avrami exponent n is obtained by linear fitting and regression analysis using a range of temperatures and pre-strains, which results in $n = 0.58$, under the current experimental conditions, as shown in Figure 5.

Taking the logarithm of both side of Equation [7], the following expression is obtained:

$$\ln t_{0.5} = \ln A + r \ln d_0 + q \ln \varepsilon + s \ln \dot{\varepsilon} + Q_s/(RT) \quad [9]$$

The values of $t_{0.5}$ under different conditions can be derived from the relationships between X_s and the corresponding interval time. Then, by substituting the values of $t_{0.5}$ and deformation temperature into Equation [9], the relationship between $\ln t_{0.5}$ and $10000/T$ can be obtained by linear fitting and regression analysis, as shown in Figure 6a; thus Q_s can be calculated as 326.05 kJ.mol⁻¹. Similarly, the values of the material-dependent constants r , q , and s are calculated as 0.86, -2.75, and -0.28 using Figures 6b, c, and d, respectively. Additionally, the constant A can be derived as 1.37×10^{-17} based on the obtained material-dependent constants.

Therefore the SRX kinetics for the Ti-Nb microalloyed high-strength steel can be represented as:

$$X_s = 1 - \exp[-0.693(t/t_{0.5})^{0.58}] \quad [10]$$

Static recrystallization behaviour of Ti-Nb microalloyed high-strength steel

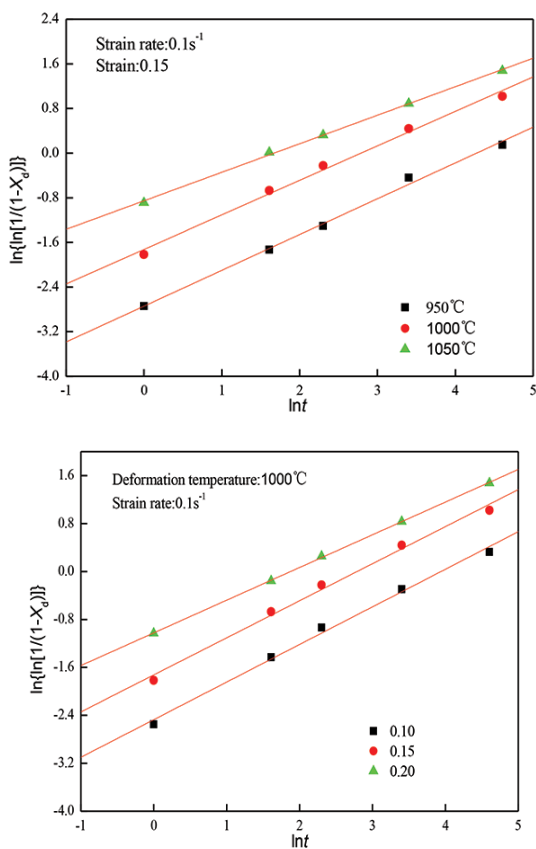


Figure 5—Relationships between $\ln\{\ln[1/(1-X_d)]\}$ and $\ln t$ at (a) different deformation temperatures, (b) different pre-strains

$$t_{0.5} = 1.37 \times 10^{-17} d_0^{0.86} \varepsilon^{-2.75} \dot{\varepsilon}^{-0.28} \exp[326050/(RT)] \quad [11]$$

Comparison between experimental and predicted results

In order to verify the developed kinetic equations [10] and [11] for Ti-Nb microalloyed high-strength steel, the experimental and predicted results were compared. Figure 7 illustrates the comparisons between the experimental and predicted times for a recrystallized fraction of 50% (Figure 7a) and the recrystallization fraction under different deformation conditions (Figure 7b). The predicted and experimental results were in good agreement, indicating that the proposed kinetic equations could give a reasonable estimate of the softening behaviour during metal-forming processes.

Conclusions

- (1) The SRX fraction of the Ti-Nb microalloyed steel increased with increasing forming temperature, pre-strain, and strain rate, and decreased with increasing initial austenitic grain size
- (2) The kinetics equations for SRX in the Ti-Nb microalloyed high-strength steel were developed to predict the softening behaviour induced by SRX, and are expressed as:

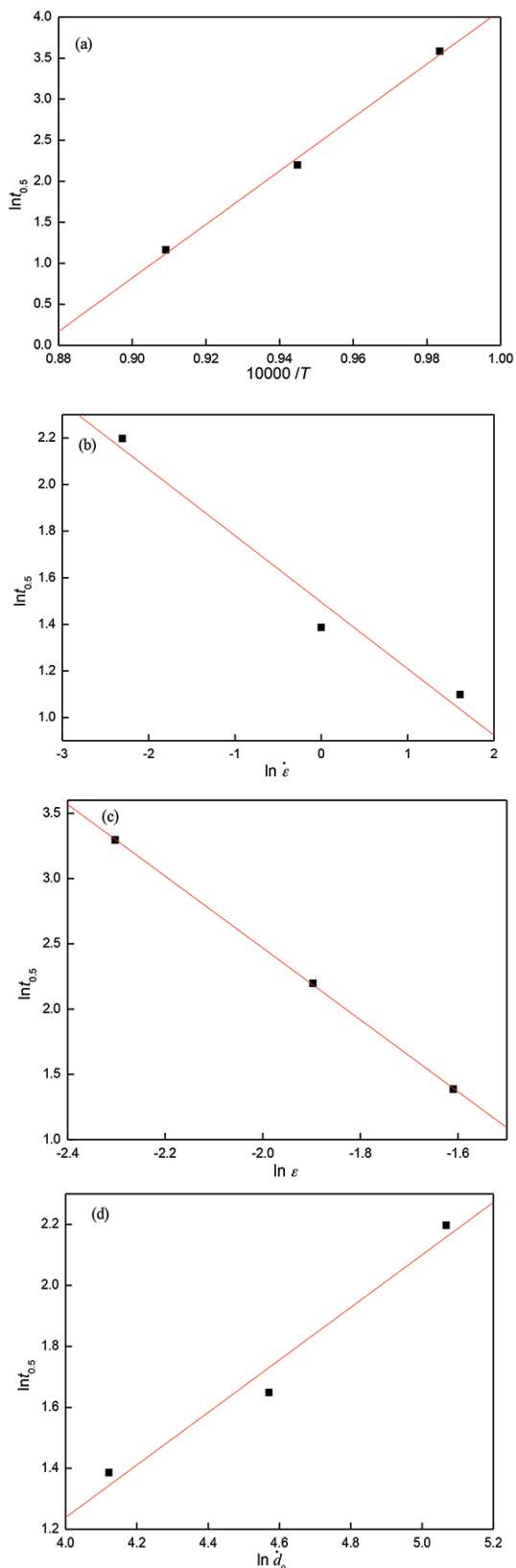


Figure 6—Relationship between $\ln t_{0.5}$ and (a) $10000/T$, (b) $\ln \dot{\varepsilon}$, (c) $\ln d_0$, and (d) $\ln \dot{\varepsilon}$

$$X_s = 1 - \exp[-0.693(t/t_{0.5})^{0.58}]$$

$$t_{0.5} = 1.37 \times 10^{-17} d_0^{0.86} \varepsilon^{-2.75} \dot{\varepsilon}^{-0.28} \exp[326050/(RT)]$$

Static recrystallization behaviour of Ti-Nb microalloyed high-strength steel

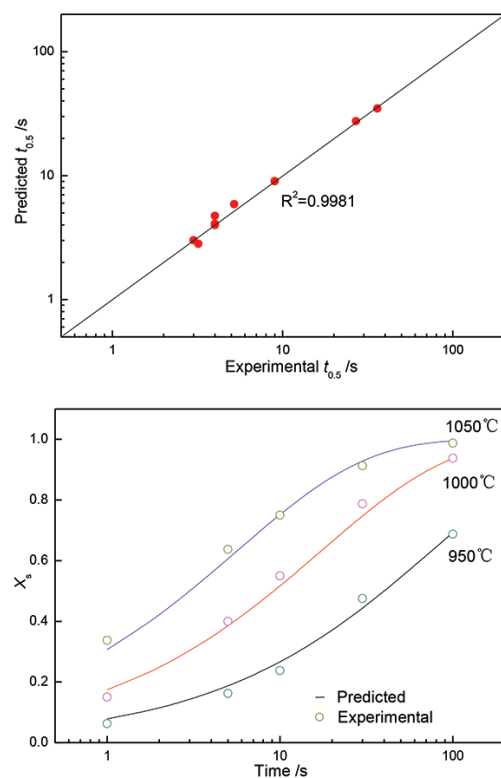


Figure 7—Comparisons between experimental results and predicted results of (a) $t_{0.5}$ and (b) recrystallization fraction

References

- BANDYOPADHYAY, P.S., KUNDU, S., GHOSH, S.K., and CHATTERJEE, S. 2011. Structure and properties of a low-carbon microalloyed ultra-high-strength steel. *Metallurgical and Materials Transactions A*, vol. 42, no. 4. pp. 1051–1061.
- CABRERA, J.M., OMAR, A.A., PRADO, J.M., and JONAS, J.J. 1997. Modeling the flow behavior of a medium carbon microalloyed steel under hot working conditions. *Metallurgical and Materials Transactions A*, vol. 28, no. 11. pp. 2233–2244.
- CHEN, B.H. and YU, H. 2012. Hot ductility behavior of V-N and V-Nb microalloyed steels. *International Journal of Minerals, Metallurgy and Materials*, vol. 19, no. 6. pp. 525–529.
- CHEN, F., SUI, D.S., and CUI, Z.S. 2014. Static recrystallization of 30Cr2Ni4MoV ultra-super-critical rotor steel. *Journal of Materials Engineering and Performance*, vol. 23, no. 8. pp. 3034–3041.
- CHEN, J., LV, M.Y., TANG, S., LIU, Z.Y., and WANG, G.D. 2015. Influence of thermomechanical control process on the evolution of austenite grain size in a low-carbon Nb-Ti-bearing bainitic steel. *Journal of Materials Engineering and Performance*, vol. 24, no. 10. pp. 3852–3861.
- FERDOWSI, M.R.G., NAKHAIE, D., BENHANGI, P.H., and EBRAHIMI, G.R. 2014. Modeling the high temperature flow behavior and dynamic recrystallization kinetics of a medium carbon microalloyed steel. *Journal of Materials Engineering and Performance*, vol. 23, no. 3. pp. 1077–1087.
- LIANG, H.Q., NAN, Y., NING, Y.Q., LI, H., ZHANG, J.L., SHI, Z.F., and GUO, H.Z. 2015. Correlation between strain-rate sensitivity and dynamic softening behavior during hot processing. *Journal of Alloys and Compounds*, vol. 632. pp. 478–485.
- LIN, Y.C., CHEN, M.S., and ZHONG, J. 2008. Study of static recrystallization kinetics in a low alloy steel. *Computational Materials Science*, vol. 44, no. 2. pp. 316–321.
- MAO, H.J., ZHANG, R., HUA, L., and YIN, F. 2014. Study of static recrystallization behaviors of GCr15 steel under two-pass hot compression deformation. *Journal of Materials Engineering and Performance*, vol. 24, no. 2. pp. 930–935.
- MIAO, C.L., SHANG, C.J., ZUROB, H.S., ZHANG, G.D., and SUBRAMANIAN, S.V. 2012. Recrystallization, precipitation behaviors, and refinement of austenite grains in high Mn, high Nb steel. *Metallurgical and Materials Transactions A*, vol. 43, no. 2. pp. 665–676.
- MIRZADEH, H., CABRERA, J.M., and NAJAFIZADEH, A. 2012. Modeling and prediction of hot deformation flow curves. *Metallurgical and Materials Transactions A*, vol. 43, no. 1. pp. 108–123.
- OPIELA, M. 2014. Effect of thermomechanical processing on the microstructure and mechanical properties of Nb-Ti-V microalloyed steel. *Journal of Materials Engineering and Performance*, vol. 23, no. 9. pp. 3379–3388.
- POLIAK, E.I. and JONAS, J.J. 2003. Initiation of dynamic recrystallization in constant strain rate hot deformation. *ISIJ International*, vol. 43, no. 5. pp. 684–691.
- SANGWOO, C. and YOUNGSEOG, L. 2002. A new approach to predicting partial recrystallization in the multi-pass hot rolling process. *Metals and Materials International*, vol. 8, no. 1. pp. 15–23.
- SHUKLA, R., DAS, S.K., RAVIKUMAR, B., GHOSH, S.K., KUNDU, S., and CHATTERJEE, S. 2012. An ultra-low carbon, thermomechanically controlled processed microalloyed steel: microstructure and mechanical properties. *Metallurgical and Materials Transactions A*, vol. 43, no. 12. pp. 4835–4845.
- SICILIANO, F. and JONAS, J.J. 2012. Mathematical modeling of the hot strip rolling of microalloyed Nb, multiply-alloyed Cr-Mo, and plain C-Mn steels. *Metallurgical and Materials Transactions A*, vol. 31, no. 2. pp. 511–530.
- WU, L.Z., LI, X.S., CHEN, J., ZHANG, H.B., and CUI, Z.S. 2010. Dynamic recrystallization behavior and microstructural evolution in SPHC steel. *Journal of Shanghai Jiaotong University (Science)*, vol. 15, no. 3. pp. 301–306.
- ZHANG, W.F., SHA, W., YAN, W., WANG, W., SHAN, Y.Y., and KE, Y. 2014. Constitutive modeling, microstructure evolution, and processing map for a nitride-strengthened heat-resistant steel. *Journal of Materials Engineering and Performance*, vol. 23, no. 8. pp. 3042–3050. ◆



Techno-economic feasibility of a pre-oxidation process to enhance prereduction of chromite

by E.L.J. Kleynhans*†, J.P. Beukes*, P.G. van Zyl* and J.I.J. Fick†

Synopsis

Ferrochrome (FeCr) is vital for the production of stainless and high-alloy ferritic steels, since it is the only source of new Cr units. FeCr production is an energy-intensive process. The pelletized chromite prereduction process is most likely the FeCr production process with the lowest specific electricity consumption (SEC), *i.e.* MWh/t, currently in operation. However, due to increases in costs, efficiency, and environmental pressures, FeCr producers are attempting to lower their overall energy consumption even further. Recently, it was proven that pre-oxidation of chromite ore prior to pelletization and prereduction significantly decreases both the SEC and lumpy carbonaceous reductants required for smelting. This paper presents the first attempt at conceptualizing the techno-economic feasibility of integrating chromite pre-oxidation into the prereduction process. Financial modelling yielded a net present value (NPV) at a 10% discount rate of approximately R900 million and an internal rate of return (IRR) of approximately 30.5% after tax, suggesting that the implementation of pre-oxidation prior to pellet prereduction may be financially viable. Sensitivity analysis indicated that the parameter with the greatest influence on project NPV and IRR is the level of prereduction. This indicates that the relationship between maintaining the optimum pre-oxidation temperature and the degree of prereduction is critical for maximum process efficiency.

Keywords

chromite prereduction, solid-state reduction, pre-oxidation, discounted cash flow model, techno-economic feasibility.

Introduction

Stainless steel is a crucial alloy in modern society. Virgin chromium (Cr) units used in the manufacturing of stainless steel are obtained from ferrochrome (FeCr) – a relatively crude alloy consisting predominantly of Cr and iron (Fe) (Murthy, Tripathy, and Kumar, 2011; Beukes, van Zyl, and Ras, 2012). FeCr is produced mainly by the carbothermic reduction of chromite ore in submerged arc furnaces (SAFs) and direct current arc furnaces (DCFs) (Neizel *et al.*, 2013; Beukes, Dawson, and van Zyl, 2010; Dwarapudi *et al.*, 2013). The energy required to heat, smelt, and reduce the chromite ore to the metallized state is supplied by electricity (Pan, 2013). FeCr production is an energy-intensive process, with a specific electricity consumption (SEC) varying from 2.4 MWh/t to more than 4.0 MWh/t FeCr produced, depending on the process applied (Pan, 2013; Neizel *et al.*, 2013). Daavittila, Honkaniemi, and Jokinen (2004) stated that

the typical operational costs of FeCr smelters can be divided into four categories, *i.e.* chromite ore (30%), carbonaceous reductant (20%), electricity (30%), and other production costs (20%). This makes electricity consumption the joint largest factor that influences operational costs in FeCr production.

Beukes, Dawson, and van Zyl (2010) presented an overview of processes utilized for FeCr production, with specific reference to the South African FeCr industry. However, similar processes are also applied internationally. According to this review, FeCr is produced in:

- (i) Conventional semi-closed/open submerged arc furnace (SAF) operations with bag filter off-gas treatment
- (ii) Closed SAF operations that usually utilize oxidized, sintered pelletized feed, with venturi scrubbing of off-gas
- (iii) Closed SAF operations consuming prereduced pelletized feed, with venturi scrubbing of off-gas
- (iv) Closed direct current (DC) arc furnace operations, with venturi scrubbing of off-gas.

Until now, these processing options have allowed for economical FeCr production, particularly in countries with local chromite resources (Daavittila, Honkaniemi, and Jokinen, 2004). Although equipment has been improved and modern automation systems implemented, there are still some significant areas in which the technology can be improved further:

* Chemical Resource Beneficiation, North-West University, Potchefstroom Campus, Potchefstroom, South Africa.

† Centre for Research and Continued Engineering Development – CRCED Vaal, Faculty of Engineering, Vaal Triangle Campus, North-West University, Vanderbijlpark, South Africa.

© The Southern African Institute of Mining and Metallurgy, 2017. ISSN 2225-6253. Paper received Nov. 2015; revised paper received May. 2016.

Techno-economic feasibility of a pre-oxidation process to enhance prerduction

- (i) The efficient use of energy (electricity and chemical energy in the form of reductants) and the utilization of secondary energy produced (*e.g.* CO-rich off-gas, radiation heat)
- (ii) Increased use of lower cost raw materials through advanced beneficiation and agglomeration, or corresponding technologies
- (iii) Larger production units in order to benefit from economies of scale
- (iv) Increased automation to improve operation (Daavittila, Honkaniemi, and Jokinen, 2004).

These factors, coupled with the fact that SAF and DC smelting operations can be regarded as having reached the 'mature' phase of development, indicate that FeCr producers and their main customers, the stainless steel producers, should consider more cost- and quality-effective production of Cr units (Slatter, 1995; Holappa, 2010). FeCr producers face significant challenges, including a downward trend in FeCr prices, increasing awareness of environmental impacts and working conditions, increasing electricity costs (and availability in some countries), and carbon footprint reduction requirements (Daavittila, Honkaniemi, and Jokinen, 2004) that will require innovative advances in process technologies (Ugwuegbu, 2012).

Various measures to improve FeCr production by the SAF process have been investigated (Kapure *et al.*, 2010; Daavittila, Honkaniemi, and Jokinen, 2004; Slatter, 1995; Goel, 1997; Ugwuegbu, 2012). These measures mainly involved prerduction and preheating methods in order to improve Cr recoveries and minimize smelting costs. The pelletized chromite prerduction process (commercially known as the Premus process), applied by two Glencore Alloys FeCr smelters in South Africa, comprising six large smelting SAFs, is considered to be the FeCr production process option with the lowest SEC currently in operation (Kleynhans *et al.*, 2012). Similar smelters are being commissioned in China, but no information regarding these operations is currently available in the peer-reviewed public domain. The SEC of the pelletized chromite prerduction process is approximately 20% lower than that of its nearest rival, the SAF smelting process with oxidized sintered pellets as furnace feed (commercially referred to as the Outotec technology) (Neizel *et al.*, 2013). The pelletized chromite prerduction process also has some disadvantages, as indicated by Mohale (2014), *i.e.* the higher capital cost and the extensive operational control required due to the variation in prerduction level and carbon content of the prerduced pelletized furnace feed material.

In view of the previously mentioned challenges faced by FeCr producers, and regardless of the lower SEC of the pelletized chromite prerduction process, it is apparent that smelters applying this process would benefit from a process improvement capable of achieving even lower SEC. Beukes, van Zyl, and Neizel (2015) developed a new process in which chromite ore is oxidized before prerduction. This patented process was reviewed by Kleynhans *et al.* (2015). They found that pre-oxidation enhanced the susceptibility of the chrome spinel to prerduction, mainly by Fe liberation and preventing the release of chromium (III) oxide (Cr_2O_3) from the spinel (Beukes, van Zyl, and Neizel, 2015; Kleynhans *et al.*, 2015). As indicated by Niayesh and Fletcher (1986), an

increase in the level of prerduction will result in a decrease in SEC. Beukes, van Zyl, and Neizel (2015) and Kleynhans *et al.* (2015) claimed that a reduction in SEC of approximately 8.5% can be achieved.

This investigation was carried out to assess the economic feasibility of the pre-oxidation process applied as a pre-treatment step in the pelletized chromite prerduction process, and to evaluate the effect on the economics of a typical FeCr smelter. This was done by analysing the cost efficiency of various cost model parameter options, as well as their subsequent development within a comprehensive cost model and discounted cash flow (DCF) model.

Background to the feasibility study

South Africa hosts the majority of global chromite reserves (Beukes, van Zyl, and Ras, 2012; Merafe Resources, 2012; Cramer, 2013). The majority of South Africa's chromite ore is relatively friable. It is therefore common to recover only 10–15% lumpy ore (15–150 mm) and 8–12% chip/pebble ore (6–15 mm) during the beneficiation process. The remaining ore would typically be in the <6 mm fraction, and would usually be crushed and/or milled to <1 mm and then upgraded utilizing gravity separation techniques (*e.g.* spiral concentrators) to approximately 45% Cr_2O_3 content. This upgraded <1 mm ore is commonly known as metallurgical grade chromite (Glastonbury *et al.*, 2010). Upgraded chromite tailings (<1 mm) from platinum group metals (PGMs) concentrators treating the UGS Reef are also utilized as feed material for the South African FeCr industry (Cramer, Basson, and Nelson, 2004).

Effective SAF smelting operation requires a permeable burden to ensure the uniform flow of reduction gases and smooth furnace operation (Dwarapudi *et al.*, 2013). The use of fine chromite ore in SAFs is limited, since fine materials increase the tendency of the surface layer of the SAF burden to sinter. This traps evolving process gas, which can result in so-called bed turnovers or blowing of the furnace, which can result in damage to equipment or injury to personnel. A process that can accommodate fine ore is therefore required. Typically an agglomeration step (*e.g.* pelletization) is employed prior to feeding into the SAF (Kleynhans *et al.*, 2012; Beukes, Dawson, and van Zyl, 2010).

There are currently 14 individual FeCr production facilities in South Africa, with a combined capacity in the region of 5.2 Mt/a (Beukes, van Zyl, and Ras, 2012; Jones, 2015). The abundant chromite resources and comparatively low historical cost of electricity enabled South Africa to maintain its dominant position in the international FeCr industry, contributing on average 44.5% to global FeCr production in the period 2000 to 2011. However, in 2012, South Africa produced only 32% of the world's output, as production decreased by 30% from 2007, with China becoming the largest FeCr producer (ICDA, 2013b). A number of factors led to this major downturn. Firstly, South Africa is facing several internal challenges that have adversely affected the manufacturing ability and production costs of FeCr producers. Historically, the country benefited from favourable, inexpensive logistics and relatively cheap labour. This is no longer the case, due to the country's energy and labour problems. By the end of 2007, the electricity demand in South Africa caught up with the generating capacity. In

Techno-economic feasibility of a pre-oxidation process to enhance prerduction

order to avoid destabilization of the national electricity grid, rolling blackouts were implemented. Erosion of surplus generation capacity led to a dramatic increase in the nominal price of electricity; by about 245% between 2007 and 2013 (Eskom, 2012).

In 2012, Eskom, the country's state-controlled energy supplier, realized that it would not be able to support total electricity demand, and agreed to reimburse FeCr smelters that did not use already-contracted electricity supply and temporarily shut down their furnaces. This lack of energy-generation capacity is the result of years of underinvestment in the electricity sector. FeCr smelters, facing low prices for their product, welcomed the proposition and started to shut down their furnaces. Anecdotal evidence indicated that it was more profitable for them to sell energy back to Eskom than to produce FeCr. Eskom announced in early 2013 that it needed R50 billion (approximately US\$5 billion) more than planned to meet funding needs in the five years until 2018. This was in addition to the R225 billion shortfall in revenue due to higher coal prices and increased capex expenses. Eskom needed to invest immensely in new capacity, but the National Electricity Regulator of South Africa (NERSA) refused the price increase of 16% per year requested by Eskom for 2013 to 2018. Instead, NERSA granted Eskom permission to raise the energy tariff by 8% per annum for the following five years, to finance investments in new generation capacity. Furthermore, Eskom struggles to source the coal it requires. Coal production has to rise from the current 254 Mt/a to more than 320 Mt/a by 2020 to satisfy demand. In addition China, South Africa main FeCr customer, has increased domestic FeCr production and reduced imports, taking advantage of the increasing demand for FeCr and filling the gap in the market. Lower shipping costs, brought about by the slowdown in the world economy, made geographical positioning of smelters less relevant. Therefore, at present, South Africa ships less FeCr to China, which now imports more chromite ore from South Africa and smelts it locally to supply its stainless steel industries (ICDA, 2013a, 2013b).

Against this background, the South African FeCr industry is ideal for this feasibility study. South Africa holds the majority of the world's chromite resources, the ore is friable which necessitates an agglomeration process step, and the energy situation justifies exploring new FeCr production technologies to reduce SEC.

Process options

Although the pre-oxidation process prior to prerduction has been patented (Beukes, van Zyl, and Neizel, 2015), it has not yet been applied on an industrial scale. The process therefore needs to be matched with appropriate equipment. Equipment used in currently applied and previously attempted pre-treatment options could be considered to serve for this purpose.

Outotec's steel belt sintering process is the only commercially applied FeCr process that utilizes oxidation as a pre-treatment method prior to smelting in the SAF. The pre-oxidation of unagglomerated chromite ore prior to prerduction (solid-state reduction of chromite) must not be confused with oxidation prior to smelting. Furthermore, reduction during smelting in an SAF, when the ore is completely reduced to the zero oxidation or metallic state,

must not be confused with prerduction, where the ore is only partially reduced. Molten or liquid materials are formed during the smelting reduction process, but not during prerduction, hence the alternative terminology 'solid-state reduction'. The primary raw materials in the Outotec steel belt sintering process, which has been the most commonly applied process over the last decade in the South African FeCr industry, are ore fines, a refined clay binder, and fine coke. The ore and coke are wet-milled in a ball mill to approximately 90% smaller (d_{90}) than 108 µm (Glastonbury *et al.*, 2015) and dewatered in capillary-type ceramic filters. The dewatered material is mixed with a clay binder and pelletized in a drum pelletizer before finally being sintered in the steel belt sintering furnace. The fixed carbon (FC) content (from coke fines) added in the steel belt sintering feed mixture is low (1–2%) compared to the FC content of the feed mixture for prerduction (12.5–15%). The sintering process is basically an oxidative process, during which the carbon in the pellets is oxidized to sinter the pellets (Beukes, van Zyl, and Ras, 2010; Glastonbury *et al.*, 2015).

In rotary hearth furnace technology, normally applied as a preliminary heating or reduction step prior to smelting, ore, reductants, and fluxes are milled to typically less than 100 µm before being blended, mixed, and fed into a pelletizing plant. The green pellets are dried using exhaust gas from the rotary hearth furnace. The furnace operates continuously and the pellets are sintered, reduced, and cooled in controlled zones with a maximum zone temperature of 1450°C (Slatter, 1995). The reduction occurs in stages in different zones of the furnace. Additional hot air is introduced into the rotary hearth furnace to control the temperature and the composition of the atmosphere in order to provide conditions conducive to the optimal reduction of chromite and minimize re-oxidation. Once the material has passed through the rotary hearth furnace, it is discharged and can be cooled using various methods. Energy for the sintering and prerduction zones can be provided by the oxidation of the CO gas obtained from the exhaust gas of SAFs (Slatter, 1995). The rotary hearth furnace, if operated with an oxidizing atmosphere, could be applied for pre-oxidation.

Fluidized beds are ideally suited for the processing of finely sized raw materials (Luckos, Denton, and den Hoed, 2007). Since the fluidized bed can be used as a preheater for chromite, it can also be considered as a means to pre-oxidize ore prior to prerduction. Laboratory-scale preheating tests with chromite ores and coals were carried out in a fluidized bed facility at Lurgi Metallurgie, followed by a pilot-scale test in a four-stage flash preheater at Polysius AG. These tests confirmed that chromite ores and fluxes can be thermally treated up to a gas temperature of 1150°C without succumbing to the forces of attrition and producing fines, or forming low-melting-point phases and agglomerating. Denton, Bennie, and de Jong (2004) stated that the best option from an economic point of view is to use CO-rich furnace off-gas to preheat the chromite and fluxes to 1200°C.

The rotary kiln serves as the process unit for a number of preheating and prerduction process technologies. In principle, rotary kilns can be effectively used for preheating charge by making use of CO-rich furnace off-gas. The use of a rotary kiln for prerduction of chromite ore was developed and applied on an industrial scale by three companies – Outokumpu, Showa Denko, and Krupp/MS&A (McCullough

Techno-economic feasibility of a pre-oxidation process to enhance prereduction

et al., 2010; Ugwuengbu, 2012). Outokumpu used a rotary kiln for preheating pellets to 1000°C before continuously feeding the preheated pellets to a closed SAF. Outokumpu studied its process for approximately ten years on the laboratory and pilot scale, as well as for two years in a commercial-scale operation utilizing a rotary kiln with a length of 55 m and an inner diameter of 2.3 m (Daavittila, Honkaniemi, and Jokinen, 2004). The process involved grinding and pelletizing of ore fines, followed by sintering of green pellets that were prereduced before smelting. The ore and coke fines used by Outokumpu were wet-ground to approximately d_{35} 37 µm and then pelletized to approximately 15 mm diameter. The bulk of the fuel for sintering and prereduction of the pellets was provided by CO-rich off-gas from closed SAFs (Goel, 1997). Showa Denko's process for prereduction of pellets is still in use. It was installed by Consolidated Metallurgical Industries in South Africa in the mid-1970s. This was the first commercial prereduction process for chromite. In this process, chromite ore fines are milled to $d_{90} < 75$ µm, pelletized with coke as reductant, and fired in a rotary kiln to approximately 1400°C. The kiln is heated by a pulverized coal burner. The pellets, with approximately 40–60% metallization of Cr and Fe, are discharged into an SAF for final smelting (Naiker, 2007; Naiker and Riley, 2006).

To address some of the apparent weaknesses of the Showa Denko K.K. (SDK) process, Krupp commenced development of a rotary kiln prerection process in 1984, based upon their CODIR process. In this process, chromite ore and coal fines react in a rotary kiln at temperatures approaching 1450°C to produce a semi-solid product consisting of highly metallized FeCr, slag, gangue, and char. A high temperature and intimate contact between the chromite grains and carbon are necessary over the entire residence time in the kiln in order to achieve a high degree of metallization (>90%). For this purpose, the burden is transformed into a semi-solid state with a combination of molten and solid phases, to allow for only a small portion of the surface of the metallized phase to be exposed to air without macroscopic phase separation occurring (McCullough *et al.*, 2010).

The Premus process, currently applied by Glencore Alloys, was developed from the SDK/CMI process. In this process, anthracite or char is used as a reductant instead of coke. Similar to the SDK/CMI process, the raw materials are dry-milled, pelletized, preheated, and fed into a rotary kiln. Pure oxygen and a pulverized carbon fuel (PF) are used to fire the kiln (Basson, Curr, and Gericke, 2007; Naiker, 2007; Naiker and Riley, 2006; Ugwuengbu, 2012). Kleynhans *et al.* (2012) indicated that while the pellets are exposed to the high temperatures inside the rotary kiln, the carbon in the outer layer of the pellets is mostly burned off and a partially oxidized outer layer is formed. A small amount of Fe reduction can occur before all the carbon is consumed in this outer layer, and this Fe can be re-oxidized. Oxygen ingress to the core does not take place, since CO gas formed from the carbon inside the pellets produces a positive partial pressure. This positive CO pressure is therefore necessary to prevent re-oxidation of the pellets. If chromite ore is fed into the kiln without a carbon reductant to generate CO, natural oxidation would consequently occur as required for the pre-oxidation process.

The disadvantage of the Outotec steel belt sintering process is that the raw materials used, including the ore, are milled and pelletized before being sintered in an oxidizing environment. These pellets would have to be pulverized in order to use them in the prereduction process. The energy and raw materials used to initially pelletize the ore for pre-oxidation would therefore be wasted. The rotary hearth furnace and fluidized-bed processes offer an interesting alternative, but although they have been tested on a pilot scale, these processes have not yet progressed to successful large-scale operation in the FeCr industry and further development is required. Of the four abovementioned options, the one most likely to be implemented by FeCr producers already utilizing the prereaction process is the rotary kiln. FeCr producers using chromite prereaction are accustomed to kiln operation and would prefer this route as it fits within their current prereaction operations culture. It also has an advantage from a maintenance perspective, *i.e.* employing a kiln with the same diameter for pre-oxidation as the kiln used for prereaction. This standardization of equipment components would reduce spare parts requirements, thereby lowering capital that is tied up.

Process descriptions

Since it is expected that a countercurrent rotary kiln will be used if the pre-oxidation process is implemented at a smelter already applying the pelletized chromite prereaction process (see discussion in the preceding section), a hypothetical process flow diagram was developed consisting of a rotary kiln and auxiliary equipment. This flow diagram, together with the flow diagram of the current industrially applied prereaction process, is presented in Figure 1. In the chromite pre-oxidation process (Figure 1A), fine chromite ore in the holding silos is fed via weight feeders onto a conveyor that feeds the kiln. Inside the kiln, the ore is oxidized by the thermal energy supplied by pulverized coal and/or furnace off-gas at the discharge end of the kiln. A gas fan at the feed end pulls air through the kiln. The air leaving the kiln is sent to a cyclone to remove coarse particles (<1 mm), and then to a baghouse for removal of finer particles (<30 µm) before being released to the atmosphere (Pšunder, 2012). The pre-oxidized fine chromite ore (OC) is then discharged into a bunker and transported to the prereaction raw material storage heaps. The oxidizing temperature inside the kiln is controlled by measuring the ore discharge temperature with an optical sensor. The pre-oxidized fine chromite ore is then fed as raw material into the prereaction process (Figure 1B), instead of normal chromite ore. The prereaction and smelting process flow (Figure 1B) is not discussed here, since detailed discussions are available elsewhere (Ugwuegbu, 2012; Naiker, 2007; Naiker and Riley, 2006; Botha, 2003). The off-gas produced during SAF smelting is cleaned through a venturi water-scrubbing system and recycled, specifically to the chromite pre-oxidation process, to serve as an energy source.

Methodology

Quantification of process benefits associated with chromite pre-oxidation

From experimental results presented by Kleynhans *et al.*

Techno-economic feasibility of a pre-oxidation process to enhance prereduction

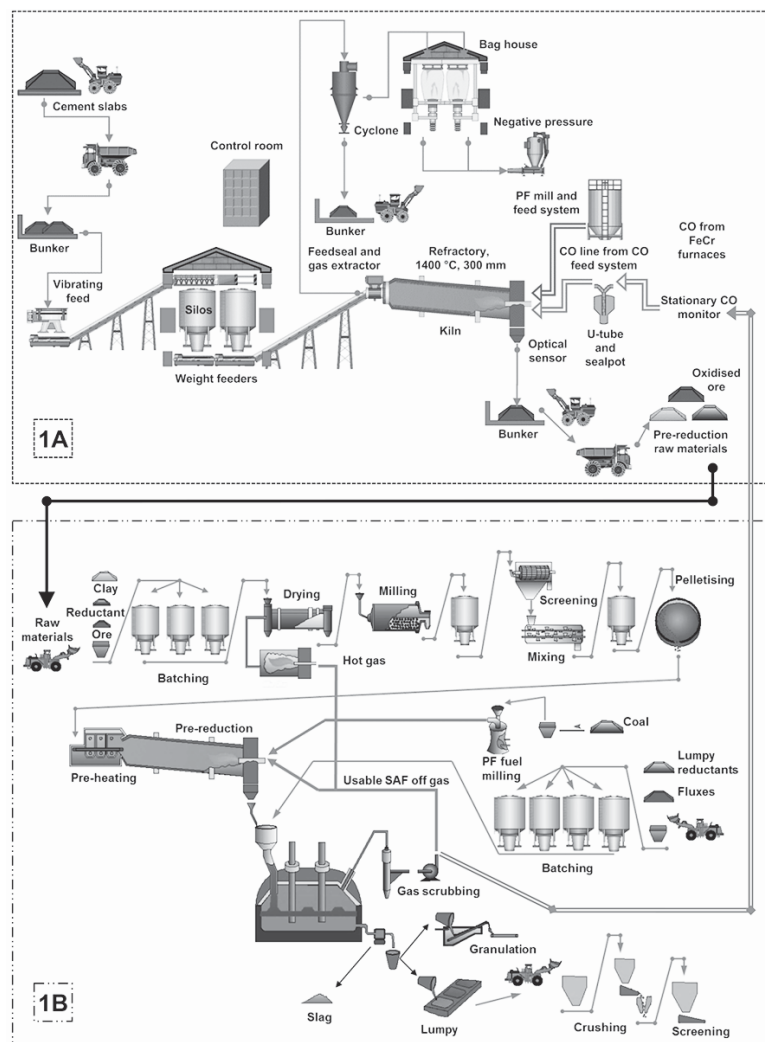


Figure 1—(A) Pre-oxidation process, (B) prereduction process

(2015), it is evident that the level of prereduction could be considerably enhanced through the pre-oxidation of chromite ore prior to prereduction. The advantages of improved prereduction can be observed in several aspects of the operation. However, the main advantages include the decrease in SEC and lumpy carbonaceous reductants required for SAF operation. Niayesh and Fletcher (1986) published a graph of chromite prereduction as a function of SEC, for different temperatures of prereduced feed material.

Kleynhans *et al.* (2015) reconstructed and empirically fitted the data from Niayesh and Fletcher (1986) to estimate the improvement in SEC. They also used the fundamental carbon-based metallization and reduction reactions for chromite presented by Barnes, Finn, and Algie (1983) to calculate the decrease in FC content associated with the lumpy reductants fed into the SAF. The improvements in both the aforementioned parameters, *i.e.* SEC and FC requirement, due to pre-oxidation are illustrated in Figure 2, utilizing the assumption that pre-oxidation of the chromite takes place at 1000°C.

From Figure 2 it is evident that with an increase in prereduction, less FC is required for smelting. Although one could directly calculate the electrical energy financial gain from the improved SEC, annual FeCr production capacity, and

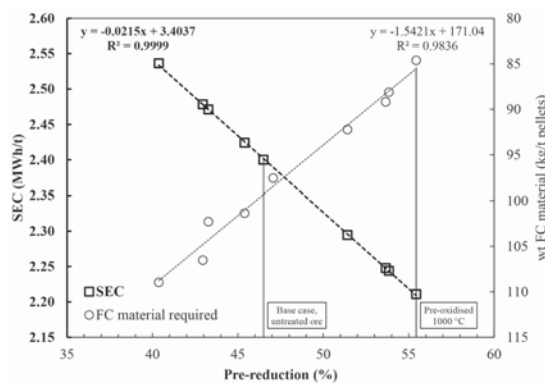


Figure 2—The effect of enhanced prereduction by utilizing pre-oxidized fine chromite ore (x-axis) on the SEC (primary y-axis), as well as on the FC required per ton of prereduced pellets (secondary y-axis) (Kleynhans *et al.*, 2015)

the current price of electricity, this would not be a true reflection of the financial advantage. An electric arc furnace is designed according to a specific apparent power (S). However, only a fraction of this power, called the power factor (K_p), is available as electrical energy for smelting. This

Techno-economic feasibility of a pre-oxidation process to enhance prerelution

total available electrical energy, called the active power (P), is a constant and cannot be changed. The production capacity of an operation is determined by dividing the active power by the SEC. Therefore, since the total energy available cannot be changed, the benefit of improved or lower SEC is realized as an increase in the production capacity. This implies that, as a result of an increase in prerelution levels, for the same total available electrical energy, FeCr production is increased.

Cost distribution

The typical cost factors for the FeCr industry in European conditions were presented by Daavittila, Honkaniemi, and Jokinen (2004). According to Biermann, Cromarty, and Dawson (2012), the cost factors for South African FeCr smelters vary to some extent, with chromite ore, reductants, and electricity each accounting for 30% of the production costs while factors such as maintenance, labour, and waste disposal account for the remaining 10%. An analysis of South African FeCr input costs conducted by Cartman (2008) differed from that of Biermann, Cromarty, and Dawson (2012), with chromite ore accounting for 38%, electricity for 18%, reductants and other raw materials for 24%, and maintenance, overheads, and labour for 20%. The difficulty in interpreting these cost distributions is that in none of these references mentioned the process(es) to which the cost distribution was linked. They could therefore refer to any of the process combinations mentioned in the 'Introduction' section (Beukes, Dawson, and van Zyl, 2010), and the cost distributions for different process combinations will certainly vary. In order to conduct the financial modelling, it was important to consider life-cycle costs associated with the implementation of the chromite pre-oxidation process and the cost distribution of the chromite prerelution smelting operation. Since previously cited FeCr costs estimates (Daavittila, Honkaniemi, and Jokinen, 2004; Biermann, Cromarty, and Dawson, 2012; Cartman, 2008) did not focus specifically on the prerelution process, a life-cycle cost factor breakdown of the chromite pre-oxidation process in combination with the prerelution process was developed, as illustrated in Figure 3.

The life-cycle costs for both the chromite pre-oxidation process and prerelution process were divided into initial development costs (*e.g.* environmental impact assessment, design), capital costs, operating costs, and decommissioning costs, with the operating costs for both processes being subdivided into fixed and variable costs. As mentioned in the previous section, increasing the prerelution level decreases the reductant content required for smelting in the furnace, as well as increasing production capacity with the same total active power. Therefore, from a cost distribution perspective, both the electricity and reductant cost factors (R/t FeCr) are lowered for the prerelution process, while production capacity is increased (refer to previous section). The net result is a decrease in other cost factors, *e.g.* maintenance, labour, waste disposal, and overheads, due to the dilution of fixed costs, and ultimately a decrease in the overall production cost (R/t FeCr).

Discounted cash flow (DCF) analysis

DCF analysis methods are capable of producing a good approximation of the value of a project in order to aid in the

feasibility evaluation process. According to Hitch and Dipple (2012), it is fairly simple to appraise a project in terms of revenue *versus* cost; however, it is imperative to consider the time value of money and the influence that substantial up-front capital costs may have. Pšunder (2012) pointed out that the use of DCF methods for engineering project evaluation has increased significantly in the last few decades. Financial analysis through DCF modelling is currently the most commonly used methodology for appraising potential investments, due to its ability to quantify the added value to shareholders (Hitch and Dipple, 2012). Pšunder and Ferlan (2007) further indicated that net present value (NPV), net present value index (NPVI), internal rate of return (IRR), and modified internal rate of return (MIRR) are some of the most commonly used DCF methods, with NPV and IRR being the most frequently applied. The use of the IRR method is justifiable since it is easy to understand, due to the result being expressed as a percentage rate of return. Furthermore, results can easily be compared between various projects and different forms of investment. The regular use of the NPV method can be justified by the simplicity of the calculation (Pšunder, 2012).

Assumptions

As indicated in the 'Process options' section, it is likely that current FeCr producers utilizing the prerelution process would employ a rotary kiln for chromite pre-oxidation. The input parameters for the combined pre-oxidation and prerelution process (Figure 1) were obtained through

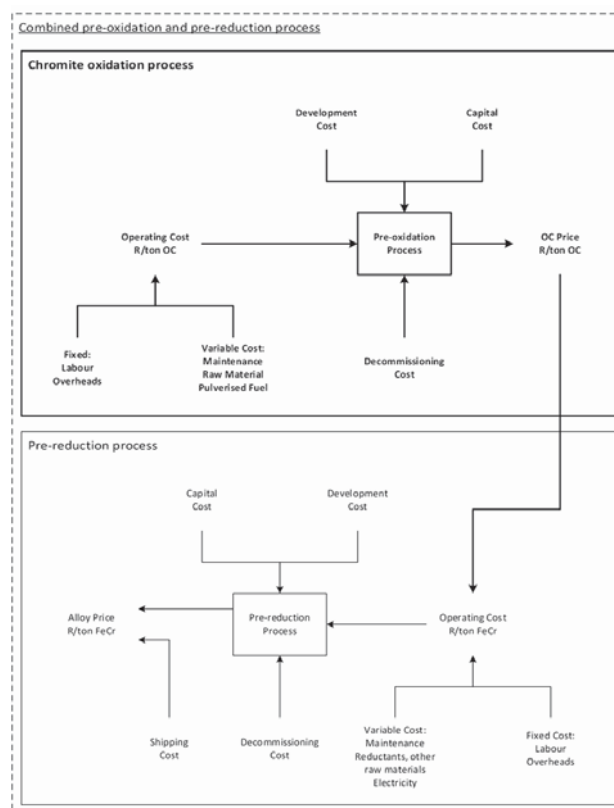


Figure 3—Life-cycle cost factor breakdown of the chromite pre-oxidation process, alone and in combination with the prerelution process

Techno-economic feasibility of a pre-oxidation process to enhance prerelution

personal communications with individuals from a large South African FeCr producer that applies the pelletized chromite prerelution process and from personal experience in the FeCr industry. Capital costs were estimated by the general works project manager responsible for the first- and second-phase development of the largest single-phase FeCr expansion in the world, with both phases employing the prerelution process (Henrico, 2014). The base case input parameters used in this study, based on costs estimated in 2015, are presented in Tables I, II, and III. In the cost modelling, the chromite pre-oxidation (Figure 1A) and prerelution (Figure 1B) processes were kept as separate business units. Figure 4 presents a conceptual flow diagram of the financial model of the combined pre-oxidation and prerelution process (Figure 4A), indicating the effect of chromite pre-oxidation on SEC, lumpy carbonaceous reductant required for furnace smelting, and FeCr production (additional FeCr produced), compared to the prerelution process (Figure 4B). Revenue generated by the chromite pre-oxidation operation was divided into two income streams (Figure 4) – pre-oxidized chromite sales and FeCr production

(increased revenue as a result of the increase in FeCr production capacity). The pre-oxidized chromite sale price is determined from the cost distribution of the prerelution process (Figure 4). The furnace reductant and electricity cost factors per ton FeCr are lowered by utilizing pre-oxidized chromite. A constant prerelution process production cost of R10 000 per ton FeCr was assumed, *i.e.* the same as before exploiting pre-oxidized ore. Therefore, the prerelution process chromite ore cost factor is increased, which sets the pre-oxidized chromite sale price. Using pre-oxidized chromite also results in an increased production capacity. The profit generated by the additional FeCr produced served as the second income stream for the chromite pre-oxidation process.

Sensitivity analysis

Although it is important to correctly approximate the operating and cost parameters of the combined pre-oxidation and prerelution process, these values will invariably change with economic circumstances and advances in research and development. Therefore, sensitivity analysis is essential in determining the overall feasibility of the process. A more

Table I

Base case model input parameters (based on costs estimated in 2015)

Input parameters	Value	Unit
Process availability	90	%/a
Available hours	7 884	h
Furnace capacity	63	MVA
Furnaces	2	-
Power factor	0.879	-
Total available electricity	873 600 000	kWh/a
Electricity price	0.74	R/kWh
R/US\$ exchange rate	10.95	R/US\$
Freight cost* (Wellmer <i>et al.</i> , 2008)	25	US\$/t FeCr
FeCr price (Merafe Resources, 2014)	1.19	US\$/lb Cr contained
Cr content in FeCr produced	50	%
Coke price (Biermann <i>et al.</i> , 2012)	4 000	R/t
Anthracite price (Biermann <i>et al.</i> , 2012)	1 100	R/t
Char price (Biermann <i>et al.</i> , 2012)	900	R/t
*Shipping distance of approx. 8 300 nmi		
Furnace reductant mixture composition:		
Furnace reductant FC content	77.8	wt%
Coke	30	%
Anthracite	20	%
Char	50	%
Prerelution pellet composition:		
Chromite/OC	76.5	wt%
Reducant	20.0	wt%
Reducant FC content	75.0	wt%
Clay binder	3.50	wt%
Prerelution process (with unoxidized chromite):		
FeCr production capacity	364 000	t FeCr/a
Chromite consumption	2.2	t chromite/t FeCr
Prerelution process pellet consumption	2.876	t pellets/t FeCr
Prerelution level	46.50	%
Production cost	10 000.00	R/t FeCr
Combined pre-oxidation and pre-reduction process:		
Prerelution increase	8.50	%
SEC	2 220	kWh/t FeCr
Kiln burner fuel composition	100	% PF
OC kiln PF consumption	0.0627	t PF/t OC
FeCr production capacity	393 523	t FeCr/a
Chromite required	865 751	t chromite/a
OC production	1.014	t OC/t chromite
OC consumption	2.231	t OC/t FeCr
OC produced	877 872	t OC/a
OC prerelution pellet consumption	2.916	t OC pellets/t FeCr
OC prerelution pellets required	1 147 545	t OC pellets/a

Techno-economic feasibility of a pre-oxidation process to enhance prerelution

Table II

Base case pre-oxidized chromite ore production costs (based on costs estimated in 2015)

Fixed costs	Quantity	Unit cost	Cost/t OC produced
Operators	4	R 240 000.00	R 1.09
Maintenance personnel	2	R 540 000.00	R 1.23
PPE	6	R 250.00	R 0.0017
Total			R 2.33
Variable costs	Value	Unit	Cost/t OC produced
Internal transport (moving)	700.00	R/h	R 6.29
Internal transport (loading)	400.00	R/h	R 3.59
Maintenance	5.70	R/t OC	R 5.70
Refractory	0.10	R/t OC	R 0.10
PF	1 038.00	R/t PF	R 65.08
Auxiliary power	0.68	R/t OC	R 0.68
Provident fund for large replacements	0.57	R/t OC	R 0.57
Chromite ore	820.00	R/t Chromite	R 808.68
Total			R 890.69
Grand total			R 893.01

Table III

Base case DCF model input parameters (based on costs estimated in 2015)

Input parameters	Value	Unit
Development phase duration	1	years
Development cost	5	% of total capital cost
Construction phase duration	2	years
Total capital cost:	383 627 322	R
Civils	71 232 000.00	R
Structural	25 446 400.00	R
Plate work	14 660 800.00	R
Mechanical	188 182 400.00	R
Electrical	32 947 376.00	R
Geotechnical studies	1 120 000.00	R
Project contingencies	15	% of capital cost
Plant life	20	years
Depreciation	5 year MACRS	
Decommissioning phase duration	2	years
Decommissioning cost	15	% of total capital cost
Cost escalation factor (inflation rate)	6	%
Benefit escalation factor (FeCr price increase)	6	%
Income tax rate	28	%
Discount rate	10	%

comprehensive understanding of the project economics and viability can be achieved only by evaluating the ranges between extreme levels for the various input parameters. Similar to Hitch and Dipple (2012), sensitivity analysis was first performed on the input parameters for the pre-oxidation process production cost model, since the pre-oxidation process production cost is subsequently required as input to the DCF analysis. This allowed for the examination of deviations from the base case to assess the impact of the various input parameters. The sensitivity of each of these input parameters allowed for a more accurate appraisal of project value and return, as determined through DCF modelling and the corresponding sensitivity analysis.

Financial modelling results and discussion

Base case results

The base case results, consisting of the pre-oxidized chromite

cost margins, the cost distributions of the prerelution process with and without pre-oxidized chromite, and the DCF model outputs, are listed in Table IV. In order to keep the production cost of the prerelution process constant at R10 000 per ton FeCr, as explained in the 'Assumptions' section, the pre-oxidized chromite sales price was determined at R905.28 per ton OC. By employing the pre-oxidation process and utilizing pre-oxidized chromite the cost distributions of furnace electricity and reductants were reduced from 17.76% and 6.87% to 16.43% and 6.04%, respectively. By applying the method used by Kleynhans *et al.* (2012) to convert improvements in electrical energy utilization to financial gains, the reduction in the furnace electricity cost distribution translated to approximately R48.5 million per annum for a 364 000 t/a prerelution process. The financial gain associated with the decrease of the furnace reductant cost distribution (Figure 2) translates to approximately R30 million per annum for the 364 000 t/a prerelution process.

Techno-economic feasibility of a pre-oxidation process to enhance prereduction

Table IV

Base case results

Parameter	Value	Unit
<i>Oxidized chromite production</i>		
Oxidized chromite production cost	893.01	R/t OC
Oxidized chromite price	905.28	R/t OC
FeCr production increase	29 523	t FeCr/a
<i>Cost distribution</i>		
Production cost (PR process)	10 000.00	R/t FeCr
<i>PR process using chromite</i>		
Chromite ore	1 804.00	R/t FeCr
Electricity	1 776.00	R/t FeCr
Furnace reductants	686.62	R/t FeCr
Other production costs	5 733.38	R/t FeCr
<i>PR process using OC</i>		
OC ore	2 019.50	R/t FeCr
Electricity	1 642.76	R/t FeCr
Furnace reductants	604.35	R/t FeCr
Other production costs	5 733.38	R/t FeCr
NPV (after tax)	R 894 489 279.24	
IRR (after tax)	30.5%	
Profitability index (after tax)	2.88	
Simple payback	3 years 0 months 16 days	
Discounted payback	4 years 0 months 11 days	

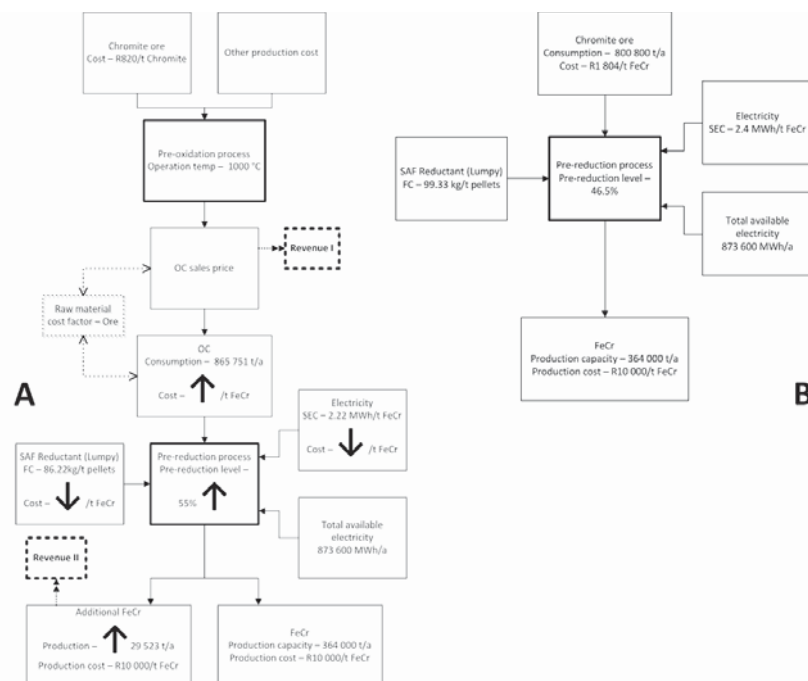


Figure 4—Conceptual flow diagram of the financial model for the combined pre-oxidation and prereduction process (A), indicating the influence of chromite pre-oxidation on SEC, lumpy carbonaceous reductant requirement for furnace smelting, and FeCr production (additional FeCr produced), the determination of the OC sales price, and the pre-oxidation process revenue streams (I and II), compared to the prereduction process (B)

It is therefore evident that applying this process has financial advantages.

Although not investigated in this study, another cost benefit resulting from employing the pre-oxidation process is the dilution of fixed costs. The large increase in production capacity effectively ensures a reduced impact of fixed cost, with the fixed cost increasing only slightly. For a pre-oxidized chromite production cost of R893.01 per ton OC and a FeCr production increase of 29 523 t/a, the DCF model yielded an NPV of approximately R895 million with an IRR of

30.5% and a profitability index (PI) of 2.88 after tax. This significantly positive base case NPV, with the IRR approximately three times greater than the 10% discount rate and PI approximately three times higher than unity, suggests that integrating the pre-oxidation process and utilizing pre-oxidized ore may be a potentially feasible development option from a project economics standpoint.

In order to put these results into perspective, it would be beneficial to compare the NPV and IRR to other reasonable values within the industry. However, economic feasibility

Techno-economic feasibility of a pre-oxidation process to enhance prerelution

results of smaller expansion or process improvement projects are not readily available in the peer-reviewed scientific domain, since the publication of such results could potentially erode the strategic advantage of the developing company. Development of the Ring of Fire, a large mineral resource-rich area of approximately 5 120 km² located in Canada's Northern Ontario region, can be considered as a recent example. Based on current projections, the chromite deposit is significant enough to sustain North American activity for a century (OCC, 2014). KWG Resources of Montreal, Canada released the preliminary economic assessment (PEA) study for the Big Daddy chromite deposit in the Ring of Fire in 2011. The PEA examined an open-pit mine, crushing plant, site infrastructure as well as development of a railway and power line to the site. Pre-production capital expenses were estimated to be around US\$784 million, which included half of the \$900 million cost of the railway, to establish an 8 000 t/d operation with a 16-year life. At a 2011 exchange rate of approximately R7 per US dollar, the capital cost to develop the Big Daddy chromite deposit amounts to approximately R5.5 billion. The Big Daddy project's undiscounted gross revenue was appraised at approximately \$12.6 billion. The after-tax evaluation estimated the NPV to be approximately \$1.6 billion at an 8% discount rate, or approximately \$1.25 billion at a 10% discount rate. The after-tax internal rate of return calculated to approximately 31.8%, resulting in a pre-tax payback period of 2.5 years (CMJ, 2011; KWG Resources, 2011).

Although the NPV and IRR look promising, it is necessary to keep in mind that this investigation is conceptual in nature and that there is an inherent uncertainty surrounding some model input parameters. Intrinsically, sensitivity analysis allowed for a more in-depth investigation of the influences of some uncertainties on the overall project appraisal, which are discussed in the following sections.

Cost sensitivity of the pre-oxidation process in isolation

The overall sensitivity of the pre-oxidized chromite production cost parameters for the pre-oxidation process, consisting of a spider plot showing parameter sensitivity and a table ranking these parameters from most to least sensitive, is presented in Figure 5. The spider plot offers a comparative representation of the sensitivity of the pre-oxidized chromite production cost model elements. Input elements with the sharpest gradients represent the parameters with the greatest impact per unit of change from the base case, as denoted by the x-axis with the base case value set at zero.

The most sensitive parameter defined through sensitivity analysis, if the pre-oxidized chromite process production cost was considered in isolation, was chromite ore cost. This is easily explained since (i) the pre-oxidation process section was considered as a separate economic component in the financial cost model to determine the oxidized chromite production cost and selling price, and (ii) approximately 90.5% of the total pre-oxidized chromite production cost is allocated to the cost of obtaining chromite ore. PF cost and PF composition were jointly the second most sensitive parameters. The cost of PF accounts for approximately 7.3% of the total pre-oxidized chromite production cost. The percentage change from the base case for the PF composition in Figure 5 is only indicated as a negative change, which can

be attributed to the kiln being operated only on PF in the base case scenario. The cost contribution of the PF to the total chromite pre-oxidizing production cost can, however, be significantly reduced if a mixture of PF and CO off-gas, or exclusively CO from the closed SAF, can be used. The use of CO off-gas in the prerelution kiln is not completely effective, since temperatures higher than 1250°C are required. Although the adiabatic flame temperature of CO gas is high enough (du Preez *et al.*, 2015; Niemelä *et al.*, 2004), it has been found in practice that PF fuel has a deeper penetrating flame. Prerelution kilns are also long (60–80 m) to ensure the required retention time of approximately 3 hours for effective prerelution. Consequently, the fuel utilized needs to be able to penetrate deep into the kiln for effective heat transfer and to maximize the area with a temperature higher than 1250°C. It will, however, be possible to use CO off-gas in the chromite pre-oxidation process since a lower temperature (1000°C) and shorter retention time (1 hour) are required, which implies a shorter kiln. The remaining pre-oxidized chromite production cost parameters account for less than 2.2% of the total production cost, and therefore, in terms of sensitivity, these parameters had minimal impact.

The prerelution level was also considered since it has an impact on the pre-oxidized chromite required for the prerelution process. If the prerelution level decreases from the base case, the FeCr production capacity also decreases, resulting in a decrease in the pre-oxidized chromite requirement. This will result in an increase in the production cost per ton of pre-oxidized chromite. The opposite would occur if the prerelution level increases. However, the sensitivity to the prerelution level was minimal, since it is approximately a 130 times less sensitive than chromite cost.

Cost sensitivity of the pre-oxidation process integrated with the pelletized prerelution process

Spider plot diagrams showing parameter sensitivity relating to the NPV and IRR, with a tabular ranking of these

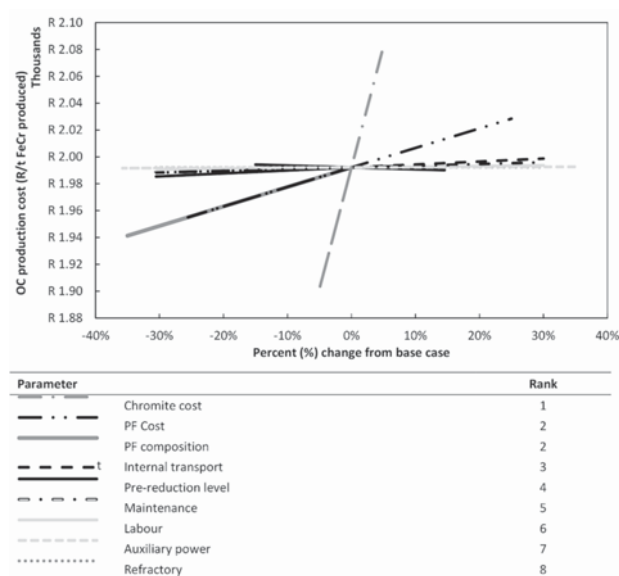


Figure 5—Overall sensitivity of pre-oxidized chromite production cost parameters

Techno-economic feasibility of a pre-oxidation process to enhance prerelution

parameters from most to least sensitive, are presented in Figure 6 in order to illustrate the overall sensitivity of the DCF model designed for the integrated pre-oxidation and prerelution process.

Although the level of prerelution was relatively insensitive with regard to the pre-oxidation process production cost, it was found to be the most sensitive parameter in determining both the NPV and IRR. The level of prerelution, accounting for approximately 34.9% of the overall DCF sensitivity, is approximately two times more sensitive than the parameter ranked second for both the NPV and IRR. The level of prerelution primarily affects the FeCr production capacity, which in turn has an effect on the pre-oxidized chromite requirement. As a result, the level of prerelution has an effect on the chromite pre-oxidation process revenue streams (Figure 4) and consequently on the operation's cash flow. Chromite cost, the second most sensitive parameter, accounted for approximately 18.3% of the overall DCF sensitivity. Four parameters – the benefit escalation factor, Cr content of FeCr, FeCr price, and cost escalation factor – could be grouped together for each, accounting for between approximately 9% and 12% of the overall DCF sensitivity. An interesting observation is that the order of importance for these four parameters was dissimilar for the NPV and IRR. Nevertheless, these cost or price parameters have significant implications for overall project feasibility by directly controlling the total available revenue from the two income streams. Specifically, significant increases in the cost of chromite and factors that adversely influence the FeCr price and income from FeCr sales will imply an inadequate source of revenue in order to offset the

associated costs. It is interesting to note that the total capital cost is the seventh most sensitive parameter for the IRR and the eighth most sensitive for NPV. It was originally assumed that the capital cost would have a bigger influence on project appraisal as a result of the front-loaded nature of the cash flows. However, it does not have a considerable impact on project valuation. The capital cost necessary for funding may have a more dramatic impact on the ability to secure project financing, either through debt or equity. Although this does not necessarily affect project valuation, it may have an impact on project feasibility in determining the ability to generate funding for construction. Factors of less significant influence include the discount rate, income tax rate, project contingencies, decommissioning cost, as well as freight and development costs. The significance and contribution of each of the individual parameters investigated through this research cannot be ignored. However, their ranking in terms of sensitivity has provided a means by which further research can be prioritized, and efforts can be focused on parameters that will result in the greatest influence on project valuation.

Conclusions

It was recently proven that pre-oxidation of fine chromite ore, prior to pelletized prerelution, significantly decreases the SEC and lumpy carbonaceous reductants required for furnace smelting. In this paper, we presented an analysis of the techno-economic feasibility of integrating chromite pre-oxidation into the currently applied pelletized prerelution process as a pretreatment method. South Africa's FeCr industry provided the ideal backdrop conditions against which the techno-economic feasibility of implementing such a process could be evaluated. Through the conceptualization of the pre-oxidation process route, it became evident that FeCr producers currently utilizing the prerelution process would most likely opt to employ an operation with a rotary kiln at its core to conduct chromite pre-oxidation. Chromite pre-oxidation at the optimum temperature of 1000°C translated to an increase in the level of achievable chromite prerelution of approximately 8.5% (from 46.5% to 55.5%), approximately 8.3% improvement in the SEC (from 2.4 to 2.2 MWh/t), and a decrease of approximately 14% (from 99.5% to 85.5 kg/t pellets) in the amount of lumpy carbonaceous material required during SAF smelting. In order to more accurately approximate input costs for further life-cycle financial modelling, a comprehensive estimate of the costs associated with pre-oxidizing the fine chromite ore was determined. The life-cycle financial model, which was built on a DCF approach, generated a base case NPV of approximately R895 million and an IRR of approximately 30.5% after tax. This strongly indicates that integration of the chromite pre-oxidation process into the currently applied prerelution process may be viable from a financial perspective. Sensitivity analysis of the pre-oxidation process in isolation indicated that the most influential parameter was chromite ore cost, whereas if the pre-oxidation process was integrated with the pelletized prerelution process, the most influential parameter was found to be the level of prerelution. The level of achievable prerelution is interrelated with the pre-oxidation temperature, which implies that the capability of maintaining the optimum pre-oxidation temperature is of critical importance.

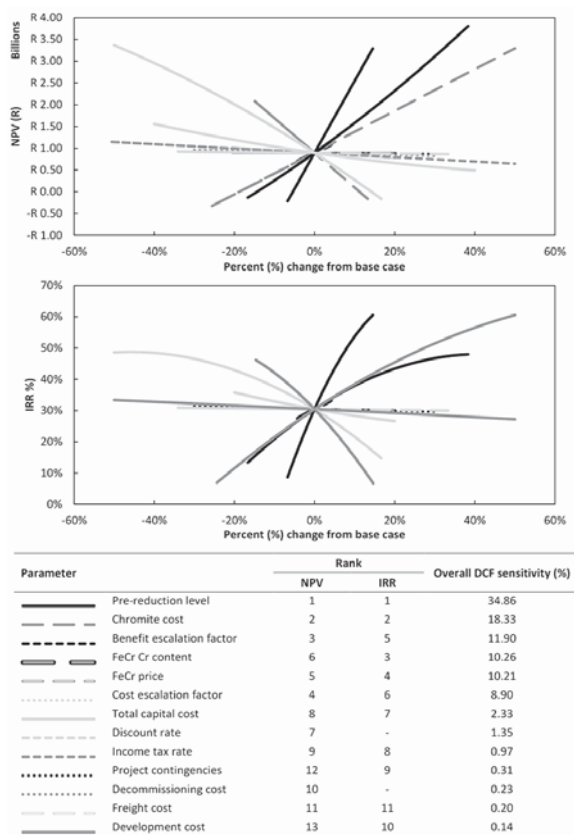


Figure 6—Overall sensitivity of the DCF model

Techno-economic feasibility of a pre-oxidation process to enhance prereduction

Acknowledgements

The authors would like to thank Glencore Alloys for technical assistance.

References

- BARNES, A.R., FINN, C.W.P., and ALGIE, S.H. 1983. The prereduction and smelting of chromite concentrate of low chromium-to-iron ratio. *Journal of the South African Institute of Mining and Metallurgy*, vol. 83 (March). pp. 49–54.
- BASSON, J., CURR, T.R., and GERICKE, W.A. 2007. South Africa's ferro alloys industry – present status and future outlook. *Proceedings of the 11th International Ferro Alloys Conference (INFACON XI)*. Das, R.K. and Sundaresan, T.S. (eds). Indian Ferro Alloys Producers Association, New Delhi. pp. 3–24.
- BEUKES, J.P., VAN ZYL, P.G., and NEIZEL, B.W. 2015. Process for enhanced pre-reduction of chromite. PCT/IB2013/056313. North-West University.
- BEUKES, J.P., VAN ZYL, P.G., and RAS, M. 2012. Treatment of Cr(VI)-containing wastes in the South African ferrochrome industry - a review of currently applied methods. *Journal of the Southern African Institute of Mining and Metallurgy*, vol. 112, no. 5. pp. 347–352.
- BEUKES, J.P., DAWSON, N.F., and VAN ZYL, P.G. 2010. Theoretical and practical aspects of Cr(VI) in the South African ferrochrome industry. *Journal of the Southern African Institute of Mining and Metallurgy*, vol. 110, no. 12. pp. 743–750.
- BIERMANN, W., CROMARTY, R.D., and DAWSON, N.F. 2012. Economic modelling of a ferrochrome furnace. *Journal of the Southern African Institute of Mining and Metallurgy*, vol. 112, no. 4. pp. 301–308.
- BOTHA, W. 2003. Ferrochrome production through the SRC process at Xstrata, Lydenburg Works. *Journal of the South African Institute of Mining and Metallurgy*, vol. 103, no. 6. pp. 373–389.
- CARTMAN, A. 2008. An analysis of ferrochrome input costs. *Proceedings of the Metal Bulletin Special and Stainless Steel Summit*. http://hatch.ca/Mining_Metals/Iron_Steel/Articles/documents/analysis_ferrochrome_input_costs.pdf [accessed 30 Jan. 2015].
- CMJ. 2011. Chromite study: Big Daddy headed for feasibility. <http://www.canadianminingjournal.com/news/chromite-study-big-daddy-headed-for-feasibility/> [accessed 22 Nov. 2015].
- CRAMER, L.A., BASSON, J., and NELSON, L.R. 2004. The impact of platinum production from UG2 ore on ferrochrome production in South Africa. *Journal of the South African Institute of Mining and Metallurgy*, vol. 104, no. 9. pp. 517–527.
- CREAMER, M. 2013. South Africa's raw chrome exports soar as ferrochrome edge is lost. *Mining Weekly*. <http://www.miningweekly.com/article/south-africas-raw-chrome-exports-soar-as-ferrochrome-edge-is-lost-2013-09-20> [accessed 15 Jan. 2014].
- DAAVITILA, J., HONKANIEMI, M., and JOKINEN, P. 2004. The transformation of ferrochromium smelting technologies during the last decades. *Journal of the South African Institute of Mining and Metallurgy*, vol. 104, no. 10. pp. 541–549.
- DENTON, G.M., BENNIE, J.P.W., and DE JONG, A. 2004. An improved DC-arc process for chromite smelting. *Proceedings of the 10th International Ferroalloys Congress (INFACON X)*. South African Institute of Mining and Metallurgy, Johannesburg. pp. 60–67.
- DU PREEZ, S.P., BEUKES, J.P., and VAN ZYL, P.G. 2015. Cr(VI) generation during flaring of CO-rich off-gas from closed ferrochromium submerged arc furnaces. *Metallurgical and Materials Transactions B*, vol. 46B (April). pp. 1002–1010. DOI: 10.1007/s11663-014-0244-3
- DWARAPUDI, S., TATHAVADKAR, V., RAO, B.C., KUMAR, T.K.S., GHOSH, T.K., and DENYS, M. 2013. Development of cold bonded chromite pellets for ferrochrome production in submerged arc furnace. *ISIJ International*, vol. 53, no. 1. pp. 9–17. DOI: 10.2355/isijinternational.53.9
- ESKOM. 2012. Eskom retail tariff adjustment for 2012/2013. <http://www.eskom.co.za/c/article/816/home/> [accessed 7 Oct. 2012].
- GLASTONBURY, R.I., BEUKES, J.P., VAN ZYL, P.G., SADIQI, L.N., JORDAN, A., CAMPBELL, Q.P., STEWART, H.M., and DAWSON, N.F. 2015. Comparison of physical properties of oxidative sintered pellets produced with UG2 or metallurgical grade South African chromite: a case study. *Journal of the Southern African Institute of Mining and Metallurgy*, vol. 115, no. 8. pp. 699–706. DOI: 10.17159/2411-9717/2015/v115n8a6
- GLASTONBURY, R.I., VAN DER MERWE, W., BEUKES, J.P., VAN ZYL, P.G., LACHMANN, G., STEENKAMP, C.J.H., DAWSON, N.F., and STEWART, H.M. 2010. Cr(VI) generation during sample preparation of solid samples – A chromite ore case study. *Water SA*, vol. 36, no. 1. pp. 105–110. DOI: 10.4314/wsa.v36i1.50913
- GOEL, R.P. 1997. Smelting technologies for ferrochromium production - recent trends. *Ferro Alloy Industries in the Liberalised Economy*. Vaish, A.K., Singh, S.D., Goswami, N.G., and Ramachandrarao, P. (eds). National Metallurgical Laboratory (NML), Jamshedpur, India.
- HENRICO, M. 2014. RE: De Oude Werf. Personal Communication, 25 September 2014. Glencore Alloys, Middelburg, Mpumalanga, South Africa.
- HITCH, M. and DIPPLE, G.M. 2012. Economic feasibility and sensitivity analysis of integrating industrial-scale mineral carbonation into mining operations. *Minerals Engineering*, vol. 39. pp. 268–275. DOI: 10.1016/j.mineng.2012.07.007
- HOLAPPA, L. 2010. Towards sustainability in ferroalloys production. *Proceedings of the 12th International Ferroalloys Congress (INFACON XII)*, Helsinki, Finland. Vartiainen, A. (ed.). Outotec Oyj. pp. 1–10.
- ICDA. 2013a. Energy update - November 2013. International Chromium Development Association, Paris, France. http://dev.icdacr.com/index.php?option=com_content&view=article&id=617&Itemid=590&lang=en [accessed 14 Sept. 2015].
- ICDA. 2013b. Statistical Bulletin 2013. International Chromium Development Association, Paris, France.
- JONES, R.T. 2015. Pyrometallurgy in Southern Africa - list of Southern African smelters. <http://www.pyrometallurgy.co.za/PyroSA/index.htm> [accessed 14 Sept. 2015].
- KAPURE, G., TATHAVADKAR, V., RAO, C.B., RAO, S.M., and RAJU, K.S. 2010. Coal based direct reduction of preoxidized chromite ore at high temperature. *Proceedings of the 12th International Ferroalloys Congress (INFACON XII)*, Helsinki, Finland. Vartiainen, A. (ed.). Outotec Oyj. pp. 293–301.
- KLEYNHANS, E.L.J., BEUKES, J.P., VAN ZYL, P.G., KESTENS, P.H.I., and LANGA, J.M. 2012. Unique challenges of clay binders in a pelletised chromite pre-reduction process. *Minerals Engineering*, vol. 34. pp. 55–62. DOI: 10.1016/j.mineng.2012.03.021
- KLEYNHANS, E.L.J., NEIZEL, B.W., BEUKES, J.P., and VAN ZYL, P.G. 2016. Utilisation of pre-oxidised ore in the pelletised chromite pre-reduction process. *Minerals Engineering*, vol. 92. pp. 114–124. DOI: 10.1016/j.Mineng.2016.03.005
- KWG Resources. 2011. Daddy chromite deposits. http://www.kwgresources.com/_resources/corp_presentations/corporate_presentation.pdf [accessed 22 Nov. 2015].
- LUCKOS, A., DENTON, G., and DEN HOED, P. 2007. Current and potential applications of fluid-bed technology in the ferroalloy industry. *Proceedings of the 11th International Ferroalloys Congress (INFACON XI)*. Das, R.K. and Sundaresan, T.S. (eds). Indian Ferro Alloys Producers Association, New Delhi. pp. 123–132.
- MCCULLOUGH, S., HOCKADAY, S., JOHNSON, C. and BARCZA, N.A. 2010. Pre-reduction and smelting characteristics of Kazakhstan ore samples. *Proceedings of the 12th International Ferroalloys Congress (INFACON XII)*, Helsinki, Finland. Vartiainen, A. (ed.). Outotec Oyj. pp. 249–262.
- MERAFFE RESOURCES. 2014. Third quarter 2014 ferrochrome price announcement. http://www.overend.co.za/download/third_quarter_2014_30072014.pdf [accessed 3 Mar. 2016].
- MERAFFE RESOURCES. 2012. Maximising South Africa's chrome ore endowment to create jobs and drive sustainable growth. http://www.meraferesources.co.za/pdf/presentations/2012/chrome_ore_brochure.pdf [accessed 14 Jan. 2014].
- MOHALE, G.T.M. 2014. SEM image processing as an alternative method to determine chromite pre-reduction. MSc (Chemical Engineering) dissertation, North-West University, South Africa.
- MURTHY, Y.R., TRIPATHY, S.K., and KUMAR, C.R. 2011. Chrome ore beneficiation challenges & opportunities – A review. *Minerals Engineering*, vol. 24, no. 5. pp. 375–380. DOI: 10.1016/j.mineng.2010.12.001
- NAIKER, O. 2007. The development and advantages of Xstrata's Premus Process. *Proceedings of the 11th International Ferroalloys Congress (INFACON XI)*. New Delhi, India. Das, R.K. and Sundaresan, T.S. (eds). Indian Ferro Alloys Producers Association. pp. 112–119.
- NAIKER, O. and RILEY, T. 2006. Xstrata alloys in the profile. *Proceedings of South African Pyrometallurgy 2006*. Southern African Institute of Mining and Metallurgy, Johannesburg. pp. 297–306.
- NEIZEL, B.W., BEUKES, J.P., VAN ZYL, P.G., and DAWSON, N.F. 2013. Why is CaCO₃ not used as an additive in the pelletised chromite pre-reduction process? *Minerals Engineering*, vol. 45. pp. 115–120. DOI: 10.1016/j.mineng.2013.02.015
- NIAYESH, M.J. and FLETCHER, G.W. 1986. An assessment of smelting reduction processes in the production of Fe-Cr-C alloys. *Proceedings of the 4th International Ferroalloys Congress (INFACON IV)*, São Paulo, Brazil. pp. 115–123.
- NIEMELÄ, P., KROGERUS, H., and OIKARINEN, P. 2004. Formation, characterisation and utilisation of CO₂-gas formed in ferrochrome smelting. *Proceedings of the 10th International Ferroalloys Congress (INFACON X)*. South African Institute of Mining and Metallurgy, Johannesburg. pp. 68–77.
- OCC. 2014. Beneath the surface - uncovering the economic potential of Ontario's Ring of Fire. Ontario Chamber of Commerce, Ontario, Canada.
- PAN, X. 2013. Effect of South Africa chrome ores on ferrochrome production. *Proceedings of the International Conference on Mining, Mineral Processing and Metallurgical Engineering (ICMME2013)* Johannesburg, South Africa, 5–16 April 2013.
- PSUNDER, I. 2012. Use of discounted cash flow methods for evaluation of engineering projects. *Mechanical Engineering*. Gokcek, M. (ed.). InTech, Rijeka, Croatia.
- PSUNDER, I. and FERLAN, N. 2007. Analysis of the knowledge and the use of investment project evaluation methods in the field of mechanical engineering. *Journal of Mechanical Engineering*, vol. 53, no. 9. pp. 569–581.
- SLATTER, D.D. 1995. Technological trends in chromium unit production and supply. *Proceedings of the 7th International Ferroalloys Congress (INFACON VII)*, Trondheim, Norway. Tveit, H., Tusset, J.K., and Page, I.G. (eds). Norwegian Ferroalloy Producers Research Organization (FFF). pp. 249–262.
- UGWUEGBU, C. 2012. Technology innovations in the smelting of chromite ore. *Innovative Systems Design and Engineering*, vol. 3, no. 12. pp. 48–55.
- Wellmer, F.-W., Dalheimer, M., and Wagner, M. 2008. Calculation of Cost Data. Economic Evaluations in Exploration. Springer, Berlin/Heidelberg. p. 249.



Numerical and physical modelling of tundish slag entrainment in the steelmaking process

by A. Mabentsela*, G. Akdogan*, and S. Bradshaw*

Synopsis

Physical and numerical modelling methods were followed to identify mechanism(s) for tundish slag entrainment in a bare tundish and one with a flow control device (FCD).

The physical and numerical models made use of water and paraffin to model steel and slag respectively. Observations from the physical model showed that the steel-slag interface remains immobile in both cases. Entrained paraffin formed droplets approximately 1 mm in diameter. Results from both models (numerical and physical) showed that in both cases (bare and FCD case), areas of high entrained slag concentration exist near the inlet region. The entrained slag concentration decreases towards the tundish endwalls.

Flow patterns and velocities tangential to the steel-slag interface from the numerical model showed that slag entrainment in both the bare tundish and tundish with a FCD possibly takes place via two mechanisms. First, the slag moves across the steel-slag interface via mass transfer; secondly small velocities tangential to the interface at depths greater than 10 mm below the interface carry the already 'entrained' slag into the bulk steel phase. These tangential flow patterns are dominant in the inlet region, hence the high concentration of entrained slag in this region.

Keywords

tundish slag entrainment, tundish slag behaviour, numerical modelling, slag shearing.

Introduction

The tundish serves as the last metallurgical vessel through which steel passes before solidifying in the moulds. It is in the tundish that the last traces of non-metallic inclusions should be removed, otherwise the inclusions carry over to the moulds and cause defects in the steel product. In the tundish, the slag is less dense than the melt and thus resides on the top of the melt. The slag provides a sink into which the non-metallic inclusions float to and dissolve. The slag also protects the melt from air and heat loss. However, when slag is entrained in the melt as a result of increased turbulence or shearing at the steel-slag interface, slag can become a source of non-metallic inclusions.

Numerous studies on flow patterns in the tundish have been carried out since the introduction of the tundish. These studies were aimed at improving the flow characteristics in the tundish (Chattopadhyay, Isac, and Guthri, 2010; Cloete, 2014; Jha, Dash, and Kumar, 2001; Jha, Rao, and Dewan, 2008;

Kumar, Koria, and Mazumdar, 2007; Kumar, Mazumdar, and Koria, 2008; Mazumdar and Guthri, 1999; Sahai and Emi, 1996; Sahai and Burval, 1992; Tripathi and Ajmani, 2011). These studies have led to the use of flow control devices (FCDs) to increase the melt residence time in the tundish and provide surface-directed flow so as to assist with inclusion removal. FCDs include dams, weirs, baffles, and turbulence inhibitors. It is now generally understood that any tundish without a FCD suffers from poor inclusion removal as a result of too short a melt residence time in the tundish (Mazumdar and Guthri, 1999).

Due to the opaqueness of the steel melt and the elevated operating temperature (1600°C) in the tundish, the abovementioned studies were carried out using a combination of physical models, otherwise known as 'cold models', and numerical models. Physical models involve the use of reduced-scale water models where water is used to represent the steel melt. Numerical models involve using computational fluid dynamics packages to model the melt flow in the tundish. When used together, the physical model can be used to verify numerical model results. Once verified, the numerical model can then be adapted without the need of a physical model. This significantly reduces the costs of exploring new designs and also saves time.

The flow behaviour studies that have led to the use of FCDs were done using both physical and numerical models. In most of these studies, the researchers were only concerned with the melt phase, *i.e.* how the FCD affects the melt residence time. Most researchers opted to use only water in their physical and numerical models (Chattopadhyay, Isac, and Guthri, 2010; Cloete, 2014; Kumar, Mazumdar,

* Department of Process Engineering, Stellenbosch University, Stellenbosch, Cape Town, South Africa.

© The Southern African Institute of Mining and Metallurgy, 2017. ISSN 2225-6253. Paper received Aug. 2016; revised paper received Nov. 2016.

Numerical and physical modelling of tundish slag entrainment

and Koria, 2008; Mazumdar and Guthri, 1999; Sahai and Emi, 2008). As a result there is little or no information on how the FCDs affect the slag layer. This is evident in the lack of mentions of slag entrainment as a result of the use of FCDs in the review of two decades of work (1979 to 1999) by Mazumdar and Guthri (1999). In a more recent review of work on tundish technology from 1989 to 2009, Chattopadhyay, Isac, and Guthri (2010) noted the lack of research on how FCDs affect the slag phase, and pointed out the lack of both physical and numerical models to predict tundish slag entrainment. There is, therefore, a general lack of understanding on how tundish slag is entrained and how FCDs affect the slag layer.

Following from the above, the purpose of this study was to numerically and physically investigate tundish slag behaviour in a bare tundish and a tundish with a FCD device.

The objectives of this study are to:

- Use physical modelling techniques to study the behaviour of tundish slag in a bare tundish and in a tundish with a FCD
- Develop a numerical model that can predict tundish slag behaviour in both a bare tundish and a tundish with a FCD
- Identify, using the physical model and the numerical model, a mechanism (or mechanisms) for slag entrainment in a bare tundish and a tundish with a FCD
- Make recommendations based on the findings.

Slag entrainment mechanism

Entrainment of tundish slag into the steel melt can occur via vortexing, high-velocity flow that shears the slag at the slag-steel interface, and turbulence at the slag-steel interface (Hagemann *et al.*, 2013).

Apart from high velocities at the interface, some authors have reported slag entrainment in slow steel melt velocity zones. This is thought to be caused by Kelvin-Helmholtz instability, which arises when two streams of fluid with different densities flow past one another. The presence of shear stress leads to instability, which causes the growth of waves which later roll into small vortices (Solhed and Jonsson, 2003). Slag entrainment can also occur as a result of Marangoni flow or by mass transfer across the interface. In Marangoni flow, the slag movement into the steel phase and *vice versa* is caused by local gradients of the interfacial tension caused by chemical reactions (Hagemann *et al.*, 2013), while in the mass transfer method, slag and steel move across the interface due to low concentrations of the two fluids across the interface.

- **Vortexing**—Nagaoka *et al.* (1986) studied the effect of bath level on slag entrainment via vortex formation. They concluded that vortexing occurs during melt transfer to the mould when the bath level inside the tundish is low. Vortexing can therefore be controlled by controlling the bath level in the tundish. It is well known in the steelmaking industry that melt transfer during low bath level causes vortex formation, which leads to slag carrying over to the mould
- **Shearing**—Entrainment of a lighter phase into a heavy phase via shearing starts with finger-like protrusions

of the lighter phase into the heavy phase. This fingering phenomenon can be described in terms of Taylor-Saffman instability, which occurs when a fluid of different density and viscosity relative to the second fluid pushes down on the second fluid. Feldabauer and Cramb, (1995) studied the entrainment of slag in the casting mould using Taylor-Saffman instability. They commented that the instability depended on interfacial tension, viscosity, and inertial energy exerted by the denser phase. The actual entrainment at the tip of a less dense protrusion into the denser phase is a function of the deforming stress exerted by the denser phase and the counteracting interfacial tension between both phases. The detachment of a droplet of the 'lighter' phase into the 'heavier' phase was further studied in a Couette device and four rollers, where the density ratio of the two fluids was unity ($\rho_{\text{heavy}}/\rho_{\text{lighter}}$). The detachment of the lighter fluid into the heavier fluid was found to be a function of the viscosity ratios of the fluids used ($\eta_{\text{heavy}}/\eta_{\text{lighter}}$) and the dimensionless critical number, known as the critical capillary number (Hagemann *et al.*, 2013). Hagemann *et al.* extended this research by studying the effect of the kinematic viscosity ratio of the two fluids ($\nu_{\text{higher}}/\nu_{\text{heavy}}$) on the critical capillary number (Ca^*). They used a water model with a rotating roller to generate shear stress at the interface. Different silicon oils were used to represent the slag layer. In their studies the following definitions applied.

$$Ca = \frac{V_2 \eta_2}{\sigma} \quad [1]$$

$$Ca^* = f(\frac{\nu_1}{\nu_2}) \quad [2]$$

where V_2 is the tangential velocity of the heavier phase below the interface, η_2 the molecular viscosity of the heavier phase, σ the interfacial tension between the two phases, ν_1 the kinematic viscosity of the lighter phase, and ν_2 the kinematic viscosity of the heavier phase. Hagemann *et al.* (2013) showed that the critical capillary number for slag entrainment is a function of the ratios of kinematic viscosities, given by:

$$Ca^* = 3 \times 10^{-6} \left(\frac{\nu_1}{\nu_2} \right) + 2.8 \times 10^{-3} \quad [3]$$

According to the above equation, increasing the ratio of kinematic viscosities of a system should raise the critical capillary number and thus reduce the chances of entrainment. If the capillary number of the system, calculated by Equation [1], is below the critical capillary number of that particular system no entrainment of slag will occur.

Hagemann *et al.* (2013) went on to study the effect of the slag layer thickness on the critical capillary number needed for slag entrainment to occur via shearing. They found that the slag layer thickness has no effect on the entrainment of slag resulting from shear stress at the interface.

A numerical study by Solhed, Jonsson, and Jonsson (2008) showed that slag entrainment in a one-strand bare tundish was caused by shearing at the interface.

Numerical and physical modelling of tundish slag entrainment

They commented that shearing was caused by a recirculating flow in the inlet region. They also showed that the highest entrained slag concentration was in the region behind the inlet. However, Solhed, Jonsson, and Jonsson (2008) did not do any mathematical investigation to establish which of the mechanisms identified above was responsible for the slag entrainment they noted.

Moreover, they did not consider FCDs and their effect on slag entrainment.

Harman and Cramb (1996) studied the size of the entrained slag droplets formed via shearing of the slag layer, using a water model. They noted that the first entrained slag droplet is the largest. They noted that the size of this droplet can be estimated by Equation [4].

$$D = 0.534 \left[\frac{\sigma^{0.639}}{g^{0.564} (\rho_2 - \rho_1)^{0.130} \rho_2^{0.306}} \right] \frac{\mu_1^{0.114}}{\mu_2^{0.372}} \quad [4]$$

where D is the diameter of droplet, σ the interfacial tension, g the gravitational acceleration, ρ_2 the density of steel, ρ_1 the density of slag, μ_1 the molecular viscosity of slag, and μ_2 the molecular viscosity of water

Hagemann *et al.* (2013) also studied the size of 'slag' droplets entrained via shearing at the interface using cld models. They found that the estimated droplet sizes were of the same order of magnitude as those of Harman and Cramb (1996). However, it is rather strange that they attempted to study the entrained droplet size with respect to changes in the kinematic viscosity ratio of the two fluids, when the empirical equation given by Harman and Cramb (1996) shows that the relationship between the droplet size and the viscosity ratio of the two fluids is not linear, and that it varies independently of each viscosity ratio.

- **Kelvin-Helmotz instability**—Kelvin-Helmholtz instability takes place when two inviscid, irrotational fluids of different densities separated by a flat interface move at different tangential velocities (Hibbeler and Thomas, 2010). The instability and entrainment of slag takes place when the difference between the velocities of the two fluids exceeds a critical velocity difference given by:

$$\Delta V_{crit} = \sqrt{\left[\frac{1}{\rho_2} + \frac{1}{\rho_1} \right] \left[\frac{g}{k} (\rho_2 - \rho_1) + k\sigma \right]} \quad [5]$$

where ΔV_{crit} is the critical tangential velocity difference between steel and the slag, ρ_2 the density of steel, ρ_1 the density of the slag, g the gravitational acceleration, σ the interfacial tension between steel and slag, and k the angular wave number of small perturbation on the interface with wavelength λ .

$$k = \frac{2\pi}{\lambda} \quad [6]$$

The minimum wavelength at which Kelvin-Helmholtz instability takes place in nature is given by:

$$\lambda = 2\pi \sqrt{\frac{\sigma}{g(\rho_2 - \rho_1)}} \quad [7]$$

This gives rise to the minimal critical velocity at which Kelvin-Helmholtz instability takes place, which is given by:

$$\Delta V_{crit} = \sqrt[4]{4g(\rho_2 - \rho_1)\sigma \left[\frac{1}{\rho_2} + \frac{1}{\rho_1} \right]^2} \quad [8]$$

Milne-Thomson (1968) extended Kelvin-Helmholtz instability to include finite fluid depth, but neglected the effect of viscosity and interfacial tension, yielding:

$$\Delta V_{crit} = \sqrt{g(\rho_2 - \rho_1) \left(\frac{H_2}{\rho_2} + \frac{H_1}{\rho_1} \right)} \quad [9]$$

where H_1 and H_2 are the thickness of the slag layer and the steel melt layer respectively.

Iguchi and co-workers confirmed this using physical experiments that involved a rotating roller under water and oils. They found that the above equation is valid for low-viscosity and low-frequency disturbances where surface tension is not important or can be neglected (Iguchi *et al.*, 2000).

- **Turbulence at the interface**—Turbulence at the steel-slag interface is caused by excessive surface-directed flow of the melt to the slag layer as a result of the flow reflecting from the bottom of the tundish or as a result of the improper use of FCDs. Too much surface-directed flow leads not only to slag entrainment but also to balding of the slag layer. In the latter case, the surface-directed flow is so high that it pushes the slag away and causes the melt to be exposed to air (Hibbeler and Thomas, 2010).
- **Marangoni flow**—Exchange reactions, such as the oxidation of dissolved aluminium, that take place at the interface reduce the local interfacial tension between steel and slag and thus increase the system's capillary number. If the system's capillary number is increased past its critical value, then emulsification can occur even at low melt velocities. Similar to the exchange reactions at the interface, bubbling of argon from the bottom of the tundish decreases the local interfacial tension between steel and the melt, thus leading to slag entrainment even at low melt velocities (Hibbeler and Thomas, 2010).
- **Gas bubbling**—Gas bubbling is often used in tundishes to promote flotation of inclusions. The gas of choice is argon due to its inertness. Gas injection may, however, lead to slag entrainment when the gas bubbles rupture at the upper slag layer. The bubbles rise due to buoyancy, they penetrate the slag layer, and once they reach the surface of the slag layer, they rupture, causing small slag droplets to enter the steel phase (Hibbeler and Thomas, 2010). Apart from this, as noted, bubbles bursting at the steel-slag interface also induce Marangoni flow.
- **Mass transfer across the interface**—Although not well documented in literature as a mechanism for slag entrainment, mass transfer across the steel-slag interface could possibly lead to low concentrations of slag in the steel phase and low steel concentrations in the slag phase. In a summary of model studies on slag entrainment mechanisms in gas-stirred ladles, Senguttuvan and Irons (2013) commented that entrainment of slag/steel across the steel-slag interface substantially increases the mass transfer rate across the interface. They go on to comment that identification or characterization of entrainment has been limited to establishing the conditions for entrainment and that

Numerical and physical modelling of tundish slag entrainment

quantifying the amount of entrainment has been neglected. Although not explicitly stated by Senguttuvan and Irons (2013), it is easy to imagine how a combination of mass transfer across the interface and relatively small shearing flow patterns can lead to entrainment of slag.

Solhed and Jonsson (2003) conducted numerical studies of slag entrainment in a full-sized tundish at industrial operation temperature. In their findings they questioned the existence of slag in the steel phase at 3 mm below the interface, despite the low tangential velocities; 7×10^{-2} m/s. The authors speculated about the cause of the existence of this slag in such a system.

Modelling theory

Physical modelling

Physical models make use of scaled-down models or equally sized models of the tundish vessel. In full-scale models all the dimensions of the model are the same as the prototype, while in a reduced scale the dimensions of the prototype are reduced by a factor, λ , given by Equation [10]. Reduced models are usually used in the laboratory, where space and finance are factors, while full-scale models are used in industry. In these models, water is used to study and simulate the steel melt flow, while paraffin or silicon oils are used to simulate the slag layer. Depending on the similarity criteria (geometric and dynamic similarities) being fully satisfied, the results from a physical model can accurately predict the performance of an actual industrial tundish.

$$\lambda = \frac{L_m}{L_p} \quad [10]$$

where L_m is the dimension (length) in the model, and L_p the dimension (length) in the prototype.

To satisfy the geometrical similarity criteria, all dimensions of the prototype must be reduced by λ and all angles in the model must be the same as in the prototype.

Dynamic similarities are concerned with the forces that act on a fluid element. It is necessary that the ratios of the corresponding forces in the model and the prototype be identical for the model to give useful results. Two force ratios are considered when modelling tundish flow patterns: Reynolds number (N_{Re}) and Froude number (N_{Fr}) (Mazumdar and Guthri, 1999). Research by Sahai and Burval (1992) shows that in turbulent regimes such as in the tundish, the magnitude of the Reynolds number, irrespective of geometry or size, is very similar. Therefore Reynold similarities are naturally satisfied as long as the model is operated in a turbulent regime. Following from the above, the only dynamic similarity that should be taken into account when modelling melt flow is the Froude similarity.

Froude similarity is achieved if Equation [11] is satisfied. From Equation [11], a number of scaling factors for different operating parameter can be formulated in order for the model to remain dynamically similar to the prototype. Table I shows such scale factors.

$$\frac{V_m^2}{gL_m} = \frac{V_p^2}{gL_p} \quad [11]$$

where V_m is the velocity of fluid or inclusion in the model, V_p the velocity of fluid or inclusion in the prototype, g the

gravitational acceleration, L_m the characteristic length of the model, and L_p the characteristic length of the prototype.

Water is the fluid of choice for modelling the steel phase. This is primarily due to the fact that water at 20°C has a similar kinematic viscosity to that of steel at 1600°C (Mazumdar and Guthri, 1999). Table II shows the properties of water and steel. As can be seen, the kinematic viscosity of steel is 91.3% of the kinematic viscosity of water.

To simulate the slag layer, a variety of fluids are used, including modified silicon oils, benzene, and paraffin (Chattopadhyay, Isac, and Guthri, 2010, Hsagemann *et al.*, 2013). Krishnapisharody and Irons (2008) recommend the use of paraffin oils for modelling tundish slag when water is used to model the steel melt. A similarity criterion known as the Weber number (We) can be used to evaluate the difference between the modelled system and the prototype tundish with respect to surface tension forces. The Weber number is the ratio of momentum to interfacial tension force, given by Equation [12] (Chattopadhyay, Isac, and Guthri, 2010).

$$We = \frac{V_2^2 L \rho_2}{\sigma} \quad [12]$$

where V_2 is the velocity of the melt phase or water phase, L the characteristic length of the tundish, ρ_2 the density of the melt or water phase, and σ the interfacial surface tension between steel melt and slag phase.

Ideally, the ratio of the model Weber number and the prototype Weber number should be unity. By using a combination of Equation [11] and Equation [12], one can calculate the ratio of the Weber number for the two systems in this study.

To maintain both significant geometric and dynamic similarities, not all dimensions can be scaled by λ . To maintain geometric similarity between the bath level of the prototype and that in the model, the outlet cross-sectional area of the model must disobey the similarity criteria or else the model may overflow or drain out. The outlet cross-sectional area in the model is calculated and designed to

Table I
Froude scaling factors

Property	Scaling factor
Velocity (V)	$\sqrt{\lambda}$
Time (t)	$\sqrt{\lambda}$
Volumetric flow (Q)	$\lambda^{2.5}$
Area (A)	λ^2

Table II
Properties of water and steel (Mazumdar and Guthri, 1999)

Property	Water	Steel
Molecular viscosity (kg/m.s)	0.001	0.0064
Density (kg/m ³)	1000	7014
Kinematic viscosity (m ² /s)	1.00×10^{-6}	0.913×10^{-6}
Surface tension (N/m)	0.073	1.60

Numerical and physical modelling of tundish slag entrainment

maintain similarity between the prototype bath level and model bath level. As a consequence:

$$A_{\text{Outlet,Model}} \neq A_{\text{outlet,Prototype}} \times \lambda^2 \quad [13]$$

If the tundish model is operated at steady state, the outlet cross-sectional area of the model can be calculated to satisfy Equation [14]:

$$Q_{\text{out,m}} = Q_{\text{in,m}} = A_{\text{out,m}} \times V_2 \quad [14]$$

where Q is the volumetric flow of water, $A_{\text{out,m}}$ the cross-sectional area of the outlet nozzle in the model, and V_2 the velocity of water at the outlet nozzle.

$$V_2 = \sqrt{\frac{2 \times (\rho_2 g h_2 + \rho_1 g h_1)}{\rho_2}} \quad [15]$$

where h_1 is the simulated slag layer thickness and h_2 the simulated melt phase thickness.

Flow characterization in physical models

A flow characterization study is a key starting point when it comes to understanding a reactor or any metallurgical vessel or optimizing its performance. Flow characterization results are the first point of comparison between a numerical model and a physical model.

Typically in such studies, a tracer (salt, dye, or acid) is injected in the inlet stream of the vessel. Its concentration is then monitored at the outlet of the vessel as a function of time. A plot of the tracer concentration at the outlet ports against time is known as the residence time distribution (RTD) curve. The RTD of the vessel can then be analysed to gain knowledge of the flow patterns inside the vessel. Such an analysis involves calculating plug flow volume fraction, dead volume fraction, and mixing volume fractions.

Research on tundish flow patterns has shown that tundishes exhibit characteristics of a combined flow model, with dispersed plug flow (Jha, Rao, and Dewan, 2008; Joo and Guthrite, 1991; Tripath and Ajmani, 2005).

For this study, it is worthwhile to physically perform the RTD study for comparison with the numerical determined RTD plot to ensure that the flow patterns are numerically modelled correctly.

Numerical modelling methods

Numerical methods makes use of computer packages to solve a series of fluid mechanics differential equations in 3D or 2D space. Whereas physical modelling incorporated with fluid flow characterization gives quantitative results about what is happening in the vessel, numerical modelling allows the investigator to gain both detailed visual and quantitative information about the flow patterns inside the vessel. In addition to this, numerical simulations allow the investigator to gain knowledge about turbulence, pressure changes, and velocity patterns inside the vessel. Results from numerical models can be verified by comparing them to results from a physical model study. Once verified, the numerical model can be adapted for use in a variety of situations without the need for any experimental work. The numerical modelling in this study was done in ANSYS® Fluent; the numerical modelling theory will thus follow the nomenclature used in this package.

In order to model fluid flow, two main equations must be solved. These are the conservation of mass equation,

otherwise known as the continuity equation Equation [16], and the conservation of momentum equation Equation [17] (ANSYS, 2011).

$$\frac{\partial \rho}{\partial t} + \frac{\partial}{\partial x_i} (\rho v_i) = S_m \quad [16]$$

$$\frac{\partial(\rho v_i)}{\partial t} + \frac{\partial(\rho v_i v_j)}{\partial x_j} = - \frac{\partial P}{\partial x_i} + \frac{\partial}{\partial x_j} \left[\mu \left(\frac{\partial v_i}{\partial x_j} + \frac{\partial v_j}{\partial x_i} \right) - \frac{2}{3} \delta_{ij} \frac{\partial v_l}{\partial x_l} \right] + \frac{\partial(-\rho v' i v' j)}{\partial x_j} + \rho \vec{g} + \vec{F} \quad [17]$$

where ρ is the density of the fluid, v_i the velocity component of the fluid in the ijk plane, P the static pressure, μ the molecular viscosity, l the unit tensor, g the gravitational acceleration, and F bodily forces

In Equation [16], the first term relates to change of density with time, the second is change of mass as a result of convection. S_m relates to source terms in the system, (inputs or outputs, reactions, and evaporation). In Equation [17] the first term represents change of momentum with time, followed by change of momentum due to convection, change of momentum due to pressure changes, change of momentum due to molecular and turbulence shear stress, change of momentum due to Reynolds stresses, change of momentum due to gravitational forces, and lastly change in momentum due to bodily forces (ANSYS, 2011).

To close Equation [17], Reynolds stresses ($\overline{\rho v' i v' j}$) must be known. In particular, the average fluctuating component of the fluid velocity must be known before the velocity flow field is known (Bakker, 2008). A common approach to overcome this is to use the Boussinesq hypothesis, which relates Reynolds stresses to the mean velocity gradient. Mathematically this is represented by (ANSYS, 2011):

$$\rho \overline{v' i v' j} = \mu_t \left[\frac{\partial u_i}{\partial x_j} + \frac{\partial u_j}{\partial x_i} \right] - \frac{2}{3} k \delta_{ij} \quad [18]$$

where μ_t is the turbulent viscosity and k the turbulent kinetic energy.

This hypothesis forms the basis of the popular $k-\varepsilon$ model, $k-\omega$ model, and Spalart-Allmaras model used to resolve turbulence (Bakker, 2008). In the $k-\varepsilon$ models (standard and realizable), two extra equations are solved: turbulence kinetic energy (k) and dissipation of turbulence kinetic energy (ε).

Turbulence kinetic energy is calculated from Equation [19]:

$$\frac{\partial}{\partial t} (\rho k) + \frac{\partial}{\partial x_i} (\rho k v_i) = \frac{\partial}{\partial x_i} \left[\left(\mu + \frac{\mu_t}{\sigma_k} \right) \frac{\partial k}{\partial x_i} \right] + G_k + G_b - \rho \varepsilon - Y_M + S_k \quad [19]$$

while the dissipation of turbulence kinetic energy (ε) can be calculated from:

$$\frac{\partial}{\partial t} (\rho \varepsilon) + \frac{\partial}{\partial x_i} (\rho \varepsilon v_i) = \frac{\partial}{\partial x_i} \left[\left(\mu + \frac{\mu_t}{\sigma_k} \right) \frac{\partial \varepsilon}{\partial x_i} \right] + C_1 \frac{\varepsilon}{k} (G_k + C_3 G_b) - C_2 \rho \frac{\varepsilon^2}{k} + S_\varepsilon \quad [20]$$

where μ_t is the kinematic turbulent viscosity, μ the molecular viscosity, G_b the generation of turbulent energy due to buoyancy, Y_M changes in dilation (compressible fluids), S_k and S_ε are user-defined source terms, and G_k the rate of generation of kinetic energy per unit mass given by:

Numerical and physical modelling of tundish slag entrainment

$$G_k = \mu_t \left[\frac{\partial v_i}{\partial x_j} + \frac{\partial v_j}{\partial x_i} \right] \frac{\partial v_i}{\partial x_j} \quad [21]$$

The turbulent viscosity can then be calculated by:

$$\mu_t = \frac{C_\mu \rho k^2}{\epsilon} \quad [22]$$

Where C_1 , C_2 , C_3 , σ_k , σ_ϵ , and C_μ are constants. Table III shows the values of these constants. It is important to note that C_3 , unlike other constants, is calculated. In the realizable $k-\epsilon$ model the C_μ term is expressed by a differential equation, as opposed to being constant; moreover, the dissipation equation is based on a dynamic equation of the mean-square vorticity fluctuation. This gives the realizable $k-\epsilon$ model an advantage over the standard $k-\epsilon$ model when calculating flows that show strong streamline curvature, vortices, and rotation (Bakker, 2008).

Two-phase modelling in ANSYS® Fluent can be done by making use of the VOF (Volume of Fluid) model, which tracks the interface on the phases throughout the calculation domain. VOF consists of three methods to model fluid interactions: a methodology to locate the free surface, an algorithm allowing the tracking of free surface as it moves through the computational domain, and a method allowing boundary conditions to be applied at the free surface (Reilly *et al.*, 2013).

In the VOF model a single momentum equation (similar to Equation [17]) is solved for all the phases, where the fluid properties are calculated using Equation [23]. The resulting velocity is shared amongst the phases, *i.e.* assumed to be equal for all phases present. Interface tracking is achieved by solving a continuity equation which incorporates the volume fraction of each phase, Equation [24] (ANSYS, 2011).

$$\dot{\phi} = \sum a_i \dot{\phi}_i \quad [23]$$

where ϕ is the average fluid property, such as (density, viscosity, *etc.*), a_i the volume fraction of the i -th phase, and $\dot{\phi}_i$ the fluid property of the i -th phase.

$$\frac{1}{\rho_i} \left[\frac{\partial(a_i \rho_i)}{\partial t} + \nabla \cdot (a_i \rho_i \vec{v}_i) \right] = S a_i + \sum_{j=1}^n (m_{ij} - m_{ji}) \quad [24]$$

where $S a_i$ is the rate of generation of the i -th phase, and m_{ij} the mass transfer rate of i -th phase into the j -th phase.

For surface tension modelling, one can choose to specify a constant surface tension coefficient or to specify a user-defined equation for surface tension. The VOF model then adds additional tangential stresses that arise due to variable changes in surface tension at the interface. Two surface

tension models exist in the VOF model, the continuum surface force (CSF) and the continuum surface stress (CSS). Essentially these models are used to calculate the surface tension force (ANSYS, 2011). In the CSF model the surface tension force is obtained by first calculating the surface curvature from local gradients in the surface normal to the interface. The CSS model is a more conservative model. It avoids calculating the surface curvature to solve for the surface tension force, and thus misses some activity at the interface (ANSYS, 2011).

Boundary conditions

Boundary conditions specify, *inter alia*, direction of flow, fluid source and sink, and how the flow must behave in certain regions. Boundary conditions can be split into inlet conditions, outlet conditions, wall conditions, and surface conditions.

Inlet conditions involve specifying the position of the inlet, direction of flow, pressure, and whether the velocity has a profile or not. In the case of a turbulent flow entering at the inlet region, the turbulent kinetic energy and dissipation have to be specified. One method of specifying the turbulence at the inlet is to specify the turbulence intensity and hydraulic diameter. The turbulence intensity is given by Equation [25], and the hydraulic diameter is the diameter of the duct (Bakker, 2008):

$$I = \frac{\sqrt{2/3k}}{V} \quad [25]$$

where I is the turbulence intensity, typically 5% for fully developed flow in a pipe, k the turbulence kinetic energy, and V the average velocity in the pipe.

For outlet conditions, the velocity at the outlet is assumed not to have a profile and is given by Equation [15]. Pressure at the outlet is given by the hydrostatic pressure. The outlets are assumed to be open to the atmosphere. All flow property gradients are zero over the outlet region, except for pressure (Bakker, 2008). Wall boundaries are specified to allow the software to know where the boundaries are. The no-slip conditions are used for viscous flows, meaning that the tangential velocity of the fluid closest to the wall has the same velocity as the wall, and that the normal fluid velocity at the wall is zero. The presence of the wall and the choice of no-slip conditions affect how turbulence is dissipated near the wall. In particular, regions closest to the wall are dominated by laminar flow where viscous forces play a significant role. At the outer parts of the wall, momentum transfer is dominated by turbulent conditions. The area between the laminar and turbulent regions is characterized by both laminar and turbulent dissipation of momentum. To resolve flow patterns in near-wall regions, one can use semi-empirical formulae known as wall functions, or modified turbulence models. In the wall functions, the viscosity-dominated region is not resolved, and instead semi-empirical models are used to calculate the flow behaviour in the viscous layer near the wall. In modified turbulence models, the flow behaviour is resolved all the way to the wall. This involves making use of fine mesh sizes near the wall region, which costs in computational time. For ϵ -based equations, wall-enhanced wall treatment functions are recommended (Bakker, 2008).

Table III

$k-\epsilon$ model constant values (Lauder and Spalding, 1972)

Constant	Typical value
C_1	1.44
C_2	1.92
C_μ	0.09
σ_k	1.00
σ_ϵ	1.30

Numerical and physical modelling of tundish slag entrainment

For top surface boundary conditions, one can also choose to specify frictionless wall conditions. This has been the norm for most researchers who have worked in the field. They specified the boundary condition at the top of the fluid layer (Cloete, 2014; Kumar, Mazumdar, and Koria, 2008; Mazumdar and Guthri, 1999; Sahai and Emi, 1996; Tripathi and Ajmani, 2011). It is worth mentioning, though, that this boundary condition was used without the presence of a slag phase.

Symmetry conditions are considered when the flow in a vessel is thought to have planes of symmetry. These can be transverse, longitudinal, or vertical. Considering symmetry planes lowers the computational time demand on the software (Bakker, 2008). When this condition is specified, the normal velocity vectors are zero at the symmetry plane, and normal gradients of all variables are zero at the symmetry plane.

Physical set-up

Physical modelling set-up

The physical model used in this study was designed by Cloete (2014). The design is based on a tundish used by Kumar, Mazumdar, and Koria (2008), but instead of a scale factor of 1/3 a scale factor of 1/2 was used. The model is constructed from clear 6 mm PVC. It has four strands instead of the normal one or two, and walls inclined at 10°. Figure 1 shows a schematic representative of the tundish. Water was used to model the tundish steel phase, and paraffin to model the slag phase.

A calculation of the Webber number ratio ($We_{model}/We_{prototype}$) based on a steel-slag system interfacial surface tension of 1.6 Nm⁻¹ (Mazumdar and Guthri, 1999; Mills, 2011) and water-to-paraffin interfacial surface tension of 0.048 Nm⁻¹ (Johansen, 1924) shows that the ratio of the model and prototype We numbers is 1.21. This is considered to be close to unity and thus justifies the use of paraffin to model tundish slag.

Table IV lists the dimensions and operating conditions of the prototype (industrial scale) and the model used in this study.

Table V lists the properties of the two liquids used in the water model.

Figure 2 shows a schematic layout of the experimental set-up. Water is fed from the mains to a feed tank, which is

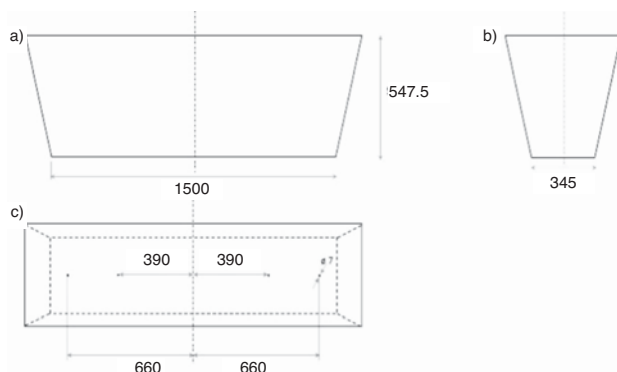


Figure 1—Dimensions of the tundish model. (a) Front view, (b) side view, and (c) top view

kept at a fixed level by a float valve. From the feed tank the water is pumped to the tundish. The inlet flow rate is controlled by a gate valve (V-2) and a rotameter (3). The four ball valves (V-3, V-4, V-5, and V-6) can be closed to stop outlet flow, which is driven by gravity, to allow the tank to fill up. The water from the outlets is fed back to a storage tank (Cloete, 2014).

Figure 3 shows the dimensions of the FCD used in this study. The design is based on those used by Cloete (2014) and Kumar, Mazumdar, and Koria, (2008). The FCD was constructed from 15 mm thick grey PVC. It was fixed in position and sealed with silicone.

Table IV

Dimensions and operating conditions of prototype and reduced model

Property	Prototype	Water model
Base length (m)	3.00	1.50
Volume (l)	2000	250
Inlet flow rate (l/h)	8 700	1572
Melt height (m)	0.78	0.39
Slag height (m)	—	0.02
Entry nozzle diameter (m)	—	0.03

Table V

Operating fluid properties

Property	Water	Paraffin
Density (kg/m ³)	998.2	780
Viscosity (kg·m ⁻¹ s ⁻¹)	1.00 × 10 ⁻³	2.40 × 10 ⁻³
Kinematic viscosity (m ² /s)	1.00 × 10 ⁻⁶	3.08 × 10 ⁻⁶
Fluid thickness (m)	0.39	0.02
Interfacial tension (N/m) (Johansen, 1924)	0.048	0.048
Operating temperature range (°C)	19–25	19–25

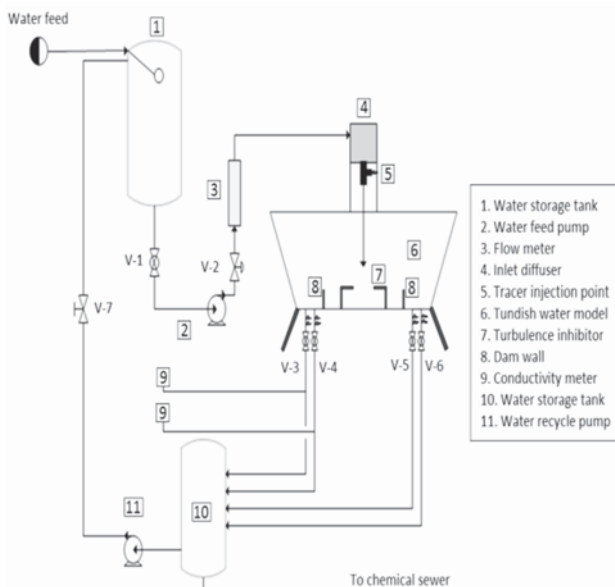


Figure 2—Experimental set-up (Cloete, 2014)

Numerical and physical modelling of tundish slag entrainment

Sampling of entrained slag entrainment was done by taking 50 ml samples with a pipette from the tundish while in operation, weighing the sample using a two-decimal-place scale, then calculating the sample's density and then the volume fraction of entrained paraffin at that location using Equation [26]. The densities of water and paraffin used in Equation [26] were determined by taking ten 50 ml samples of each fluid and weighing them. This was done every day during the sampling period to account for changes in water density due to the weather.

$$x_{vol.fraction} = \frac{\rho_{sample} - \rho_{water}}{\rho_{paraffin} - \rho_{water}} \quad [26]$$

To avoid systematic errors, the location at which a sample was to be taken was programmed into Microsoft Excel® to be random. Five repeats of each sampling location were taken.

To determine where samples were to be taken, Cloete's results were used. Cloete (2014) studied the flow patterns in the tundish model used in this study, and investigated the effect of different FCDs on the melt flow behaviour. However, like other authors, he did not include the slag layer. Based on his work, areas where entrainment at the interface might occur can be predicted. Moreover, dead volumes where entrained 'slag' might accumulate can be identified. This was the basis for the physical grid design and sampling locations. Based on Cloete's results it was decided to sample at a depth of 220 mm (total depth).

Five repeats of each sampling point were taken over a period of 5 hours. The five repeats were averaged to give one value for the volume fraction of entrained paraffin. It is worth mentioning that the residence time of the cold model is 8 minutes, and that the sampling method followed in this study mimicked a number of hits, *i.e.* a number of ladles transferring melt to the tundish.

Weather changes had a significant effect on the water density, thus sampling had to be done during settled weather conditions. In this study sampling was done over a week to account for weather changes, and each day the density of water was calculated by weighing 50 ml of water and paraffin.

Five repeats of the RTD study were done. The following guidelines applied. When the system had stabilized (after 45

minutes), the tracer was injected into the model via the tracer injection point (see Figure 2). 60 ml of 300 g/l table salt solution was used for these tests. The injection was done over 5 seconds. After injection, the concentration of the tracer in the outlet stream of two strands was monitored using a calibrated conductivity meter. The concentration of the tracer at the outlets was recorded at 30-second intervals for 20 minutes; this is more than twice the theoretical residence time of the model.

Numerical modelling set-up

The realizable $k-\epsilon$ model was used for the turbulence model, while the VOF model was used to model the two faces (water and paraffin).

Boundary conditions

- The velocity inlet was at the top of the entry nozzle. The velocity was specified as 0.614 m/s. The turbulence intensity was left as 5 % and the hydraulic diameter was specified as 30 mm
- On the strand outlets, the settings were left as pressure-based. The default gauge pressure of zero and the turbulence intensity of 5% were used. The hydraulic diameter was specified as 7 mm
- Symmetry conditions were applied along the transverse and longitudinal planes of the tundish, thus reducing the computational domain to a quarter of the full-scale model
- The sidewalls, bottom of the tundish, and FCD walls were specified as no-slip conditions
- No extra boundary conditions were specified at the interface since the continuity equation and momentum equations were naturally satisfied across the interface. The VOF also inherently specifies a balance of forces due to pressure difference across the interface and interfacial tension at the interface.

Solver settings

- The pressure-based solver was used. SIMPLE scheme was used for pressure-velocity calculations
- All convective parameters were first interpolated using first-order upwind, and later changed to second-order upwind once the solutions had stabilized
- Volume fraction was solved using second-order upwind throughout
- Gradients of solutions were evaluated using the least-square cell-based scheme. This was chosen to reduce false (numerical) diffusion
- The pressure was interpolated using the PRESTO! scheme.

Flow characterization in numerical modelling

A comparison between the results of a numerical RTD and those of the physical model is often the first step towards validating the numerical results. To study the RTD of a vessel numerically using ANSYS® Fluent, Equation [27] is solved for the tracer element.

$$\frac{\partial \rho Y_i}{\partial t} + \nabla \cdot (\rho \vec{V} Y_i) = -\nabla \cdot J_i + R_i + S_i \quad [27]$$

where Y_i is the mass fraction of the tracer in the calculation domain, J_i the effective mass transfer in the calculation

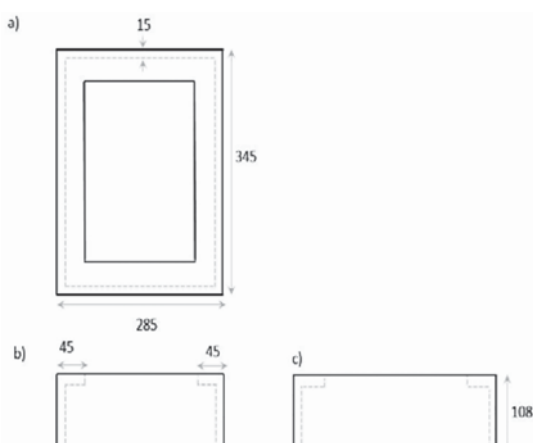


Figure 3—Turbulence Inhibitor dimensions. (a) Top view, (b) front view, (c) side view

Numerical and physical modelling of tundish slag entrainment

domain given by Equation [28], R_i the rate of production of the tracer by reaction, S_i the rate of production of the tracer via addition, and ρ the density of the primary fluid or fluid in which the tracer is flowing.

$$J_i = -\left(\rho D_i + \frac{\mu_t}{Sc_t}\right) \nabla Y_i \quad [28]$$

where D_i is the molecular diffusion of tracer in the main fluid, Sc_t the turbulent Schmidt number, with a value of 0.7, and μ_t the turbulent viscosity.

Physical modelling observations and results

Observations

While running the physical model, it was noticed that there seemed to be little to no movement of the water-paraffin interface, which implies that there is no turbulence at the interface and that slag entrainment does not take place via turbulence at the interface. There was no visual evidence of paraffin entrainment as a result of shearing at the interface, as was seen by other workers. Small droplets of entrained paraffin (approximately 1 mm) could be seen floating in low concentrations at a depth of 300 mm. Initial measurements showed that a small amount of paraffin is entrained, with a maximum volume fraction of approximately 0.02, even at a depth of 220 mm. These observations suggest that the entrainment of the paraffin 'slag' does not take place via macroscopic shearing of the interface, but by microscopic entrainment, possibly assisted by mass transfer at the steel-slag interface. By studying the interfacial velocities using the numerical model developed in this study, more insight will be gathered on this.

It was also noted that as the pipette was being immersed in the paraffin layer and bulk water phase for sampling, a small amount of paraffin (simulated slag layer) and a mix of 'entrained' paraffin and water from shallower depths (<220 mm) in the bulk water phase tended to be forced into the pipette before a sample could be taken. This caused a high bias in the results. The bias resulting from the pipette going through the paraffin phase can be measured by sampling the model at 220 mm depth when there is no flow, *i.e.* paraffin phase and water phase present, close all the strand outlets, and sample at 220 mm depth with no flow entering the model. Thus this error can be eliminated. The error or bias resulting from the 'entrained' paraffin and water mixture could not be measured. See the comparison between the numerical and physical model results for how much this error affected the results.

Entrained slag behaviour

Figures 4 and Figure 5 show contour plots of entrained paraffin (slag) in a bare tundish and a tundish with FCD respectively. The zero on the x-axis represents the centreline where the inlet is located. The y-axis represents the length of the model. Note that 130 mm of sampling location was lost due to structural interference, hence the y-axis starts at 200 mm.

To investigate the use of symmetry conditions along the longitudinal and transverse centrelines in the numerical model, a parity chart based on entrained 'slag' concentrations was drawn, shown in Figure 6. Figures 4 to 6 should be

examined in conjunction with Figure 7 for orientation and an explanation of the meaning of side 1 and side 2.

From Figure 4 it can be seen that entrained slag in a bare tundish tends to accumulate in the region closest to the inlet. The concentration of entrained slag tends to decrease towards the endwalls. This is a similar to findings of Solhed, Jonsson,

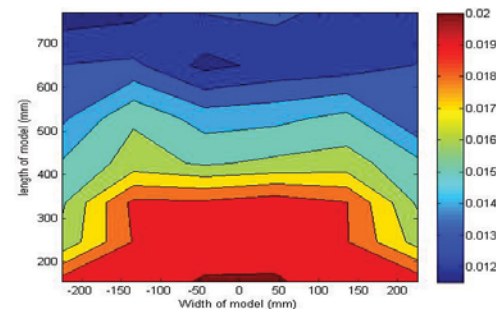


Figure 4—Top view of tundish showing contour plot of entrained 'slag' concentration (volume fraction) at 220 mm depth in a bare tundish

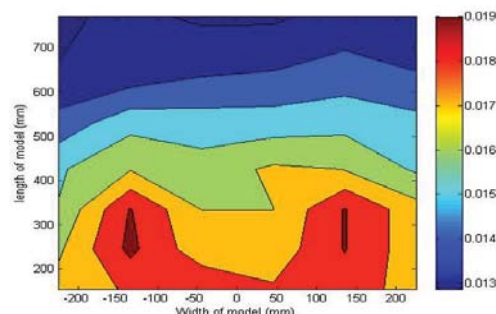


Figure 5—Top view of tundish showing contour plot of entrained 'slag' concentration (volume fraction) at 220 mm depth in tundish with a FCD

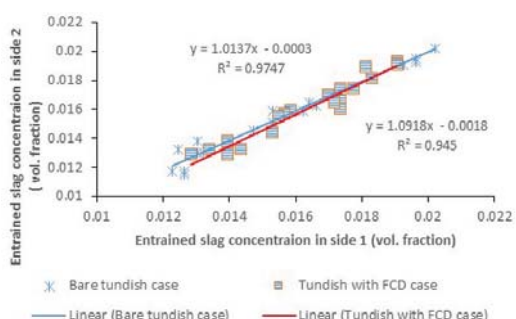


Figure 6—Parity chart of entrained 'slag'—concentration expressed as volume fraction

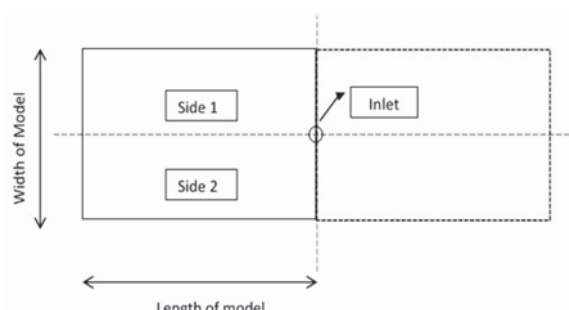


Figure 7—Top view of tundish to show location of side 1 and side 2

Numerical and physical modelling of tundish slag entrainment

and Jönsson (2008). Interestingly, a slightly similar pattern is seen in the tundish with a flow control device (Figure 5); however, with the FCD device the entrained 'slag' seems to appear in more localized pockets that form two parallel slits. From the parity charts (Figure 6), it can be seen that the concentration of entrained 'slag' is indeed symmetrical about the longitudinal centreline. These results make it acceptable to numerically model only a quarter of the tundish and assume symmetry planes along the longitudinal and transverse centrelines, instead of the full tundish. This saves a significant amount of computational time when solving the flow equations.

As noted, when the pipette was being immersed in the paraffin layer and bulk water phase for sampling, a small amount of paraffin (from the simulated slag layer) and a mix of 'entrained' paraffin and water from shallower depths (<220 mm) in the bulk water phase tended to be forced into the pipette, due to hydrostatic pressure, before a sample could be taken. This caused a high bias in the results shown in Figure 4 and Figure 5. To account for this bias, ten blank samples (at 220 mm depth with no flow) were taken and the concentration of paraffin was measured. Table VI shows the results from this test. Since this error is inherent throughout the model it can be subtracted from the data shown in Figure 4 and Figure 5, thus giving more accurate results. Figure 8 and Figure 9 show results with reduced inherent error. It is important to note that although further analysis will be done using these figures (Figure 8 and Figure 9), these results still contain a portion of the inherent sampling error and thus could be higher than the true concentration of the entrained paraffin. However, of importance to this study is the ability of the numerical model to predict the entrained slag behaviour and to give the same order of magnitude of entrained paraffin concentration as in the physical model, as opposed to the actual value entrained paraffin concentration.

Numerical modelling results

Numerically predicted RTD

Figures 10 and 11 show a comparison between the numerically predicted RTD and the physically produced RTD curve for the bare tundish and tundish with FCD, respectively. In both cases (the bare tundish and tundish with FCD)

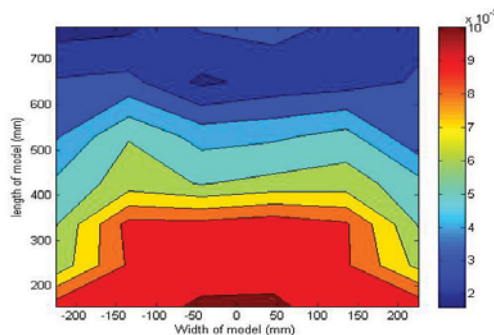


Figure 8—Top view of tundish showing adjusted contour plot of entrained 'slag' concentration (volume fraction) at 220 mm depth in a bare tundish

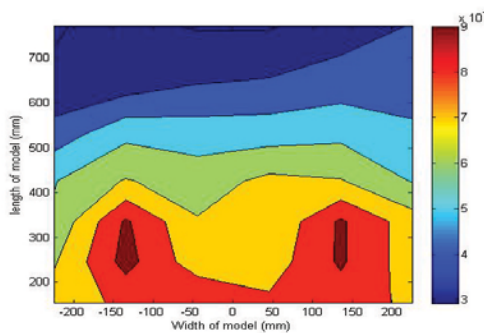


Figure 9—Top view of tundish showing adjusted contour plot of entrained 'slag' concentration (volume fraction) at 220 mm depth in a tundish with FCD

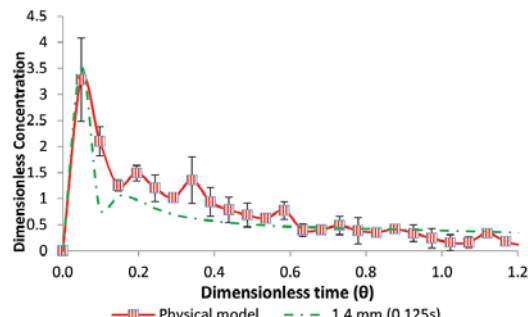


Figure 10—Comparison between numerically predicted RTD and RTD from physical model for a bare tundish

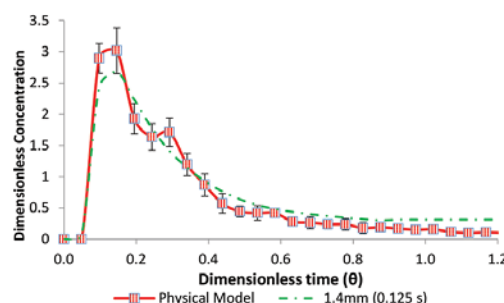


Figure 11—Comparison between numerically predicted RTD and RTD from physical model for a tundish with a FCD

a match between the physical model and the numerical model was achieved with a mesh of 1.4 mm at a time step of 0.125 seconds. It is quite interesting to note that the spread was

Table VI

Concentration of paraffin resulting from inherent error in sampling method

Sample no.	Paraffin volume fraction
1	0.0098
2	0.0089
3	0.0089
4	0.0098
5	0.0108
6	0.0108
7	0.0098
8	0.0108
9	0.0108
10	0.0089
Average	0.0099

Numerical and physical modelling of tundish slag entrainment

numerically modelled well in the FCD case, but the details of the second peak were not. In the bare tundish, the spread was not modelled well but the details of the second peak were captured well. This allows for further analysis of the numerical model.

Numerically predicted entrained slag behaviour

Figures 12 and 13 show numerically developed contour plots of entrained paraffin concentration (slag) at a depth of 220 mm in a bare tundish and a tundish furnished with a FCD respectively. As in the physical model, the entrained slag concentration is highest behind the inlet shroud. The concentration of entrained slag tends to decrease towards the endwalls. It is interesting to note that the concentration of entrained slag is lower in the case of the FCD than in the case of the bare tundish (38% lower, based on the highest entrained 'slag' concentration). However, this does not imply that less slag is entrained in the case of the FCD. Such a conclusion can be made only if the concentration of the entrained 'slag' were to be measured at the strands for both cases. This was not done in this study due to the complexity of acquiring accurate results, given the low concentration. It is also interesting to note that the numerically predicted entrained slag concentration is 55% and 68% lower than found in the cold model for the bare tundish and tundish with FCD respectively (based on highest seen concentration).

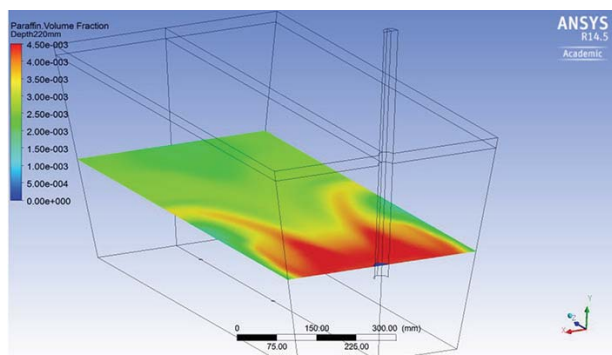


Figure 12—Numerically developed contour plot of entrained paraffin 'slag' in a bare tundish

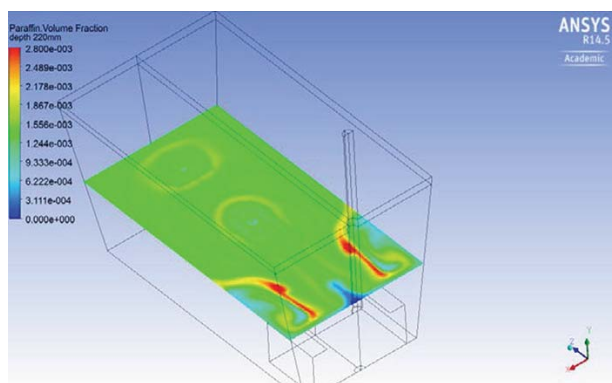


Figure 13—Numerically developed contour plot of entrained paraffin 'slag' in a tundish with a FCD

This high bias in the cold model results was noted in the observations. It results from fluid in shallower depths being pushed into the pipette as a result of hydrostatic pressure. It is important to note that an attempt was made to reduce this error and the residual error as highlighted earlier.

Flow patterns that lead to slag entrainment

Having found a numerical model that can predict the slag entrainment behaviour and flow patterns, the mechanism that results in tundish slag entrainment can be studied using the numerical models.

Bare tundish flow patterns

Figures 14 and 15 depict the longitudinal view of the flow patterns in a bare tundish. In Figure 14 it can be seen that the flow exits the inlet shroud, impinges at the bottom of the tundish, and reports to the inner strand. The displacement of the melt at the bottom of the tundish causes a draft of melt from the outer walls of the tundish (region A). In this view it can be seen that there is no excessive tangential flow close to the steel-slag interface. Thus the entrainment does not arise from longitudinally directed flow. In Figure 15, downwards-directed flow from the sidewalls can be seen (region B). Figures 16 and 17 depict the flow patterns in transverse view. The flow impinges at the bottom of the tundish, and then moves up the sidewalls to cause shearing below the steel-slag interface (region C). It is this flow being assisted by mass transfer at the interface that is believed to

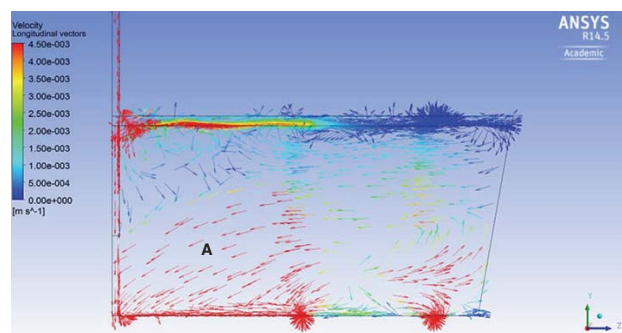


Figure 14—Longitudinal view of flow vectors at the centreline of a bare tundish

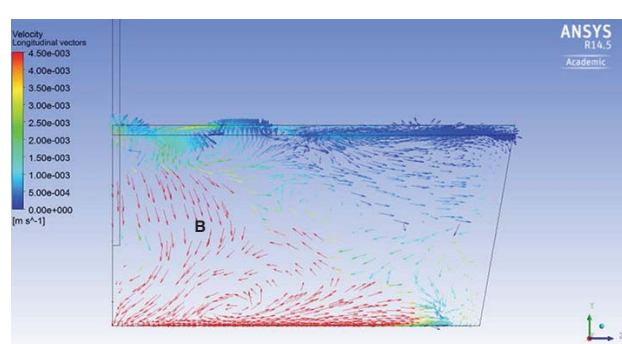


Figure 15—Longitudinal view of flow vectors 100 mm away from centreline of a bare tundish

Numerical and physical modelling of tundish slag entrainment

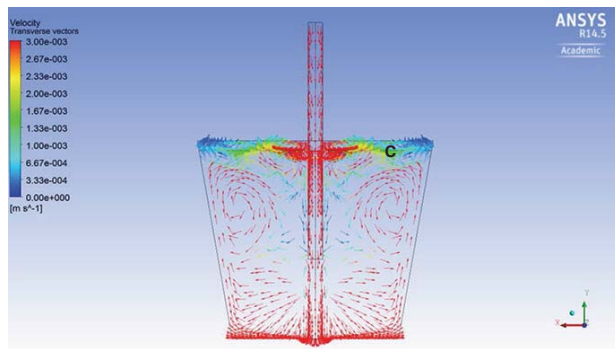


Figure 16—Transverse view of flow vectors at the centreline in a bare tundish

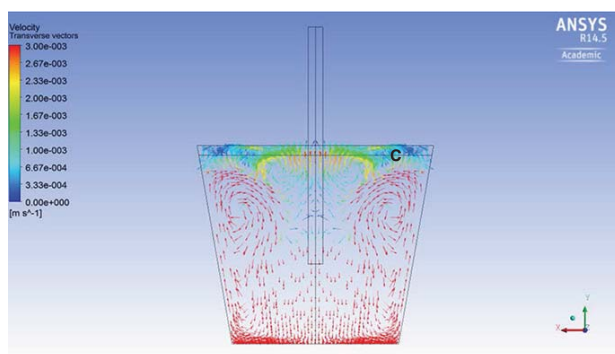


Figure 17—Transverse view of flow vectors at 100 mm from the centreline in a bare tundish

aid slag entrainment in bare tundishes. Figure 18 and 19 show the flow patterns in the transverse plane superimposed on a contour plot of entrained paraffin 'slag' concentration at a depth of 220 mm. It can be seen that the areas of high paraffin (slag) concentration are the areas where the flow that impinged on the bottom of the tundish falls on itself (region D). The entrained slag is then carried down by the flow until the flow turns into itself in region D. As the flow that rises up the sidewalls decreases, less slag is seen in the steel phase in region E (see Figure Figure 19).

Tundish with FCD flow patterns

Figure Figures 20 and 21 show longitudinal flow patterns in a tundish with a FCD. The flow exits the inlet shroud and is immediately directed to the steel-slag interface by the FCD, as intended (region F). There are two clear vortices above the inner and outer strand, which did not show in previous studies such as that by Cloete (2014). These vortices do not extend to the top of the slag layer, possibly due to the viscosity of the paraffin (slag) layer (regions G and H). Similarly to the bare tundish case, the displacement of fluid close to the inlet region causes flow to the inlet region from nearby areas (region I).

The transverse view (Figure Figure 22) shows that most of the flow exiting from the inlet shroud is reflected from the bottom of the tundish and directed to the slag layer, as intended. This flow then impinges on the slag layer, where it results in tangential flow to the slag layer (region J). This

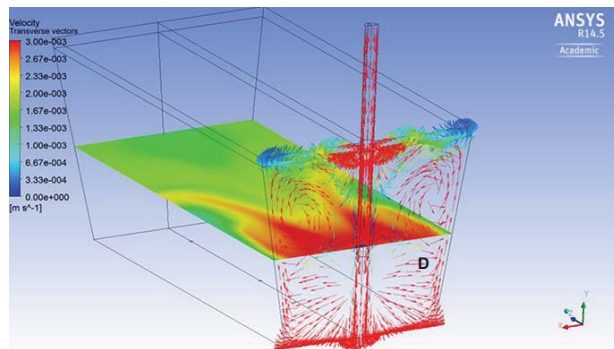


Figure 18—Transverse flow vectors at the centreline superimposed with entrained slag concentration at a depth of 220 mm

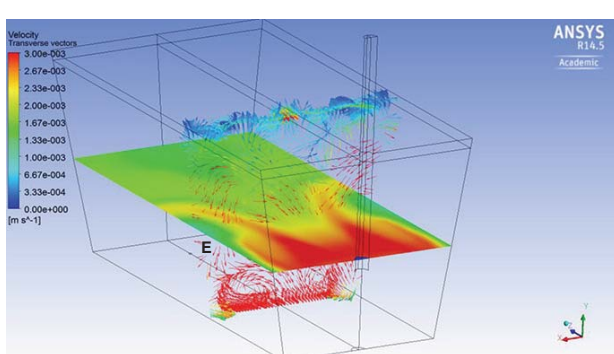


Figure 19—Transverse flow vectors at 300 mm from the centreline superimposed with entrained slag concentration at a depth of 220 mm

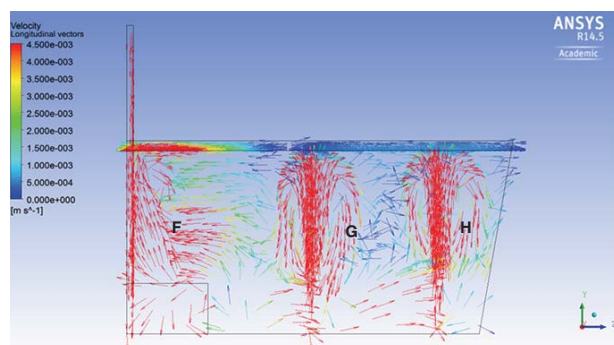


Figure 20—Longitudinal view of flow vectors in a tundish FCD

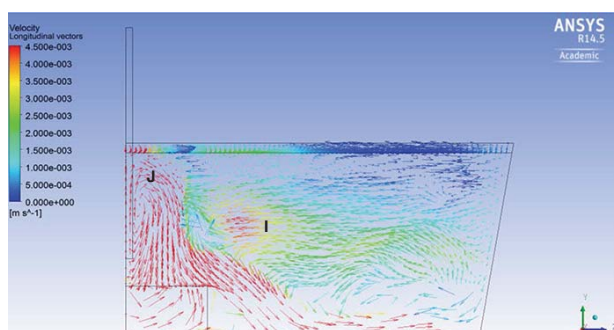


Figure 21—Longitudinal view of flow vectors 120 mm away from the centreline

Numerical and physical modelling of tundish slag entrainment

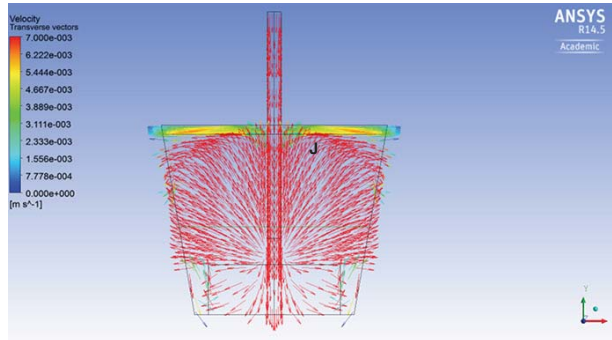


Figure 22—Transverse view of flow vectors in a tundish with FCD

tangential flow can even be seen in. It is quite interesting to note that a similar tangential flow in the bare tundish is created by the FCD, the only difference being that in the FCD case, the flow is from inside going out to the sidewalls, whereas in the bare tundish case it is from the sidewalls going towards the inlet region. It is possible that the entrainment first takes place in region J, where the flow is tangential to the interface.

Figure 23 shows flow patterns in the longitudinal plane 120 mm away from the centreline superimposed on the entrained 'slag' concentration at a depth of 220 mm. From this figure it is evident that the entrained 'slag' from area J moves with the prevailing flow to accumulate in region K.

Slag entrainment mechanisms in a bare tundish

In order to understand the main mechanism behind slag entrainment in tundishes, it is important to understand the critical velocities at which slag entrainment takes place and then compare these to the numerically simulated interfacial velocities to identify which mechanisms are responsible for slag entrainment. Table VII shows the various slag entrainment mechanisms considered in this study, the criteria for entrainment, and the calculated critical velocities for the water-paraffin case used in this study. It can be seen that the critical velocities for slag entrainment in the water model range from 1.34×10^{-1} to 9.44×10^{-1} m/s.

Figures 24 to 26 show velocity vectors tangential to the water-paraffin interface (steel-slag interface) in the bare tundish case. In Figure 25 it can be seen that there are no clear tangential velocities even at 10 mm below the interface. However, in Figure 26 one can see relatively high velocity vectors tangential to the interface. The highest of these vectors is 3×10^{-3} m/s. However, this is significantly lower than the velocities calculated for macroscopic shearing methods considered in Table VII.

The lack of tangential velocities directly at the interface suggests that the paraffin initially moved by mass transfer across the interface, and that shearing occurs only at a depth of 50 mm.

Slag entrainment mechanisms in a tundish with FCD

Figures 27–29 depict tangential velocity vectors to the interface at varying depths in a tundish with FCD. It can be seen that even at just below the interface, high tangential velocities exist (the highest is 6×10^{-3} m/s). However,

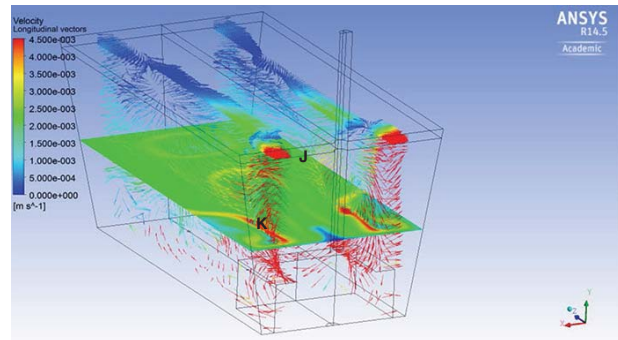


Figure 23—Longitudinal low vectors in plane at 120 mm away from the centreline superimposed on entrained slag concentration at a depth of 220 mm

Table VII

Entrainment limits specific to this study

Entrainment criteria	Calculated critical velocity (m/s)
$Ca = \frac{V_2 \eta_2}{\sigma}$	1.34×10^{-1}
$Ca^* = 3 \times 10^{-6} \left(\frac{\nu_1}{\nu_2} \right) + 2.8 \times 10^{-3}$	2.15×10^{-1}
$\Delta V_{crit} = \sqrt[4]{4g(\rho_2 - \rho_1)\sigma \left[\frac{1}{\rho_2} + \frac{1}{\rho_1} \right]^2}$	9.44×10^{-1}

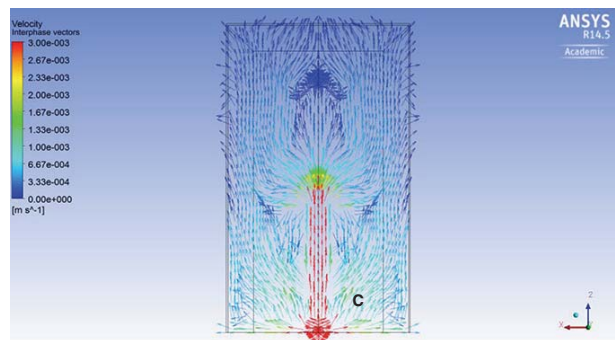


Figure 24—Tangential velocity vectors at the water-paraffin (steel-slag) interface in a bare tundish

none of these velocity vectors pass the threshold of 1.34×10^{-1} m/s.

This provides proof that entrainment in a tundish with a FCD does not take place via the macroscopic methods considered in this study, but perhaps takes place via mass transfer across the interface, assisted by minor velocity shearing close to the interface.

Numerical and physical modelling of tundish slag entrainment

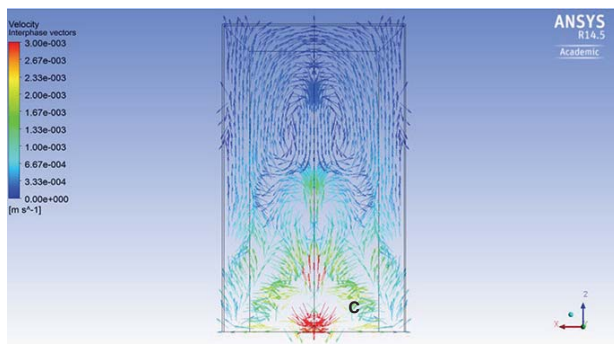


Figure 25—Tangential velocity vectors 10 mm below the interface in a bare tundish

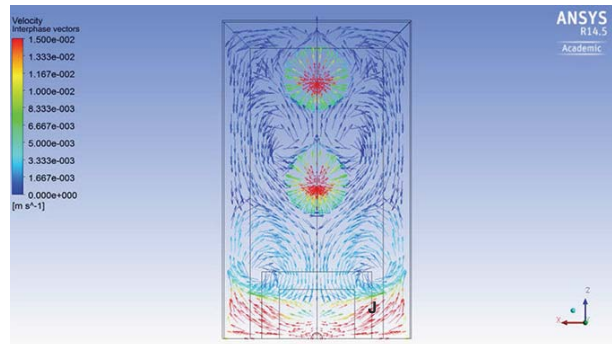


Figure 28—Tangential flow to the interface at a depth of 10 mm in the case of FCD

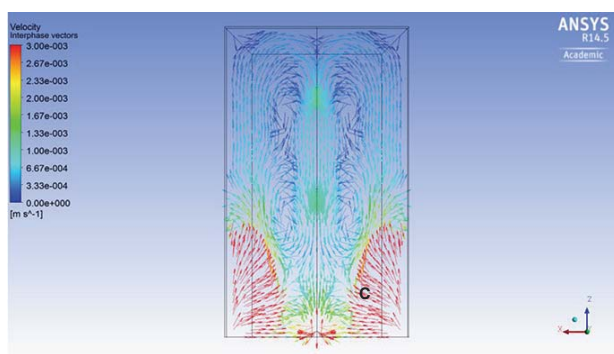


Figure 26—Tangential velocity vectors 50 mm below the interface in a bare tundish

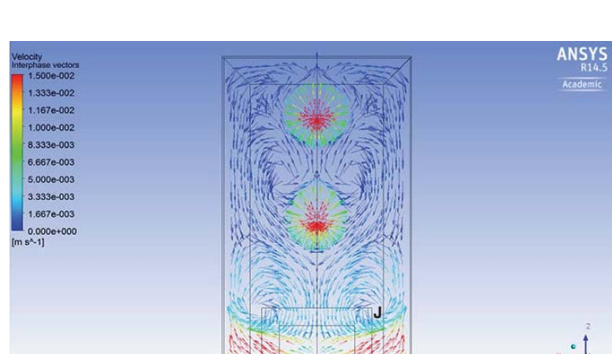


Figure 29—Tangential flow to the interface at a depth of 50 mm in the case of FCD

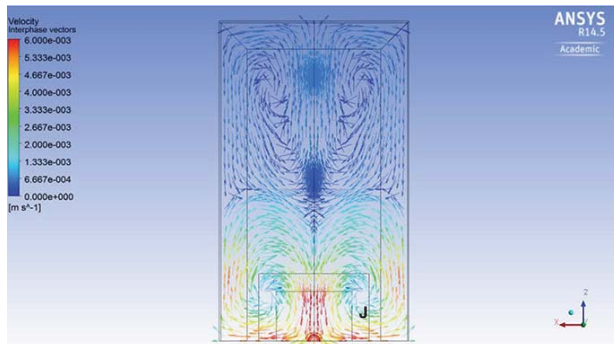


Figure 27—Tangential flow to the interface at 0 mm depth in the case of FCD

Conclusions

Tundish slag behaviour

Results from the physical model showed that the steel-slag interface remains immobile during operation with both the bare tundish and the tundish with a FCD. Sampling of entrained paraffin 'slag' at a depth of 220 mm showed that the entrained tundish 'slag', in the case of both bare and FCD tundishes, tended to concentrate behind the inlet shroud. There is less concentration of entrained slag towards the tundish endwalls.

Numerical model for slag entrainment

A numerical model was developed using the realizable k- ϵ model with mesh size of 1.4 mm and a time step of 0.125 seconds. The numerically modelled residence time distribution and entrained slag behaviour agreed strongly with those of the physical model.

Mechanisms for tundish slag entrainment

An analysis of numerically developed tangential velocities below the steel-slag interface (0–50 mm below the interface) showed that in both the bare tundish and tundish with a FCD, the tangential velocities are a factor of 10 less than the critical velocities necessary for Kelvin-Helmholtz instability and any other form of macroscopic entrainment.

The existence of relatively high tangential velocity vectors only 10 mm or more below the steel-slag interface, resulting in shearing of the slag layer, suggests that the slag moves across the interface by mass transfer. Then, shearing caused by low tangential velocities below the interface is responsible for carrying the slag into the bulk steel phase.

It can therefore be concluded that slag entrainment in both the bare tundish and the tundish with a FCD takes place by two mechanisms: mass transfer across the interface and low-velocity shearing.

Numerical and physical modelling of tundish slag entrainment

Recommendations

Incorporate the slag phase in future tundish studies

This study has resulted in new information being added to the already extensive literature on tundish operations. It was shown that a physical model and a numerical study involving tundish slag can be constructed with relative ease.

To provide more complete models, it is recommended that future work involving tundishes includes the slag layer. This will help provide more comprehensive solutions that will aid in improving tundish performance.

Validate both numerical and physical data with experimental work

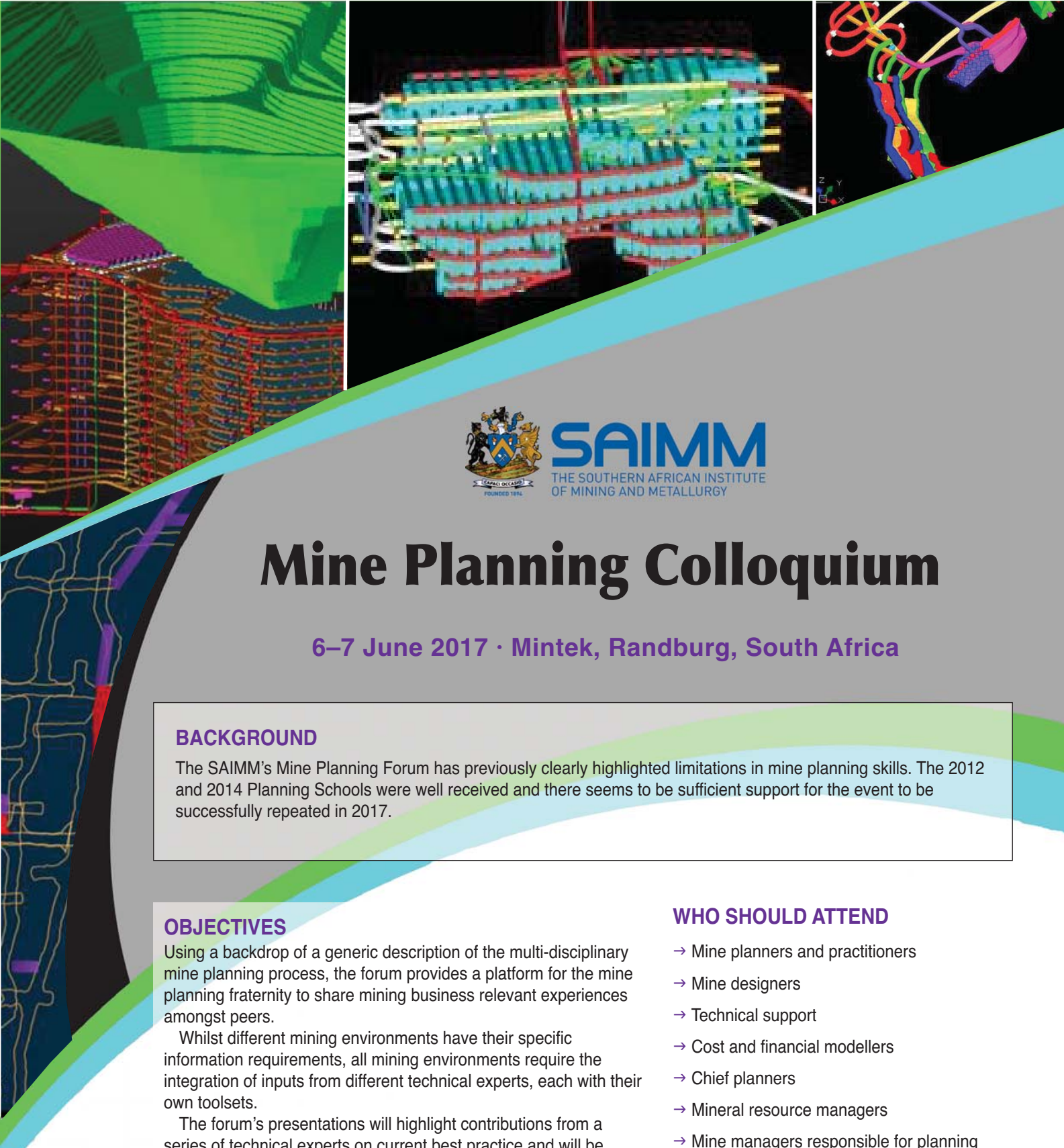
Although appropriate dimensionless numbers were used in this work, and the results ought therefore to be the same as the prototype results, it is still recommended that the concentration of slag entrained at the depths studied in this work and the mechanism of tundish slag entrainment be verified in an industrial tundish.

Incorporate inclusion modelling (numerical and physical)

In this study the concept of tundish modelling has been expanded by including a slag phase. However, there is still scope to extend studies by incorporating inclusion modelling in the existing tundish slag model. Such work will help researchers to gain a complete understanding of how the tundish behaves under the influence of a flow control device. The size and properties of the particles to be used will have to satisfy the requirements of dimensionless number similarities.

References

- ANSYS. 2011. ANSYS Fluent theory guide, version 14.
- BAKKER, A. 2008. Computational Fluid Dynamics. <http://www.bakker.org/> [Accessed 27 April 2014].
- CHATTOPADHYAY, K., ISAC, M., and GUTHRI, R.I.L. 2010. Physical and mathematical modelling of steelmaking tundish operations: a review of the last decade (1999–2009). *ISIJ International*, vol. 50, no. 3. pp. 331–348.
- CLOETE, J.H. 2014. Flow analysis of a four-strand steelmaking tundish using physical and numerical modelling. Master's thesis, University of Stellenbosch.
- FELDBAUER, S. and CRAMB, A.W. 1995. *Proceedings of the 13th Process Technology Conference*, Nashville, TN, 2–5 April 1995. Iron and Steel Society, Warrendale, PA. pp. 327–340.
- HAGEMANN, R., RÜDIGER, S., HELLER, H.P., and SCHELLER, P.R. 2013. Model investigations on the stability of the steel-slag interface in continuous-casting process. *Metallurgical and Materials Transactions*, vol. 44, no. 1. pp. 80–90.
- HARMAN, J.M. and CRAMB, A.W. 1996. A study on the effect of fluid physical properties on droplet emulsification. *Proceedings of the 79th Steelmaking Conference*, Pittsburgh, PA, 24–27 March 1996. Iron and Steel Society of AIME, Warrendale, PA. pp. 773–784.
- HIBBELER, L.C. and THOMAS, B.G. 2010. Investigation of mold flux entrainment in CC molds due to shear layer instability. *Proceedings of the 2010 AISTech Steelmaking Conference*. Association for Iron & Steel Technology, Warrendale, PA. pp. 1215–1230.
- IGUCHI, M., YOSHIDA, J., SHIMIZU, T., and MIZUNO, Y. 2000. Model study on entrapment of mold powder into molten steel. *ISIJ International*, vol. 40, no. 7. pp. 658–691.
- JHA, P.K., DASH, S.K., and KUMAR, S. 2001. Fluid flow and mixing in a six strand billet caster tundish: a parametric study. *ISIJ International*, vol. 41, no. 12. pp. 1437–1446.
- JHA, P.K., RAO, P.S., and DEWAN, A. 2008. Effect of height and position of dams on inclusion removal in a six strand tundish. *ISIJ International*, vol. 48, no. 2. pp. 154–160.
- JOHANSEN, E.M. 1924. The interfacial tension between petroleum products and water. *Industrial and Engineering Chemistry*, vol. 16, no. 2. pp. 132–135.
- JOO, S. and GUTHRIE, R.I.L. 1991. Heat flow and inclusion behaviour in a tundish for slab casting. *Canadian Metallurgical Quarterly*, vol. 30. pp. 261–269.
- KRISHNAPISHARODY, K. and IRONS, G.A. 2008. An extended model for slag eye size in ladle metallurgy. *ISIJ International*, vol. 48, no. 12. pp. 1807–1809.
- KUMAR, A., KORIA, S.C., and MAZUMDAR, D. 2007. Basis for systematic hydrodynamic analysis of a multi-strand tundish. *ISIJ International*, vol. 47, no. 11. pp. 1618–1624.
- KUMAR, A., MAZUMDAR, D., and KORIA, S.C. 2008. Modeling of fluid flow and residence time distribution in a four-strand tundish for enhancing inclusion removal. *ISIJ International*, vol. 48. pp. 38–47.
- LAUNDER, B.E. and SPALDING, D.B. (eds.). 1972. *Lectures in Mathematical Models of Turbulence*. Academic Press, London.
- MAZUMDAR, D. and GUTHRI, R.I.L. 1999. The physical and mathematical tundish systems. *ISIJ International*, vol. 39, no. 6. pp. 524–547.
- MILLS, K. 2011. The estimation of slag properties. *Proceedings of Southern African Pyrometallurgy 2011*, Misty Hills Conference Centre, Muldersdrift, Gauteng, South Africa, 6–9 March 2011. Jones, R.T. and den Hoed, P. (eds.). Southern African Institute of Mining and Metallurgy, Johannesburg, pp. 1–52.
- MILNE-THOMSON, L.M. 1968. *Theoretical Hydrodynamics*. 5th edn. Macmillan, London.
- NAGAOKA, T., RADOT, J.P., REYNOLDS, T., VATERLAUS, A., and WOLF, M. 1986. The basic concept of the extra low head caster for slabs and blooms. *Proceedings of the 69th Steelmaking Conference*, Washinton, 6–9 April 1986. Lucenti, G.S. (ed.). Iron and Steel Society of AIME, Warrendale, PA. vol. 69. pp. 799–810.
- REILLY, C., GREEN, N.R., JOLLY, M.R., and GEBELIN, J. 2013. The modelling of oxide film entrainment in casting systems using computational modelling. *Applied Mathematical Modelling*, vol. 37. pp. 8451–8466.
- SAHAI, Y. and BURVAL, M.D. 1992. *Proceedings of the 50th Electric Furnace Conference*, Atlanta, GA, 10–13 November 1992. Iron and Steel Society of AIME, Warrendale, PA. pp. 469–474.
- SAHAI, Y. and EMI, T. 1996. Melt flow characterization in continuous casting tundishes. *ISIJ International*, vol. 36, no. 6. pp. 667–672.
- SAHAI, Y. and EMI, T. 2008. *Tundish Technology for Clean Steel Production*. World Scientific Publishing, Singapore.
- SENGUTTUAN, A. and IRONS, G.A. 2013. Model studies on slag metal entrainment in gas-stirred ladles. *AIST Transactions*, vol. 1, no. 1. pp. 230.
- SOLHED, H. and JONSSON, L. 2003. An investigation of slag floatation and entrapment in a continuous-casting tundish using fluid-flow simulations, sampling and physical metallurgy. *Scandinavian Journal of Metallurgy*, vol. 32, no. 1. pp. 15–30.
- SOLHED, H., JONSSON, L., and JÖNSSON, P. 2008. Modelling of steel/slag interface in a continuous casting tundish. *Steel Research International*, vol. 79, no. 5. pp. 348–357.
- TRIPATHI, A. and AJMANI, S.K. 2005. S.K. Numerical investigation of fluid flow phenomenon in a curved shape tundish of billet caster. *ISIJ International*, vol. 45, no. 11. pp. 1616–1625.
- TRIPATHI, A. and AJMANI, S.K. 2011. Effect of shape and flow control devices on the fluid flow characteristics in three different industrial six strand billet caster tundish. *ISIJ International*, vol. 51, no. 10. pp. 1647–1656. ◆



SAIMM
THE SOUTHERN AFRICAN INSTITUTE
OF MINING AND METALLURGY

Mine Planning Colloquium

6–7 June 2017 · Mintek, Randburg, South Africa

BACKGROUND

The SAIMM's Mine Planning Forum has previously clearly highlighted limitations in mine planning skills. The 2012 and 2014 Planning Schools were well received and there seems to be sufficient support for the event to be successfully repeated in 2017.

OBJECTIVES

Using a backdrop of a generic description of the multi-disciplinary mine planning process, the forum provides a platform for the mine planning fraternity to share mining business relevant experiences amongst peers.

Whilst different mining environments have their specific information requirements, all mining environments require the integration of inputs from different technical experts, each with their own toolsets.

The forum's presentations will highlight contributions from a series of technical experts on current best practice and will be augmented by displays of state of the art mine planning tools in order to create a learning experience for increased planning competencies.

WHO SHOULD ATTEND

- Mine planners and practitioners
- Mine designers
- Technical support
- Cost and financial modellers
- Chief planners
- Mineral resource managers
- Mine managers responsible for planning
- Consultants
- Independent mine planning consultants.

FOR FURTHER INFORMATION CONTACT:

Head of Conferencing,
Camielah Jardine, SAIMM,
Tel: +27 11 834-1273/7 · Fax: +27 11 833-8156
E-mail: camielah@saimm.co.za
Website: <http://www.saimm.co.za>

SPONSORS:

UKWAZI
www.ukwazi.com

UNIVERSITY OF THE
WITWATERSRAND,
JOHANNESBURG

Conference Announcement



Towards an inclusive model to address unsuccessful mine closures in South Africa

by E.S. van Druten* and M.C. Bekker*

Synopsis

The complete and successful closure of a mine in the South African environment remains problematic. Closure remains an elusive mining phase due to unclear roles and responsibilities, inaccurate closure management data, and the inability of stakeholders to conceptualize and integrate closure information into business processes. Currently there are no proven methods available to address the complexities encountered during a closure application, and to date no mine has been granted full closure. Many mines are left abandoned and unrehabilitated, resulting in risk to investors, surrounding communities, and regulators. This investigation aimed to determine, categorize, and rank reasons for unsuccessful mine closures. Focus groups consisting of public and private stakeholders were identified and surveyed through a structured, rank-order questionnaire to determine the relative importance of reasons why achieving formal and final mine closure remains elusive. Various requirements and aspects were identified and listed according to four categories: namely, primary, secondary, process drivers, and information sources. These aspects should be considered in the development of an integrated mine closure model.

Keywords

mine closure, rehabilitation, planning process, integrated mine closure model.

Background and rationale

Prior to 1956, mine closures were not subject to legislative requirements, being merely governed by insufficient environmental regulations under the Mines and Works Act 27 (MWA) (Swart, 2003). In 1981 the Chamber of Mines (COM) published a document titled '*The rehabilitation of land disturbed by surface coal mining*', which constituted the first notable contribution to environmental protection. This guideline was later referenced in the Minerals Act of 1991, which for the first time laid definite environmental burdens on the Mining Right Holder (MRH). The Minerals Act of 1991 was superseded by the current Mineral and Petroleum Resources Development Act (MPRDA) and the Mineral and Petroleum Resources Development Act Regulations (MPRDAR), which specify a regulatory process for mine closure applications and financial provisions.

Notwithstanding, it is estimated that there are approximately 5700 derelict and ownerless mines in South Africa which will require 800 years to rehabilitate at a cost of R100 billion

(Brown, 2007; Nzimande and Chauke, 2012). An investigation by the Auditor General (2009) identified and listed 5906 abandoned mines as of May 2008. As of 2011 no closure certificate had been issued under the Minerals Act of 1991 or the MPRDA (Botham, 2011), and mine closure has become the focus of mining companies, governments, and non-governmental organizations (Laurence, 2000). Formal mine closure remains an elusive undertaking presenting various risks and significant liabilities affecting investor confidence, and threatening the viability of the mining industry in South Africa.

This study was prompted by the increasing statutory pressure exerted on mines to achieve closure. It was believed that there are critical reasons for unsuccessful mine closures (van Druten, 2015). The study aimed to identify, categorize, and rank those reasons, and put forward considerations for improved mine closures.

The research problem

Successful mine closure applications remain elusive, resulting in adverse impacts on the environment, investor confidence, and the viability of the South African mining industry.

In an attempt to address the research problem the following research questions were formulated:

- What are the main reasons for unsuccessful mine closure applications?
- What aspects should be considered towards the development of an integrated closure model?

Although mining presents opportunities for economic growth, it remains difficult to secure attractive investments in sustainable

* Graduate School of Technology Management,
University of Pretoria, South Africa.

© The Southern African Institute of Mining and Metallurgy, 2017. ISSN 2225-6253. Paper received Apr. 2016; revised paper received Sep. 2016.

Towards an inclusive model to address unsuccessful mine closures in South Africa

mining scenarios that include successful mine closure. Mine closure remains an elusive mining phase and the sector is under statutory pressure to prove its sustainability, not only through its economic contribution but also by achieving sustainable post-mining conditions. The purpose of this paper is therefore to further investigate and identify the specific reasons for unsuccessful mine closure in South Africa and to present considerations toward the development of an improved mine closure process model.

Literature review

The closure and rehabilitation of a mine entails a formal, approved programme to restore the physical, chemical, and biological quality of air, land, and water where mining took place (Australian and New Zealand Minerals and Energy Council, 2000). Mine closure forms part of the mine's long-term planning (Kloppers, Horn, and Visser, 2015) and aims towards the creation of sustainable living outcomes through the minimization of environmental, social, and economic impacts on host communities once mining has ceased (Logan, Murphy, and Beale, 2007). The process of mine closure occurs at the point where the development and revenue costs of the mining operation approach zero value and the remediation cost becomes evident (Turton, 2008). Unfortunately, the closure of a mine is a complex process that is influenced by a variety of political, social, economic, and technical factors that need to be balanced to ensure a successful mine closure application. Due to the disruptive nature of mining it has become synonymous with adverse environmental and social effects. Adverse environmental effects are manifest particularly in surface and groundwater systems, pollution of agricultural soil, air pollution, sinkholes due to the accelerated weathering of dolomites by acid minewater, unsafe living conditions in adjacent communities, dust generation, and the destruction of ecosystems (Auditor General, 2009).

The reasons reported for unsuccessful closure are numerous, and are often associated with organizational and stakeholder interaction, poor scope definition and planning, unclear relinquishment criteria, legal and financial constraints, and social, scientific, or environmental concerns.

Hordley (cited in Australian and New Zealand Minerals and Energy Council, 2000, p. 6) describes closure as 'the converse of closure skill levels, operational experience, motivation and commitment'. Mine closure necessitates specialist and administrative skills and input at national, provincial, and local levels. According to Mhlongo and Ampsonah-Dacosta (2016, p. 279) the lack of clear assigned responsibilities as well as the absence of criteria and standards for rehabilitation are major causes for delays in rehabilitation. Van Eeden, Lieferink, and du Rand (2009 p. 52) agree with the multidisciplinary requirement and stress the importance of addressing differences of interpretation between government and the MRH. Du Plessis (n.d.) contextualizes the responsibilities created by a mine closure application through the Constitution at national, provincial, and local levels which leads to misalignment among the hierarchical reporting structures. This results in all three spheres of government being 'distinctive, interdependent and interrelated', and all of them have environmental responsibilities during a closure application. Adding to the dilemma of

closure, there seems to be no clear and widely accepted definition of abandoned mines (Mhlongo, 2012).

The disparity among stakeholders representing statutory institutions and subsequent delays in decision-making and progress results in defensive behaviour from MRHs. Adler *et al.*, (2007, p. 36) argue that mining companies have held production costs artificially low, deflecting rehabilitation costs to the State and third parties.

Integrated mine closure planning (IMCP) requires closure planning and execution to start prior to the commencement of physical mining activities and continue until final closure of a mining operation. Unfortunately, the planning process is often fast-tracked, causing some technical and statutory aspects to be omitted during the early phases and then to be re-addressed and compensated for during the closing phases of the project life-cycle (Anglo American, 2013). The Government of Western Australia (GWA) (2011, p. 3) reflects a similar stance and reports that planning for mine closure should start before mining commences and continue throughout the life of the mine until final closure is achieved.

The International Council on Mining and Metals (ICMM, 2006, p. 5) recognizes the responsibilities of the MRH during closure. The responsibilities shall include the provision of adequate financial resources, definition of a clear mining closure process, and ensuring that the public is not left with a liability.

Du Plessis (n.d.) recognized the existence of mine closure functions in law, emphasizing that government officials are often unwilling to cooperate. He reports that the fragmentation of departments dealing with different aspects of the environment results in uncoordinated application of environmental legislation. The accompanying lack of skills and funds compounds the poor effort towards the mine closure process.

Dual responsibilities towards mine activities remains a recurring dilemma. Even as far back as 1998 the Department of Environmental Affairs and Tourism (DEAT) was the designated competent authority for Environmental Impact Assessment (EIA) authorization. The Department of Minerals and Energy (DME) was, however, the competent authority for mining projects. This dual approach to EIA is mentioned as a major contributor to delays in closure activities (Sandham, Hoffmann, and Retief, 2008).

Financial assurances for eventual mine closure are required by section 41 of the MPRDA and implemented through the Department of Mineral Resources (DMR) financial provision guideline (2005). The MRH is therefore required to determine the closure obligation and report a financial provision to the DMR. The accuracy of the provision is often questioned due to inaccurate assessments, shortfalls, over-provisions, and inconsistent regulatory expectations.

IMCP is exemplified by integrating mine closure requirements into core business, legal, operational, and relevant external processes instead of relying on retrofitted closure plans. The intent is that IMCP should consequently offer improved stakeholder and regulatory interaction and have a positive influence on concurrent rehabilitation planning and execution (Limpitlaw and Briel, 2014). It is notably a concept omitted as a mine closure principle from sections 56 and 57 of the MPRDA, creating uncertainty of its relevancy and consequently being overlooked by stakeholders.

Towards an inclusive model to address unsuccessful mine closures in South Africa

Environmental and social closure outcomes rely on the accuracy of scientific and social indicator data, as well as the ability of stakeholders to conceptualize data to produce effective closure objectives and relinquishment criteria. This is often hampered by vague directives in the MPRDA, highly complex environmental aspects during closure, unpredictability of post-closure impacts, inconsistent, inaccurate closure performance reviews, and an inability to secure stakeholder inputs on closure requirements. Despite all the shortcomings, it remains important to approach any form of rehabilitation in a structured manner and identify commonly agreed key performance areas (Dougall and Mmola, 2015, 1003).

Research design

In summarizing the literature findings, the reasons for mine closure failure can be clustered in seven categories: organiza-

tional, planning, relinquishment, legal, financial, social, and scientific, which also addresses the environmental influences. A total of 37 possible causes for unsuccessful mine closure were identified and allocated to the appropriate categories (see Table I). It was also evident from the literature that the poor record of mine closure was predominately due to the actions, or lack thereof, of direct role-players from formal institutions as opposed to wider society.

In order to assess the influence of the identified reasons on the poor performance of mine closure, six focus groups (FGs) comprising 31 individual representatives were identified from various stakeholders involved in mine closure efforts. The six FGs were national regulators (NR), educational research facilities (ERF), consultants (C), non-governmental organizations (NGO), mine management (MM), and environmental legal specialists (LSpec). The C group comprised three subgroups, namely engineering

Table I

Reasons for unsuccessful mine closure per category

Number	Reason	
A: Organizational	A1	Disengagement among regulators and stakeholders
	A2	Unclear roles and responsibilities of regulators and stakeholders
	A3	Shortage of relevant skills and knowledge with regulators
	A4	Lack of a dedicated MCPT
	A5	Lack of qualified and experienced mine closure auditors
B: Planning	B1	Lack of closure planning and integration during feasibility stages
	B2	Mine closure requirements not included in operational processes
	B3	Lack of concurrent rehabilitation planning
	B4	Non-alignment of closure plans with local or regional spatial development plans
	B5	Non-responsiveness to changing closure requirements over time
	B6	Regulator and stakeholder disregard of IMCP practices
C: Relinquishment	C1	Deficient post-closure risk assessment reports
	C2	Inaccurate social relinquishment criteria
	C3	Inaccurate environmental relinquishment criteria
	C4	Inaccurate aesthetical relinquishment criteria
	C5	Inaccurate land use relinquishment criteria
D: Legal	D1	Overlapping and contradicting regulatory mandates
	D2	Inaccurate financial provisions (MPRDA Section 41 (1))
	D3	Lack of DWS and DMR interaction on closure approvals (MPRDA Section 43 (5))
	D4	Incomplete closure applications (MPRDA Section 43 (4): I)
	D5	Nonspecific environmental objectives approved in EMP's (MPRDAR 51 (a) i)
	D6	Incorrect itemization of closure items (MPRDA Regulations 54 (1))
E: Financial	E1	Lack of internalized financial provisions
	E2	Lack of accurate and comprehensive financial liability assessments
	E3	Non standardized methods and mechanisms for financial provision
	E4	Unrealistic regulatory closure provision requirements
	E5	Inaccessibility of funds during closure
F: Social	F1	Uncertainty of health risks around un-rehabilitated mining areas
	F2	Agricultural potential of land and social structures
	F3	Ineffective conceptualization of social issues toward closure
	F4	Ineffective social interaction when establishing closure objectives
	F5	Understated social considerations during closure
G: Scientific	G1	Incorrect quantification of lasting environmental impacts (MPRDA Regulations 56 (d))
	G2	Incorrect quantification of latent environmental impacts (MPRDA Regulations 56 (d))
	G3	Insufficient internal skillset required to conceptualize scientific results
	G4	Absence of an ongoing closure performance auditing and reporting plan
	G5	Lack of effective interaction between scientists during closure planning

Towards an inclusive model to address unsuccessful mine closures in South Africa

consultants (CEng), environmental consultants (CE), and social consultants (CS). The MM group comprised four subgroups, namely safety, health, environmental, and quality managers (MMSHEQ), environmental managers (MME), operational managers (MMOPS), and strategic managers (MMStrat). The overall profile of the complete FG is presented in Table II.

To determine the relative importance of an identified reason for unsuccessful mine closures, a rank order approach was adopted. A questionnaire was compiled requesting the FG members to rank the various contributing reason per category. The most important contributing reason to their view was to be ranked '1', second most important reason as '2', and the least important reason '5' or '6', depending on the category ranked. An average rank for each categorized reason per FG was determined by averaging the individual rankings of the FG respondents in that group (Table III).

Table II
Composition of the focus group

Number	Description	Abbreviation	Members
1	National Regulator	NR	2
2	Educational research facility	ERF	3
3	Consultants	C	9
3.1	Engineering consultants	CEng	3
3.2	Environmental consultants	CE	3
3.3	Social consultants	CS	3
4	Non-governmental organizations	NGO	2
5	Mine management	MM	12
5.1	SHEQ	MMSHEQ	2
5.2	Environmental	MME	4
5.3	Operational	MMOPS	3
5.4	Strategic	MMStrat	3
6	Legal specialists	LSpec	3
Total	31		

Table III

Ranked reasons per FG stakeholder group

Category	Reason	Focus Group														Overall	
		NR		ERF		C		NGO		MM		LSpec					
		Av	R	Av	R	Av	R	Av	R	Av	R	Av	R	Av	R		
A: Organizational	A1	3.50	3	4.00	4	3.22	3	3.50	3	2.02	1	3.00	3	3.21	3		
	A2	3.00	2	4.67	5	3.11	2	2.50	1	3.06	4	4.00	5	3.39	5		
	A3	1.00	1	2.67	3	2.78	1	3.00	2	3.04	3	1.67	1	2.36	1		
	A4	4.00	4	2.00	2	3.11	2	2.50	1	2.71	2	2.67	2	2.83	2		
	A5	3.50	3	1.67	1	2.78	1	3.50	3	4.17	5	3.67	4	3.21	4		
B: Planning	B1	4.50	4	2.33	2	2.22	1	3.00	2	3.04	2	1.33	1	2.74	1		
	B2	3.50	3	2.00	1	3.33	4	3.00	2	2.54	1	4.33	4	3.12	2		
	B3	3.00	2	4.00	4	2.78	2	4.00	3	3.10	3	4.00	3	3.48	4		
	B4	1.50	1	5.33	5	3.22	3	4.50	4	4.42	6	4.00	3	3.83	5		
	B5	3.50	3	4.00	4	4.56	5	2.50	1	4.00	5	1.67	2	3.37	3		
	B6	5.00	5	3.33	3	4.89	6	4.00	3	3.9	4	5.67	5	4.46	6		
C: Relinquishment	C1	2.00	1	3.00	2	1.67	1	2.00	1	2.83	4	2.67	3	2.36	1		
	C2	2.00	1	3.67	3	3.89	4	3.00	3	2.67	3	2.33	2	2.93	4		
	C3	4.50	2	2.00	1	2.56	2	2.50	2	2.48	1	1.67	1	2.62	3		
	C4	4.50	2	4.33	4	4.11	5	5.00	4	4.4	5	5.00	5	4.56	5		
	C5	2.00	1	2.00	1	2.78	3	2.50	2	2.63	2	3.33	4	2.54	2		
D: Legal	D1	3.00	3	4.33	5	3.11	2	1.00	1	2.42	1	1.00	1	2.48	2		
	D2	2.00	1	1.67	1	3.44	3	4.50	4	2.46	2	4.00	3	3.01	3		
	D3	2.50	2	3.00	2	2.44	1	2.00	2	2.48	3	2.00	2	2.40	1		
	D4	5.50	6	4.67	6	3.78	4	4.50	5	4.75	5	4.33	4	4.59	5		
	D5	3.50	4	3.33	3	3.78	4	3.00	3	3.77	4	4.00	3	3.56	4		
	D6	4.50	5	4.00	4	4.44	5	6.00	6	5.13	6	5.67	5	4.96	6		
E: Financial	E1	5.00	4	1.33	1	3.00	3	3.00	2	3.4	4	4.67	4	3.4	4		
	E2	3.00	3	2.00	2	2.56	2	3.00	2	2.71	2	2.67	2	2.66	2		
	E3	3.00	3	4.67	5	3.56	4	4.00	3	3.42	5	2.33	1	3.5	5		
	E4	2.50	2	4.00	4	2.33	1	2.00	1	2.63	1	2.33	1	2.63	1		
	E5	1.50	1	3.00	3	3.56	4	3.00	2	2.85	3	3.00	3	2.82	3		
F: Social	F1	4.50	4	4.67	4	2.67	1	4.00	2	4.31	5	3.67	4	3.97	5		
	F2	4.50	4	3.00	3	3.33	3	5.00	3	3.88	4	3.33	3	3.84	4		
	F3	2.00	2	2.67	2	2.78	2	2.00	1	2.33	2	3.67	4	2.57	2		
	F4	1.50	1	2.00	1	2.67	1	2.00	1	1.9	1	2.00	1	2.01	1		
	F5	2.50	3	2.67	2	3.56	4	2.00	1	2.58	3	2.33	2	2.61	3		
G: Scientific	G1	3.50	3	2.67	2	2.33	1	2.50	2	2.23	1	1.67	1	2.48	1		
	G2	3.50	3	2.67	2	2.89	3	4.00	4	3.15	4	2.67	2	3.5	3		
	G3	3.00	2	3.67	3	3.78	5	3.00	3	2.96	3	4.00	5	3.40	5		
	G4	3.00	2	1.00	1	2.44	2	4.00	4	2.92	2	3.00	3	2.73	2		
	G5	2.00	1	5.00	4	3.56	4	1.50	1	3.75	5	3.67	4	3.25	4		

Towards an inclusive model to address unsuccessful mine closures in South Africa

Results

A fair level of agreement among the FGs were observed regarding the relative importance of the various reasons for unsuccessful mine closure, especially with respect to the top three reasons under each category.

Under category A (Organizational), all six FGs ranked 'Shortage of relevant mine closure skills and knowledge within the regulator' among the top three reasons. Even though 'Lack of qualified and experienced mine closure auditors' scored the highest rank (lowest influence), it was ranked by C (rank 2) and NGO (rank 1) as significant. This could be a result of these FGs believing that once their work is completed, auditing of the closure process is not completed satisfactorily. Apart from NR (rank 4), all other FGs ranked 'Lack of a dedicated mine closure project management team (MCPT)' high with either rank 1 or rank 2.

In order to improve organizational effectiveness towards mine closure, the level of skills within the regulator needs to be addressed as well as the mobilization of dedicated project teams.

Apart from NR (ranked 4) 'Lack of closure planning during feasibility stages' was ranked the most, or second most, important reason under category B (Planning). The reason could be that the NR is not integrally involved during the feasibility stages of the project. It is interesting to note that the NR group viewed 'Non-alignment of closure plans with the regional spatial development plans' as the most important reason, whereas the overall rank for this reason is 5. In recognition of the importance of planning, the overall rank for 'Regulatory disregard for IMCP practices' was the lowest (6).

Under category C (Relinquishment), 'Deficient post closure risk assessment reports' and 'Inaccurate land use relinquishment criteria' appear to be the most significant reasons for unsuccessful mine closure.

The dual-responsibility dilemma and fragmentation among statutory bodies (du Plessis, n.d.) was emphasized under category D (Legal). 'Lack of interaction between Department of Water Affairs (DWA) and DMR on closure approvals in accordance with MPRDA Section 43 (5)' and 'Overlapping and contradicting regulatory mandates' were strongly regarded by the majority of FGs as the key reasons for failure. This disparity is an institutional problem that needs government intervention to resolve towards a single point of responsibility.

It is significant that 'Incorrect itemization of closure items required by the MPRDA Regulations 54 (1)' was not deemed an important reason for failure, indicating that role-players do comply with statutory formalities. The process seems to halt at decision-making activities.

Under category E (Financial) no significant reason was identified as a distinct contributor to failure. The average rating scores were fairly close, with 'Unrealistic regulatory closure provision requirements' rating first and 'The lack of accurate and comprehensive financial liability assessments' a close second. The provision of financial resources is accepted by stakeholders and it is believed that most will adhere to the provision requirements.

All participating FGs agreed that 'Ineffective social interaction when establishing closure' was the main reason for failure under category F (Social). The knowledge and awareness of stakeholder regarding the health risks around

unrehabilitated areas were confirmed with 'The uncertainty of health risks around un-rehabilitated mining areas' regarded as the least significant reason for failure.

Under category G (Scientific), a general consensus is observed among FGs that 'The incorrect quantification of lasting environmental impacts (MPRDA Regulations 56 (d))' is the most significant reason for unsuccessful mine closure. This could be due to the lack of extended historical data on the long-term impact of rehabilitation. The fact that 'The insufficient internal skillset required to conceptualize scientific results' was considered as the least significant reason for failure indicates that the FG stakeholders acknowledge that skilled scientists put effort into better understanding the rehabilitation of mining areas.

Conclusions

The formal and successful closure of depleted mining complexes remains an elusive goal. Through a literature study of the poor performance of this final stage of the mining life-cycle, 37 potential contributing reasons for failure were identified and clustered into seven categories. A total of 31 stakeholders in the mine closure process were identified and clustered in six FGs. A ranking questionnaire was circulated to the various stakeholders and their feedback was analysed.

The categorized ranking quantified the reasons for consideration toward improved mine closure, while the comparison amongst the FGs confirmed specific opinions and expectations.

It was commonly agreed that the lack of skills and dedicated project teams were significant contributors to poor performance, and therefore a formal and concerted effort should be launched to train and educate stakeholders. Lack of planning during the feasibility stages was a contributing factor, while deficient post-closure risk assessment reports and inaccurate land use relinquishment criteria were also mentioned. Institutional uncertainties and dual responsibilities paralyse decision-making at top management level, thereby effectively halting any form of progress. Government intervention is urgently required to address the current fragmentation among government departments. Insufficient financial provision does not seem to be a major contributing factor. However, ineffective social interaction when establishing closure objectives appears to be the most agreed upon reason for social failure among FGs. A concerted effort should be launched to communicate to stakeholders, especially those physically and financially affected, regarding the process and impact of mine closure on their livelihood.

Scientifically, it seems as if experts are doing what they can; however, the long-term process and effects of mine rehabilitation are still unknown.

Given the findings of the research, an integrated mine closure model is proposed.

Recommendations

An integrated mine closure model should aim to include all the aspects that could influence the closure process. Such a model should structure all the data, information, processes, activities, deliverables, interactions, and decisions required for successful mine closure. Based on the findings in this research, four categories of aspects were identified that should be considered towards the development of an all-inclusive mine closure model.

Towards an inclusive model to address unsuccessful mine closures in South Africa

Firstly, five primary considerations (PC), and four secondary considerations (SC) were identified as most important regarding successful mine closure. These considerations are shown in Table IV.

Secondly, the combined ranking and comparison results highlighted critical closure process drivers (PD) and information sources (IS) that are required to inform and contextualize the PC and SC during closure planning. Table V depicts these PD and IS requirements for improved mine closures.

When considering a mine closure model it will be advisable to integrate the PC, SC, PD, and IS aspects. This model should complement the overall life-cycle management (LCM) of the mine and provide a real-time reference to the

mining phase and the immediate and future rehabilitation liability while securing closure expectations from the regulator, the MRH, and other stakeholder groups.

References

- ADLER, R.A., CLAASSEN, M., GODFREY, L., and TURTON, A.R. 2007. Water, mining, and waste: An historical and economic perspective on conflict management in South Africa. *Economics of Peace and Security Journal*, vol. 2, no. 2. pp.33–41.
- ANGLO AMERICAN. 2013. Mine closure toolbox version 2. Anglo American plc. Johannesburg, South Africa
- AUDITOR GENERAL. 2009. Report to Parliament on a performance audit of the rehabilitation of abandoned mines at the Department of Minerals and Energy. Pretoria, South Africa.
- AUSTRALIAN AND NEW ZEALAND MINERALS AND ENERGY COUNCIL. 2000. Strategic framework for mine closure. Report no. ISR 2000/155. Minerals Council of Australia, Canberra, Australia.
- BOTHAM, N.D. 2011. A critical analysis of the mine closure process as followed by the De Beers Oaks diamond mine. MSc thesis, University of Johannesburg, South Africa.
- BROWN, J. 2007. Derelict mines to cost state R100bn. *Business Report*, 23 May 2007. p 22.
- CHAMBER OF MINES OF SOUTH AFRICA. 2007. Guidelines for the rehabilitation of mined land. Chamber of Mines of South Africa, Coaltech Research Association, Johannesburg.
- DOUGALL, A.W. and MMOLA, T.M. 2015, Identification of key performance areas in the Southern Africa surface mining delivery environment. *Journal of the Southern African Institute of Mining and Metallurgy*, vol. 115. pp. 1001–1006.
- DU PLESSIS, A. and BRENT, A.C. 2006. Development of a risk-based mine closure cost calculation model. *Journal of the South African Institute of Mining and Metallurgy*, vol. 106. pp. 443–450.
- DU PLESSIS, M. Not dated. Legal mechanisms for cooperative governance in South Africa: successes and failures. LLB dissertation, University of Cape Town.
- GOVERNMENT OF WESTERN AUSTRALIA (GWA). 2011. Guidelines for preparing mine closure plans. Government of Western Australia, Environmental Protection Authority. Australia.
- ICMM (International Council on Mining and Metals). 2006. Guidance paper for financial assurance for mine closure and reclamation. London, UK.
- ICMM (International Council on Mining and Metals). 2008. Planning for integrated mine closure: toolkit. London, UK.
- KLOPPERS, B.J., HORN, C.J., and VISSER, J.V.Z. 2015. Strategic and tactical requirements of a mining long-term plan. *Journal of the Southern African Institute of Mining and Metallurgy*, vol. 115. pp. 515–521.
- LOGAN, R.B., MURPHY, D.P., and BEALE, C.A. Mine closure risk and decision analysis. *Proceedings of the Second International Seminar on Mine Closure*, Brisbane, Australia. pp. 1–2.
- LAURENCE, D.C. 2000. Optimisation of the mine closure process. *Journal of Cleaner Production*, vol. 14. pp. 285–298.
- LIMPITLAW, D. and BRIEL, A. 2014. Post-mining land use opportunities in developing countries – a review. *Journal of the Southern African Institute of Mining and Metallurgy*, vol. 114. pp. 899–903.
- MHLONGO, S.E. 2012. Development of a modeling framework for design of low-cost and appropriate rehabilitation strategies for Nyala abandoned mine. MSc dissertation, Department of Mining and Environmental Geology, University of Venda, South Africa.
- MHLONGO, S.E. and AMPONSAH-DACOSTA, F. 2016, A review of problems and solutions of abandoned mines in South Africa. *International Journal of Mining, Reclamation and Environment*, vol. 30, no. 4. pp. 279–294.
- NZIMANDE, Z. and CHAUKE, H. 2012, Sustainable through responsible environmental mining. *Journal of the Southern African Institute of Mining and Metallurgy*, vol. 112. pp. 135–139.
- SANDHAM, L.A., HOFFMANN, A.R., and RETIEF, F.P. 2008. Reflections on the quality of mining EIA reports in South Africa. *Journal of the Southern African Institute of Mining and Metallurgy*, vol. 108. pp. 701–706.
- SOUTH AFRICA. Mineral and Petroleum Resources Development Act 28 of 2002. Government Printer, Pretoria.
- SWART, E. 2003. The South African legislative framework for mine closure. *Journal of the South African Institute of Mining and Metallurgy*, vol. 10. pp. 45–54.
- TURTON, R.A. 2008. Water and mine closure in South Africa: development that is sustainable? On-line dialogue: *Development 2008 'Water and Development'*. CSIR, Pretoria. http://www.researchgate.net/publication/242598362_Water_and_Mine_Closure_in_South_Africa_Development_that_is_sustainable
- VAN EEDEN, E.S., LIEFERINK, M., and DU RAND, J.F. 2009. Legal issues concerning mine closure and social responsibility on the West Rand. *Journal for Transdisciplinary Research in Southern Africa*, vol. 5, no. 1. pp. 51–71.
- VAN DRUTEN, E. 2015. A critical analysis of reasons for unsuccessful mine closures in South Africa. MSc thesis, Department of Engineering and Technology Management, University of Pretoria, South Africa. ♦

Table IV

Primary and secondary considerations for improved mine closure applications

Primary considerations (PC)	
PC 1	Availability of accurate closure management data and information
PC 2	Competence of the stakeholders and the regulator to conceptualise data and information
PC 3	Ability of organizations to integrate mine closure requirements into various business processes
PC 4	Allocation of definitive roles and responsibilities to all stakeholders and regulatory institutions
PC 5	Endorsement of mine closure planning through a dedicated project management structure
Secondary considerations (SC)	
SC 1	Accurate mine closure objectives and targets
SC 2	Qualified mine closure auditors and auditing programmes
SC 3	Elevated levels of skill and knowledge of the stakeholders involved
SC 4	Clear and communicated functional tasks of the stakeholders

Table V

Process drivers and information sources for improved mine closure applications

Process drivers (PD)	
PD 1	Social interventions during closure planning
PD 2	Inter-scientist communication during closure planning
PD 3	Long-term impact identification
PD 4	Consideration to changing environmental conditions
PD 5	Ongoing concurrent rehabilitation planning and reviews
PD 6	Ongoing regulator dexterity development initiatives
PD 7	Clear legal compliance requirements
PD 8	Effective cooperative governance amongst stakeholders
Information sources (IS)	
IS 1	Social abandonment criteria
IS 2	Land use abandonment criteria
IS 3	Environmental abandonment criteria
IS 4	Closure risk assessment report
IS 5	Closure liability assessment
IS 6	Closure performance audit
IS 7	Feasibility planning document
IS 8	Organization procedures and processes
IS 9	Regional spatial development programmes
IS 10	Job description of the mining right holder
IS 11	Job descriptions of other stakeholders
IS 12	Job description of the regulators



Methodology for evaluation of mud rush risk in block caving mining

by J. Vallejos*†, K. Basaure*†, S. Palma*‡, and R.L. Castro*†

Synopsis

Mud rushes are sudden inflows of fine wet ore within underground mines; they can harm people and equipment as well as cause production delays. Block and panel caving mines are prone to mud rushes in their production levels, with mud flowing from the drawpoints. Different mines have developed methods to control drawpoint conditions and thus perform safe ore extraction. The aim of this study is to develop a decision matrix and apply it to samples from drawpoints for the Diablo Regimiento mine, Codelco, El Teniente Division (Chile). The Abrams's Cone was used to perform slump tests on mud samples and characterize their consistency by setting the saturation degree and packing. The unconfined strength for different saturation degrees and packing was then evaluated. The results show that conditions for fluid response in slump tests correspond to conditions for low strength in unconfined compression tests. We also found the water content value at which the flowing consistency changes from plastic to soft behaviour according to the slump test classification for each sample. This value varied between 12.2% and 16.9%, depending on the sample tested. Finally, a fluid security factor was defined in order to design an extraction pattern for the samples tested, based on the water content. We conclude that a very densely packed ore is not prone to flowing. The flow properties depend strongly on the specific properties of the ore tested, and consequently a specific criterion should be developed for different types of ore at a particular mine. The criterion developed for Diablo Regimiento ore provides critical water content values from 11% to 15%, depending on the ore type.

Keywords

mud rush, block caving, risk evaluation.

Introduction

Block/panel caving has the lowest cost and the highest production rates of all underground methods (Heslop, 2000; Hubert *et al.*, 2000). Good management of the risks is important to ensure the security of personnel and infrastructure. Operational risks for the method include rockbursts, air blasts, and mud rushes (Hubert *et al.* 2000). A mud rush is defined as a sudden inflow of mud from a drawpoint or other underground opening into the mine (Butcher, Joughin, and Stacey, 2000; Butcher, Stacey, and Joughin, 2005). Mud rushes can cause dilution, production delays, and damage to equipment as well as injuries and fatalities. The elements necessary for mud rushes are mud-forming material, disturbances, a discharge point, and water (Butcher, Joughin, and Stacey, 2000). All these elements are present in block/panel

caving mines. Mud-forming material comes from ore milled by the caving process; water comes from underground and surface sources. Drawpoints in the production level are discharge points for the mud. Finally, several types of disturbance could trigger the mud rush phenomena: blasting, earthquakes, operation of equipment (Call & Nicholas, Freeport McMoRan, and Hydrologic Consultants, 1998; Jakubec, Clayton, and Guest, 2012), arch collapse above drawbells (Butcher, Joughin, and Stacey, 2000; Butcher, Stacey, and Joughin, 2005; Jakubec, Clayton, and Guest, 2012) and ore drawing (Butcher, Joughin, and Stacey, 2000; Butcher, Stacey, and Joughin, 2005; Call & Nicholas, Freeport McMoRan, and Hydrologic Consultants, 1998; Jakubec, Clayton, and Guest, 2012).

Shear strength loss is considered in two mechanisms for mud rushes postulated by different authors: an increase in water content that changes the mud properties, thus decreasing the shear strength (Butcher, Stacey, and Joughin, 2005; Jakubec, Clayton, and Guest, 2012); and induced pore pressure that causes sudden strength loss (Call & Nicholas, Freeport McMoRan, and Hydrologic Consultants, 1998; Jakubec, Clayton, and Guest, 2012). In this paper we focus on one aspect and study the impact of the variation in the water content, which modifies the mechanical properties of mud ore. Samples were taken from Diablo Regimiento sector (DR), El Teniente Mine, Codelco, Chile, located in the Andes Mountains, 80 km southeast from Santiago, where the mining method employed is panel caving. The aim is to present a method for risk classification of ore in drawpoints in order to prevent the uncontrolled flow of ore into the mine.

* Advanced Mining Technology Center, University of Chile, Santiago, Chile.

† Block Caving Laboratory, Department of Mining Engineering, University of Chile, Santiago, Chile.

‡ School of Civil Engineering, The University of Queensland, Brisbane, Australia.

© The Southern African Institute of Mining and Metallurgy, 2017. ISSN 2225-6253. Paper received Apr. 2016; revised paper received Feb. 2017.

Methodology for evaluation of mud rush risk in block caving mining

Table I

Mud ore classes proposed for IOZ mine (call & Nicholas, Freeport McMoRan, and Hydrologic Consultants, 1998)

ω : Water Content (%)	G: Grain size less than 50 mm	
	G < 30%	G > 30%
$\omega < 8.5\%$	A: Coarse Dry	B: Fine Dry
$\omega > 8.5\% \text{ and } \omega < 11\%$	C: Coarse wet	E: Fine wet
$\omega > 11\%$	D: Coarse very wet	F: Fine very wet

Background

Relevant risk classification

Mud ore from IOZ mine, Freeport, Indonesia was characterized geotechnically by Call & Nicholas, Freeport McMoRan, and Hydrologic Consultants (1998). It was concluded that size distribution of the ore involved in mud rushes was $>20\% <2 \text{ mm}$. Additionally, at saturations greater than 80%, the material was prone to liquefaction due to the excess pore pressure. The density of the ore pile in drawpoints was also measured in order to establish the water content at which the ore reaches 80% saturation. Finally, a classification system was proposed, which recommends a draw procedure depending on the grain size and water content of ore in drawpoints. Six classes for mud ore were defined, each associated with a recommendation of how the ore should be drawn. The classes defined for IOZ mine are summarized in Table I. Classes A and B were recommended to be drawn with any loader with even draw and twice-weekly checking for changes. C and D were recommended to be drawn with a closed cabin loader with supervision, even draw, dry ore blend, and twice-weekly checking for changes. Classes E and F were recommended to be drawn with remote loader, supervision, checking for changes every shift, and at least six buckets per shift drawing. The water content of this classification system was established specifically for IOZ ore, and a different material requires a new water content evaluation. Furthermore, the density measured in the ore pile could differ from that in the ore column, as the degree of saturation depends on density. This method could be inaccurate for predicting the risk of mud rushes that involve the ore column, since it uses only the density of the ore pile for water content recommendations. Finally, drawing recommendations are fitted to IOZ-specific shovels and mine conditions; a different mine will require different, specific recommendations.

El Teniente mine uses a criterion based on historical data on ore grain size and water content from seven drawpoints in which a mud rush has taken place. A risk classification (Becerra, 2011) with three classes is defined: normal condition (NC), in observation (IO), and critical risk (CR).

Table II summarizes the grain sizes and moisture contents for risk classification at El Teniente. The use of seven cases with historical data from different sectors of El Teniente can be inaccurate for predicting the risk in particular zones and for different types of ore.

Both IOZ and El Teniente use grain size and water content to classify ore in drawpoints. The criterion for IOZ (Table I) is based on geotechnical characterization of six samples (Call & Nicholas, Freeport McMoRan, and Hydrologic Consultants, 1998); for El Teniente's criterion, historical data from seven events is used (Becerra 2011). One difference in these criteria is the grain size: IOZ uses 5 cm as the relevant grain size and El Teniente uses 25 cm. Another difference is that the El Teniente classification takes coarse grain size as a 'critical risk' if moisture content is more than 10%, while IOZ only recommends use of a closed cabin loader for the same condition.

The type of clay in ore from different drawpoints can play a crucial role in water-absorbing properties and consequently in flow risk evaluation (Call & Nicholas, Freeport McMoRan, and Hydrologic Consultants, 1998). Also, the influence of density must be considered in the physical characterization of the ore. In order to develop an improved classification system it is necessary to characterize the behaviour of specific ores, using not only the water content and degree of saturation, but also relating those parameters to density. In this paper a new method is proposed to develop classification systems for specific ores, based on a simple characterization of ore with different densities and saturation values.

Density and water content

In the previous section we presented relevant criteria for ore evaluation, depending on the water content, which is easy to measure in the laboratory. As mentioned in the introduction, one of the mud rush mechanisms is an increase in water content. In granular materials the water content is mostly held in the voids between the solid particles. A granular material with high density has fewer voids than the same material with a low density; consequently a material with high density can hold less water than a low-density material. This is why the importance of density is emphasized when water content is involved. The density of mud in the ore

Table II

Mud risk classification for drawpoints in El Teniente mine (Becerra, 2011)

Moisture content	Grain size (G) $\leq 25 \text{ cm}$		
	G < 30% (Mostly thick granulometry)	30% $\leq G \leq 70\%$	G $\geq 70\%$ (Mostly fine granulometry)
<4%	NC	NC	NC
4% - 7%	IO	IO	IO
7% - 10%	IO	IO	CR
$\geq 10\%$	CR	CR	CR

Methodology for evaluation of mud rush risk in block caving mining

column is uncertain because of the changes caused by the ore flow, by which the density changes as material is extracted from draw points, as demonstrated by Kvapil (1992). Nevertheless, the range of density that can develop in a certain granular material can be calculated by measuring its minimum and maximum void ratios. The range of maximum and minimum void ratio is used to define the relative density (RD), which assigns a value of zero to the maximum void ratio (e_{\max}) and 100% to the minimum void ratio (e_{\min}). Equation [1] shows the RD parameter defined by maximum and minimum void ratios.

Saturation is the ratio between the volume of water and volume of voids. Consequently, it depends on the void ratio and water content, and therefore is an important parameter for mud rush risk evaluation. Previous studies have posited a direct relationship between saturation and mud rush risk (Becerra, 2011; Call & Nicholas, Freeport McMoRan, and Hydrologic Consultants, 1998). Equation [2] shows the relationship between void ratio (e), saturation (S), water content (ω), and specific gravity (G_s).

$$RD(\%) = \frac{e_{\max} - e}{e_{\max} - e_{\min}} \times 100 \quad [1]$$

$$G_s \omega = S e \quad [2]$$

where specific gravity is the unit weight of solid divided by the unit weight of water, and the water content is the ratio of water weight to solid weight (Lambe and Whitman, 1969). In the next section these parameters are used as inputs for testing the mud samples.

Materials and methods

Samples

Tests were performed on three samples obtained from the Diablo Regimiento sector, El Teniente mine. In this sector, three types of mud ore have been identified by visual characterization according to mine personnel: (1) grey mud, (2) yellow mud, and (3) mixture mud, which are associated with sulphide, oxide, and a mixture of sulphide and oxide minerals respectively. The three samples were collected from different drawpoints, each sample representing one of the above types of mud. The drawpoints chosen for sampling extraction are classified in critical risk categories according to the risk classification used at El Teniente (Becerra, 2011). Table III lists the samples with their descriptions and compositions. The sampling was undertaken by mine personnel responsible for water content control, using a hand shovel to extract increments across the drawpoint on a horizontal level 1.5 m above the floor. This method is regularly used at El Teniente for the representative sampling



Figure 1—Abram's cone used for slump tests

of mud ore for water content control. The samples were packed and transported in sealed plastic bags to the laboratory.

Experimental method

Samples were tested in the Solids Laboratory facilities of the Civil Engineering Department at the Universidad de Chile. Slump tests were carried out in order to classify the behaviour of mud ore based on the slump results for different conditions. The grain sizes of the samples were 95% <5 cm. Slump tests were performed using an Abram's cone – a standard metal mould (according to ASTM C143 standard) shaped as the surface of a frustum cone, with a base of 200 mm diameter, top of 100 mm diameter, and height of 300 mm (Figure 1). The mould is filled with material through the top while the base is placed on a flat surface, and is then removed vertically. The slump is the difference between the height of the mould and the height of the material, which is measured with 1 mm precision immediately after the mould has been removed.

We also conducted unconfined compression tests in order to compare the slump behaviour results with the unconfined strength (in units of kPa). Unconfined compression testing involves axial loading of a cylindrical specimen in a strain-controlled device until failure (according to ASTM D2166 standard). Force and strain are measured with 0.001 kN and 0.001 mm precision respectively. The test ends when the force decreases or the vertical strain reaches 20%. The initial cross-sectional area (A_0) is measured from the average of nine diameter measurements; it is corrected during the test depending on the vertical strain (ϵ) according to Equation [3].

$$A = \frac{A_0}{1 - \epsilon} \quad [3]$$

In this study, slump tests and unconfined compression tests were carried out at different degrees of saturation and

Table III

Samples and visual appearance

Sample	Description	Composition
1	Grey	Sulphides
2	Yellow	Oxides
3	Mixed	Mixture

Methodology for evaluation of mud rush risk in block caving mining

Table IV

Relative density and saturation conditions for slump tests

Relative density (%)	Saturation (%)
45	60
45	80
45	100
65	60
65	80
65	100
85	60
85	80
85	100

Table V

Relative density and saturation conditions or unconfined compression tests

Relative density (%)	Saturation (%)
20	45
20	60
20	75
60	45
60	60
60	75
90	45
90	60
90	75

relative densities. Table IV lists the values of the variables set for each slump test, and Table V the values for each unconfined compression test. Three different relative densities and saturations were used for each sample, resulting in nine tests for each sample. The variables were carefully set when the mould was filled, by calculating the water content and mass necessary for each combination. For

Table VI

Consistency classification based on slump according to BS-8500 standard

Consistency	Slump range (cm)
Dry	0 – 5
Plastic	4 – 10
Soft	9 – 16
Fluid	15 - 30

the slump tests, the mould was filled in three layers in order to obtain a uniform density of material inside. For unconfined compression, the mould was filled with five layers.

Geotechnical indexes of specific gravity and maximum and minimum void ratios were obtained in order to set variables from Tables IV and V according to Equations [1] and [2]. Specific gravity was obtained using two different methods, depending on the grain size. For particle sizes smaller than 4.75 mm the water pycnometer method was used. For the particle sizes greater than 4.75 mm, Archimedes' method used (the dry weight divided by the difference between the dry weight and the weight while submerged under water). The maximum void ratio was obtained by pouring the material into a cylindrical mould of known volume to obtain the minimum density (according to the ASTM D4254 standard). The minimum void ratio was obtained using a modified Proctor test, in which the material is compacted in layers within a container of known volume (according to the ASTM D1557 standard).

Risk classification

In order to develop a risk classification decision matrix, the classification system for concretes presented in Table VIII was used. Each consistency represents one type of behaviour of the ore. The slump corresponding to dry and plastic consistency is classified as non-flowing behaviour, and a soft or greater slump as flowing behaviour. The aim is to ascertain the minimum water content for each sample at which the slump changes from plastic to soft behaviour; this value is termed the fluid limit (FL). In order to find the FL the slump is plotted *versus* the water content, thus drawing curves for slump results at the same degree of saturation. The required water content values are given by the intercept between the plastic-soft limit (9.5 cm of slump) and each saturation curve. Finally, the minimum water content is selected as the FL for each sample.

Results

Tests

The geotechnical indexes obtained are presented in Table VII. These indexes are necessary to set the conditions for the unconfined compression and slump test according to Equations [1] and [2]. The three samples have similar specific gravities and maximum and minimum void ratios; sample 2 tends to have higher void ratios.

Methodology for evaluation of mud rush risk in block caving mining

Table VII

Relative density and saturation for unconfined compression tests

Parameter	Test	ASTM standard	Results		
			Sample 1	Sample 2	Sample 3
Specific gravity	Water pycnometer, water immersion	D854, C127	2.76	2.68	2.72
Minimum void ratio	Pouring in cylinder of known volume.	D4254	0.27	0.28	0.22
Maximum void ratio	Modified Proctor	D1557	0.90	1.00	0.93

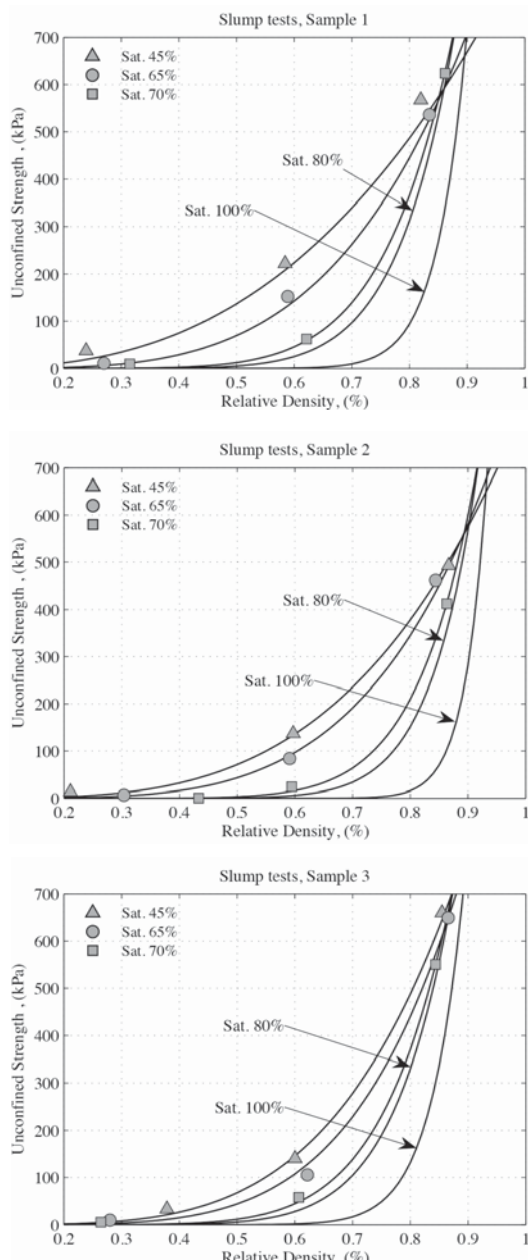


Figure 2—Slump test results, consistency classification and FL determination

Table VIII

Parameters for Equation [4]

Constant	Sample 1	Sample 2	Sample 3
P (kPa)	12 882	11 439	11 993
Q (kPa)	-12 288	-11 416	-12 132
R (kPa)	3 810	3 656	4 276
a	45	80	39
b	-39	-78	-36
c	11	22	12

The results for unconfined compression strength are shown in Figure 2. The strength increases with RD and decreases with saturation. The parameters were obtained by fitting data, in order to ascertain the effect of RD and saturation on the strength. The equation has six experimental adjustment parameters (p , q , r , a , b , c), and Table VIII shows the values obtained for these constants for the three samples. Here, U_s is the unconfined strength for a given RD and saturation (S). Figure 2 also shows the curves for 80% and 100% saturation according to Equation [4] and the parameters in Table VIII.

$$U_s = (pS^2 + qS + r)RD^{(aS^2 + bS + c)} \quad [4]$$

Figure 3 shows the results of the slump tests: the vertical axis shows the slump and the horizontal axis the water content. Each curve shows a different saturation degree, so there are also three states of compaction represented on each curve. Horizontal divisions indicate different classes of consistency depending on the slump, according to Table VI. Figure 3 reveals that slump increases with increasing saturation, but decreases with increasing relative density. A RD of 85% indicates a dry consistency for all cases. The oxide sample requires 100% saturation to reach fluid consistency, the mixed sample requires 80% saturation, and the sulphide sample requires only 60% saturation. Vertical dashed lines show the value of the fluid limit (FL). Water content values

Methodology for evaluation of mud rush risk in block caving mining

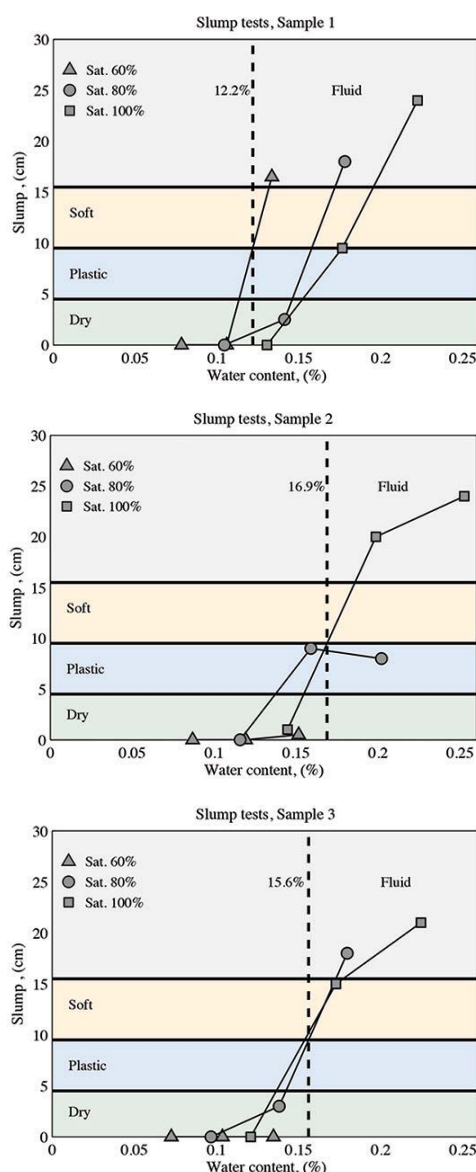


Figure 3—Slump tests, consistency classification, and FL determination. The solid lines are for visual aid

obtained from this intercept indicate that sample 1 (sulphide mud) is prone to flow at a lower water content than the other samples: 12.2% compared with 16.9% for sample 2 (oxide mud) and 15.6% for sample 3 (mix). Equation [4] was used to calculate unconfined strength using the conditions for the slump tests (Table IV). In Table VII all the results for slump, the consistency category, and unconfined strength are summarized using Equation [4]. Fluid and liquid states are achieved with an unconfined compressive strength of less than 46 kPa. Nevertheless, in some cases the U_s is very low with a dry consistency (RD 45% and 60% saturation). These cases imply that Equation [4] is not entirely valid for explaining slump, and the values obtained should be used only as reference values, owing to the fact that the range of saturation was different for slump tests and unconfined compression tests.

Risk classification

The consistency fluid limits (FL) from Figure 2 were used to define a fluid security factor (SF_f):

$$SF_f = \frac{FL}{\omega} \quad [5]$$

where ω is water content. The water content for the risk classification for DR drawpoints are shown in Tables X, XI, and XII for samples 1, 2, and 3, respectively. Each pattern is specific for each mud type. Sample 1 has lower water content values for the same risk level than the other samples. The last row in each table contains the critical water content value at which the drawpoint is classified as critical risk regardless of the grain size.

Discussion and conclusions

Different mud rush risk and operational criteria have been developed in the past, all based on grain size and water content. The El Teniente criterion does not take into account

Table IX

Results for slump tests, consistency classification, and equivalent unconfined strength

RD	S	Sample 1			Sample 2			Sample 3		
		Slump (mm)	Consistency	U_s (kPa)	Slump (mm)	Consistency	U_s (kPa)	Slump (mm)	Consistency	U_s (kPa)
45%	60%	165	Liquid	46	5	Dry	27	0	Dry	26
45%	80%	180	Liquid	2	80	Soft	0	18	Liquid	2
45%	100%	240	Liquid	0	240	Liquid	0	21	Liquid	0
65%	60%	0	Dry	196	0	Dry	137	0	Dry	159
65%	80%	25	Dry - plastic	51	90	Soft	15	3	Dry	55
65%	100%	95	Soft - fluid	3	200	Liquid	0	15	Fluid	5
85%	60%	0	Dry	566	0	Dry	450	0	Dry	593
85%	80%	0	Dry	534	0	Dry	299	0	Dry	556
85%	100%	0	Dry	267	10	Dry	70	0	Dry	336

Methodology for evaluation of mud rush risk in block caving mining

Table X

Risk classification for DR, sample 1

SF_f	ω	Grain size ($G \leq 25$ cm)	
		$G < 70\%$	$G > 70\%$
>1.5	< 8%	NC	NC
1.5 - 1.2	8% - 10%	IO	IO
1.2 - 1.1	10% - 11%	IO	CR
<1.1	> 11%	CR	CR

Table XI

Risk classification for DR, sample 2

SF_f	ω	Grain size ($G \leq 25$ cm)	
		$G < 70\%$	$G > 70\%$
>1.5	< 11%	NC	NC
1.5 - 1.2	11% - 14%	IO	IO
1.2 - 1.1	14% - 15%	IO	CR
<1.1	> 15%	CR	CR

Table XII

Risk classification for DR, sample 3

SF_f	ω	Grain size ($G \leq 25$ cm)	
		$G < 70\%$	$G > 70\%$
>1.5	< 10%	NC	NC
1.5 - 1.2	10% - 13%	IO	IO
1.2 - 1.1	13% - 14%	IO	CR
<1.1	> 14%	CR	CR

differences in the behaviour of ore due to compositional variation. The IOZ criterion assumed a constant density. The method presented in this study is specific for DR-type ore, and also takes density into account. A highly compacted ore is not able to flow, whereas medium-compact and loose ores can flow, depending on their saturation values: the higher the saturation, the greater the propensity to flow. The water contents required for flow behaviour were determined as 12.2% for sulphide ore, 16.9% for oxide ore, and 15.6% for mixed ore. Consequently, different samples have different propensities to flow with the same water content; sulphide ore is more prone to flow than oxide and mixed ore. The application of the developed criterion for drawpoint ore classification provides different critical values for water content: 11% for sulphide ore, 15% for oxide ore, and 14% for mixed ore. In order to improve the mine's production, a criterion for each ore type must be developed, thus enabling operation of the drawpoint until the ore reaches its critical

value for specific water content. If a general mine criterion is developed, the criterion with the minimum water content value should be selected. In this case, sample 1 (sulphide) has the lowest values for water content, with 11% being the critical value.

Acknowledgments

The authors acknowledge the support of the Department of Mining Engineering and the Advanced Mining Technology Center of the University of Chile and Codelco, Chile. Additionally, we would like to thank Dr Adeline Delonca for her comments on the article.

References

- BECERRA, C. 2011. Controlling draw points prone to pumping. El Teniente División, Codelco, Chile. *Proceedings of the 2nd International Seminar on Geology for the Mining Industry (Geomin 2011)*, Antofagasta, Chile, 8–10 June 2011. Session 7: Mine Production Geology / Geometallurgy. Gecamin, Santiago, Chile.
- BUTCHER, R., JOUGHIN, W., and STACEY, T.R. 2000. Methods of combating mud rushes in diamond and base metal mines. Safety in Mines Research Advisory Committee (SIMRAC), Johannesburg.
- BUTCHER, R., STACEY, T., and JOUGHIN, W. 2005. Mud rushes and methods of combating them. *Journal of the South African Institute of Mining and Metallurgy*, vol. 105, pp. 807–824.
- CALL & NICHOLAS INC., Freeport McMoRan Copper and Gold, Co., and Hydrologic Consultants, Inc. 1998. IOZ wet muck study.
- HESLOP, T. 2000. Block caving — controllable risks and fatal flaws. *Proceedings of Massmin 2000*, Brisbane, Australia, 29 October–2 November. Australasian Institute of Mining and Metallurgy, Melbourne.
- HUBERT, G., DIRJDOSUWONDO, S., PLAISANCE, R., and THOMAS, L. 2000. Tele-operation at Freeport to reduce wet muck hazards. *Proceedings of Massmin 2000*, Brisbane, Australia, 29 October–2 November. Australasian Institute of Mining and Metallurgy, Melbourne.
- JAKUBEC, J., CLAYTON, R., and GUEST, A. 2012. Mud rush risk evaluation. *Proceedings of Massmin 2012*, Sudbury, Ontario, 10–14 June 2012. Canadian Institute of Mining, Metallurgy and Petroleum, Montreal.
- KVAPIL, R. 1992. Sublevel caving. *SME Mining Engineering Handbook* (2nd edn). Society for Mining, Metallurgy and Exploration, Littleton, CO. Chapter 20.2.
- LACY W. and LACY J. 1992. History of mining. *SME Mining Engineering Handbook* (2nd edn). Society for Mining, Metallurgy and Exploration, Littleton, CO. Chapter 1.1.
- Lambe W. and Whitman R. 1969. Soil Mechanics. Massachusetts Institute of Technology. Chapters 3, 9, and 27.
- TAPIA, C. 2011. Definition of potential mudflows from extraction points at Rio Blanco underground mine. *Proceedings of the 2nd International Seminar on Geology for the Mining Industry (Geomin 2011)*, Antofagasta, Chile, 8–10 June 2011. Session 7: Mine Production Geology / Geometallurgy. Gecamin, Santiago, Chile. ♦

*Back by
popular demand!!
Previous three schools
were fully subscribed
Book your seats
early!*



For further information contact:
Camielah Jardine
Head of Conferencing • Saimm
P O Box 61127, Marshalltown 2107
Tel: +27 (0) 11 834-1273/7
E-mail: camielah@saimm.co.za
Website: <http://www.saimm.co.za>

4th Mineral Project Valuation Colloquium

27–29 June 2017

The University of the Witwatersrand

BACKGROUND

The SAIMM announces the 4th Mineral Project Valuation Colloquium following three previous successful schools in 2011, 2012, and 2014 that were fully subscribed. The audience included international delegates from the United Kingdom, Australia, Namibia, Zambia and Zimbabwe. This Colloquium will provide you with insights into these and other developments that will affect the way you conduct mineral project valuations and equip you with relevant techniques for undertaking MAV. Seats are limited so book your seats early as the next SAIMM Mineral Asset Valuation Colloquium will only be run in 2019.

OBJECTIVES

- To cover basic theory and principles of valuation techniques and focus on the commonly used valuation approaches (cost, market, income) and methods
- To evaluate risk in mineral project evaluation
- To critically assess the pros and cons of the valuation approaches and methods
- To cover the integration of inputs and assumptions from resource to market and their impact on mineral asset valuation
- The impact of sustainability (social, government, environment) on mineral asset valuation and decisions
- Beyond DCF - future applications, scenario planning, opportunity identification and options selection and alternative valuation techniques as it applies to the mining industry
- To cover aspects that mining companies and banks (commercial and development) consider in evaluation and valuation of mineral assets
- Industry leader perspective through a panel discussion.

- MRM managers
- Mineral industry advisory consultants and academics
- Accountants involved in mining project feasibility studies
- Professionals involved with mining project reviews
- Financial managers
- Chief financial officers
- HSE managers.

SPONSORSHIP

Sponsorship opportunities are available. Companies wishing to sponsor or exhibit should contact the Conference Coordinator.

WHO SHOULD ATTEND

- Exploration geologists
- Mining engineers involved in feasibility studies
- Project managers

Event Announcement



An improved flotation test method and pyrite depression by an organic reagent during flotation in seawater

by R.I. Jeldres*, D. Calisaya*, and L.A. Cisternas*

Synopsis

Flotation of copper-molybdenum sulphide ores in seawater entails critical challenges such as selective recovery of molybdenite, effective pyrite depression, and reducing the lime addition required to reach highly alkaline conditions. It is essential that laboratory flotation tests aimed at solving these problems give reliable, reproducible results and indicate the correct approach for industrial operations. Rougher flotation of copper-molybdenum sulphide ores in seawater was investigated using two different cells: a modified Denver cell and a standard commercial cell. The effect of an organic reagent on the flotation performance was tested, and the fast/slow-floating model was used to describe the results. The modified Denver cell significantly improved the reproducibility of the flotation test results, due to technological enhancements such as the impeller being driven from below without a stator, which enables the whole froth surface to be scraped with a paddle at a constant depth and rate. Organic reagents are a promising alternative to inorganic reagents for depressing pyrite in seawater. However, further studies should be conducted to investigate their impact on molybdenite recovery, as well as to evaluate the possibility of depressing pyrite after molybdenite separation. The fast/slow-floating model was found to be appropriate for describing the flotation kinetics of the copper-molybdenum ores. The parameters are useful for comparing the performance at different conditions.

Keywords

flotation, seawater, modified Denver cell, organic pyrite depressant, fast/slow-floating model.

Introduction

Owing to the increasing scarcity of fresh water, the use of seawater mining and mineral processing is becoming increasingly important (Cisternas and Moreno, 2014). Seawater can be desalinated by reverse osmosis, but this involves considerable costs, limiting it to the big mining companies (Akgul *et al.*, 2008; Leidner *et al.*, 2012; Ghaffour, Missimer, and Amy, 2013). Furthermore, desalination has environmental consequences (Lee, Arnot, and Mattia, 2011); for example, a desalination plant designed to process 2.5 m³/s requires an electrical energy supply of around 30 MJ/s. To supply this power demand, a thermoelectric plant burning bituminous/sub-bituminous coal mixtures at a thermal power generation efficiency of 35% might release around 1200–1500 t of CO₂ per day. Furthermore, the effluents from desalination plants are typically discharged into the sea, and their high temperature and ionic content inevitably modifies the marine environment, with

unknown consequences. The direct use of seawater is, therefore, more attractive, but it also poses major challenges since seawater contains ions that adversely affect mineral recoveries. In particular, in the flotation of sulphide ores in seawater, the floatability of molybdenite is depressed (Castro, 2012; Laskowski, Castro, and Ramos, 2014).

Copper recovery in flotation plants is usually in the range of 81–85% (Monardes, 2009), but even small improvements are important considering the large quantities of ores that are treated. Flotation of valuable minerals is assisted by the addition of several types of reagents, the most important of which are collectors. For example, there are thiol collectors such as xanthates, dithiophosphates, thiocarbamates, and mercaptans (Veki, 2013). The primary objective of a collector is to adsorb onto the mineral surface to impart a hydrophobic character, while keeping gangue minerals in a hydrophilic form. Additionally, bubble coalescence in any saline water is hindered. Bournival, Pugh, and Ata (2011) noted that the effects of dissolved salts are still not understood, and the exact mechanism is a matter of debate. Nevertheless, in highly saline media, the bubble size is influenced mainly by inorganic electrolytes, and the frother has only a minor effect (Laskowski, Castro, and Ramos, 2014). This is an important issue, considering that frothers might adsorb onto the hydrophobic mineral surfaces, decreasing their floatability (Kursun, 2014).

An essential requirement in sulphide flotation is to achieve a good level of pyrite depression, since pyrite diminishes the quality of the concentrate and increases the quantity of sulphur compounds produced in the base metal extraction processes. Pyrite depression is usually reached at highly alkaline conditions

* Depart of Chemical Engineering and Mineral Process, University of Antofagasta, Antofagasta, Chile.

© The Southern African Institute of Mining and Metallurgy, 2017. ISSN 2225-6253. Paper received Oct. 2016; revised paper received Mar. 2017.

An improved flotation test method and pyrite depression by an organic reagent

(pH above 10.5), wherein the pyrite surface is covered by hydrophilic iron oxides such as Fe(OH)_3 , Fe(OH)_2 , or $\alpha\text{-FeOOH}$ (Wang, 1989; Mermilled-Blondin *et al.*, 2005). A high pH is commonly attained by lime addition, but the required amount is excessive due to the buffering effect of seawater, which increases the lime consumption by 5–10 times compared to fresh water (Castro, 2012; Veki, 2013). However, at pH values over 10.5, both calcium and magnesium ions form colloidal hydroxides, carbonates, and sulphates, which are detrimental for the recovery of molybdenite, and the quality of the concentrate is reduced (Castro and Laskowski, 2011; Ramos, Castro, and Laskowski, 2013; Jeldres *et al.*, 2017). Some researchers have proposed that these complexes might precipitate onto the molybdenite surfaces and render them hydrophilic (Parraguez, Bernal, and Cartagena, 2009; Lucay *et al.*, 2015). For this reason, operating rougher flotation at pH values lower than 9 to avoid MoS_2 depression has been recommended, with pyrite depression by alternative reagents. In this regard, the use of inorganic depressants such as cyanides, sulphites, or ferrocyanides has raised concerns on environmental grounds. Therefore, organic polymers have been studied, in view of their natural, biodegradability and non-toxicity (Lopez-Valdivieso *et al.*, 2004; Bicak *et al.*, 2007; Liu *et al.*, 2009; Bulut *et al.*, 2011; Koleini, Abdollahy, and Soltani, 2012; Sarquis *et al.*, 2014; Mu, Peng, and Lauten, 2015). However, there is currently a lack of knowledge about the interaction between these additives and solid surfaces in highly saline environments. Some studies have shown that reagent behaviour in saline solutions depends on the type of salt in solution (maker or breaker), and the electrical charge of both the solid surface and the reagents (Hancer, Celik, and Miller, 2000; Jeldres *et al.*, 2014). For a complete review of the use of saline water and seawater in flotation, see Jeldres, Forbes, and Cisternas (2016).

Consequently, the objectives of this paper are to (i) evaluate the rougher flotation of copper-molybdenum sulphide ores in seawater with different reagents, including an organic pyrite depressant, and (ii) compare the reproducibility of the results using two types of flotation cell: a modified Denver cell and standard commercial cell. The CSIRO has developed a novel flotation cell that corresponds to a modified Denver cell. The impeller and shaft are driven from below the cell, which allows the whole surface of the froth to be scraped with a paddle at constant depth and rate (Forbes, Davey, and Smith, 2014). The cell is fitted with a rubber diaphragm, sight tube, and electronic sensor for automatic detection and control of the pulp level (Forbes,

Table I

Composition of seawater from the city of Antofagasta, Chile (Ordoñes *et al.*, 2013)

Anions	g/l	Mol/l	Cations	g/l	Mol/l
NO_3^-	0.21	0.0034	Na^+	11.124	0.4837
SO_4^{2-}	2.66	0.0277	K^+	0.361	0.0093
IO_3^-	0	0.0000	Mg^{2+}	1.576	0.0649
Cl^-	19.71	0.5560	Ca^{2+}	0.171	0.0043
ClO_4^-	0.12	0.0012			
BO_3^{3-}	0.16	0.0027			

Davey, and Smith, 2014). Koh and Smith (2011) have used computational fluid dynamics (CFD) to describe the effect of stirring speed in this cell. Finally, a new parameter obtained from the fast/slow-floating model is proposed as an indicator of the 'global flotation performance.'

Methodology

Seawater flotation of copper-molybdenum sulphide minerals was carried out in two different flotation cells: (i) the modified Denver cell developed by CSIRO, and (ii) a standard commercial cell. The impact of various reagents, including an organic pyrite depressant, was investigated. Finally, the flotation kinetic was modelled by using the fast/slow-floating model. All tests were performed in duplicate to ensure good reproducibility of the results. Seawater from the coast in the vicinity of Antofagasta, Chile was used. Its composition is shown in Table I.

Mineral samples

Copper-molybdenum sulphide ore samples were acquired from a mining operation in the Antofagasta region. Chemical analysis indicated that the elemental composition was Cu: 0.55%, Mo: 0.010%, Fe: 4.26%. Chalcopyrite is the main copper-bearing mineral.

Flotation reagents

Two different set of reagents, based on xanthate (set 1) and isothiazole (set 2) as primary collectors, were tested (Table II). The best option set (set 1) was used to evaluate the effect of an organic pyrite depressant obtained from corn (Oxi 300, 50 g/t).

Flotation tests

The ore was ground in a ceramic mill for 11.9 minutes to a size distribution of $P_{80}<170 \mu\text{m}$. The ground samples were transferred into the batch cell and made up to a volume of

Table II

Reagents employed in flotation tests

Set 1		Set 2	
Reagent	Dose (g/t)	Reagent	Dose (g/t)
Oxi-2650 (primary xanthate collector)	45	Oxi-320B (primary isothiazole collector)	45
Oxi-41 (secondary dithiophosphate collector)	22	Oxi-41 (secondary dithiophosphate collector)	22
Oxi-92 (frother)	30	Oxi-92 (frother)	30

An improved flotation test method and pyrite depression by an organic reagent

2750 ml, giving a flotation pulp density of 30 wt%. The reagents were all added 5 minutes before the start of flotation. The flotation gas was air at a flow rate of 8 l/min, producing 0.70 cm/s superficial air velocity. Froth depth of the order of 1 cm was scraped every 10 seconds during the test, and the concentrate was collected in trays.

Modelling

The fast/slow-floating particles model was used to describe the flotation kinetics. The model is expressed as:

$$R(t) = R_{\infty}(\emptyset(1 - \exp(-k_f t)) + (1 - \emptyset)(1 - \exp(-k_s t)) \quad [1]$$

where $R(t)$ is the recovery as a function of time t , \emptyset is the fraction of flotation components with a fast rate constant, and k_f and k_s are the rate constants for fast and slow components respectively.

The parameter K is defined as:

$$K = R_{\infty}(\emptyset k_f + (1 - \emptyset) k_s)^n \quad [2]$$

where n is a weighting index for the flotation rate constants. In this work, $n = 0.1$. Besides the modified flotation parameter defined by Ucurum and Bayat (2007), the indicator K defined here is useful for selecting the optimum flotation performance since it describes the global flotation performance, considering both maximum recovery and flotation rate. Note that to obtain the indicator K all the parameters in Equation [1] are used.

The Effronis pseudo-R-squared measured was used as goodness of fit (GoF), that is,

$$GoF = 1 - \frac{\sum_{i=1}^N (R_i^{exp} - R_i^{mod})^2}{\sum_{i=1}^N (R_i^{exp} - \bar{R})^2} \quad [3]$$

where N is the number of data values and \bar{R} the mean of R . Predicted flotation kinetic curves from each model were compared with the experimental data.

Results and discussion

Flotation in highly alkaline conditions

The buffering effect of seawater (Figure 1) starts at pH 10.2,

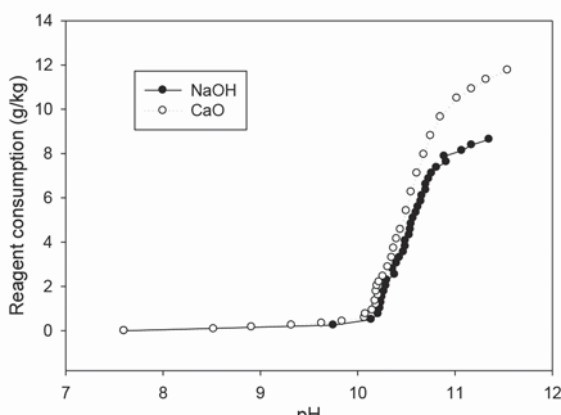


Figure 1—Lime (CaO) and sodium hydroxide (NaOH) required to modify pH in the rougher flotation of copper sulphide in seawater

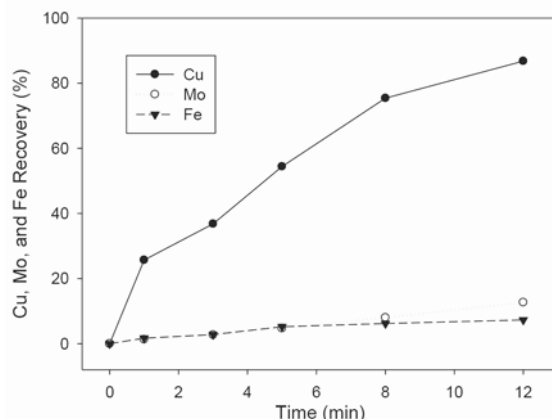


Figure 2—Cu, Mo, and Fe recoveries by flotation in seawater at pH 11.5 modified with lime (CaO)

and the CaO and NaOH consumption is strongly increased, discouraging operation at this condition. It is also observed that at pH approximately 11, around 25% more CaO than NaOH is required. Additionally, the recovery of molybdenum is poor (Figure 2). Therefore the usual strategy entails maximizing the copper and molybdenum recoveries in the rougher stage, working at a pH near 8, and rejecting the pyrite in the rougher concentrate in the cleaner stage.

Effect of reagents

The effects of two primary copper collectors (Oxi 2650 and Oxi 320B) on seawater flotation of chalcopyrite, molybdenite, and pyrite were compared. A secondary collector (Oxi 41) and frother (Oxi 92) were also incorporated (details in Table II). The experiments were performed at natural pH because this condition maximizes Cu and Mo recoveries. All tests were conducted in duplicate to ensure good reproducibility.

Good recoveries of Cu and Mo were achieved, and the flotation kinetics were similar for both set of reagents. The chalcopyrite recovery after 12 minutes' flotation was 89.2% for reagent set 1, and 89.5% for set 2 (Figure 3). For molybdenum, the recoveries were 79.6% for set 1 and 80.3% for set 2 (Figure 4). The pyrite recoveries were 33.9% for reagent set 1 and 36.6% for set 2 (Figure 5).

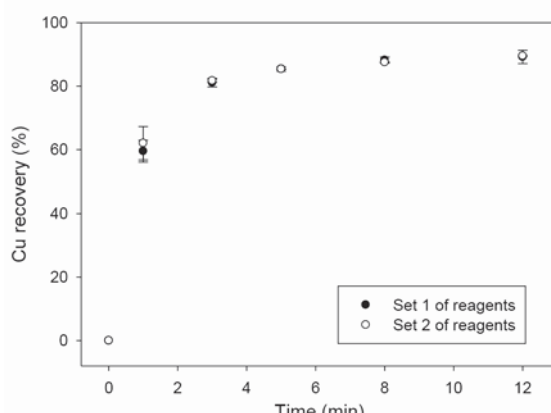


Figure 3—Cumulative copper recovery as a function of time for the two sets of reagents. Tests were performed in a modified Denver cell

An improved flotation test method and pyrite depression by an organic reagent

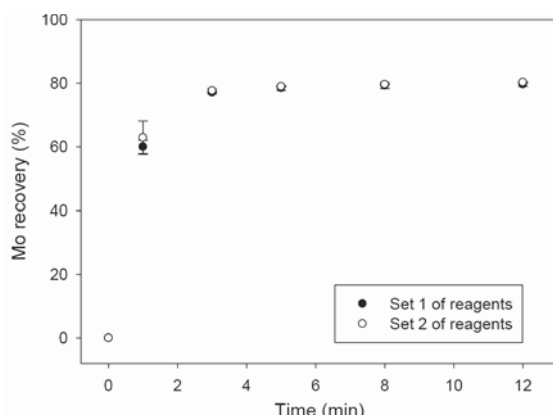


Figure 4—Cumulative molybdenum recovery as a function of time for the two sets of reagents. Tests were performed in a modified Denver cell

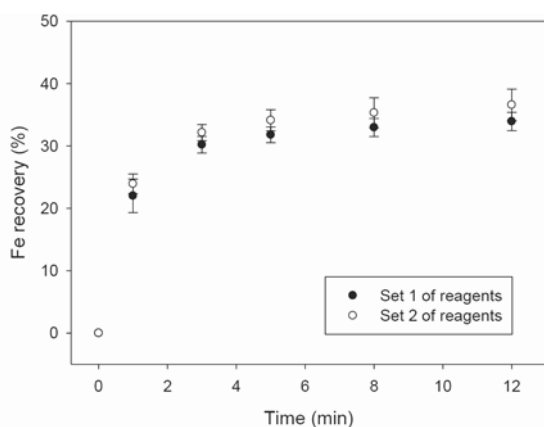


Figure 5—Cumulative iron recovery as a function of time for the two sets of reagents. Tests were performed in a modified Denver cell

Rougher flotation in seawater at natural pH offers promising benefits since a meaningful Mo recovery is obtained, and excessive lime consumption is avoided. However, at this condition, pyrite does not oxidize; it remains hydrophobic and reports to the concentrate, decreasing the concentrate grade. Therefore, finding new pyrite depressants would confer an advantage. A recommendable option is the use of organic reagents (López-Valdivieso *et al.*, 2004; Bicak *et al.*, 2007; Sarquís *et al.*, 2014).

Organic pyrite depressant

An organic pyrite depressant obtained from corn (Oxi-300, 100 g/t) was incorporated in reagent set 1. The flotation results are presented in Figures 6–8.

Figure 6 shows that Oxi-300 improves the flotation kinetics of copper slightly, but the ultimate recovery is similar with and without Oxi-300. Moreover, the recovery of pyrite after 12 minutes is reduced by 12.2% (from 38.5% to 26.3%) by the addition of Oxi-300 (Figure 8). This encouraging result shows that organic pyrite depressants can be applied not only in fresh water, but also in seawater. However, Figure 7 indicates that this reagent has a detrimental effect on molybdenum floatability; the molybdenum recovery after 12 minutes for reagent set 1 was 78.1%, decreasing to 71.0% in the presence of Oxi-300. Thus, although the use of organic

reagents might be considered for pyrite depression in seawater flotation, further studies should be conducted to investigate the impact on the molybdenite recovery. Another alternative that should be explored is pyrite depression after molybdenite separation.

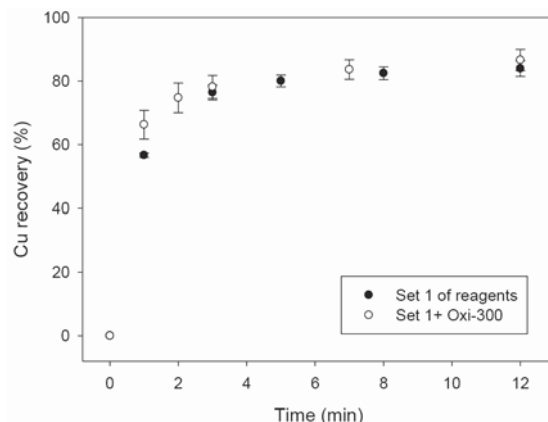


Figure 6—Impact of organic reagent on cumulative copper recovery as a function of time. Tests were performed in a commercial flotation cell

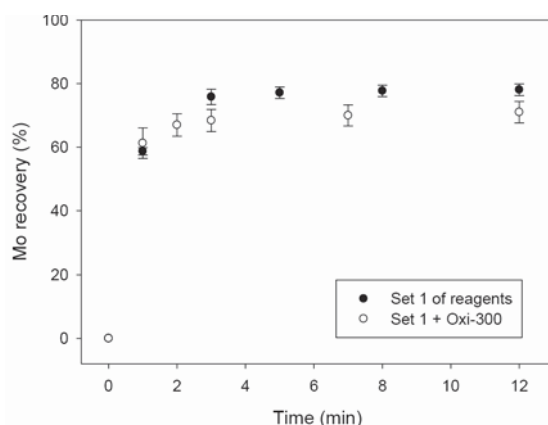


Figure 7—Impact of organic reagent on cumulative molybdenum recovery as a function of time. Tests were performed in a commercial flotation cell

Modified Denver cell vs. commercial cell

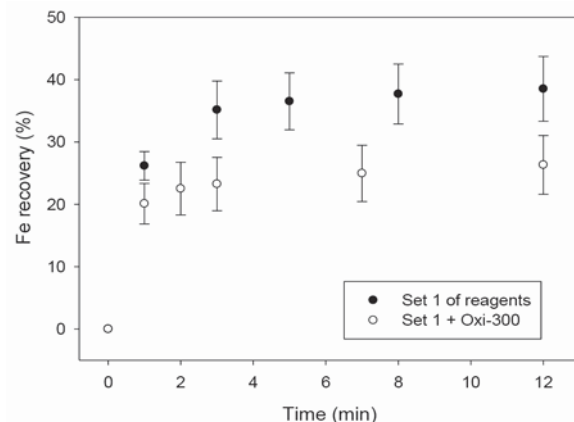


Figure 8—Impact of organic reagent on cumulative pyrite recovery as a function of time. Tests were performed in a commercial flotation cell

An improved flotation test method and pyrite depression by an organic reagent

Figure 9 shows the standard deviations for the recoveries of Cu, Mo, and Fe after 12 minutes' flotation in the modified Denver cell and the commercial cell. Interestingly, higher standard deviations were always assigned to the conventional flotation cell, indicating that the experiments performed in the modified Denver cell have better reproducibility. This might be explained by the impeller and shaft configuration in the modified Denver cell, which are driven from below the cell, allowing the whole froth surface to be scraped with a paddle at a constant depth and rate. The automatic pulp level detection and control may also contribute to the reliability of the tests.

Modelling

Figures 10 and 11 show the fast/slow-floating model fitting (Equation [1]) for the flotation of copper in the modified Denver cell and commercial cell, respectively. The model was applied to all the tests previously reported, and the parameters are summarized in Tables III and IV.

The fast/slow-floating model captures very well the experimental data, and for all cases the goodness of fit (GoF) was higher than 0.999. The parameters obtained from the model (Tables III and IV) are used to calculate the indicator K (Equation [2]), which represents the flotation kinetic global performance and includes both flotation rate and maximum recovery.

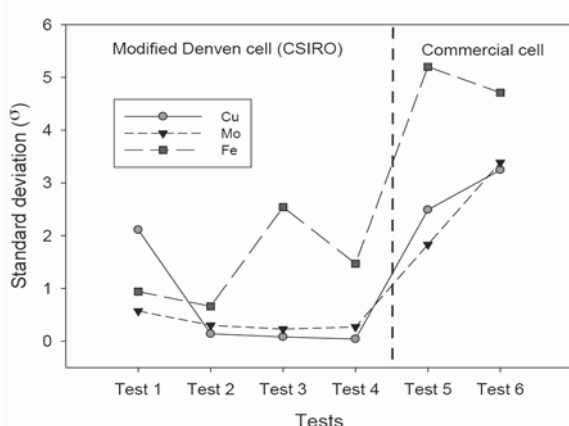


Figure 9—Comparison of reproducibility through the standard deviation for flotation tests in modified Denver cell (tests 1–4) and commercial cell (tests 5 and 6)

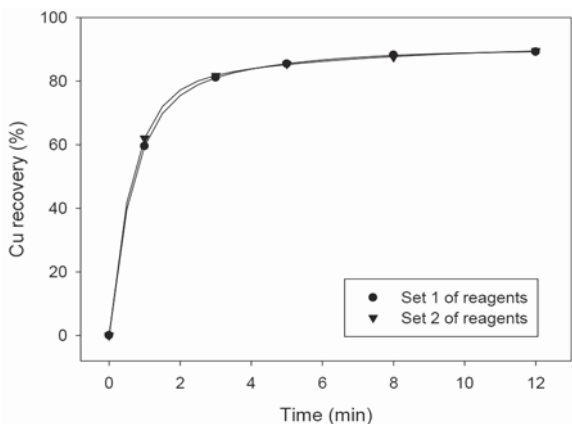


Figure 10—Flotation kinetics of copper in modified Denver cell. Symbols are experimental data, and solid curves are obtained by the fast/slow-floating model

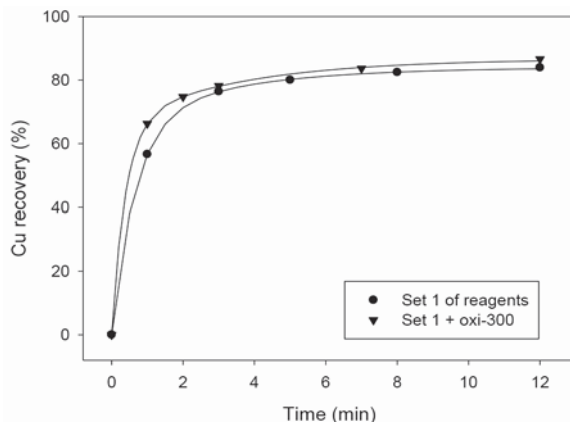


Figure 11—Flotation kinetics of copper in the commercial cell. Symbols are experimental data, and solid curves are obtained by the fast/slow-floating model

Table III

Parameters obtained by fitting the fast/slow-floating particles model to experimental data. Tests performed at natural pH with two sets of reagents in modified Denver cell

Mineral-set of reagents	R_{∞}	k_s	k_f	ϕ	K
Cu-set 1	89.2	0.38	1.59	0.73	91.3
Cu-set 2	89.5	0.29	1.60	0.81	92.3
Mo-set 1	79.9	0.22	1.51	0.95	83.0
Mo-set 2	81.0	0.15	1.67	0.95	84.8
Fe-set 1	35.1	0.15	1.37	0.80	35.5
Fe-set 2	37.7	0.16	1.49	0.78	38.4

Table IV

Parameters obtained by fitting the fast/slow-floating model to experimental data. Tests performed at natural pH with set 1 of reagents and testing an organic pyrite depressant (Oxi-300). Flotation tests conducted in the commercial cell

Mineral-set of reagents	R_{∞}	k_s	k_f	ϕ	s
Cu-set 1	83.9	0.32	1.54	0.78	86.9
Cu-set 1+oxi-300	86.6	0.29	2.59	0.76	93.0
Mo-set 1	78.1	0.30	1.56	0.95	81.3
Mo-set 1+oxi-300	71.0	0.27	2.34	0.92	76.7
Fe-set 1	38.5	0.27	1.51	0.81	39.5
Fe-set 1+oxi-300	23.6	0.23	2.68	0.77	28

From Table III it is seen that K is very similar for Cu and Mo flotation kinetics. However, a small difference is noted for Fe, where K indicates that the global floatation performance is higher with reagent set 2.

The values of K obtained for the tests in the commercial cell (Table IV) indicate that the flotation kinetics of copper are benefited by the organic pyrite depressant, since K increased from 86.9 to 93.0. In the case of molybdenum, K was reduced from 81.3 to 76.7, indicating that the organic reagent has a detrimental effect on global floatation performance. Moreover, it is proved that the reagent promotes pyrite depression, since K decreased from 39.5 to 28.4.

The fast/slow-floating model is thus appropriate to describe the flotation kinetics of copper-molybdenum ores in

An improved flotation test method and pyrite depression by an organic reagent

seawater suspensions, since the GoF in all cases was higher than 0.999. Furthermore, the parameters obtained from the model can be useful for comparing the performance of each test under different conditions, wherein K is treated as an indicator of the global flotation performance.

Conclusions

Rougher flotation tests of Cu-Mo sulphide ores in seawater were carried out in two different flotation cells at the natural pH of the suspensions. This option avoids excessive lime consumption due to the buffering effect of seawater. However, a significant amount of pyrite is recovered, decreasing the quality of the concentrate. The main conclusions of this work are listed below.

- High copper and molybdenum recoveries in seawater at natural pH were achieved with both xanthate and isothiazole as primary collector
- Organic reagents are promising options for depressing pyrite in seawater. However, further studies of their impact on the floatability of molybdenum should be conducted. Organic reagents may be used when recovery of molybdenum is not important
- The modified Denver cell allows the whole froth surface to be scraped at constant depth and rate. This increases the quality of the concentrate, and improves the reproducibility of the results
- The fast/slow-floating model is appropriate for describing the flotation kinetics of copper-molybdenum sulphide ores in seawater.

The parameters obtained from the fast/slow floating-model are useful for comparing flotation tests carried out under different conditions, since the K indicator represents the global flotation performance. This takes into account simultaneously both maximum recovery and flotation rate.

Acknowledgements

The authors thank INNOVA CORFO Projects Csiro Chile 10CEII-9007, and L.A.C also thanks CONICYT and the Regional Government of Antofagasta for funding through the PAI programme, Project Anillo ACT 1201.

References

- AKGUL, D., CAKMAKC, M., KAYAALP, N., and KOYUNCU, I. 2008. Cost analysis of seawater desalination with reverse osmosis in Turkey. *Desalination*, vol. 220. pp. 123–131.
- BICAK, O., EKMEKCI, Z., BRADSHAW, D.J., and HARRIS, P.J. 2007. Adsorption of guar gum and CMC on pyrite. *Minerals Engineering*, vol. 20. pp. 996–1002.
- BOURNIVAL, G., PUGH, R.J., and ATA, S. 2011. Examination of NaCl and MIBC as bubble coalescence inhibitor in relation to froth flotation. *Minerals Engineering*, vol. 25, no. 1. pp. 47–53.
- BULUT, G., CEYLAN, A., SOYLU, B., and GOKTEPE, F. 2011. Role of starch and metabisulphite on pure pyrite and pyritic copper ore flotation. *Physicochemical Problems of Mineral Processing*, vol. 48, no. 1. pp. 39–48.
- CASTRO, S. 2012. Challenges in flotation of Cu-Mo sulfide ores in sea water. *Proceedings of the 1st International Symposium: Water in Mineral Processing*. Drelich, J. (ed.). SME, Englewood, CO. pp. 29–40.
- CASTRO, S., and LASKOWSKI, J.S. 2011. Froth flotation in saline water. *Powder and Particle Journal*, vol. 29. pp. 4–15.
- CISTERNAS, L. and MORENO, L. 2014. Sea water in mining: fundamentals and applications. Master Rill, Santiago (in Spanish).
- FORBES, E., DAVEY, K.J., and SMITH, L. 2014. Decoupling rheology and slime coating effect on the natural floatability of chalcopyrite in a clay-rich flotation pulp. *Minerals Engineering*, vol. 56. pp. 136–144.
- GHAFFOUR, N., MISSIMER, T.M., and AMY, G.L. 2013. Technical review and evaluation of the economics of water desalination: Current and future challenges for better water supply sustainability. *Desalination*, vol. 309. pp. 197–207.
- HANCER, M., CELIK, M.S., and MILLER, J.D. 2000. The significance of interfacial water structure in soluble salt flotation systems. *Journal of Colloid and Interface Science*, vol. 235. pp. 150–161.
- JELDRES, R.I., ARANCIBIA-BRAVO, M.P., REYES, A., AGURRE, C.E., CORTES, L., and CISTERNAS, L.A. 2017. The impact of seawater with calcium and magnesium removal for the flotation of copper-molybdenum sulphide ores. *Minerals Engineering*, vol. 109. pp. 10–13.
- JELDRES, R., FORBES, L., and CISTERNAS, L.A. 2016. Effect of seawater on sulfide ore flotation: a review. *Mineral Processing and Extractive Metallurgy Review*, vol. 37, no. 6. pp. 369–384.
- JELDRES, R.I., TOLEDO, P.G., CONCHA, F., STICKLAND, A.D., USHER, S.P., and SCALES, P.J. 2014. Impact of seawater salts on the viscoelastic behavior of flocculated mineral suspensions. *Colloids and Surfaces A: Physicochemical and Engineering Aspects*, vol. 461. pp. 295–302.
- KOH, P.T. and SMITH, L.K. 2011. The effect of stirring speed and induction time on flotation. *Minerals Engineering*, vol. 24, no. 5. pp. 442–448.
- KOLEINI, S.M., ABDOLLAHY, M., and SOLTANI, F. 2012. The comparison between sodium cyanide and white dextrin as pyrite depressants in the sequential flotation Cu-Zn massive sulphide ore-irantaknar. *Proceedings of the 26th International Mineral Processing Congress*, New Delhi, India. 24–28 September 2012. Indian Institute of Metals. pp. 5120–5128.
- KURSUN, H. 2014. Adsorption and flotation characteristics of the different types of frothers. *Particulate Science and Technology*, vol. 32. pp. 632–636.
- LASKOWSKI, J.S., CASTRO, S., and RAMOS, O. 2014. Effect of seawater main components n frothability in the flotation of Cu-Mo sulfide ore. *Physicochemical Problems of Mineral Processing*, vol. 50. pp. 17–29.
- LEE, K., ARNOT, T., and MATTIA, D. 2011. A review of reverse osmosis membrane materials for desalination-development to date and future potential. *Journal of Membrane Science*, vol. 370. pp. 1–22.
- LEIDNER, A.J., RISTER, M.E., LACEWELL, R.D., WOODARD, J.D., and STURDIVANT, A.W. 2012. An analysis of input choice, input prices, and environmental factors on the costs of seawater reverse osmosis systems. *Desalination*, vol. 291. pp. 48–55.
- LIU, R., SUN, W., HU, Y., and WANG, D. 2009. Effect of organic depressant lignosulfonate calcium on separation of chalcopyrite from pyrite. *Journal of Central South University of Technology*, vol. 16. pp. 753–757.
- LÓPEZ VALDIVIESO, A., CELEDÓN CERVANTES, T., SONG, S., ROBLEDO CABRERA, A., and LASKOWSKI, J. 2004. Dextrin as a non-toxic depressant for pyrite in flotation with xanthates as collector. *Minerals Engineering*, vol. 17. pp. 1001–1006.
- LUCAY, F., CISTERNAS, L.A., GÁLVEZ, E., and LÓPEZ-VALDIVIESO, A. 2015. Study of the natural floatability of molybdenite fines in saline solutions. Effect of gypsum precipitation. *Minerals and Metallurgical Processing Journal*, vol. 32. pp. 203–208.
- MERMILLÉ-BLONDIN, R., KONGOLO, M., DE DONATO, P., BENZAZOUS, M., BARRES, O., BUSSIERE, B., and AUBERTIN, M. 2005. Pyrite flotation with xanthate under alkaline conditions-application to environmental desulfurization. *Proceedings of the Centenary of Flotation Symposium*, Brisbane, Queensland, 6–9 June 2005. Australasian Institute of Mining and Metallurgy, Melbourne. pp. 683–692.
- MONARDES, A. 2009. Use of seawater in grinding-flotation operations and tailing disposal. *Proceedings of the XI Symposium on Mineral Processing Moly-Cop 2009*.
- MU, Y., PENG, Y., and LAUTEN, R.A. 2015. Electrochemistry aspects of pyrite in the presence of potassium amyl xanthate and a lignosulfonate-based biopolymer depressant. *Electrochimica Acta*, vol. 174. pp. 133–142.
- ORDÓÑEZ, J.J., MORENO, L., GÁLVEZ, E.D., and CISTERNAS, L.A. 2013. Sea water leaching of caliche mineral in column experiments. *Hydrometallurgy*, vol. 139. pp. 79–87.
- PARRAGÜEZ, L., BERNAL, L., and CARTAGENA, G. 2009. Chemical study for selectivity and recovery of metals sulphides by flotation using seawater. *Proceedings of the 6th International Mineral Processing Seminar*, Santiago, Chile. pp. 323–333.
- RAMOS, O., CASTRO, S., and LASKOWSKI, J.S. 2013. Copper-molybdenum ores flotation in seawater: Floatability and frothability. *Minerals Engineering*, vol. 53. pp. 108–112.
- SARQUÍS, P.E., MENÉNDEZ-AGUADO, J.M., MAHAMUD, M.M., and DSIOBA, R. 2014. Tannins: the organic depressants alternative in selective flotation of sulfide. *Journal of Cleaner Production*, vol. 84. pp. 723–726.
- UCURUM, M. and BAYAT, O. 2007. Effects of operating variables on modified flotation parameters in the mineral separation. *Separation and Purification Technology*, vol. 55. pp. 173–181.
- VEKI, L. 2013. The use of seawater as process water in concentration plant and the effects on the flotation performance of Cu-Mo ore. Master's thesis, University of Oulu, Finland.
- WANG, X.-H. 1995. Interfacial electrochemistry of pyrite oxidation and flotation. II. FTIR studies of xanthate adsorption on pyrite surfaces in neutral pH solutions. *Journal of Colloid and Interface Science*, vol. 171. pp. 413–428. ◆



The use of fuzzy-weighted binary integer goal programming to select the optimum site for a central processing plant

by E. Bakhtavar*, D. Khademi*, and R. Mikaeil*

Synopsis

Fuzzy-weighted integer goal programming has been developed and used to select the most suitable site to construct a central processing plant for several adjacent small-scale dimension stone quarries, based on the most effective criteria. In the first step of mathematical modelling, the most important goals and decision variables were defined. Accordingly, an objective function was used in the model for minimizing the sum of undesired fuzzy-weighted deviations. Fuzzy weights were determined by a matrix of pairwise comparisons of various expert judgments in this field and the fuzzy geometric mean. The goal and systemic constraints were also modelled. The most suitable site for the construction of the plant was selected after solving the mathematical model in the Excel® Solver add-in. The selected site had various advantages over the other sites, such as the shortest average distance to the quarries, the shortest distance to power access and workforce, and the lowest land price.

Keywords

fuzzy multi-objective, goal programming, binary integer, dimension stone quarry, processing plant.

Introduction

Selection of the most suitable site of a plant is one of the most important considerations when constructing an industrial project. A suitable site has a significant effect on a company's competitiveness in the market. Selecting a desirable location for constructing plants such as mineral processing facilities is an essential part of the economic planning that will enable a company to meet the needs of related upstream and downstream operations. These units are considered to be best built near the relevant mining sites because of technical difficulties, the cost of transporting minerals, and the traffic hazard caused by the movement of trucks transporting materials. Two main types of research using multi-attribute decision-making models have been reported for selection of a processing plant site (Safari *et al.* 2010, 2012). In that research, the analytic hierarchy process (AHP) and fuzzy technique for order preference by similarity to ideal solution (TOPSIS) approach were applied to select the suitable locations for the mineral processing plants for phases 1 and 2 of Sangari iron ore mine.

Fuzzy goal programming has been developed to solve decision-making problems

in a variety of specific scientific applications. However, this technique has not been applied to date for processing plant site selection. A vendor selection decision in a supply chain was formulated as a fuzzy mixed integer goal programming by Kumar, Vrat, and Shankar (2004). A fuzzy multi-goal programming model was developed to select 'thin film transistor liquid crystal display suppliers for cooperation' (Lee, Kang, and Chang, 2009). A fuzzy AHP approach was used to analyse the importance of effective factors based on experts' judgment. Arikán (2013) developed a multi-objective linear programming method to select a multi-source supplier. The programming approach was based on a fuzzy mathematical model and a specific solution using the decision-maker's aspirations for fuzzy goals. Jadidi, Cavalieri, and Zolfaghari (2015) proposed a multi-choice goal programming approach to solve a supplier selection problem, taking into consideration the preferences of decision-makers. Jinturkar and Deshmukh (2011) developed a fuzzy mixed integer goal programming model to plan rural energy for domestic use. Izadikhah (2015) introduced a fuzzy goal programming approach to select a practical machine tool for a manufacturing company. Jones and Wall (2015) developed an extended goal programming model to select an offshore wind farm site in the UK, using a parametric analysis at a meta-objective level.

The most important aspects specific to the current investigation, which have not been considered in other research related to site selection for a processing plant, are as follows:

- Consideration of several small-scale quarries (mines) that are adjacent to each other rather than selection for a processing plant site for one particular mine

* Department of Mining and Material Engineering, Urmia University of Technology, Urmia, Iran.
© The Southern African Institute of Mining and Metallurgy, 2017. ISSN 2225-6253. Paper received Dec. 2015; revised paper received Mar. 2017.

The use of fuzzy-weighted binary integer goal programming

- Selection of a site for a dimension stone processing plant. The decision-making process for selecting a plant site for a dimension stone quarry are completely different from those for a metal mine
- A multi-objective mathematical goal programming model with fuzzy weights was developed in the objective function and binary integer decision variables.

Due to the large number of dimension stone quarries in the West Azerbaijan province of Iran and their importance, there is a need to solve a more complex problem. This paper proposes an integrated multi-attribute and multi-objective model to select the most suitable site for a processing plant in all cases where there are several adjacent small-scale dimension stone quarries.

Material and methods

Selection of the most suitable site to construct a processing plant for several adjacent dimensional small-scale stone quarries has a multi-objective nature, and as such, goal programming is used for base modelling. Also, the objective here is to select one alternative among others, indicating the necessity of using (0-1) binary integer variables, in which the value of 'one' signifies selection of an alternative, and 'zero' signifies rejection. Each of the criteria (goals) has different importance, so each should be assigned a different weight. The following criteria are considered in order to identify the most suitable site for construction of a dimensional stone processing plant:

- Depth of groundwater
- Distance to high-voltage power source
- Distance to urban gas supply
- Average distance of the quarries from the alternative plant sites
- Distance to the point of consumption and processed stone markets
- Closest distance to local labour
- Topography
- Land price.

The fuzzy-weighted geometric mean of pairwise comparisons from different experts can be used to apply real conditions that are often uncertain and fuzzy in nature. Hence, the proposed approach is termed *fuzzy-weighted binary integer goal programming* and is, in fact, a developed version of the goal programming model. Firstly, we examine the steps and nature of the proposed approach, using a mining region that includes four small-scale travertine dimension stone quarries. The most important criteria and related effective goals on theoretical problem-solving are then expressed. In the next step, taking into account the degree of importance and the effectiveness of each goal in selecting the most desired alternative, the method of the fuzzy-weighted geometric mean from pairwise comparisons from different experts is used. After defining both types of systemic and goal variables, the fuzzy objective function and the related constraints are modelled mathematically.

Studied sites and quarries

Three sites were pre-selected for the study to find the most suitable site for a plant to process the stone extracted from

four adjacent small-scale travertine quarries within the city limits of Takab, located in Western Iran. The names of the quarries and the distance of each from the studied sites are listed in Table I.

The first alternative plant site is near the village of Bashbarat and the road of Shahindezh-Takab in close proximity to the city of Takab. The second alternative is located about 2 km from the village of Chapli towards Shahindezh. The third alternative is located about 3 km from the village of Chapli towards Shahindezh. Photographs of the quarries are given in Figure 1.

Table I
Distances of alternative plant sites from the quarries

	Quarry				Average distance
	Chapli 1	Chapli 2	Chapli 3	Bashbarat	
Distance from alternative 1 (km)	8.5	5.1	10.45	1.81	6.465
Distance from alternative 2 (km)	7.43	4.97	2.95	7.48	5.707
Distance from alternative 3 (km)	8.48	6.29	2.04	8.72	6.382



Figure 1—The four small-scale dimension stone quarries

Table II
Values of the most important criteria at each plant site

Criterion	Alternative		
	1	2	3
Depth of groundwater (m)	50	45	40
Distance to high-voltage power source (km)	8.67	2.12	3.17
Distance to urban gas supply (km)	19.51	25.94	28.07
Average distance of quarries to plant site (km)	6.465	5.707	6.382
Distance to the point of consumption and market (km)	19.51	25.94	28.07
Closest distance to local labour (km)	8.67	2.12	3.17
Topography	5	2	4
Land price (tormans)	100	40	70

The use of fuzzy-weighted binary integer goal programming

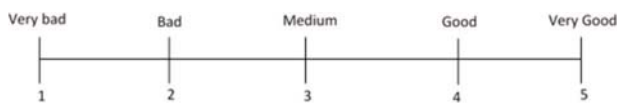


Figure 2—Quantitative scale to evaluate the topography criterion

Goals

Table II summarizes the most important criteria and the related data based on the three considered alternatives. The topography criterion is initially evaluated by a qualitative scale, then by using the quantitative scale shown in Figure 2.

According to the criteria in Table II, the goals considered in the case study are as follows:

- *Goal 1:* Maximum distance between the plant site and the quarries. The maximum distance for the case study is 5 km
- *Goal 2:* Maximum distance between the plant site and the point of consumption (sales market). The maximum distance for the case study is 20 km
- *Goal 3:* Maximum distance between the plant site and high-voltage power source. The maximum distance for the case study is 1 km
- *Goal 4:* Maximum distance between the plant site and the workforce. This maximum distance for the case study is 4 km
- *Goal 5:* Maximum depth to access groundwater. In the study region, the cost of drilling is approximately doubled at depths of over 45 m. Therefore, the maximum depth is considered to be 45 m
- *Goal 6:* According the classification for topography (Figure 2), the desirable topography is in the category 'good'
- *Goal 7:* A maximum cost should be assigned to acquiring the land for the plant site. Regarding the initial investment limitation and conditions in the region, the maximum land price is 70 million tomans (\$21 000)
- *Goal 8:* Maximum distance between the plant site and gas supply. This maximum distance for the case study is 10 km.

Determining weights for goals

First, a qualitative questionnaire was prepared and completed by 12 experts in the field to determine the weights of the goals. Pairwise comparison matrices composed of triangular fuzzy numbers are formed using information collected from the completed questionnaires and regarding a common fuzzy scale. An example of a fuzzy triangular pairwise comparison

matrix resulting from the judgments of experts is given in Table III.

In the next step, the weighted geometric mean method, which was introduced by Aczel and Saaty (1983) as the best method for the aggregation of individual judgments, is developed to apply in the fuzzy form according to Equations [1] and [2]. Each goal's fuzzy weight is determined using Equations [1] to [3]. First, the fuzzy triangular geometric mean weight of criterion (goal) i in comparison with criterion j based on the judgments by all experts is determined using Equation [1]. Then, Equations [2] and [3] are used to determine the fuzzy triangular geometric weight of each goal. Finally, the fuzzy triangular geometric weights are defuzzified using Equation [4] as the centre of area defuzzification method to obtain crisp weights; the results are given in Table IV.

$$\tilde{w}_{i,j} = \left(\prod_{k=1}^K \tilde{w}_{i,j}^k \right)^{1/K} \quad [1]$$

$$\tilde{w}_i = \left(\prod_{j=1}^n \tilde{w}_{i,j} \right)^{1/n} \quad \forall i = (1, 2, \dots, m) \quad [2]$$

$$\tilde{W}_i = \frac{\tilde{w}_i}{\sum_{i=1}^m \tilde{w}_i} \quad [3]$$

$$W_i = \frac{(u_i - l_i) + (m_i - l_i)}{3} + l_i \quad [4]$$

where

$\tilde{w}_{i,j}$ is the fuzzy triangular geometric mean weight of criterion (goal) i in comparison with j based on the judgments by all experts

$\tilde{w}_{i,j}^k$ is the fuzzy triangular weight of criterion (goal) i in comparison with j based on the judgment of k th expert

K is the number of experts

\tilde{w}_i is the fuzzy triangular geometric mean weight of i th goal

\tilde{W}_i is the fuzzy triangular geometric weight of i th goal; it is defined as (l_i, m_i, u_i)

W_i is the crisp weight of i th goal

l_i is the lower point of the fuzzy triangular weight of i th goal

m_i is the middle point of the fuzzy triangular weight of i th goal

u_i is the upper point of the fuzzy triangular weight of i th goal

Table III

An example triangular fuzzy pairwise comparison matrix resulting from expert judgment

	G1			G2			G3			G4			G5			G6			G7			G8			
G1	1.0	1.0	1.0	0.3	0.5	1.0	3.0	4.0	5.0	0.2	0.3	0.3	0.2	0.3	0.3	0.3	0.5	1.0	1.0	1.0	1.0	1.0	1.0	2.0	3.0
G2	1.0	2.0	3.0	1.0	1.0	1.0	5.0	6.0	7.0	0.3	0.5	1.0	0.3	0.5	1.0	1.0	1.0	1.0	1.0	1.0	2.0	3.0	3.0	4.0	5.0
G3	0.2	0.3	0.3	0.1	0.2	0.2	1.0	1.0	1.0	0.1	0.1	0.1	0.1	0.1	0.1	0.1	0.2	0.2	0.2	0.3	0.3	0.3	0.5	1.0	
G4	3.0	4.0	5.0	1.0	2.0	3.0	7.0	8.0	9.0	1.0	1.0	1.0	1.0	1.0	1.0	1.0	2.0	3.0	3.0	4.0	5.0	5.0	6.0	7.0	
G5	3.0	4.0	5.0	1.0	2.0	3.0	7.0	8.0	9.0	1.0	1.0	1.0	1.0	1.0	1.0	1.0	2.0	3.0	3.0	4.0	5.0	5.0	6.0	7.0	
G6	1.0	2.0	3.0	1.0	1.0	1.0	5.0	6.0	7.0	0.3	0.5	1.0	1.0	1.0	1.0	1.0	1.0	1.0	1.0	1.0	2.0	3.0	3.0	4.0	5.0
G7	1.0	1.0	1.0	0.3	0.5	1.0	3.0	4.0	5.0	0.2	0.3	0.3	0.3	0.5	1.0	1.0	1.0	1.0	1.0	1.0	1.0	2.0	3.0	3.0	4.0
G8	0.3	0.5	1.0	0.2	0.3	0.3	1.0	2.0	3.0	0.1	0.2	0.2	0.1	0.2	0.2	0.2	0.3	0.3	0.3	0.5	1.0	1.0	1.0	1.0	1.0

The use of fuzzy-weighted binary integer goal programming

Table IV Fuzzy and crisp weights using weighted geometric mean method		
Goal	Fuzzy weight	Crisp weight
G1	(0.042,0.073,0.135)	0.083
G2	(0.078,0.14,0.259)	0.159
G3	(0.015,0.023,0.039)	0.026
G4	(0.149,0.257,0.417)	0.274
G5	(0.149,0.257,0.417)	0.274
G6	(0.078,0.14,0.259)	0.159
G7	(0.042,0.073,0.135)	0.083
G8	(0.023,0.039,0.074)	0.045

Definition of systemic and goal decision variables

The first step of mathematical modelling and formulating a mathematical model is to define the decision variables that form the base of the mathematical programming. The nature of programming for this investigation is a little different because it is multi-objective and based on goal binary integer programming, in that a series of goal variables should be defined in addition to systemic decision variables, which in fact indicate amounts of desirable and undesirable deviations from the goals. Goal variables (desirable and undesirable deviations (d_i^- , d_i^+ , where i is an index for the goals), unlike systemic variables (x_j , where j is the index for the alternatives) that have the nature of zero and unity are both in the objective function and the constraints. In fact, the objective function is only based on goal variables (undesirable deviations) and goal constraints are modelled using all systemic and goal variables. Systemic and goal variables used in this case study are as follows:

$$x_j \in \{0,1\}, \quad \forall j = (1, 2, 3) \\ d_i^-, d_i^+ \geq 0, \quad \forall i = (1, 2, \dots, 8)$$

Definition of the objective function and constraints

The general mathematical expression of the objective function in the developed approach is according to Equation [5]. It indicates minimization of the sum of undesirable deviations from different goals by considering the degree of importance and affecting the weight of each. The objective function is modelled as Equation [6] by considering the effect of the fuzzy weights for each of the goals. The goal constraints are expressed as Equations [8] to [15] based on Equation [7] and using the data summarized in Table II. The only systemic constraint is modelled as Equation [16].

$$(Min) Z = \sum_{i=1}^m W_{N_i} \cdot d_i \quad \forall d_i = (d_i^- \text{ or } d_i^+) \\ (Min) Z = W_{N_1} \cdot d_1^+ + W_{N_2} \cdot d_2^+ + \dots + W_{N_6} \cdot d_6^- + W_{N_7} \cdot d_7^+ + W_{N_8} \cdot d_8^+ \Rightarrow [5] \\ (Min) Z = \left(\frac{0.274}{5} \right) \cdot d_1^+ + \left(\frac{0.274}{20} \right) \cdot d_2^+ + \left(\frac{0.159}{1} \right) \cdot d_3^+ + \left(\frac{0.159}{4} \right) \cdot d_4^+ \\ + \left(\frac{0.083}{45} \right) \cdot d_5^+ + \left(\frac{0.083}{4} \right) \cdot d_6^- + \left(\frac{0.045}{70} \right) \cdot d_7^+ + \left(\frac{0.026}{10} \right) \cdot d_8^+ \Rightarrow [6] \\ (Min) Z = 0.0548 \cdot d_1^+ + 0.0137 \cdot d_2^+ + 0.159 \cdot d_3^+ + 0.0398 \cdot d_4^+ \\ + 0.0018 \cdot d_5^+ + 0.0208 \cdot d_6^- + 0.0006 \cdot d_7^+ + 0.0026 \cdot d_8^+$$

$$\sum_{j=1}^n c_j \cdot x_j + d_i^- - d_i^+ = b_i \quad \forall i = (1, 2, \dots, m) \quad [7]$$

$$6.46x_1 + 5.7x_2 + 6.38x_3 + d_1^- - d_1^+ = 5 \quad [8]$$

$$19.51x_1 + 25.94x_2 + 28.07x_3 + d_2^- - d_2^+ = 20 \quad [9]$$

$$8.67x_1 + 2.12x_2 + 3.17x_3 + d_3^- - d_3^+ = 1 \quad [10]$$

$$8.67x_1 + 2.12x_2 + 3.17x_3 + d_4^- - d_4^+ = 4 \quad [11]$$

$$50x_1 + 45x_2 + 40x_3 + d_5^- - d_5^+ = 45 \quad [12]$$

$$5x_1 + 2x_2 + 4x_3 + d_6^- - d_6^+ = 4 \quad [13]$$

$$100x_1 + 40x_2 + 70x_3 + d_7^- - d_7^+ = 70 \quad [14]$$

$$19.51x_1 + 25.94x_2 + 28.07x_3 + d_8^- - d_8^+ = 10 \quad [15]$$

$$x_1 + x_2 + x_3 = 1 \\ x_j \in \{0,1\}, \quad j = (1, 2, 3) \quad d_i^-, d_i^+ \geq 0, \quad i = (1, 2, \dots, 8) \quad [16]$$

Results and discussion

In this section, the model formulated as Equations [5] to [16] is used to select the most suitable processing plant site from the three pre-selected sites. The model was solved using Excel® Solver on a computer with a 2.4 GHz processor and 4 GB RAM. The results, including both deviational and systemic decision variables as well as achievement values of goals, are presented in Table V.

According to the results given in Table V and the software output (Figure 3), the second alternative is the most suitable site. The second site is closer to the quarries, the high-voltage power source, and workforce, although it has only a moderate access level to groundwater and a moderate distance to the market and gas supply. Furthermore, it is more desirable than other sites on the basis of topography and land price. The first alternative (site) is well positioned in terms of distance to the market and gas supply, but in other aspects it is less desirable. The third alternative has only the best access to water.

The resulting deviational values for the four goals 1, 2, 3, and 8 are 0.7, 5.9, 1.1, and 15.9, respectively. However, other deviational values for goals 4, 5, 6, and 7 were zero. It is worth noting that only undesirable goal variables 1, 2, 3, and 8 influence the total value of the objective function (0.3393). As observed, goals 4, 5, 6, and 7 are satisfied by the exact upper bound values of 4, 45, 4, and 70, respectively; without any deviation. On the other hand, goals 1, 2, 3, and 8 have been satisfied through the values

The use of fuzzy-weighted binary integer goal programming

Table V

Excel® Solver output for the case study based on the developed model

	x_1	x_2	x_3	d_1^+	d_1^-	d_2^+	d_2^-	d_3^+	d_3^-	d_4^+	d_4^-	d_5^+	d_5^-	d_6^+	d_6^-	d_7^+	d_7^-	d_8^+	d_8^-	Total	Bound
DV	0	1	0	0.7	0.0	5.9	0.0	1.1	0.0	0.0	1.9	0.0	0.0	2.0	0.0	0.0	30.0	15.9	0.0		
OF	0	0	0	0.0548	0	0.0137	0	0.159	0	0.0398	0	0.0018	0	0	0.0208	0.0006	0	0.0026	0	0.3393	
OC	1	1	1	0	0	0	0	0	0	0	0	0	0	0	0	0	0	0	0	1	1
G1	6.46	5.70	6.38	-1	1	0	0	0	0	0	0	0	0	0	0	0	0	0	0	5	5
G2	19.51	25.94	28.07	0	0	-1	1	0	0	0	0	0	0	0	0	0	0	0	0	20	20
G3	8.67	2.12	3.17	0	0	0	0	-1	1	0	0	0	0	0	0	0	0	0	0	1	1
G4	8.67	2.12	3.17	0	0	0	0	0	0	-1	1	0	0	0	0	0	0	0	0	4	4
G5	50	45	40	0	0	0	0	0	0	0	0	-1	1	0	0	0	0	0	0	45	45
G6	5	2	4	0	0	0	0	0	0	0	0	0	0	1	-1	0	0	0	0	4	4
G7	100	40	70	0	0	0	0	0	0	0	0	0	0	0	0	-1	1	0	0	70	70
G8	19.51	25.94	28.07	0	0	0	0	0	0	0	0	0	0	0	0	0	0	-1	1	10	10

DV=decision variables; OF=objective function; OC=one choice

Microsoft Excel 15.0 Answer Report				
Worksheet: [94-03-13-Solver-GP-Modified.xlsx]Sheet1				
Report Created: 6/4/2015 3:09:33 AM				
Result: Solver found a solution. All Constraints and optimality conditions are satisfied.				
Solver Engine				
Engine: Simplex LP Solution Time: 0.031 Seconds Iterations: 15 Subproblems: 0				
Objective Cell (Min)				
Cell	Name	Original Value	Final Value	
\$U\$3	Objective Function totals	0.0000	0.3393	
Variable Cells				
Cell	Name	Original Value	Final Value	Integer
\$B\$2	x1_	0	0	Binary
\$C\$2	x2_	0	1	Binary
\$D\$2	x3_	0	0	Binary
\$E\$2	b1_	0.0	0.7	Contin
\$F\$2	d1_	0.0	0.0	Contin
\$G\$2	b2_	0.0	5.9	Contin
\$H\$2	d2_	0.0	0.0	Contin
\$I\$2	b3_	0.0	1.1	Contin
\$J\$2	d3_	0.0	0.0	Contin
\$K\$2	b4_	0.0	0.0	Contin
\$L\$2	d4_	0.0	1.9	Contin
\$M\$2	b5_	0.0	0.0	Contin
\$N\$2	d5_	0.0	0.0	Contin
\$O\$2	b6_	0.0	2.0	Contin
\$P\$2	d6_	0.0	0.0	Contin
\$Q\$2	b7_	0.0	0.0	Contin
\$R\$2	d7_	0.0	30.0	Contin
\$S\$2	b8_	0.0	15.9	Contin
\$T\$2	d8_	0.0	0.0	Contin
Constraints				
Cell	Name	Cell Value	Formula	Status
\$U\$4	One choice totals	1.000	\$U\$4=\$V\$4	Binding
\$U\$5	Distance to mines totals	5.000	\$U\$5=\$V\$5	Binding
\$U\$6	Distance to market totals	20.000	\$U\$6=\$V\$6	Binding
\$U\$7	Distance to power totals	1.000	\$U\$7=\$V\$7	Binding
\$U\$8	Distance to working force totals	4.000	\$U\$8=\$V\$8	Binding
\$U\$9	Depth of water level totals	45.000	\$U\$9=\$V\$9	Binding
\$U\$10	Topography conditions totals	4.000	\$U\$10=\$V\$10	Binding
\$U\$11	Ground investment cost totals	70.000	\$U\$11=\$V\$11	Binding
\$U\$12	Distance to gas totals	10.000	\$U\$12=\$V\$12	Binding
\$B\$2:\$D\$2=Binary				

Figure 3—Excel® Solver output report of the developed model

The use of fuzzy-weighted binary integer goal programming

5.03836, 20.08083, 1.1749, and 10.4134, respectively after adding deviational values (0.03836, 0.08083, 0.1749, and 0.4134) to their upper bounds. The third goal constraint includes a higher deviation than other goal constraints.

According to goal constraint 8, access to gas supply includes an additional cost. Goal constraint 1, with a very low deviation, reveals that if the distance of the quarries from a given plant site is less and connection is possible in all seasons of the year, it could be considered as effective regarding the supply of raw materials. Goal constraint 2 includes a negligible deviation. Based on that, being near to the point of consumption (market) is one of the most important parameters for a construction site.

Other goal constraints (4, 5, 6, and 7) have no deviation. In this case, based on goal constraint 4, many personnel are indoors workers and less experienced people, and for this reason, the maximum distance to a workforce is 4 km, with no deviation value. One of the basic requirements for a stone cutting and processing plant is a plentiful water supply to cool the cutting and polishing machinery. Water wells are usually used for this purpose. According to goal constraint 5, the best location for the plant will be where the groundwater is closest to the surface, where minimum drilling will be required to access the water. The maximum drilling depth is 45 m with no deviation value, and the cost of drilling doubles at greater depths. As goal constraint 6 is defined, in areas with flatter topography less excavation is required, and there is more flexibility in the location and extent of activities. As considered in goal constraint 7, the price of land is an important parameter. However, this is a one-time payment, so the maximum price is considered as being 70 million tomans (\$21000) without any deviation.

Considering the *in-situ* investigations in the studied area and based on the priorities of the related goals, the second alternative seems to be the most suitable site. This indicates that the results of the fuzzy goal programming model are valid. Despite the acceptable responses from the developed model, the result depends on the accuracy of the data collected from the field.

Conclusions

Selection of the most suitable site for a processing plant is a key step in the construction process, in that the results of this decision could have an important and long-term impact on various aspects on the plant and the related upstream and downstream industries. Owing to the cost of transportation of stone from quarries to the plant and the point of marketing, such plants are built near quarries and as close as possible to where the stone is marketed. Selection of the most desirable place to construct a processing plant to serve several quarries that are adjacent to each other is a consideration that has not yet been studied in other research, especially by multi-objective modelling. Accordingly, a multi-objective approach has been developed with fuzzy weights and priorities and using binary integer decision variables for a locality with four quarries, and three possible alternatives for a plant site. Local surveys and research were conducted, and information obtained from several experts was examined to determine acceptable numbers to start the activity. After introducing the fuzzy goal programming mathematical model, Excel® Solver

was used to solve the model and determine the best site for plant construction. The best alternative was selected based on the shortest distance to the quarries, the workforce, and the high-voltage power source.

References

- ARIKAN, F. 2013. A fuzzy solution approach for multi objective supplier selection. *Expert Systems with Applications*, vol. 40. pp. 947–952.
- ACZEL, J. and SAATY, T.L. 1983. Procedures for synthesizing ratio judgements. *Journal of Mathematical Psychology*, vol. 27, no. 1. pp. 93–102.
- IZADIKAH, M. 2015. A fuzzy goal programming based procedure for machine tool selection. *Journal of Intelligent & Fuzzy Systems*, vol. 28, no. 1. pp. 361–372.
- JADIDI, O., CAVALIERI, S., and ZOLFAGHARI, S. 2015. An improved multi-choice goal programming approach for supplier selection problems. *Applied Mathematical Modelling*, vol. 39, no. 14. pp. 4213–4222.
- JINTURKAR, A.M. and DESHMUKH, S.S. 2011. A fuzzy mixed integer goal programming approach for cooking and heating energy planning in rural India. *Expert Systems with Applications*, vol. 38, no. 9. pp. 11377–11381.
- JONES, D.F. and WALL, G. 2015. An extended goal programming model for site selection in the offshore wind farm sector. *Annals of Operations Research*. DOI 10.1007/s10479-015-1828-2.
- KUMAR, M., VRAT, P., and SHANKAR, R. 2004. A fuzzy goal programming approach for vendor selection problem in a supply chain. *Computers and Industrial Engineering*, vol. 46, no. 1. pp. 69–85.
- LEE, A.H.I., KANG, H.Y., and CHANG, C.T. 2009. Fuzzy multiple goal programming applied to TFT-LCD supplier selection by downstream manufacturers. *Expert Systems with Applications*, vol. 38. pp. 6318–6325.
- SAFARI, M., ATAEI, M., KHALOKAKAEI, R., and KARAMOZIAN, M. 2010. Mineral processing plant location using the analytic hierarchy process—a case study: the Sangan iron ore mine (phase 1). *Mining Science and Technology*, vol. 20, no. 5. pp. 691–695.
- SAFARI, M., KHALOKAKAEI, R., ATAEI, M., and KARAMOZIAN, M. 2012. Using fuzzy TOPSIS method for mineral processing plant site selection. *Arabian Journal of Geosciences*, vol. 5. pp. 1011–1019. ◆

INTERNATIONAL ACTIVITIES

2017

20–27 May 2017 — ALTA 2017 Nickel-Cobalt-Copper, Uranium-REE and Gold-PM Conference and Exhibition
Pan Pacific Perth, Australia
Contact: Allison Taylor
Tel: +61 (0) 411 692 442, E-mail: allisontaylor@altamet.com.au
Website: <http://www.altamet.com.au/conferences/alta-2017/>

6–7 June 2017 — Mine Planning Colloquium 2017
Mintek, Randburg, South Africa
Contact: Camielah Jardine
Tel: +27 11 834-1273/7, Fax: +27 11 838-5923/833-8156
E-mail: camielah@saimm.co.za, Website: <http://www.saimm.co.za>

7–8 June 2017 — AIMS - Aachen International Mining Symposia Second International Conference: Mining in Europe
Aachen, Germany
Contact: Iris Schümmer
Tel: +49-(0) 241-80 95673, Fax: +49-(0) 241-80 92272
E-mail: aims@mre.rwth-aachen.de
Website: <http://www.aims.rwth-aachen.de>

19–20 June 2017 — Chrome Colloquium 2017
What's next for Chrome? A debate on the tough questions
Mintek, Randburg, South Africa
Contact: Camielah Jardine
Tel: +27 11 834-1273/7, Fax: +27 11 838-5923/833-8156
E-mail: camielah@saimm.co.za, Website: <http://www.saimm.co.za>

25–28 June 2017 — Emc 2017: European Metallurgical Conference
Leipzig, Germany
Contact: Paul-Ernst-Straße
Tel: +49 5323 9379-0, Fax: +49 5323 9379-37
E-mail: EMC@gdmg.de, Website: <http://emc.gdmb.de>

27–29 June 2017 — 4th Mineral Project Valuation Colloquium
Mine Design Lab, Chamber of Mines Building,
The University of the Witwatersrand, Johannesburg
Contact: Camielah Jardine
Tel: +27 11 834-1273/7, Fax: +27 11 838-5923/833-8156
E-mail: camielah@saimm.co.za, Website: <http://www.saimm.co.za>

10–11 July 2017 — Water 2017 Conference
Lifeblood of the Mining Industry
Emperors Palace, Hotel Casino Convention Resort, Johannesburg
Contact: Camielah Jardine
Tel: +27 11 834-1273/7, Fax: +27 11 838-5923/833-8156
E-mail: camielah@saimm.co.za, Website: <http://www.saimm.co.za>

25–26 July 2017 — Entrepreneurship in Mining Forum
A Focus on new Business in the Value Chain
Johannesburg
Contact: Camielah Jardine
Tel: +27 11 834-1273/7, Fax: +27 11 838-5923/833-8156
E-mail: camielah@saimm.co.za, Website: <http://www.saimm.co.za>

3–4 August 2017 — Building a Robust Mineral Industry
Thriving under prolonged low commodity price environment
Mandel Training Centre, Marlborough, Harare
Contact: Camielah Jardine
Tel: +27 11 834-1273/7, Fax: +27 11 838-5923/833-8156
E-mail: camielah@saimm.co.za, Website: <http://www.saimm.co.za>

7–9 August 2017 — Rapid Underground Mine & Civil Access Conference 2017
Emperors Palace, Hotel Casino Convention Resort, Johannesburg
Contact: Camielah Jardine
Tel: +27 11 834-1273/7, Fax: +27 11 838-5923/833-8156
E-mail: camielah@saimm.co.za, Website: <http://www.saimm.co.za>

15–16 August 2017 — The SAMREC and SAMVAL Codes Advanced Workshop: Can you face your peers?
Emperors Palace, Hotel Casino Convention Resort, Johannesburg
Contact: Camielah Jardine
Tel: +27 11 834-1273/7, Fax: +27 11 838-5923/833-8156
E-mail: camielah@saimm.co.za, Website: <http://www.saimm.co.za>

22–24 August 2017 — The biennial Southern African Coal Processing Society Conference and Exhibition
'Coal Processing – the key to profitability'
Graceland Hotel, Casino and Country Club, Secunda
Contact: Gerda Craddock
Tel: +27 11 432-8918, E-mail: gerdac@mineralconcepts.co.za
Website: www.sacoalprep.co.za

30 August–1 September 2017 — MINESafe Conference 2017
Striving for Zero Harm—Driving Excellence through Compliance
Emperors Palace, Hotel Casino Convention Resort, Johannesburg
Contact: Camielah Jardine
Tel: +27 11 834-1273/7, Fax: +27 11 838-5923/833-8156
E-mail: camielah@saimm.co.za, Website: <http://www.saimm.co.za>

11–15 September 2017 — Uranium 2017 International Conference
Extraction and Applications of Uranium — Present and Future
Swakopmund Hotel, Swakopmund, Namibia
Contact: Camielah Jardine
Tel: +27 11 834-1273/7, Fax: +27 11 838-5923/833-8156
E-mail: camielah@saimm.co.za, Website: <http://www.saimm.co.za>

30 September–6 October 2017 — AfriRock 2017: ISRM International Symposium—Rock Mechanics for Africa
Cape Town Convention Centre, Cape Town
Contact: Camielah Jardine
Tel: +27 11 834-1273/7, Fax: +27 11 838-5923/833-8156
E-mail: camielah@saimm.co.za, Website: <http://www.saimm.co.za>

17–20 October 2017 — AMI Precious Metals 2017
The Precious Metals Development Network (PMDN)
Protea Hotel Ranch Resort, Polokwane
Contact: Camielah Jardine
Tel: +27 11 834-1273/7, Fax: +27 11 838-5923/833-8156
E-mail: camielah@saimm.co.za, Website: <http://www.saimm.co.za>

18–20 October 2017 — 7th International Platinum Conference
Platinum—A Changing Industry
Protea Hotel Ranch Resort, Polokwane
Contact: Camielah Jardine
Tel: +27 11 834-1273/7, Fax: +27 11 838-5923/833-8156
E-mail: camielah@saimm.co.za, Website: <http://www.saimm.co.za>

25 October 2017 — 14th Annual Student Colloquium
Johannesburg
Contact: Camielah Jardine
Tel: +27 11 834-1273/7, Fax: +27 11 838-5923/833-8156
E-mail: camielah@saimm.co.za, Website: <http://www.saimm.co.za>

Company Affiliates

The following organizations have been admitted to the Institute as Company Affiliates

3M South Africa (Pty) Limited	Expectra 2004 (Pty) Ltd	Ncamiso Trading (Pty) Ltd
AECOM SA (Pty) Ltd	Exxaro Coal (Pty) Ltd	New Concept Mining (Pty) Limited
AEL Mining Services Limited	Exxaro Resources Limited	Northam Platinum Ltd - Zondereinde
Air Liquide (PTY) Ltd	Filtquip (Pty) Ltd	PANalytical (Pty) Ltd
AMEC Foster Wheeler	FLSmidth Minerals (Pty) Ltd	Paterson & Cooke Consulting Engineers (Pty) Ltd
AMIRA International Africa (Pty) Ltd	Fluor Daniel SA (Pty) Ltd	PerkinElmer
ANDRITZ Delkor (Pty) Ltd	Franki Africa (Pty) Ltd-JHB	Polysius A Division Of Thyssenkrupp Industrial Sol
Anglo Operations (Pty) Ltd	Fraser Alexander Group	Precious Metals Refiners
Arcus Gibb (Pty) Ltd	Geobrugg Southern Africa (Pty) Ltd	Rand Refinery Limited
Aurecon South Africa (Pty) Ltd	Glencore	Redpath Mining (South Africa) (Pty) Ltd
Aveng Engineering	Goba (Pty) Ltd	Rocbolt Technologies
Aveng Mining Shafts and Underground	Hall Core Drilling (Pty) Ltd	Rosond (Pty) Ltd
Axis House Pty Ltd	Hatch (Pty) Ltd	Royal Bafokeng Platinum
Bafokeng Rasimone Platinum Mine	Herrenknecht AG	Roytec Global Pty Ltd
Barloworld Equipment -Mining	HPE Hydro Power Equipment (Pty) Ltd	RungePincockMinarco Limited
BASF Holdings SA (Pty) Ltd	IMS Engineering (Pty) Ltd	Rustenburg Platinum Mines Limited
BCL Limited	Ivanhoe Mines SA	Salene Mining (Pty) Ltd
Becker Mining (Pty) Ltd	Joy Global Inc.(Africa)	Sandvik Mining and Construction Delmas (Pty) Ltd
BedRock Mining Support Pty Ltd	Kudumane Manganese Resources	Sandvik Mining and Construction RSA(Pty) Ltd
Bell Equipment Limited	Leco Africa (Pty) Limited	SANIRE
Blue Cube Systems (Pty) Ltd	Longyear South Africa (Pty) Ltd	Schauenburg(Pty) Ltd
Bluhm Burton Engineering Pty Ltd	Lonmin Plc	SENET (Pty) Ltd
CDM Group	Magotteaux (Pty) Ltd	Senmin International (Pty) Ltd
CGG Services SA	MBE Minerals SA Pty Ltd	Smec South Africa
Concor Mining	MCC Contracts (Pty) Ltd	SMS group Technical Services South Africa (Pty) Ltd
Concor Technicrete	MD Mineral Technologies SA (Pty) Ltd	Sound Mining Solution (Pty) Ltd
Cornerstone Minerals Pty Ltd	MDM Technical Africa (Pty) Ltd	South 32
Council for Geoscience Library	Metalock Engineering RSA (Pty) Ltd	SRK Consulting SA (Pty) Ltd
Cronimet Mining Processing SA (Pty) Ltd	Metorex Limited	Technology Innovation Agency
CSIR Natural Resources and the Environment (NRE)	Metso Minerals (South Africa) Pty Ltd	Time Mining and Processing (Pty) Ltd
Data Mine SA	MineRP Holding (Pty) Ltd	Tomra (Pty) Ltd
Department of Water Affairs and Forestry	Mintek	Ukwazi Mining Solutions (Pty) Ltd
Digby Wells and Associates	MIP Process Technologies (Pty) Ltd	Umgeni Water
DRA Mineral Projects (Pty) Ltd	MSA Group (Pty) Ltd	Webber Wentzel
DTP Mining - Bouygues Construction	Multotec (Pty) Ltd	Weir Minerals Africa
Duraset	Murray and Roberts Cementation	WorleyParsons RSA (Pty) Ltd
Elbroc Mining Products (Pty) Ltd	Nalco Africa (Pty) Ltd	
eThekweni Municipality	Namakwa Sands (Pty) Ltd	

Forthcoming SAIMM events...

EXHIBITS/SPONSORSHIP

Companies wishing to sponsor and/or exhibit at any of these events should contact the conference co-ordinator as soon as possible.

SAIMM DIARY

2017

For the past 123 years, the Southern African Institute of Mining and Metallurgy, has promoted technical excellence in the minerals industry. We strive to continuously stay at the cutting edge of new developments in the mining and metallurgy industry. The SAIMM acts as the corporate voice for the mining and metallurgy industry in the South African economy. We actively encourage contact and networking between members and the strengthening of ties. The SAIMM offers a variety of conferences that are designed to bring you technical knowledge and information of interest for the good of the industry. Here is a glimpse of the events we have lined up for 2017. Visit our website for more information.

- ◆ COLLOQUIUM
Mine Planning Colloquium 2017
6–7 June 2017, Mintek, Randburg
- ◆ COLLOQUIUM
Chrome Colloquium 2017
19–20 June 2017, Mintek, Randburg
- ◆ COLLOQUIUM
4th Mineral Project Valuation Colloquium
27–29 June 2017, Mine Design Lab, Chamber of Mines Building, The University of the Witwatersrand, Johannesburg
- ◆ CONFERENCE
Water 2017: Lifeblood of the Mining Industry Conference 2017
10–11 July 2017, Emperors Palace, Hotel Casino Convention Resort, Johannesburg
- ◆ FORUM
Entrepreneurship in Mining Forum
25–26 July 2017, Johannesburg
- ◆ CONFERENCE
Building a Robust Mineral Industry
3–4 August 2017, Mandel Training Centre, Marlborough, Harare
- ◆ CONFERENCE
Rapid Underground Mine & Civil Access 2017 Conference
7–9 August 2017, Emperors Palace, Hotel Casino Convention Resort, Johannesburg
- ◆ WORKSHOP
The SAMREC and SAMVAL Codes—Advanced Workshop: Can you face your peers?
15–16 August 2017, Emperors Palace, Hotel Casino Convention Resort, Johannesburg
- ◆ CONFERENCE
MINESafe Conference 2017
30 August–1 September 2017, Emperors Palace, Hotel Casino Convention Resort, Johannesburg
- ◆ CONFERENCE
Uranium 2017 International Conference
11–15 September 2017, Swakopmund Hotel, Swakopmund, Namibia
- ◆ SYMPOSIUM
AfriRock 2017: ISRM International Symposium '*Rock Mechanics for Africa*'
30 September–6 October 2017, Cape Town Convention Centre, Cape Town
- ◆ CONFERENCE
AMI Precious Metals 2017 'The Precious Metals Development Network (PMDN)'
17–20 October 2017, Protea Hotel Ranch Resort, Polokwane
- ◆ CONFERENCE
7th International Platinum Conference
18–20 October 2017, Protea Hotel Ranch Resort, Polokwane
- ◆ COLLOQUIUM
14th Annual Student Colloquium
25 October 2017, Johannesburg



For further information contact:

Conferencing, SAIMM
P O Box 61127, Marshalltown 2107
Tel: (011) 834-1273/7
Fax: (011) 833-8156 or (011) 838-5923
E-mail: raymond@saimm.co.za



New Concept Mining

Integrated systems of safety and support

Welded Mesh



Roofbolts

Pre-Stressing
Units



Early Warning
Devices



Safety Nets